

UNIVERSITÀ DEGLI STUDI DI PISA

FACOLTÀ DI SCIENZE MATEMATICHE, FISICHE E NATURALI

PHD THESIS IN APPLIED PHYSICS

APRIL 2006

**The control of the Virgo interferometer  
for gravitational wave detection**

SUPERVISORS:

**Prof. Francesco Fidecaro**

**Dr. Matteo Barsuglia**

AUTHOR:

**Lisa Barsotti**



*...e ho scritto nemmeno la metà di ciò che ho visto.*

Marco Polo



# Acknowledgments

My first idea was to use this space to thank one by one all the people who somehow helped me in my 3 years long journey. I realize only now that this would imply to write some other tens of pages, and the dimension of this thesis would become quite embarrassing. So, I need to change strategy.

To Francesco, the I.N.F.N Pisa group and the Virgo collaboration, thank you for believing in me and giving me the possibility to present our results to the international scientific community.

To Edwige and all the commissioning group, thanks for the time spent together in control room (e in particolare per le cene a base di pizza e cinque e cinque).

To Giovanni, thank you for all your useful suggestions.

To Raffaele, thank you for always being around.

To Paolo, thank you for answering to all my daily questions.

To Adalberto, thank you for showing me the enthusiasm with which this work should be done.

To Maddalena, thanks for your encouragement and all the nice figures you did for me (and all the pictures you took when I was sleeping on my chair..).

To Gary and Matt, for your patience with my poor English. Thank you.

To Matt, thank you also for all your *Evans comments*. And thank you more for showing me how many things can enter in a small zaino.

*Al mio maestro*, Stefano, thanks. I hope to have understood the message.

At the end, *al mio capo*, Matteo. Per questa nostra mitica avventura insieme, grazie. Grazie di tutto.



# Contents

<b>1</b>	<b>Gravitational Waves and their Detection</b>	<b>13</b>
1.1	Sources . . . . .	13
1.1.1	Supernovae . . . . .	15
1.1.2	Coalescent Binaries . . . . .	15
1.1.3	Neutron Stars . . . . .	16
1.1.4	Stochastic Background . . . . .	17
1.2	Interferometric detection . . . . .	17
1.2.1	Michelson interferometer . . . . .	18
1.2.2	Fabry-Perot cavities . . . . .	22
1.2.3	Recycling of the light . . . . .	23
1.2.4	Seismic noise . . . . .	24
1.2.5	Thermal noise . . . . .	25
<b>2</b>	<b>The VIRGO Detector</b>	<b>27</b>
2.1	Injection system . . . . .	30
2.1.1	The input mode-cleaner . . . . .	30
2.2	Detection system . . . . .	31
2.3	The Mirrors . . . . .	33
2.4	Mirror suspension system . . . . .	34
2.4.1	Main elements of the SA . . . . .	35
2.4.2	Inertial damping . . . . .	37
2.4.3	Local control . . . . .	38
2.4.4	Performance . . . . .	38
2.5	Control and Signal Readout . . . . .	40
2.5.1	Longitudinal control . . . . .	40
2.5.2	Frequency stabilization . . . . .	43
2.5.3	Angular control . . . . .	46

2.5.4	The control chain . . . . .	48
<b>3</b>	<b>The Longitudinal Control</b>	<b>53</b>
3.1	Specifications . . . . .	54
3.1.1	Common arm length and recycling cavity length . . . . .	55
3.1.2	Differential arm length and differential Michelson length . . . . .	56
3.2	Single Fabry-Perot Cavity . . . . .	57
3.2.1	Pound-Drever-Hall locking . . . . .	57
3.2.2	Lock acquisition . . . . .	61
3.3	The Recombined ITF . . . . .	64
3.3.1	Operating Point . . . . .	65
3.3.2	Locking Scheme . . . . .	66
3.4	The Recycled ITF . . . . .	68
3.4.1	Locking signal readout . . . . .	71
3.4.2	Lock acquisition . . . . .	74
<b>4</b>	<b>The Commissioning of Virgo</b>	<b>83</b>
4.0.3	Commissioning evolution and commissioning runs . . . . .	86
4.0.4	The new suspended input bench . . . . .	87
4.1	Simulation of the Interferometer . . . . .	88
<b>5</b>	<b>Control of the 3 km cavity</b>	<b>91</b>
5.1	Experimental set-up . . . . .	91
5.2	Single Arm Locking Scheme . . . . .	94
5.3	Simulation . . . . .	95
5.3.1	Cavity length reconstruction . . . . .	96
5.3.2	Feedback to the mirror . . . . .	99
5.3.3	Locking efficiency . . . . .	100
5.4	Check of sub-system specifications . . . . .	101
5.5	Experimental performance . . . . .	106
5.6	Commissioning of the single arm . . . . .	108
5.6.1	Lock of the OMC . . . . .	108
5.6.2	Automatic alignment (AA) . . . . .	110
5.6.3	Frequency stabilization . . . . .	111
5.6.4	Noise reduction . . . . .	112

<b>6</b>	<b>Control of the Fabry-Perot Michelson (<i>recombined</i>) interferometer</b>	<b>117</b>
6.1	Lock acquisition strategy for the Recombined ITF . . . . .	118
6.1.1	Simulation . . . . .	118
6.1.2	The <i>Anderson offset</i> . . . . .	123
6.1.3	Simulation . . . . .	125
6.1.4	Generation Mechanism . . . . .	125
6.1.5	How to deal with the Anderson offset . . . . .	129
6.2	Linear Locking . . . . .	131
6.2.1	Controller . . . . .	132
6.3	Commissioning of the Recombined ITF . . . . .	133
6.3.1	Suspension hierarchical control . . . . .	134
6.4	Sensitivity and Noise Budget . . . . .	135
6.4.1	Commissioning run C4 . . . . .	136
6.4.2	Commissioning run C5 . . . . .	138
<b>7</b>	<b>Lock Acquisition of the Recycled Interferometer</b>	<b>141</b>
7.1	Simulation of the multi-step technique . . . . .	142
7.2	Use of the $3\Omega$ signal . . . . .	143
7.3	Experimental tests of the multi-step technique - I . . . . .	146
7.3.1	Lock of the central ITF (CITF) . . . . .	147
7.3.2	<i>Step3North</i> and <i>Step3West</i> . . . . .	149
7.4	Absence of optical isolation between input mode-cleaner and interferometer . . . . .	151
7.5	The control of the power recycling mirror . . . . .	154
7.6	Experimental tests of the multi-step technique - II . . . . .	156
7.7	<i>Variable finesse</i> locking technique . . . . .	157
7.7.1	Reconstruction of the lengths . . . . .	159
7.8	Feedback to the mirrors . . . . .	164
7.8.1	The control filters . . . . .	164
7.8.2	The driving matrix . . . . .	164
7.9	Misalignment of the PR mirror . . . . .	166
7.10	Moving to the dark fringe . . . . .	166
7.10.1	The dynamic sensing matrix . . . . .	168
7.11	The frequency stabilization servo . . . . .	169
7.12	Lock acquisition sequence . . . . .	171
7.12.1	Evolution of the recycling gain . . . . .	173

<b>8</b>	<b>Commissioning of the recycled ITF</b>	<b>177</b>
8.1	Commissioning run C5 . . . . .	178
8.1.1	C5 noise budget . . . . .	179
8.2	Instabilities in the ITF power . . . . .	180
8.3	Interferometer automation . . . . .	183
8.4	Automatic alignment . . . . .	183
8.5	Reduction of the longitudinal control noise . . . . .	185
8.5.1	Use of more sensitive signals . . . . .	186
8.5.2	Optimization of the control filters . . . . .	189
8.5.3	Subtraction of the beam-splitter control noise . . . . .	190
8.5.4	Next steps . . . . .	192
8.6	Commissioning run C6 . . . . .	193
8.6.1	Duty-cycle and lock losses . . . . .	194
8.6.2	C6 noise budget . . . . .	195
8.7	Commissioning run C7 . . . . .	196
8.7.1	Noise hunting: next steps . . . . .	198
<b>A</b>	<b>Definition of Acronyms</b>	<b>203</b>
<b>B</b>	<b>Fabry-Perot cavities</b>	<b>205</b>
B.1	The reflected field . . . . .	207
B.2	Operating point . . . . .	208
<b>C</b>	<b>Pound-Drever-Hall signals in the recombined ITF</b>	<b>211</b>
C.1	Asymmetric-Port signals . . . . .	211
C.2	Reflected port signals . . . . .	214

# Introduction

The General Theory of Relativity developed by Einstein in 1916 predicts the existence of *gravitational waves*. These can be described as perturbations of the space-time metric propagating at the speed of light, produced by the acceleration of bodies. Because of the weakness of the intensity of a gravitational wave, only astrophysical sources are able to produce effects detectable on Earth. Since relative positions of free masses are determined by the the space-time metric, in principle it is possible to experimentally detect the passage of a gravitational wave by measuring the relative distance variation induced in a set of suspended masses. However, the foreseen intensities of gravitational waves are so weak that length variations of the order of  $10^{-18}$  m have to be measured. Because of the difficulties connected with such small effects, no direct detection has been accomplished so far. Indirect proof of the existence of gravitational waves was discovered by J.H.Taylor and R.A.Hulse in 1992 [1]. They measured energy losses in the orbit of the binary system PSR 1913+16, which turned out to be in agreement with results predicted by the gravitational waves emission.

The idea of using interferometry to detect gravitational waves started to be explored a few decades ago [2], and in the last few years a number of ground-based laser interferometers have been put into operation: the three LIGO interferometers in the United States [3], the German-British GEO600 [4], the Japanese TAMA300 [5] and the Italian-French VIRGO [6].

VIRGO is a recycled Michelson interferometer (ITF) where each arm is replaced by a 3 km long Fabry-Perot cavity. It is located at the European Gravitational Observatory (EGO), close to Cascina (Pisa, Italy), and is designed to detect gravitational waves emitted by astrophysical sources. Mirrors are suspended in vacuum by high performance suspensions, so that detection is possibly starting from very low frequencies, a few Hz, up to a few kHz. The main subsystems of VIRGO were tested in 2001-2002, during the commissioning of the *Central Interferometer*, a 6m-long

recycled Michelson interferometer [52]. In September 2003, following completion of the installation of the 3km arms, VIRGO commissioning began, with the goal of putting into operation the detector and reaching the designed sensitivity in a few years.

The work presented in this thesis is focused on the *longitudinal control* of VIRGO, that is the control of the position of the test masses along the light beam direction. Relative displacements of the mirrors need to be actively controlled in order to bring and keep the interferometer on its working point. By following the evolution of the VIRGO commissioning, suitable strategies have been designed and applied to different optical configurations: a single Fabry-Perot cavity, a Michelson interferometer with Fabry-Perot cavities in the arms (the *recombined* ITF), and finally the full interferometer (the *recycled* ITF). Once the lock of full VIRGO was achieved, the process of investigating and reducing the longitudinal control noises coupled into the dark fringe signal began.

*Chapter 1* describes possible sources of gravitational waves, and principles of their interferometric detection. VIRGO is presented in *Chapter 2*, where the main characteristics of the sub-systems composing the detector are shown. In *Chapter 3* the main aspects of longitudinal control of the ITF are introduced, together with techniques currently adopted by detectors with an optical configuration similar to VIRGO, such as LIGO and TAMA. The organization of the commissioning of Virgo is summarized in *Chapters 4*. *Chapters 5* and *6* describe the design and implementation of the longitudinal control in simpler optical configurations: the single Fabry-Perot cavity and the recombined ITF.

The longitudinal control of VIRGO in its final recycled configuration, achieved by means of an original technique called *variable finesse* locking, is detailed in *Chapter 7*. Development and application of this technique represents the primary original contribution of the author to the Virgo commissioning effort. The concept behind the technique is new to the community and broadly applicable to existing and future gravitational wave detectors.

Performance of the VIRGO interferometer and progress in its sensitivity are finally shown in *Chapter 8* on the basis of the data collected in three commissioning runs, the last one performed in September 2005.

# Chapter 1

## Gravitational Waves and their Detection

This first chapter briefly presents the expected gravitational waves sources and the principle of interferometric detection with a simple Michelson ITF. The optical configuration adopted in Virgo, a power recycled Michelson ITF with Fabry-Perot cavities in the arms, allows the interferometer sensitivity to be increased.

The three fundamental noises limiting the present interferometric detectors sensitivity are *seismic noise*, *thermal noise* and *shot noise*. In particular, their contributions to the Virgo design sensitivity, better described in the next chapter, are introduced here.

### 1.1 Sources

Gravitational waves are produced by the acceleration of bodies. The conservation of mass-energy, linear momentum, and angular momentum makes null the gravitational wave emission associated with monopole, dipole, and magnetic dipole radiation, respectively. The first contribution different from zero is given by the quadrupole moment, producing an oscillating strain transverse to the propagation direction:

$$h_{jk} = \frac{2G}{rc^4} \left[ \frac{d^2 Q_{jk}}{dt^2} \right]_{t-r/c} \quad (1.1)$$

where  $r$  is the distance between the source and the observer and  $Q_{jk}$  is the reduced quadrupole term associated with the mass distribution  $\rho(\vec{x})$ :

$$Q_{jk} = \int \rho(\vec{x}) \left[ x_j x_k - \frac{1}{3} \delta_{ij} |\vec{x}|^2 \right] d|\vec{x}|$$

The quadrupole moment of a body of mass  $M$  and characteristic radius  $R$  can be estimated as:

$$Q \sim MR^2 \quad (1.2)$$

The order of magnitude of the strain amplitude of the gravitational wave is therefore:

$$h \sim \frac{1}{r} \frac{G}{c^4} \frac{MR^2}{T^2} \quad (1.3)$$

where  $T$  is the typical time of variation of the mass distribution. In terms of the typical speed of displacement  $v = R/T$ ,  $h$  can be written as:

$$h \sim \frac{1}{r} \frac{GM}{c^2} \left( \frac{v}{c} \right)^2 \quad (1.4)$$

The designed sensitivity of detectors such as LIGO and VIRGO is of the order of  $10^{-22}$  at 100 Hz. Since  $G/c^2$  is a very small quantity<sup>1</sup>, only astrophysical massive bodies can be detected on Earth.

On the base of the time evolution of the emitted signals, gravitational waves sources can be classified as:

- **impulsive sources** (*bursts*), such as supernovae explosions or coalescent binary systems at their merging phase;
- **quasi-periodic sources**, such as coalescent binary systems;
- **periodic sources**, such as spinning neutron stars;
- **stochastic background** from either astrophysical or cosmologic origin.

In the following sections, detection rates of gravitational waves for *first generation* interferometers, operative in the short term (2006-2007), are described.

---

<sup>1</sup>  $\frac{G}{c^2} \sim 10^{-29} \frac{m^3}{s^4 Kg}$

### 1.1.1 Supernovae

The gravitational wave signal associated with a supernova explosion typically lasts a few ms, and thus exhibits a broadband high-frequency spectrum, extending to a few Hz. The amplitude of the emitted pulse is modeled as:

$$h \sim 2.7 \times 10^{-20} \left( \frac{\Delta E}{M_{\odot} c^2} \right)^{1/2} \left( \frac{1 \text{ kHz}}{f} \right)^{1/2} \left( \frac{10 \text{ Mpc}}{r} \right) \quad (1.5)$$

where  $f$  is the inverse of the collapse time and  $\Delta E$  is the energy emitted in the form of a gravitational wave, depending both on the collapse speed and its degree of asymmetry.

Advanced astrophysical simulations predict an emitted energy  $\Delta E/M_{\odot}c^2 \sim 10^{-6}$  [8]. This scarce value makes the amplitude too low to detect a supernova in the nearest galaxy cluster (Virgo), where several events per months are expected [7]. In our galaxy the expectation is reduced to only a few events per century, so that the first generation of interferometers are not supposed to detect more than one event every several years.

### 1.1.2 Coalescent Binaries

Gravitational waves are emitted by binary systems composed of compact objects: a couple of neutron stars (NS), a couple of black holes (BH), or one NS and one BH. Energy is progressively lost through gravitational radiation. The orbital radius is reduced accordingly, so that the emission frequency increases until the coalescence of the two bodies (corresponding to a frequency of about 1 kHz for NS-NS<sup>2</sup>). Binary systems can only be detected by ground-based interferometers in the last minutes of their life, when the emission frequency is higher than several Hz. The rate of available signals is therefore low, despite the large number of compact binary systems in the close universe.

The *horizon* is defined as the maximum distance to which an optimally positioned and oriented binary can be detected<sup>3</sup> with a minimum signal-over-noise ratio (SNR) of 8. The estimates of the event rate are affected by large uncertainties [10], as reported in table 1.1:

---

<sup>2</sup>The NS mass is known to be around  $1.4 M_{\odot}$ . For the BH mass,  $10 M_{\odot}$  will be used in the following pages.

<sup>3</sup>The effective range of the interferometer is also averaged over all sky positions and binary orientations, and is called the *inspiral range*. According to this definition, the inspiral range has to be multiplied by a factor  $\sim \sqrt{5}$  to obtain the *horizon*.)

*1<sup>st</sup> generation interferometers*

	Horizon	Rates (min - max)
NS-NS	30 Mpc	0.0003/yr – 0.3/yr
NS-BH	40 Mpc	0.0004/yr – 0.5/yr
BH-BH	145 Mpc	0.001/yr – 3/yr

Table 1.1: Horizon and detection rates for coalescing binary sources.

Recent studies [11] suggest that short-hard gamma rays bursts result from a long-lived progenitor system, such as NS-NS or NS-BH binary systems. According to this model, the predicted rate of such signals, detectable by first generation interferometers, increases from one every few years to several events per year. One of the most relevant aspects in the detection of compact objects inspiral signals is that their waveforms are considered to be known well enough to be detected by a matching filter technique.

### 1.1.3 Neutron Stars

Spinning neutron stars with asymmetry around the rotation axis emit gravitational waves mainly at twice their rotation frequency. About  $10^9$  spinning neutron stars are present in our galaxy, with rotation frequencies of between fractions of Hz and a few hundred Hz [9]. However, only a few percent neutron stars emit at a frequency  $f$  within the detection band of ground-based interferometers, above the tens of Hz. The amplitude strength of the emitted signal is:

$$h \sim 10^{-21} \epsilon \left( \frac{f}{100 \text{ Hz}} \right)^2 \left( \frac{10 \text{ kpc}}{r} \right) \quad (1.6)$$

where  $\epsilon$  is the asymmetry of the mass distribution. The SNR for a signal emitted at a fixed frequency is proportional to the square root of the integration time, so that it can be increased by means of a long observation time. The problem is that the Doppler effect due to the Earth motion has to be subtracted independently for every direction of the sky, requiring very large calculation times.

Upper limits for  $\epsilon$  can be given by attributing the entire spin-down of the pulsar to the gravitational wave emission. For the Crab pulsar, spinning at 30 Hz, this is  $7 \times 10^{-4}$ , corresponding to a maximum possible amplitude around  $10^{-24}$  for a gravitational wave signal emitted at 60 Hz. Under this hypothesis, such a signal could be detected in one year by first generation interferometric ground-based detectors [12].

### 1.1.4 Stochastic Background

Gravitational waves are also present in the Universe as a stochastic background. They are formed by a superposition of random signals coming from all directions at all frequencies, produced by both cosmological and astrophysical sources.

The proposed detection scheme generally involves correlation techniques between different detectors. As shown in [13], the stochastic background floor is presently estimated to be well below the sensitivity of even the more advanced detectors, so that this gravitational wave source can be sensibly neglected for first generation interferometers.

As shown in the previous sections, the rate estimates are very uncertain and largely depend on the applied model. It is therefore very difficult to evaluate the effective possibility of detecting gravitational waves with the current interferometric detectors.

The most promising sources are presently considered to be coalescent binaries, with several events per year according to recent encouraging studies. Moreover, the evolution of the signals can be well modeled, so that a matching filter technique can be applied.

## 1.2 Interferometric detection

A gravitational wave detector has to convert the effects produced by a gravitational wave passage into a measurable signal. The base of the interferometric detection of all the large-scale instruments is a Michelson ITF with suspended mirrors [14], illuminated by a monochromatic laser source. Above the frequency of the pendulum resonance, suspended mirrors behave as free masses, therefore forming a free falling reference system. The passage of a gravitational wave induces a change in the relative distance of the mirrors (see figure 1.1). A consequent variation occurs in the power transmitted at the anti-symmetric (ASY) port, detected by means of a photo-detector (see figure 1.2).

Different variants of this scheme are currently adopted by the interferometric detectors all over the world.

Virgo, in particular, is a power-recycling Michelson interferometer with Fabry-Perot cavities in the arms. The reasons for this choice are briefly summarized here.

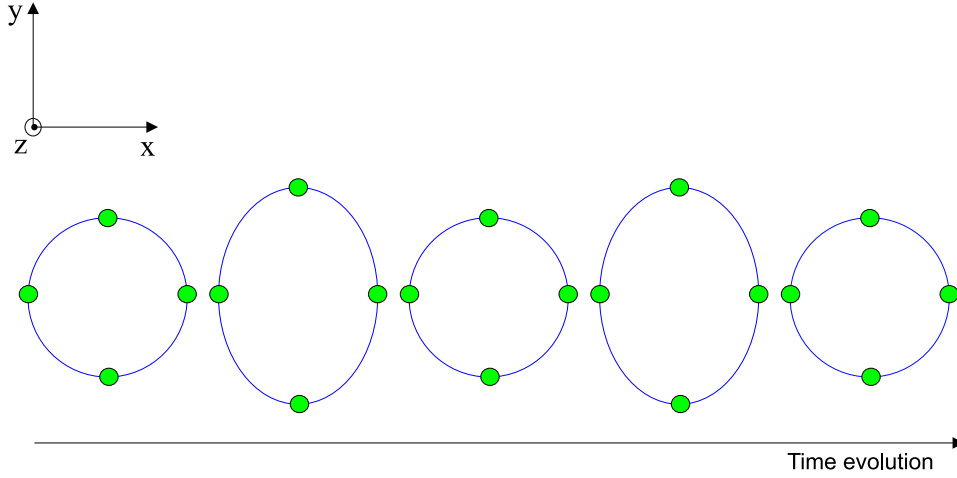


Figure 1.1: Effect of a gravitational wave propagating along the  $z$  direction on free falling test masses placed in a ring.

### 1.2.1 Michelson interferometer

The Michelson ITF optical configuration is shown in figure 1.3. A beam splitter mirror (BS) is impinged upon by a laser source. Half of the light is transmitted along the laser propagation direction, the other half is reflected into the perpendicular axis. The two beams are reflected from the input ( $IM_1$ ) and end ( $IM_2$ ) mirrors and recombined at the BS.

The passage of a gravitational wave with amplitude strain  $h$  and optimal orientation and polarization produces a differential change  $\Delta l_{GW}$  in the length of the two Michelson arms, which is given by:

$$\Delta l_{GW} = l_0 h \quad (1.7)$$

where  $l_0$  is the average of two unperturbed arm lengths.  $\Delta l_{GW}$  is measured by means of the differential phase shift  $\Delta\phi_{GW}$  induced in the light returning to the BS:

$$\Delta\phi_{GW} = \frac{4\pi}{\lambda} h l_0 \quad (1.8)$$

where  $\lambda$  is the wavelength of the laser light.

The wave passage can be detected by a photo-detector placed at the ASY port.

Given a power  $P_{in}$  impinging on the BS, the power detected by the photo-detector is:

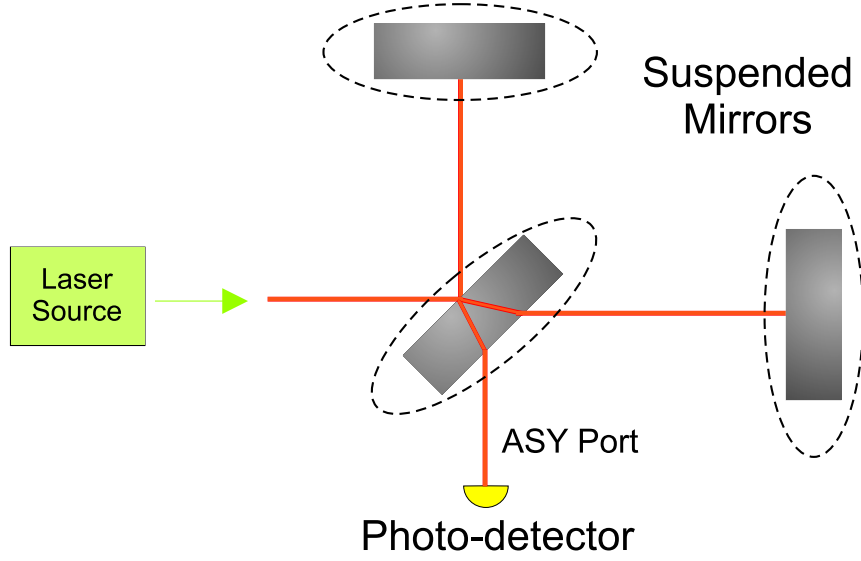


Figure 1.2: Base of the interferometric detection: a Michelson ITF with suspended mirrors, illuminated by a monochromatic laser source. The beam transmitted to the anti-symmetric port is measured by a photo-detector.

$$P_{asy} = r_{BS}t_{BS}[r_1^2 + r_2^2 + 2r_1r_2\cos(2k\Delta l)]P_{in} \quad (1.9)$$

where  $r_1$  and  $r_2$  are the amplitude reflectivity of the end mirrors,  $r_{BS} = t_{BS} = \sqrt{2}/2$  are the reflectivity and the transmissivity of the BS and  $\delta l = l_1 - l_2$  is the length asymmetry between the two arms. By introducing the contrast defect  $C$ , defined as

$$C = \frac{P_{asy}^{max} - P_{asy}^{min}}{P_{asy}^{max} + P_{asy}^{min}} = \frac{2r_1r_2}{r_1^2 + r_2^2} \quad (1.10)$$

equation 1.9 becomes:

$$P_{asy} = \frac{P_{in}}{2}[1 + C\cos(2k\Delta l)] \quad (1.11)$$

The length asymmetry  $\Delta l$  between the two arms is composed of a static difference  $\Delta l_{12}$  plus the perturbation due to the passage of the gravitational wave  $\delta l_{GW}$ . By considering the corresponding phase shift and keeping the first order terms, the previous expression can be written as:

$$P_{asy} = \frac{P_{in}}{2}[1 + C\cos(\Delta\phi_{12}) - C\sin(\Delta\phi_{12})\delta\phi_{GW}] \quad (1.12)$$

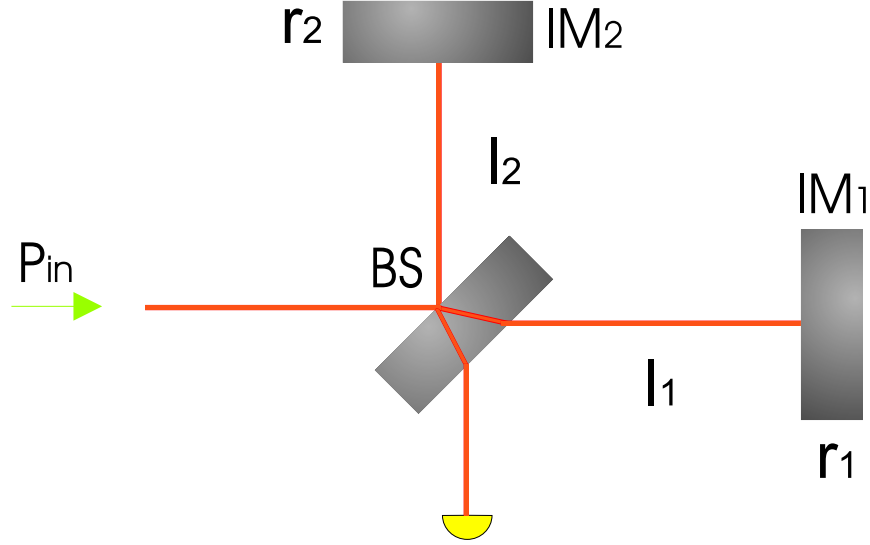


Figure 1.3: Michelson ITF optical configuration.

The variation produced by the wave passage is therefore:

$$\delta P_{GW} = -\frac{P_{in}}{2} C \sin(\Delta\phi_{12}) \delta\phi_{GW} \quad (1.13)$$

In order to get the maximum sensitivity of the detector,  $\Delta\phi_{12}$  has to be optimized considering the limitation imposed by the **shot-noise** on the minimum detectable phase. The number of photons  $N$  with frequency  $\omega/2\pi$  impinging upon the photodiode having efficiency  $\eta$  in the interval time  $\delta t$  is given by:

$$N = \frac{\eta P_{asy} \Delta t}{\hbar P_{Planck} \omega} \quad (1.14)$$

Because of the Poissonian statistics associated with this process,  $\delta N_{shot} \sim \sqrt{N}$ , so that the corresponding variation induced in the power is:

$$\delta P_{shot} = \sqrt{\frac{P_{asy} \hbar P_{Planck} \omega}{\eta \Delta t}} \quad (1.15)$$

The optimal value of  $\Delta\phi_{12}$  can be found by maximizing the signal to noise ratio:

$$\frac{S}{N} = \frac{|\delta P_{GW}|}{\delta P_{shot}} \quad (1.16)$$

The dark fringe condition of the instrument, that is null power going out of the ITF at the ASY port, corresponds to:

$$\cos\Delta\phi_{12} \approx -1, \quad \text{with } C \sim 1 \quad (1.17)$$

The minimum value of the detectable phase is found by imposing  $S/N = 1$ . Its corresponding linear spectral density is:

$$\tilde{\delta}\phi_{GW}^{min} = \sqrt{\frac{\hbar_{Planck}\omega}{\eta P_{in}}} \quad (1.18)$$

and, in terms of the amplitude strain linear spectral density of the gravitational wave:

$$\tilde{h}^{min} = \frac{1}{2\pi(l_1 + l_2)} \sqrt{\frac{\hbar_{Planck}c\lambda}{P_{in}\eta}} / \sqrt{\text{Hz}} \quad (1.19)$$

By considering the nominal Virgo parameters ( $\lambda = 1.064 \mu\text{m}$ ,  $\eta \approx 0.78$  and incoming power  $P = 20$  Watt), and by assuming 3 km long Michelson arms ( $l_1 \sim l_2 \sim 3$  km):

$$\tilde{h}^{min} \sim 2 \cdot 10^{-21} / \sqrt{\text{Hz}} \quad (1.20)$$

The linear spectral density of a typical gravitational wave signal with amplitude  $h = h_{RMS} \sim 10^{-22}$  in a frequency band  $\Delta f \sim 100$  Hz is instead:

$$\tilde{h}^{GW} \sim 10^{-23} / \sqrt{\text{Hz}} \quad (1.21)$$

which is a few orders of magnitude less.

According to the previous equation, in order to further improve the sensitivity, longer arms and more powerful lasers should be used. However, arms longer than a few kilometers are not feasible, and more powerful lasers do not satisfy the required frequency stability. The alternatives adopted by Virgo and other detectors consist of amplifying the phase shift accumulated in the arms by means of *Fabry-Perot* cavities, and increasing the power inside the ITF by using the technique of *power-recycling*.

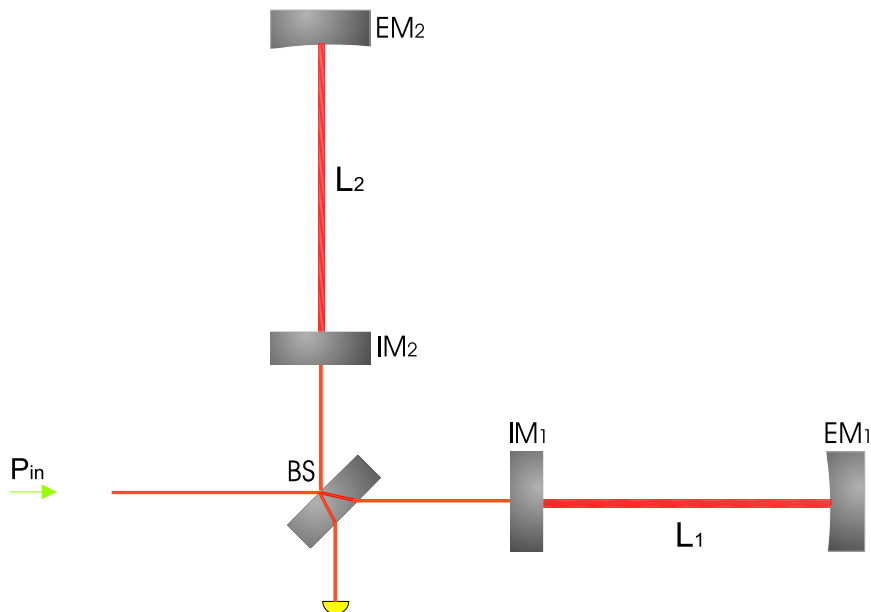


Figure 1.4: Optical configuration consisting of Michelson ITF with Fabry-Perot cavities in the arms.

### 1.2.2 Fabry-Perot cavities

In order to amplify the optical path of the light inside the ITF, Fabry-Perot cavities are inserted in the arms (see figure 1.4).

The response of a Fabry Perot cavity is detailed in appendix B. Its remarkable property is that when the cavity is at resonance the phase shift induced by the gravitational wave's passage is increased, with respect to the single mirror configuration, proportionally to the finesse  $\mathcal{F}$  of the cavity. The amplification given by the cavity is valid only if the period of the gravitational wave is longer than the storage time of the light inside the cavity itself.

The shot-noise limited sensitivity of a Michelson with Fabry-Perot cavities in the arms is:

$$\tilde{h}_{shot}(f) = \frac{1}{4(L_1 + L_2)\mathcal{F}} \sqrt{2h_{Planck} \frac{\lambda c}{\eta P_{in}} \sqrt{1 + \left(\frac{f}{f_{FP}}\right)^2}} / \sqrt{\text{Hz}} \quad (1.22)$$

where  $L_1$  and  $L_2$  are the lengths of the two cavities and  $f_{FP} = c/4L\mathcal{F}$  is the Fabry-Perot cut-off frequency.

For Virgo, the finesse of the Fabry-Perot cavities is  $\mathcal{F} = 50$  [17].

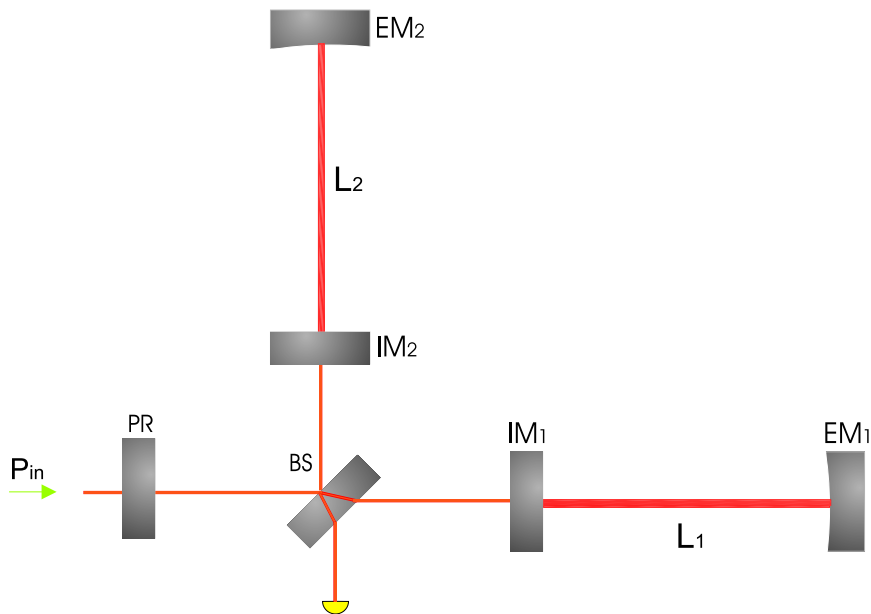


Figure 1.5: Optical configuration consisting of a power recycling Michelson ITF with Fabry-Perot cavities in the arms.

### 1.2.3 Recycling of the light

In order to increase the power impinging on the BS, the technique of light recycling is applied [15] [16]. As shown before, the dark fringe condition is required to optimize the interferometer response. This implies that, by assuming low light losses and a good contrast of the ITF, a large part of the light is reflected back from the ITF to the laser source. By appropriately placing a *power recycling* mirror (PR) in between the BS and the laser source (see figure 1.5), the light reflected from the ITF can be made resonant with the incoming one. The maximum *recycling gain*  $G_{rec}$  of the circulating power depends on the total losses of the ITF  $L_{tot}$ :

$$G_{rec} \approx \frac{1}{L_{tot}}$$

and it can therefore be increased by reducing, as much as possible, the losses of the ITF. For Virgo, the nominal recycling gain is  $G_{rec} \approx 50$  [17]. The resulting configuration is therefore a power recycling Michelson ITF with Fabry-Perot cavities in the arms.

With respect to the previous configuration, without PR, the shot-noise limit

improves by a factor  $1/\sqrt{G_{ric}}$ :

$$\tilde{h}_{shot}(f) = \frac{1}{4(L_1 + L_2)\mathcal{F}} \sqrt{2h_{Planck} \frac{\lambda c}{\eta G_{ric} P_{in}}} \sqrt{1 + \left(\frac{f}{f_{FP}}\right)^2} / \sqrt{\text{Hz}} \quad (1.23)$$

According to the Virgo parameters, the linear spectral density of the shot noise is of the order of  $10^{-23}/\sqrt{\text{Hz}}$ , two orders of magnitude less than would be obtained in simple Michelson configuration. The shot noise limits the Virgo sensitivity at high frequency, starting from 500-600 Hz.

The other limiting *fundamental* noise sources in the low and mid frequency region for this kind of detector are *seismic noise* and *thermal noise*. These are described in the next paragraphs.

#### 1.2.4 Seismic noise

The seismic noise transferred from the ground to the mirrors is the low frequency limiting noise source for interferometric detection. The amplitude and spectrum of the seismic noise of the ground where the ITF is located are strongly dependent on its geologic conformation and on human activities, but is always several orders of magnitudes higher than the required sensitivity. For instance, on the Virgo site, the contribution of the seismic noise at  $f \geq 0.5$  Hz is:

$$\tilde{h}_{sism}(f) \sim 10^{-9} \left(\frac{1 \text{ Hz}}{f}\right)^2 / \sqrt{\text{Hz}}$$

Therefore, without a high performance mirror suspension system, detection would not be possible.

The simplest system is to suspend the mirrors of the ITF to pendulums. Above its resonance frequency  $f_0$ , a simple pendulum is actually a second order low pass filter, so that the pendulum displacement  $x(f)$  is depressed with respect to the displacement of the pendulum suspension point  $x_{susp}(f)$ . In terms of their linear spectral density, it can be written as:

$$\frac{\tilde{x}(f)}{\tilde{x}_{susp}(f)} = -\frac{f_0^2}{f^2} \quad (1.24)$$

On the basis of this principle, different solutions are currently adopted by ground-based interferometric detectors. As described in the next chapter, Virgo uses the Superattenuators, high performance multi-pendulum stages. The detection is therefore enabled down to 4 Hz. At that frequency the *newtonian noise*, induced by local gravity field fluctuations, is a limiting noise source as well.

### 1.2.5 Thermal noise

Thermal noise is another fundamental noise source limiting interferometric detection. A system in thermal equilibrium with the environment is affected by state fluctuations, connected with dissipation phenomena. In the mechanical system constituted by the mirror suspension, internal dissipation is present both in the mirror substrates and in the suspension wires.

The suspended mirror can be assimilated to a simple pendulum of mass  $m$ , having a resonant angular frequency  $\omega_0$  immersed in a thermal background at the temperature  $T$ . In the hypothesis of dissipation due to the material structure, the equation of the pendulum motion can be modeled in the frequency domain by including an imaginary part  $\phi(\omega)$  in the Hook law [19]:

$$\ddot{x}(\omega) + \omega_0^2[1 + i\phi(\omega)]x(\omega) = F/m \quad (1.25)$$

Experimentally,  $\phi(\omega) \sim 10^{-6}$ .

The system dynamics and the frequency spectrum of the thermal noise can be connected by means of the *fluctuation and dissipation theorem* [18]:

$$S_{\dot{x}} = 2k_B T \text{Re}(Y(\omega)) \quad (1.26)$$

where  $Y(\omega) = \dot{x}/F$ . For a low loss oscillator,  $Q = \phi^{-1}(\omega_0)$ , so that the thermal noise spectrum of the oscillator can be written as:

$$\tilde{x}_{term}(\omega) = \sqrt{\frac{4k_B T \omega_0^2}{mQ\omega} \frac{1}{(\omega^2 - \omega_0^2)^2 + \frac{\omega_0^4}{Q^2}}}$$

The frequency dependence of the thermal noise is therefore:

- $\propto \omega^{-1/2}$ , when  $\omega \ll \omega_0$ ;
- $\propto \omega^{-5/2}$ , when  $\omega \gg \omega_0$

The limit in detector sensitivity due to thermal noise is mainly dependent on the structure of the adopted suspension mirror. In Virgo pendulum movements have very high  $Q$  ( $\sim 10^6$ ) resonant frequencies below 10 Hz. The transverse *violins* modes are present starting from a few hundreds of Hz, the vertical ones are around a few tens of Hz, with  $Q \sim 10^5$ . Internal vibrational modes of the mirrors are of the order of a few kHz, with  $Q \sim 10^6$ . As will be shown in the next chapter, thermal

noise limits the Virgo sensitivity curve from 4 Hz to 500 Hz.

Not fundamental but *technical* noises, mainly connected with the control of the instrument, are the limiting sources of noise in the preliminary *commissioning phase* of any interferometric detector. Some of the noises presently limiting the Virgo sensitivity curve will be described in the next chapters. All of these noises are supposed to be reduced below the required level by the end of the commissioning phase.

## Chapter 2

# The VIRGO Detector

Virgo is located in the plain of Cascina, near Pisa (see figure 2.1).



Figure 2.1: The Virgo site.

All of the large optics are suspended in an ultra-high vacuum system by the so-called *superattenuators*, multipendulum isolators able to greatly reduce seismic noise at a very low frequency, thus enabling a high sensitivity down to a few Hz.

The Virgo optical scheme is described in figure 2.2. The input beam is produced

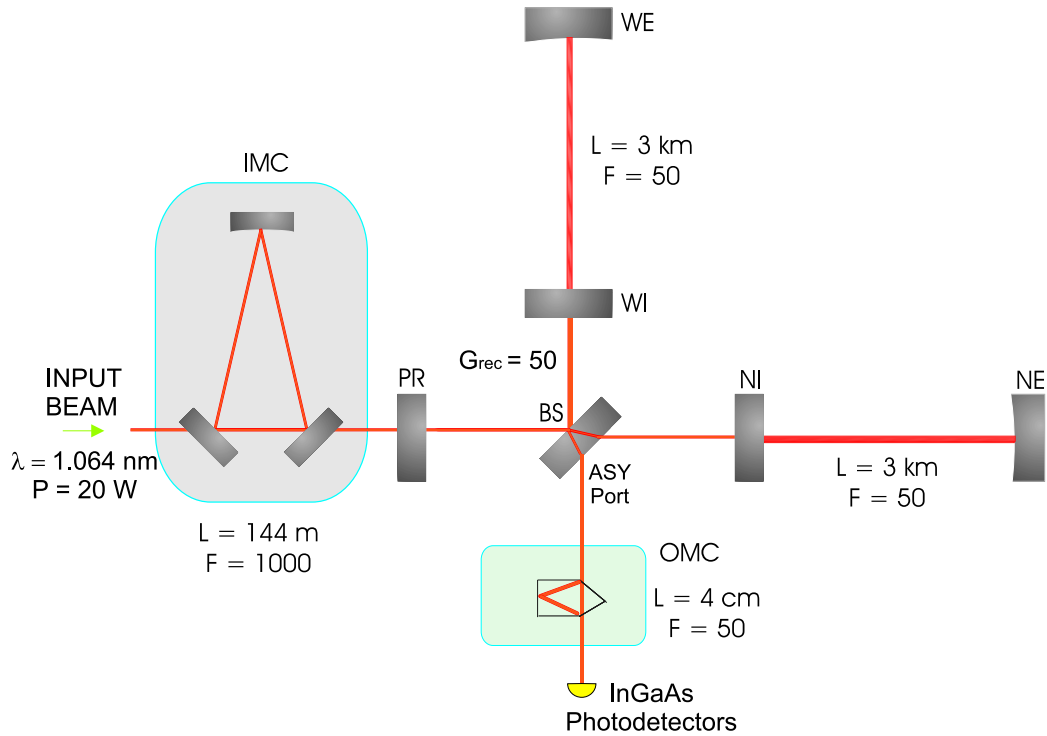


Figure 2.2: Virgo optical scheme.

by a laser Nd:Yag ( $\lambda = 1064 \text{ nm}$ ) with a power of 20 Watt. It is stabilized in frequency and position both by active controls and by passive filtering through a suspended triangular cavity, the *input mode-cleaner* (IMC). Mainly because of IMC internal losses, only half of the incoming power enters the interferometer, through the power-recycling mirror (PR). The beam is then split by the beam-splitter mirror (BS) into two beams which enter the two long Fabry-Perot cavities, to be then reflected to the BS, where they are recombined. Together with the Fabry-Perot Michelson ITF, the PR forms another Fabry-Perot cavity of about 12 m, the *power recycling cavity*, having a designed gain of 50. The power upon the BS is therefore 500 Watts.

The light passes many times through the optical substrates, so these need to be extremely pure, with low diffusion and low absorption. Mirror coatings also need to fulfill constraints on the wavefront surface deformation of less than  $\lambda/100$ . Total losses are around tens of ppm.

In order to improve the contrast, a suspended *output mode-cleaner* (OMC) filters the interferometer out-going main beam, which is then focalized onto InGaAs

photodiodes.

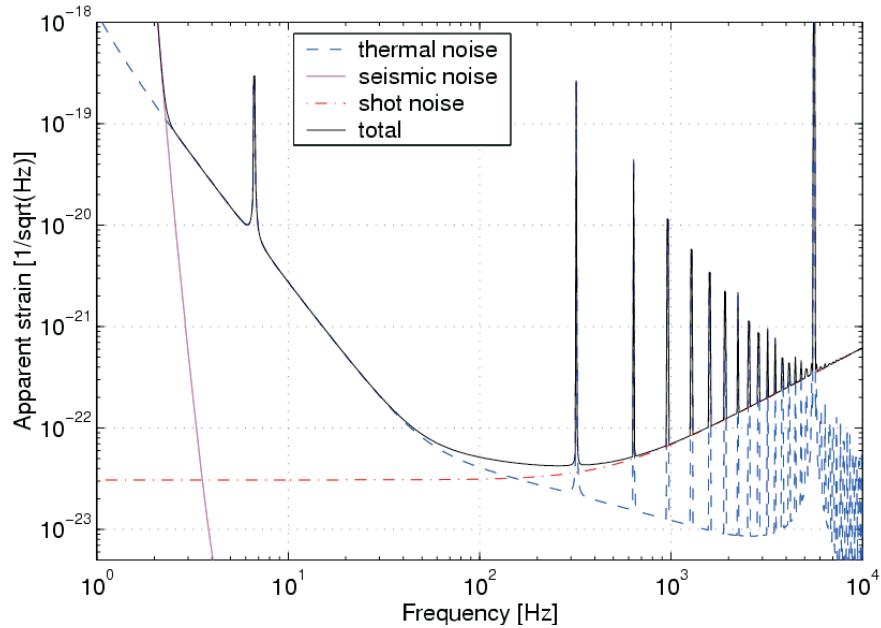


Figure 2.3: Virgo design sensitivity (See also the official Virgo Sensitivity curve repository <http://www.virgo.infn.it/senscurve>).

The noises limiting the Virgo design sensitivity, already described in the previous chapter, are:

- *seismic noise*, up to 4 Hz. The high superattenuator performance, guarantees a reduction by a factor of  $10^{15}$  at 10 Hz of the seismic noise transferred to the mirrors, enabling detection down to a very low frequency;
- *thermal noise*, dominating the sensitivity in the intermediate frequency region, with the pendulum thermal noise up to 30 Hz and the mirror thermal noise from 30 Hz to about 500 Hz;
- the *shot noise*, together with the low pass filter of the Fabry-Perot cavities above 500 Hz.

The Virgo design sensitivity, shown in figure 2.3, is planned to be:

$$\tilde{h} \simeq 3 \times 10^{-21} \frac{1}{\sqrt{\text{Hz}}} @ 10 \text{ Hz} \quad (2.1)$$

$$\tilde{h} \simeq 7 \times 10^{-23} \frac{1}{\sqrt{\text{Hz}}} @ 100 \text{ Hz} \quad (2.2)$$

## 2.1 Injection system

The *injection system* is the ensemble of components needed to produce the laser beam entering the ITF, to pre-stabilize it and to spatially adapt it to the ITF. The laser beam (20 Watts at  $\lambda = 1064 \text{ nm}$ ) is produced by a slave  $Nd : YVO_4$  high power laser injection-locked to a 1 Watts  $Nd : YAG$  master laser. The laser is located on a bench rigidly connected to the ground, in air. It is found in the laser laboratory, a room separated from the experimental main area. The laser light is modulated in phase at the frequencies of 6.26 MHz and 22 MHz (see sections 2.5.2 and 3.4.1) before passing through the *suspended injection bench*, placed in vacuum.

The following main components are located on the suspended external bench (see figure 2.4):

- the input and output plane mirrors, which compose the input mode-cleaner;
- two mirrors ( $M_5$  and  $M_6$ ) of a three mirror spherical telescope, which adapts the beam coming out the mode-cleaner (having a waist of 5 mm) to the ITF (waist  $w_0 = 2 \text{ cm}$  on the input mirrors). The last mirror of the telescope is the power recycling mirror;
- a 30 cm ultra-stable monolithic triangular cavity (RFC), used as reference for frequency pre-stabilization.

Together with the two mirrors located on the bench, a third suspended curved mirror at a distance of 144 m composes the IMC.

### 2.1.1 The input mode-cleaner

The main goal of the IMC is to filter the fluctuations of the laser beam position (*beam jitter*). The filtering properties of a suspended cavity can be explained in the following way. The fundamental mode of a misaligned laser beam is seen in the optical axis of a cavity as a linear combination of higher order modes in the base of the cavity itself. In the same way, any input jittering beam is seen by the cavity

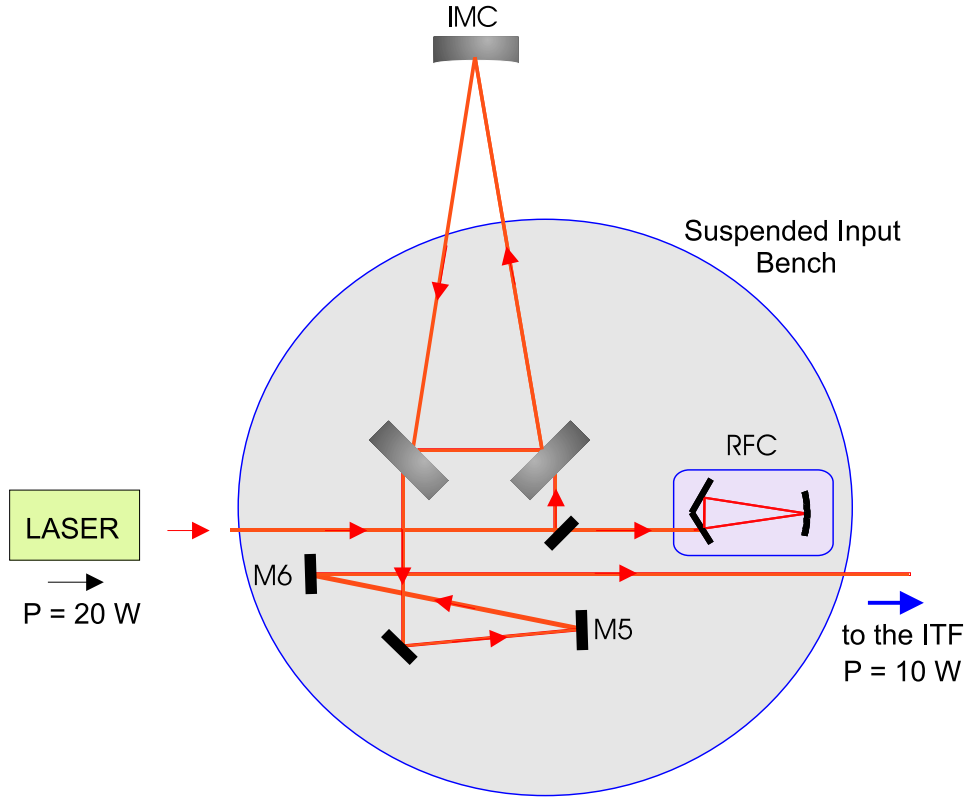


Figure 2.4: Schematic view of the injection system.

as composed of a linear combination of transverse modes. Since only the  $TEM_{00}$  mode is kept resonant and since the cavity is suspended, the IMC out-going beam is stable in position.

The Virgo IMC is a triangular Fabry-Perot cavity 144 m long, with finesse  $\mathcal{F} \sim 1000$ . The amplitude of the higher order modes entering the ITF is reduced by a factor  $10^3$ , reducing by the same amount the phase noise induced by the beam jitter. Moreover, as in all the Fabry-Perot cavities, the IMC is a first order low-pass filter for power and frequency fluctuations of the laser, with a cut-off frequency equal to its cavity pole ( $f_0 = \frac{c}{4L\mathcal{F}} \sim 500Hz$ ).

## 2.2 Detection system

The detection system is composed of two parts: the suspended detection bench, placed in vacuum, and the external detection bench, not suspended and in air. The

suspended detection bench mainly holds the output telescope and the *output mode cleaner* (OMC), a monolithic optical cavity 2.5 cm long of finesse  $\mathcal{F} = 50$ , which filters higher order modes of the beam, transmitting only the fundamental one. The main beam leaves the suspended bench to reach the external bench, where a set of InGaAS photodiodes ( $B1$ ) are located in order to detect the signal. About 1% of the beam coming out of the anti-symmetric port is directly detected by a different photodiode ( $B1p$ ), still located on the external bench, without passing through the OMC. The read-out scheme of the signals demodulated at the modulation frequency ( $\Omega$ -demodulated signals, see section 3.4.1) is done as shown in figure 2.6.

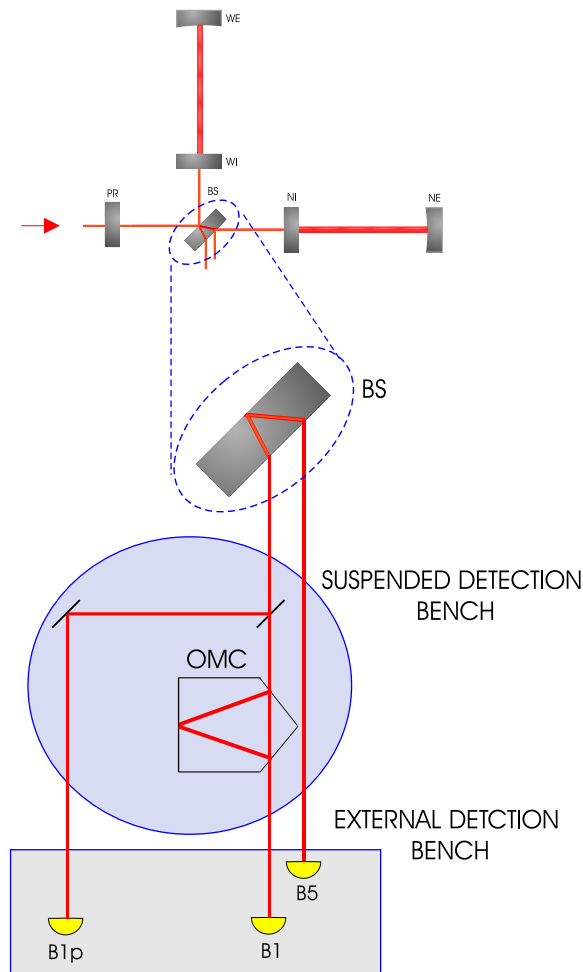


Figure 2.5: Scheme of the detection bench.

The signal produced by each photodiode first goes through a tuned preamplifier, attached to the photodiode, in order to amplify the  $\Omega$ -component with respect to

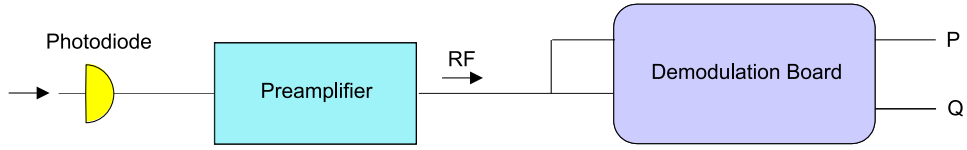


Figure 2.6: Read-out scheme of the signal demodulated at the modulation frequency.

the harmonics. Then, the RF signal coming from the preamplifier is split into two signals, both of which are transferred to the demodulation board 2.7. Each of these is passed through a mixer, using, as a second input signal, a  $\Omega$ -modulated reference signal provided by the Local Oscillator board (LO). One of the two LO signals is de-phased by  $90^\circ$  before entering the mixer, in order to produce, as output, the two signals, demodulated at  $0^\circ$  (in-phase,  $P$ ) and at  $90^\circ$  (quadrature-phase,  $Q$ ).

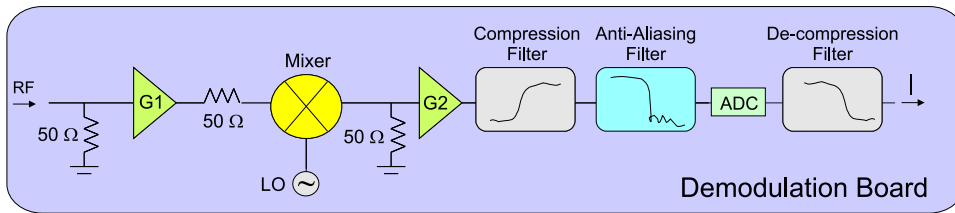


Figure 2.7: Schematic view of the demodulation board for one channel ( $P$ ). After the mixer, the signal is passed through a compression filter, which increases the gain above 10 Hz by a factor of 35. After an anti-aliasing filter, the signal is sampled at 20 kHz by a 16 bit ADC.

## 2.3 The Mirrors

The input and end mirrors of the ITF are fused silica cylinders, with a diameter of 35 cm and mass of 20 kg. The BS mirror is smaller, with a diameter of 23 cm and mass of 5 kg. The PR mirror has a mass of 20 kg, but presents a composite structure that is different with respect to all the other mirrors, as will be better described in chapter 6.

The main parameters of the mirrors: the radius of curvature (ROC), the reflectivity (R) and transmissivity (T), the losses of the high reflectivity (HR) and anti reflectivity (AR) coatings, are reported in the following tables.

	Shape 1 <sup>st</sup> face	Shape 2 <sup>nd</sup> face	R 1 <sup>st</sup> face	T 2 <sup>nd</sup> face	Losses HR	Losses AR
NI	Flat	Flat	132 ± 2 ppm	11.8 ± 0.03%	9.25 ppm	0.9 ppm
WI	Flat	Flat	171 ± 0.6 ppm	11.66 ± 0.02%	15.38 ppm	1.7 ppm

Table 2.1: Input mirror parameters

	Shape 1 <sup>st</sup> face	Shape 2 <sup>st</sup> face	T 2 <sup>st</sup> face	Losses HR
NE	Concave - ROC=3580 ± 17 m	Flat	42.9 ± 0.02 ppm	4.67 ppm
WE	Concave - ROC=3601 ± 15 m	Flat	38.3 ± 0.7 ppm	9.19 ppm

Table 2.2: End mirror parameters

	Shape 1 <sup>st</sup> face	Shape 2 <sup>nd</sup> face	R 1 <sup>st</sup> face	R 2 <sup>nd</sup> face	Losses HR	Losses AR
BS	Flat	Flat	50.25 ± 0.18%	519 ± 10 ppm	6.85 ppm	ppm

Table 2.3: BS mirror parameters

	Shape 1 <sup>st</sup> face	Shape 2 <sup>nd</sup> face	R 1 <sup>st</sup> face	T 2 <sup>nd</sup> face
PR	Convex - 4.3 ± 0.04 m	Flat	135 ± 2 ppm	7.3 ± 0.03 %

Table 2.4: PR mirror parameters

## 2.4 Mirror suspension system

The Virgo main optics are suspended in vacuum to multi-stages pendulums, the superattenuators (SA). The SA has been designed in order to greatly suppress the seismic noise transmitted to the mirror, with an attenuation factor of ten orders of magnitude starting at 4 Hz. Attenuation is needed not only for the horizontal displacement along the laser beam direction, but also, because of couplings between the different degrees of freedom, for the vertical displacement and the rotation of the pendulum chain around the vertical axis. The seismic attenuation is based on the following principles:

- the horizontal displacement of the suspension point of a pendulum is reduced by  $(f_0/f)^2$ , at a frequency  $f$  above the frequency  $f_0$  of the pendulum normal mode. With a n-stages pendulum it is possible to obtain a total attenuation factor proportional to  $1/f^{2n}$ , at frequencies above the highest resonance of the chain.
- the vertical displacement reduction is achieved having using triangular blade

springs that allow oscillation in the vertical direction;

- the rotational mode frequencies are confined below a few Hz by locating the mass in structures that have a high momentum of inertia. Moreover, a connection of two consecutive stages by suspension wire with small diameter and located close to their centers of mass makes it possible to reduce the frequency rotational modes.

### 2.4.1 Main elements of the SA

The main elements of the SA are (see figure 2.8):

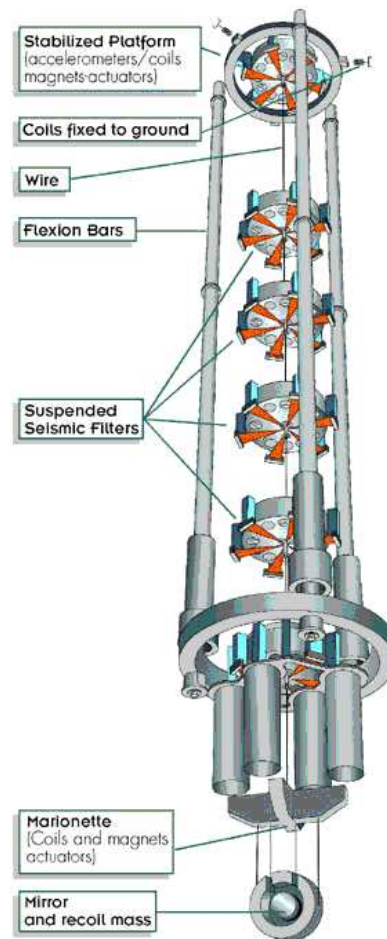


Figure 2.8: The Superattenuator.

**The inverted pendulum** The suspension point of the multi-stage pendulum is attached on the top of an *inverted pendulum* (IP), a 6 m structure constituted by three aluminium legs connected at the bottom by a flexible joint, supporting a metallic ring on its top. It acts as a second order low-pass filter above its resonance frequency, forming a "pre-isolator" for the seismic noise reaching the chain.

By modeling it as a massless vertical bar of length  $l$ , connected to the ground by an elastic joint with linear stiffness  $k$  and having a mass  $m$  at its top, the resonant frequency  $f_0$  can be written as:

$$f_0 = \frac{1}{2\pi} \sqrt{\frac{k}{m} - \frac{g}{l}} \quad (2.3)$$

For Virgo, by suitably tuning these parameters,  $f_0 \sim 30 \text{ mHz}$ .

**The seismic filters** A sequence of five mechanical filters replace the pendulum masses in the chain. Each mechanical filter is a rigid drum-shaped metallic structure with a total mass of about 100 kg. Each stage is connected to the following one through blade springs. Their stiffness is such that in the vertical direction the natural resonant frequency of the filter is about 1.5 Hz. The highest mode of the chain would be therefore fixed to 7.5 Hz, well above the designed detection frequency threshold of 4 Hz. A system of magnetic *anti-springs* has been developed to reduce the vertical stiffness of the blades and to confine the main vertical resonant frequency of each filter below the pendulum one [25].

**The last stage** The last stage of the SA consists of an element with four wings, called "marionette", from which four wires originate, supporting a reference mass and a mirror, as shown in figure 2.9. Displacement of the mirrors along the beam directions are controlled by means of four coils placed on the reference mass, acting on magnets glued to the back of the mirror. This guarantees that the reference mass recoils against the mirror, so that the center of mass of the reference mass-mirror system is at rest. The pendulum length of the last stage is about 0.7 m, corresponding at a resonance frequency along the beam direction of 0.6 Hz.

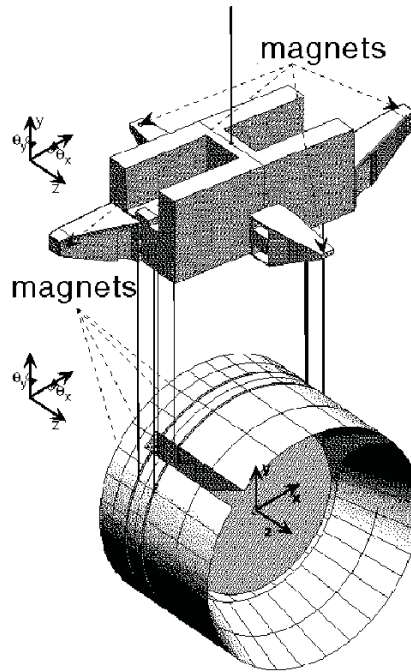


Figure 2.9: Last stage of the SA, formed by the marionette, the reference mass, and the mirror.

### 2.4.2 Inertial damping

The SA provides very good seismic isolation in the detection frequency band, above 4 Hz. However, at very low frequency, seismic noise is integrally transferred to the mirrors or even amplified by the 90 normal modes of the chain. An active control of the SA is therefore needed in order to reduce the residual motion of the suspended mirrors.

The basic idea of the *inertial damping* is to control the position of the suspension point using inertial sensors (accelerometers) to produce suitable error signals. However, accelerometers are sensitive to the acceleration of the pendulum, but not to the motion of the pendulum at constant velocity. For this reason such a kind of control would be unstable with respect to drifts. Position sensors based on Linear Voltage Differential Transformers (LVDT) are therefore used as well to extract suitable signals in order to extend the control bandwidth down to DC. LVDT are however referred to ground and may cause seismic noise injected in the feedback loop.

LVDT and accelerometers are mounted on the top stage of the SA in a triangular configuration. They produce signals sensitive to movements of the inverted

pendulum in all its three normal modes: two horizontal translations and the rotation around the vertical axis. These signals are appropriately combined, filtered and sent to pairs of coil-magnet actuators, able to move the inverted pendulum. Thanks to its very low stiffness, the inverted pendulum can be moved by applying very small forces. With a control bandwidth of 4 Hz, the seismic noise transferred to the mirror is reduced so as to produce displacement along the beam direction limited to a few microns.

### 2.4.3 Local control

The *inertial damping* previously described is not able to control some internal modes of the suspension involving the mirror. Moreover, a way to perform the alignment of the mirrors in DC is needed. A dedicated control system of the last stage of the superattenuator was therefore designed, in order to damp the angular and longitudinal modes involving the mirror and to be able to set and recover the reference angular position of each mirror. This *local control* system is referred to the ground.

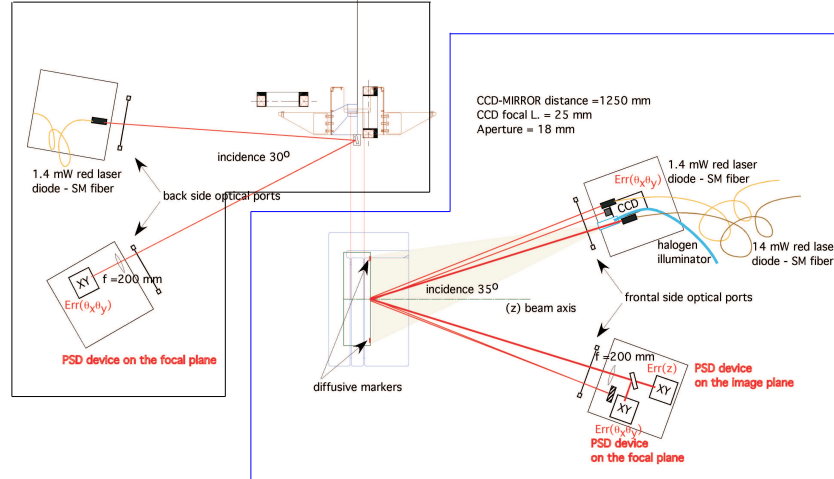
Longitudinal and angular local positions of the mirror are reconstructed measuring the position of a laser diode beam reflected by the mirror surface which works as an optical lever. A position sensing device (PSD) fixed to the tower is used (see figure 5.13). The marionette positions are measured through an additional optical lever reflected by a mirror attached to the bottom of the marionette. Four magnets are attached to the marionette and four coils are placed in front of them, at the level of the Filter 7. A similar system is made by four coils located on the reference mass, acting on four magnets glued to the back of the mirror. This guarantees the control of the mirror along the laser beam direction (*z-axis*), together with the control of rotations around the vertical axis (*yaw*) and around the axis perpendicular to the beam (*pitch*). A further reduction of longitudinal and angular motion of the mirror has been measured, below respectively, 1 micron and 1 microrad.

The local control system can not be used when the ITF is in its working condition because it uses ground as a reference. However, it plays a crucial role in damping the mirror oscillations in order to permit the engagement of longitudinal and angular *global* control systems.

### 2.4.4 Performance

The measurement of the SA seismic isolation was done with the the *Central Interferometer* (CITF) commissioned in 2001-2002. The CITF a power recycled Michelson ITF with 6 m long arms, which differs with respect to the final configuration for

## Readout of angular positions of the marionette



## Readout of angular and longitudinal positions of the mirror

Figure 2.10: Readout of mirror and marionette positions in the local control scheme.

the absence of the 3 km Fabry-Perot cavities, replaced by high reflectivity mirrors. The mirrors were suspended from the same SA as in Virgo. The CITF was kept locked on the dark fringe, so that any deviation from the destructive interference was compensated for by a feedback loop acting on one of the end mirrors. In this way, it could be used as a very sensitive instrument to measure the residual motion of the mirrors, in order to study the vibration isolation performance of the Virgo SA [25].

The measurement was done at a few Hz, where the displacement sensitivity of the CITF is around  $10^{-12} m/\sqrt{Hz}$ . In order to measure the filter chain attenuation, the SA was excited with sinusoidal lines with frequencies around 4 Hz, both in horizontal and vertical directions, acting at the level of the inverted pendulum. The motion transmitted to the mirror was measured by the feedback voltage applied to the end mirror to keep the CITF locked. Due to the strong attenuation of the SA, the mirror residual displacement at those frequencies was so small that it could not be distinguished from the CITF noise floor. As a consequence, only an upper limit of the horizontal and vertical attenuation was provided. The upper limits of the mirror

displacements along the beam, induced by vertical and horizontal ground vibrations, could be inferred by multiplying the standard input seismic noise detected at the top stage by the measured filter chain transmission. At 4 Hz, they are:

$$\tilde{z}_{ver} = 2 \cdot 10^{-17} \text{ m}/\sqrt{\text{Hz}} \quad (2.4)$$

$$\tilde{z}_{hor} = 4 \cdot 10^{-18} \text{ m}/\sqrt{\text{Hz}} \quad (2.5)$$

Both these upper limits are well below the thermal noise floor expected to limit the antenna sensitivity in the low frequency range. This result should guarantee that the seismic noise at the mirror level is completely negligible in all the Virgo detection band.

## 2.5 Control and Signal Readout

As described in the previous section, the SA provides very good seismic isolation in the detection frequency band above 4 Hz. At lower frequency, where the seismic noise is instead transferred to the mirror, the inertial damping and the local control system are able to keep longitudinal and angular displacements of the mirrors below the order of 1  $\mu\text{m}$  and 1  $\mu\text{rad}$  respectively. As will be detailed in the next sections, these levels of performance are quite far from those required to reach the design sensitivity. Active feedback control systems are therefore needed to *globally* control the position of the mirrors in their **longitudinal** and **angular** degrees of freedom. Moreover, an active frequency servo is needed to stabilize the laser frequency.

### 2.5.1 Longitudinal control

The nominal sensitivity of a power recycled Michelson ITF such as Virgo is achieved when the laser light is resonant in the optical cavities, and minimum possible light comes from the output port (*dark fringe*). In this condition, the ITF is said to be on its *operating point*. These conditions imply constraints on the tolerable fluctuations of the relative position of the mirrors.

As for other similar interferometric detectors, the longitudinal control scheme of Virgo is based on a standard Pound-Drever-Hall technique. By means of radio frequency modulation, signals sensitive to deviations of the relative position of the mirrors from the operating point can be detected at the output ports of the ITF by demodulation, as described in section 3.4.1. These error signals can be used *to lock* the ITF on its operating point by sending a feedback force on the mirrors,

computed using linear control theory. Several aspects considerably complicate this approach. In particular, the Pound-Drever-Hall technique provides signals sensitive to interferometer length variations only in the *steady-state* regime of the ITF, that is to say around its operating point.

Outside of this condition any useful error signal could be extracted. A suitable strategy needs therefore to be designed in order to bring the ITF from the initial uncontrolled state, where mirrors are freely swinging, to the locked state, where all the four lengths of the ITF are kept controlled on their operating point. The problem is usually referred to as *lock acquisition*, and the following chapters will be mostly dedicated to this topic.

### Longitudinal signal readout

In order to detect the gravitational wave signal, detection needs to be shifted from DC to higher frequencies, such as the radio frequency region. In fact, laser power fluctuation requirements<sup>1</sup> are too demanding to be fulfilled at low frequency. Furthermore, low frequency detection is limited by the  $1/f$  electronic noise.

According to the frontal modulation technique, the beam is phase modulated before entering the ITF. The modulation frequency is 6.26 MHz, tuned so that sidebands are in the IMC and are transmitted to the ITF. The output signal detected at the anti-symmetric port is then demodulated at the modulation frequency, so as to extract a signal sensitive to the ITF length variation induced by the gravitational wave's passage. Moreover, in order to achieve the design sensitivity the ITF needs to be kept on its operating point. This means to have the light resonant inside the cavities, and requires the active control of the main lengths of the ITF (*longitudinal control*), as will be described in the next chapter.

Photodiodes are placed at the different output ports of the ITF (in transmission from the end mirrors, in reflection from the ITF, and in reflection from the second face of the BS). By demodulation, Pound-Drever-Hall signals [21] [22] sensitive to the cavity length variations and suitable for control purposes are extracted. Since the control of the ITF lengths is the main subject of this thesis, the longitudinal signal readout is detailed here.

The modulation-demodulation technique can be described as follows. The incoming laser beam of angular frequency  $\omega_0 = 2\pi \times 3 \times 10^{14}$  rad/s is modulated in

---

<sup>1</sup>Laser power fluctuations couple with a detuning  $\Delta\phi$  to give a phase noise  $\Delta\phi$  present at the dark port of the ITF. In order to be shot-noise limited the following condition on the linear density power fluctuations  $\delta\hat{P}$  has to be verified:  $\delta\hat{P}/P = 10^{-8} \frac{1}{\sqrt{\text{Hz}}}$ .

phase at the radio frequency  $\Omega = 2\pi \times 6.26$  rad/s. The resulting electric field is given by:

$$E_{in} = E_0 e^{i(\omega_0 + m \cos \Omega)t} \quad (2.6)$$

which can be developed in terms of the  $n^{\text{th}}$ -order Bessel functions  $J_n$ , dependent on the modulation depth  $m$ :

$$E_{in} = E_0 \sum_{n=-\infty}^{n=+\infty} J_n(m) e^{i(\omega_0 + n\Omega)t} \quad (2.7)$$

Therefore the modulated beam is the sum of the carrier field with frequency  $\omega_0$ , and the sidebands fields, with frequency  $\omega_0 \pm n\Omega$ .

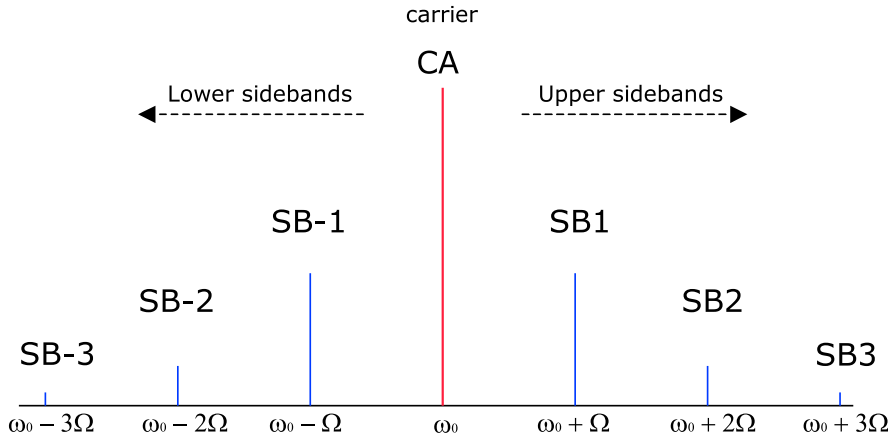


Figure 2.11: Modulation sidebands spaced by  $\Omega$  around the carrier frequency  $\omega_0$ .

Each field composing the incoming beam can be considered as independently propagating inside the ITF. In general, the signal  $S_{det}$  detected by a given photodiode can be written in the following form:

$$S_{det} = S_{DC} + I_{det,1} \cos(\Omega t) + Q_{det,1} \sin(\Omega t) + I_{det,2} \cos(2\Omega t) \quad (2.8)$$

$$+ Q_{det,2} \sin(2\Omega t) + \dots + I_{det,n} \cos(n\Omega t) + Q_{det,n} \sin(n\Omega t) \quad (2.9)$$

where the  $n\Omega$  components  $I_{det,n}$  and  $Q_{det,n}$  are the in-phase and in-quadrature phase signals<sup>2</sup> extracted by demodulating, at the  $n\Omega$  frequency, the radio frequency

<sup>2</sup>In the gravitational wave community is usually referred to as  $I$  component. In Virgo, instead,

signal impinging upon the photodiode (cfr. section 2.2). In particular, the demodulation at the modulation frequency  $\Omega$  generates Pound-Drever-Hall signals involved in the lengths control<sup>3</sup>. Their analytical expression can be computed by considering that, with  $|m| \ll 1$  as in Virgo, the sum in equation 2.7 can be truncated to contain only  $n = -1, 0, 1$ , so that the incoming modulated beam becomes:

$$E_{in} = E_0 [J_0(m) + iJ_1(m)e^{i\Omega t} + iJ_1(m)e^{-i\Omega t}] e^{i\omega_0 t} \quad (2.10)$$

$S_{det}$  can therefore be written in terms of the complex amplitudes of carrier ( $A_{det0}$ ) and first-order sidebands ( $A_{det1}$  and  $A_{det-1}$ ) as detected by the photodiode:

$$S_{det} \propto [A_{det0} + A_{det1}e^{i\Omega t} + A_{det-1}e^{-i\Omega t}e^{i\omega_0 t}]^2 \quad (2.11)$$

Consequently:

$$S_{det} \propto |A_{det0}|^2 + |A_{det1}|^2 + |A_{det-1}|^2 + 2\Re [A_{det-1}^* A_{det0} + A_{det0}^* A_{det1} e^{i\Omega t}] + o(2\Omega) \quad (2.12)$$

The corresponding in-phase and the quadrature-phase demodulated signals are<sup>4</sup>:

$$I_{det} = \frac{1}{T} \int S_{det} \cos(\Omega t) dt = \Re [A_{det-1}^* A_{det0} + A_{det0}^* A_{det1}] \quad (2.13)$$

$$Q_{det} = \frac{1}{T} \int S_{det} \sin(\Omega t) dt = -\Im [A_{det-1}^* A_{det0} + A_{det0}^* A_{det1}] \quad (2.14)$$

with  $T \gg 1/\Omega$ , so that only the lowest frequency component remains after integration.

Since these signals contain information about amplitude and phase of carrier and sidebands inside the ITF, that is to say on the state of the ITF itself, they can be used for feedback controls.

## 2.5.2 Frequency stabilization

Asymmetries between the two arms of the ITF, such as arm length difference  $\Delta L$ , finesse difference  $\Delta \mathcal{F}$  and losses difference  $\Delta L_{losses}$  make the anti-symmetric port the in-phase signal is known as  $P$  component (see section 2.2. Demodulated signals are labeled as  $ACp$  and  $ACq$ .

<sup>3</sup>At some output ports, even the  $2\Omega$  and the  $3\Omega$  signals are extracted. In particular, the  $3\Omega$  demodulated signal extracted in reflection from the ITF plays an important role in the Virgo locking scheme, as will be explained in the following chapters.

<sup>4</sup>Except where explicitly specified,  $I_{det}$  and  $Q_{det}$  will refer to the signals detected by demodulation at the modulation frequency  $\Omega$ .

signal sensitive to frequency fluctuations  $\tilde{\nu}$  of the input beam. The equivalent spectral density of the induced noise can be written as [33]:

$$\tilde{h}_{\delta\nu} = \frac{\delta\tilde{\nu}}{\nu} \left( \frac{\Delta L}{L} + \frac{\Delta\mathcal{F}}{\mathcal{F}} + \frac{\Delta L_{losses}}{L_{losses}} \right) \quad (2.15)$$

By assuming a total asymmetry of a few per cent, and in order to have  $\tilde{h}_{\delta\nu}$  lower than the designed sensitivity, frequency fluctuations requirements are:

$$\delta\tilde{\nu} \sim 10^{-5} Hz / \sqrt{Hz} @ 10 Hz \quad (2.16)$$

$$\delta\tilde{\nu} \sim 10^{-6} Hz / \sqrt{Hz} @ 100 Hz \quad (2.17)$$

Since the available lasers have a performance eight orders of magnitude worse than this, these requirements can only be fulfilled by an active *frequency stabilization*.

Frequency fluctuations are connected to cavity length fluctuations by:

$$\frac{\delta\tilde{\nu}}{\nu} = \frac{\delta\tilde{L}}{L} \quad (2.18)$$

The ITF itself, because of its kilometric length, provides, at a frequency above the internal resonances of the mirror suspensions, the best reference to stabilize the laser frequency. However, the ITF is a good reference only once it is kept controlled on its operating point, as described in the previous paragraph. In order to achieve this condition, the frequency noise level needs to already be reduced to a few Hz rms before entering the ITF. The frequency stabilization strategy was therefore designed in two steps [23] [24]:

- the frequency *pre-stabilization*, in order to reduce the frequency noise to a few Hz rms and to allow the ITF to be brought on its operating point;
- the *Second Stage of Frequency Stabilization*, engaged once the ITF is kept controlled on its operating point and the ITF itself is used as reference.

### Pre-stabilization

As already said, 22 MHz modulation frequency is applied to the beam before entering the ITF. 22 MHz sidebands are not resonant inside the IMC. By demodulation, a Pound-Drever-Hall signal is extracted in reflection from the IMC, and it used to pre-stabilize the laser frequency to the length of the IMC, up to a frequency of 300 kHz.

In order to reduce the low-frequency fluctuations, a fraction of the light impinging on the IMC is split off and injected into the RFC. Another Pound-Drever-Hall loop is used to control the length of the IMC with respect to the length of the ultra-stable RFC, for frequencies below 150 Hz.

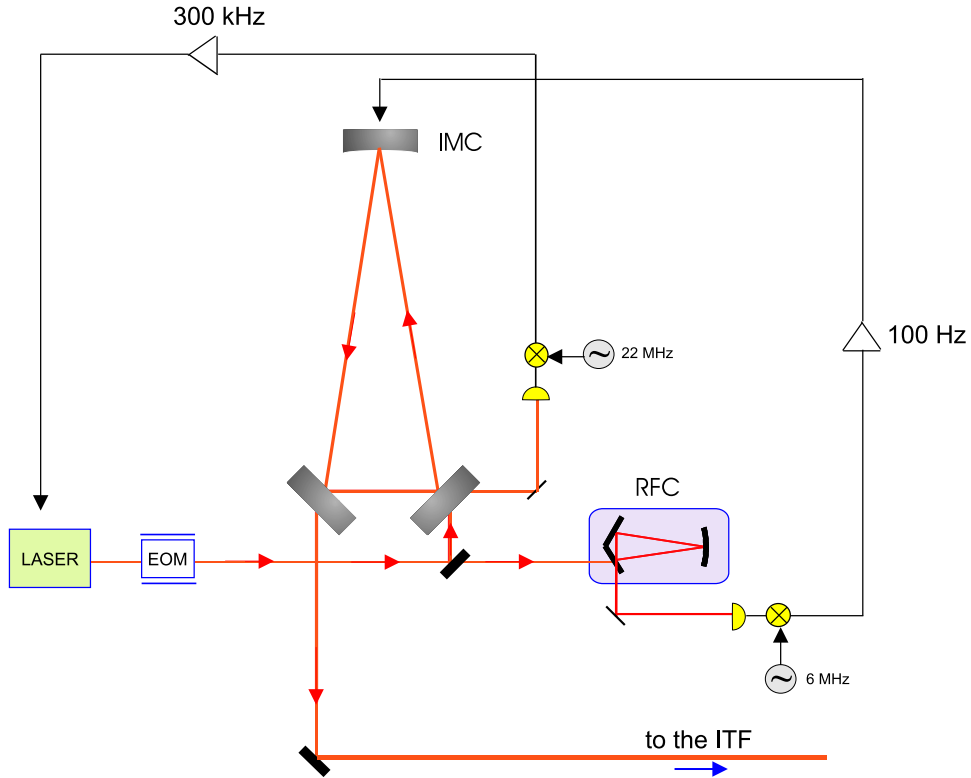


Figure 2.12: Scheme of the frequency pre-stabilization.

### The Second Stage of Frequency Stabilization (SSFS)

Once the ITF is on its operating point, the frequency stabilization scheme is changed and the ITF itself is used as reference to stabilize the laser frequency. The laser frequency remains stabilized on the IMC length. A Pound-Drever-Hall signal extracted from the ITF, sensitive to the common mode motion of the long cavities, is added into the error point of the IMC-loop to control the length of the IMC, typically with a bandwidth of 150 Hz.

Details of the SSFS schemes adopted in course of the commissioning activity are described in the next chapters.

	RMS [rad]
Power recycling	$10^{-7}$
Arm input mirrors	$2 \cdot 10^{-8}$
Arm end mirrors	$3 \cdot 10^{-9}$

Table 2.5: Requirement for RMS residual angular motion of all mirrors.

### 2.5.3 Angular control

The longitudinal control of the ITF is not sufficient to guarantee long stable operations of the detector and a high sensitivity. All the mirrors of the ITF have also to be well-aligned with respect to each other and with respect to the incoming beam. In fact, misalignments of the mirrors not only make impossible a long term longitudinal control, but also increase the coupling of other noise sources into the detector dark port. In particular, the main contribution comes from the coupling of angular motions with the input beam jitter. The jitter of the input beam is of the order of  $10^{-11} \text{ rad}/\sqrt{\text{Hz}}$ . By imposing that the phase noise induced by this coupling at the dark fringe port is at least three times lower than the requirements to reach the designed sensitivity, the limits for the residual RMS motion of all the mirrors are computed [17] (see table 2.5). As previously said, by using a local control system the position of the mirrors can be controlled with an accuracy of the order of  $1 \mu\text{rad}$ , which is not sufficient to fulfill the requirements. An angular control system which uses global error signals derived from the interferometer itself is therefore needed.

Angular misalignments of the mirror can be sensed using a *wave front sensing* technique, which provides error signals for the automatic alignment control. The sensors for the alignment control are *quadrant split photo detectors*. These are photodiodes with four separate elements, known as *quadrants*. Signals containing information about the relative position of the phase front between carrier and first-order sidebands inside the ITF can be obtained by demodulating the differential quadrant diode outputs at the modulation frequency. By opportunely arranging the optical setup so that a mirror misalignment produces a misalignment between carrier and sidebands inside the cavities, these signals can be applied as error signals for an automatic alignment system. For a single Fabry-Perot cavity, alignment control signals can be derived from the light reflected (*Ward* method [30]) or transmitted (*Anderson* method [31]) from the cavity. The automatic alignment scheme designed for Virgo [36] is based on the Anderson technique. The phase modulation of the incoming beam is done at such a frequency that the first transverse modes of the



## 2.5.4 The control chain

### The suspension control

All the signals extracted from the suspension sensors are acquired by Analog-to-Digital Converters (ADC) at 16 bit, and suitably recombined and filtered by a digital signal processor (DSP) running at 10 kHz. The computed correction signals are applied to coil-magnet actuators by Digital-to-Analog Converters (DAC) at 20 bit. Each coil actuator steering the Virgo optics is driven with a power voltage amplifier connected to the DAC board. Forces applied on suspended masses are directly proportional to the current flowing in the coil.

With a sampling frequency of 10 kHz, the input-to-output delay of the DSP system is about  $540 \mu\text{s}$ , taking into account the delay introduced by the anti-aliasing filter in front of the ADC and the corresponding reconstructing filter behind the DAC (see figure 2.14). This delay introduces phase lag in the control band of the mirrors of about  $20^\circ$  at 100 Hz, low enough to deal with typical control bandwidth lower than 10 Hz [27].

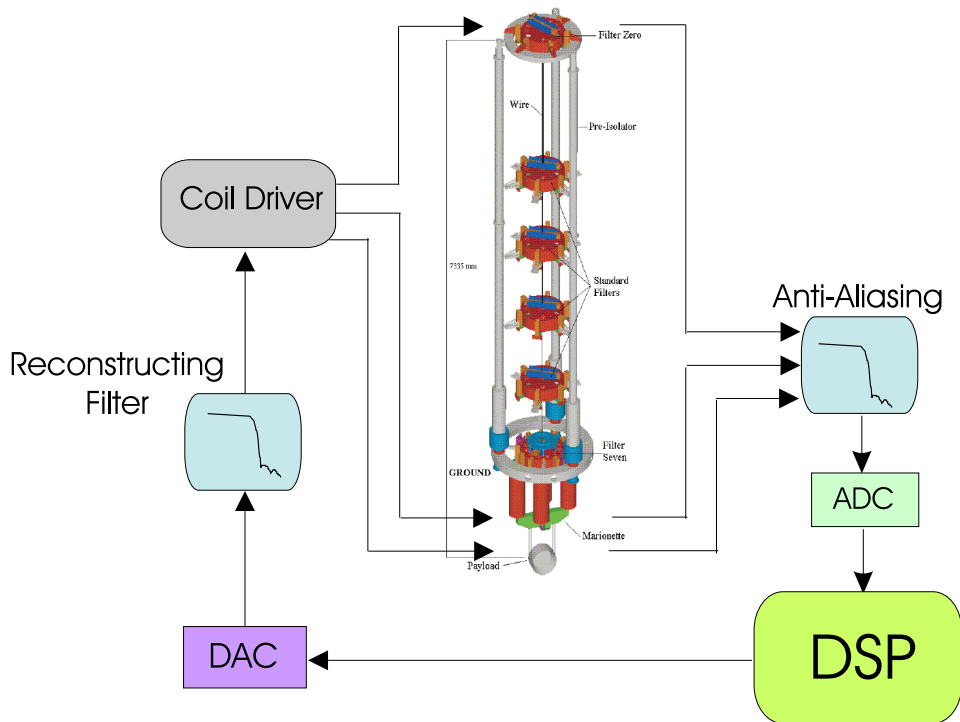


Figure 2.14: Suspension control chain.

## The global control

In both the longitudinal and the angular control of the ITF, the reconstruction of the error signals and the actuation at the suspension level involves the *Global Control* [29]. It is a real time control system<sup>6</sup>, which receives the digital signals extracted from the photo detectors (photodiodes and quadrants diodes), elaborates them by computing longitudinal and angular correction signals and passes them to the DSP of the suspensions and to the Virgo Data Acquisition system.

The *Locking* process runs at 10 kHz. In less than 100  $\mu$ s the signals have to be collected from the photodiodes, elaborated, filtered and sent by corrections to the mirror actuators (see figure 2.15) with control bandwidth of tens of Hz. Any jitter or delay can make the feedback loops unstable: this is most stringent constraint of the Global Control architecture (see next paragraph).

The *Alignment* process is similar like the Locking one, but since small bandwidths of the feedback loop are involved (a few Hz), it runs at 500 Hz.

The longitudinal control chain is summarized in figure 2.15. The minimum computational time delay accumulated in the longitudinal control chain can be estimated in the following way [38]:

- signals extracted from the ITF are sampled at a frequency  $f_s = 20$  kHz and averaged every two times. This adds a delay  $\Delta t_1 = 1/f_s = 50$   $\mu$ s;
- the Global Control runs at 10 kHz. By considering at least two sampling periods to process the signals and send them to the suspension crates, the accumulated time delay is  $\Delta t_2 = 200$   $\mu$ s;
- suspension DSP run at 10 kHz. One sampling period is needed to process the data, causing a time delay  $\Delta t_3 = 100$   $\mu$ s;

The estimated total delay  $\Delta t$  is at least:

$$\Delta t = \Delta t_1 + \Delta t_2 + \Delta t_3 = 350 \mu s$$

The corresponding phase delay at a given frequency  $f$  is:

$$\Delta \phi = 2\pi f \Delta t \tag{2.19}$$

At 500 Hz, for instance, the accumulated phase delay is  $63^\circ$ . By also considering phase delays added by the analog filters (anti-aliasing filters in front of the ADC and

---

<sup>6</sup>For a detailed description of the Global Control architecture see [28].

reconstruction filters behind the DAC), it turns out that the longitudinal control is stable only with a unity gain frequency lower than 100 Hz.

### **The *Global Control* architecture**

The Global Control hardware is made of three components: two crates housing the hardware dedicated to the fast feedback loops and a workstation in charge of monitoring the system. The main goal of this separation is to split different functions into independent processes, in order to minimize the interference on the fastest Locking loop.

The Locking process runs on a CES RIO8062 CPU. It has to collect photodiode signals from five boards and to send correction signals to other eight boards (one for each suspension mirror, one for the input bench, one for the data acquisition). The various Virgo sub-systems exchange digital data through Digital Optical Link (DOL), a VME/VSB module able to send some kilobytes of data over long distances (up to 3.2 km, which is the maximal distance between two buildings at the Virgo site) without latency. A central timing is needed to synchronize all of the Virgo sub-systems. This is achieved with a master clock, derived from a GPS system located in the central building, which drives a set of Timing boards. Since the CPU in question is not able to quickly read and write data, due to the large amount of boards with which it is connected, a faster data transfer board<sup>7</sup> has been developed in-house.

An analog CPU manages the Alignment process. Since there is only one optical fiber between the Global Control and the DSP of each suspension, alignment corrections are sent by means of the Locking process, without interfering with the Locking loop. A workstation is connected via Ethernet with the real time machine. As with all the other on-line applications, a client-server scheme is followed. The server acts on the hardware, and the interface with the user is done by the client in such a way that only one client (the Master) is able to change the server state.

The Global Control is composed of many servers, devoted to different functionalities. In particular, the Locking server handles two main tasks: the data exchange between the different sub-systems and the application of the control algorithms

---

<sup>7</sup>The Transparent Memory Board (TMB) is synchronized to the Timing board and is able to quickly transfer data from the VME to the VSB bus and vice versa, in order to fulfill the requirements.

which manipulate the collected data in order to compute correction signals. The structure is such that the developing of the control algorithms, written in *C++*, can be done by users, where the input-output data exchange is managed by experts.

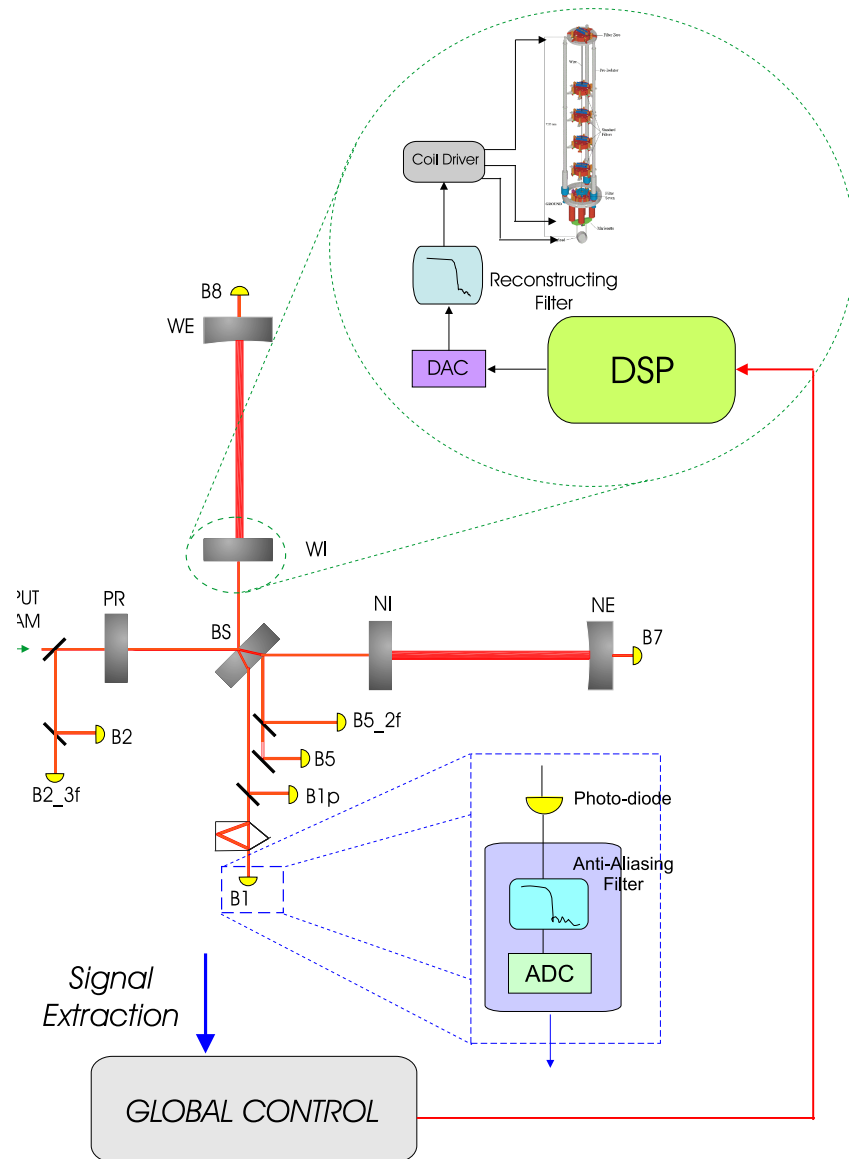


Figure 2.15: Longitudinal control chain. Signals extracted from the ITF by photodiodes are sent to the Global Control, which combines them in order to compute corrections, which are sent to the DSP of the involved suspensions.

## Chapter 3

# The Longitudinal Control

In order to be sensitive to the passage of a gravitational wave, the recycled ITF has to be locked on its operating point, with the laser light resonant inside the ITF and the ASY port on the dark fringe. In terms of carrier and sideband fields, it needs to have:

- the carrier field resonant inside the recycling cavity and in the Fabry-Perot arms, and onto the dark fringe at the ASY port;
- the modulation frequency  $\Omega$  is chosen so that the recycling cavity is resonant for the sidebands, where the arm cavities are nearly anti-resonant.

In order to fulfill these conditions, the maximum tolerable displacement of the mirrors around their operating point is of the order of  $10^{-12}$  m RMS, as is shown in section 3.1. This result cannot be achieved by locally controlling the mirrors. In fact, suspension system performance are such that longitudinal displacements of mirrors are a few orders of magnitude away from the requirements (for instance,  $10^{-6}$  m RMS for Virgo). A global control system of the mirrors is therefore needed.

By means of the frontal modulation scheme, Pound-Drever-Hall signals, sensitive to the cavity length variations around resonance, are extracted at the output ports of the ITF. After filtering these signals are sent to the actuators, which impress a force upon the mirrors in order to bring them to the required positions. However, Pound-Drever-Hall signals are not available far from the resonance, so that feedback loops to control the mirrors relative position can be engaged only when the ITF crosses its operating point. The recycled ITF is a multiple cavity system, where the stringent constraints on multiple degrees of freedom have to be fulfilled at the same time: the operating point is therefore crossed quite rarely. Moreover, the forces

which can be applied to the mirrors by the actuators are limited by the dynamics of the actuation system, so that forces typically not higher than a few tens of mN are available.

How to bring the ITF from the uncontrolled state where mirrors are freely swinging to its operating point is the goal of the *lock acquisition* strategies.

In order to introduce the base concepts related with lock acquisition it is more useful to deal first with a simpler optical configuration such as the single Fabry-Perot cavity, where only one degree of freedom (the relative distance between the two mirrors) has to be controlled.

As an intermediate step towards the final recycled configuration, the longitudinal control of the recombined ITF will be described. It is characterized by three degrees of freedom: the length of the two Fabry-Perot cavities and the differential length of the two short Michelson arms. Since they can be independently controlled, the locking problem is largely reduced to one of a single cavity.

The longitudinal control of the full recycled ITF will be discussed last. Solutions designed and adopted by detectors with an optical configuration similar to Virgo, like LIGO and Tama, will be shown.

### 3.1 Specifications

In order to keep the recycled ITF on its operating point, the four main lengths of the interferometer have to be controlled. They are defined as shown in figure 3.1, where the direction parallel to the incident beam is referred to as  $X$ , the perpendicular one as  $Y$ . The same indexes are used to indicate the lengths of each arm and phase shifts accumulated in a round-trip:

- the length of the two long arms is  $L_X$  and  $L_Y$ ;
- the length of the recycling cavity is  $l_+ = l_0 + \frac{l_X + l_Y}{2}$ ;
- the differential length of the Michelson arms is  $l_- = l_X - l_Y$ .

In some cases it will be useful to deal with common and differential arm lengths:

$$L_+ = L_X + L_Y \tag{3.1}$$

$$L_- = L_X - L_Y \tag{3.2}$$

$$\tag{3.3}$$

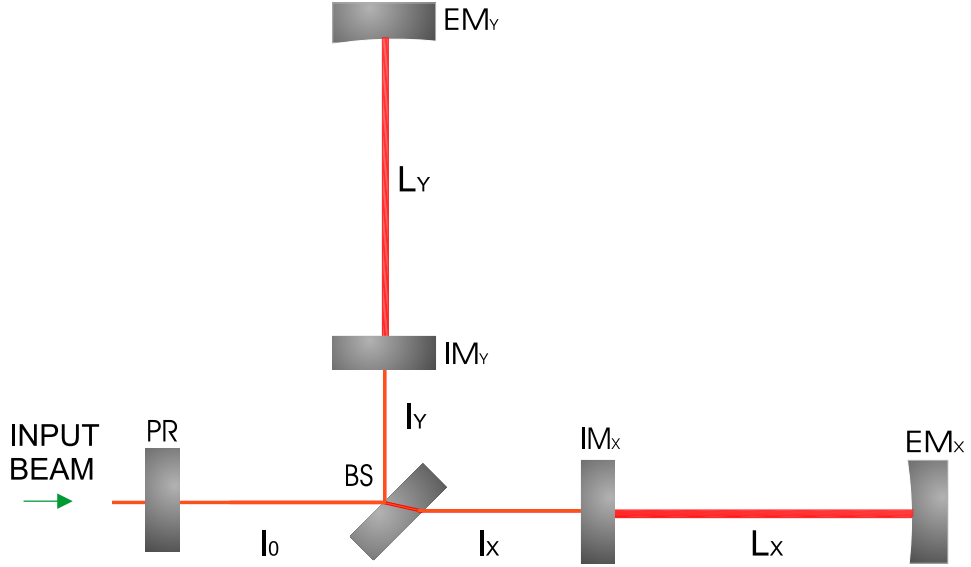


Figure 3.1: Lengths of the recycled ITF.

Requirements on the allowed mirror motion can be set in terms of the total rms deviation from resonance of the lengths of the ITF.

### 3.1.1 Common arm length and recycling cavity length

The resonance conditions for the recycling cavity put constraints on the length fluctuations of the recycling cavity and the common mode of the arms, since they have to be much lower (at least one order of magnitude) than the width of the recycling cavity resonance:

$$\Delta l_+ + \frac{2\mathcal{F}_{FP}}{\pi} \Delta L_+ < \frac{1}{10} \frac{\lambda}{4\mathcal{F}_{rec}} \quad (3.4)$$

where  $\mathcal{F}_{rec}$  is the finesse of the recycling cavity. With the Virgo parameters ( $\mathcal{F}_{rec} \sim 75$ ):

$$\Delta l_+ + \frac{2\mathcal{F}_{FP}}{\pi} \delta L_+ < 3.5 \times 10^{-10} m \text{ RMS} \quad (3.5)$$

Because of the enhancement due to the Fabry-Perot cavities, the constraint on  $\Delta L_+$  is more stringent:

$$\Delta l_+ < 2 \times 10^{-10} m \text{ RMS} \quad (3.6)$$

$$\Delta L_+ < 6 \times 10^{-12} m \text{ RMS} \quad (3.7)$$

### 3.1.2 Differential arm length and differential Michelson length

The most stringent constraint on the differential lengths of the ITF is due to the coupling between a dark fringe offset  $\Delta\phi$  and the power fluctuations of the laser. The spectral density of the phase noise produced by  $\Delta\phi$  is given by:

$$\delta\tilde{\phi} = \frac{\delta\tilde{P}}{P} \Delta\phi \quad (3.8)$$

where  $\delta\tilde{P}/P$  is the linear spectral density of the relative laser power fluctuations. In order to be shot-noise limited:

$$\delta\tilde{\phi} < \sqrt{\frac{2\hbar\nu}{\eta P}} \quad \implies \quad \Delta\phi < \frac{\sqrt{\frac{2\hbar\nu}{\eta P}}}{\delta\tilde{P}} P \quad (3.9)$$

By writing the dark fringe phase noise in terms of the corresponding variation of the interferometer lengths, the requirement is that<sup>1</sup>:

$$\Delta l_- + \frac{2\mathcal{F}_{FP}}{\pi} \Delta L_- < \frac{\frac{\lambda}{4\pi} \sqrt{\frac{2\hbar\nu}{\eta P}}}{\frac{\delta\tilde{P}}{P}} \quad (3.10)$$

With the nominal Virgo parameters (power impinging on the BS mirror  $P = 500$  W, power fluctuations  $\delta\tilde{P}/P = 10^{-8}1/\sqrt{\text{Hz}}$  and an efficiency  $\eta = 0.78$ ), constraints on  $\Delta L_-$  and  $\Delta l_-$  are:

$$\Delta l_- < 1 \times 10^{-9} m \text{ RMS} \quad (3.11)$$

$$\Delta L_- < 3 \times 10^{-11} m \text{ RMS} \quad (3.12)$$

The residual longitudinal motion of locally controlled mirrors are several orders of magnitude far from these requirements. A global longitudinal control system is therefore needed to fulfill the specifications.

---

<sup>1</sup>Constraints on  $\Delta L_-$  requiring that both the laser amplitude noise and the oscillator amplitude noise are a factor 10 below the sensitivity goal are discussed in [35].

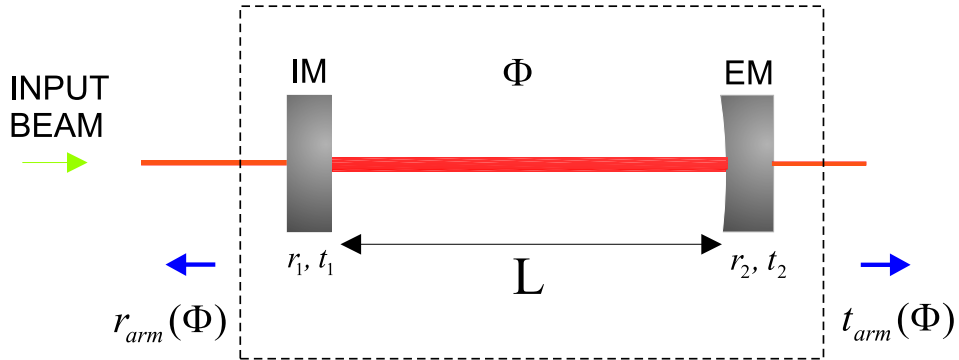


Figure 3.2: Single Fabry-Perot cavity optical configuration.

## 3.2 Single Fabry-Perot Cavity

In the following considerations the Fabry-Perot cavity is assumed to be well aligned and well mode-matched to the input beam. The input beam enters the Fabry-Perot cavity at the level of the input mirror (*IM*). The light exits in two ways: reflected back from the cavity, or transmitted from the cavity beyond the end mirror (*EM*) (see figure 3.2).

The relative distance  $L$  between the two mirrors of the Fabry-Perot cavity, along the longitudinal axis, has to be controlled in order to make the cavity resonant with the incoming light. The Pound-Drever-Hall locking technique is adopted, as detailed in the next paragraphs.

### 3.2.1 Pound-Drever-Hall locking

#### Reflection locking

The standard technique adopted in the keeping on resonance of a single Fabry-Perot cavity is use of the Pound-Drever-Hall signal extracted from the *reflected* beam. In order to find the analytical expression in-phase and in quadrature-phase equation 2.13 is applied. The amplitudes of the reflected fields of carrier ( $A_{ref0}$ ) and of upper and lower sidebands ( $A_{ref1}$  and  $A_{ref-1}$ ) are specified in terms of the amplitude reflectivity and transmissivity of the cavity (see appendix B).

Since the Pound-Drever-Hall signal is generated by the beating of the carrier with the static fields of first-order sidebands, which are almost all reflected by the cavity, they can be assumed to be constant. By considering the property of the

Bessel functions  $J_{-n}(m) = (-1)^n J_n(m)$ , these amplitudes are written as:

$$A_{ref1} = -A_{ref-1} \simeq EJ_1 t_{ref} \quad (3.13)$$

$$A_{ref0} = r_{arm,0}(\Phi_0) EJ_0 t_{ref} \quad (3.14)$$

where  $t_{ref}$  is the amplitude transmissivity of the optical path followed by the reflected beam from the input mirror to the photo-detector. By using equation 3.13, and since  $A_{ref-1}^* = A_{ref-1}$ :

$$[A_{ref-1}^* A_{ref0} + A_{ref0}^* A_{ref1}] = 2Im(A_{ref0}^* A_{ref1}) \quad (3.15)$$

The in-phase component vanishes, while the Pound-Drever-Hall survives in the quadrature-phase component. By combining all the previous formula:

$$Q_{ref} = -2t_{ref}^2 P_{in,0} \frac{J_1(m)}{J_0(m)} \Im m \left( \frac{r_1 - r_2 e^{i\Phi_0}}{1 - r_1 r_2 e^{i\Phi_0}} \right)^* \quad (3.16)$$

$$= 2t_{ref}^2 P_{in,0} \frac{J_1(m)}{J_0(m)} \Im m \left( \frac{r_1 - r_2 e^{i\Phi_0}}{1 - r_1 r_2 e^{i\Phi_0}} \right) \quad (3.17)$$

$$= -2t_{ref}^2 r_2 P_{in,0} \frac{J_1(m)}{J_0(m)} \frac{t_1^2}{|1 - r_1 r_2 e^{i\Phi_0}|^2} \text{sen}(\Phi_0) \quad (3.18)$$

where  $P_{in,0} = |E_{in}|^2 J_0^2(m)$  is the incoming carrier beam power.

By developing at the first order the previous expression with respect to a small phase variation  $\Delta\Phi_0$  around resonance ( $\Phi_0 = \bar{\Phi}_0 + \Delta\Phi_0$ , see appendix B), it can be demonstrated that  $Q_{ref}$  is proportional to the length variation  $\Delta L$ . The region of linearity approximately corresponds at half width at half maximum of resonance:

$$|\Delta L| < \frac{\lambda}{4\mathcal{F}} \quad (3.19)$$

as it can also be seen in figure 3.3:

Within this region the Pound-Drever-Hall signal can be written as:

$$Q_{ref} \simeq 4t_{ref}^2 r_2 \frac{\omega_0}{c} P_{in,0} \frac{2\mathcal{F}}{\pi} \frac{J_1(m)}{J_0(m)} \Delta L \quad (3.20)$$

and it can be filtered to derive a controller proportional to the relative velocity of the mirrors, according to linear control theory. The corresponding control signal can be sent to one of the two mirrors of the cavity in order to keep it on resonance.

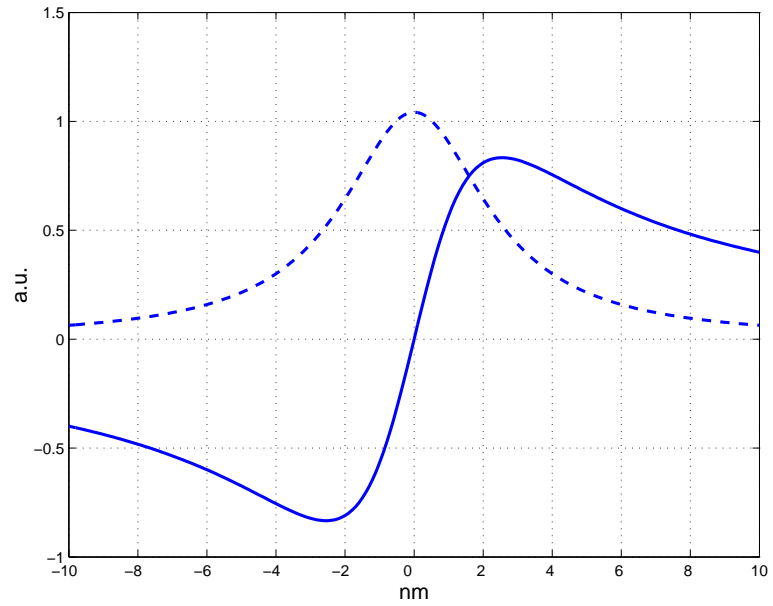


Figure 3.3: Pound-Drever-Hall signal (solid line) and transmitted power (dotted line).

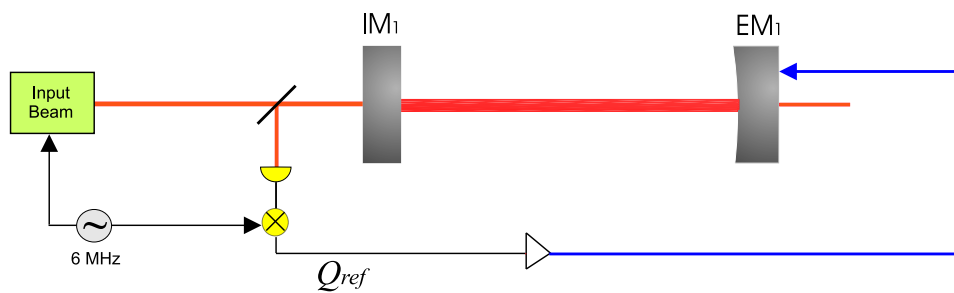


Figure 3.4: Locking scheme of the single Fabry-Perot cavity. The Pound-Drever-Hall signal extracted in reflection to the cavity is filtered in order to derive a controller proportional to the relative velocity of the mirrors, and it fed back to the end mirror.



Figure 3.5: Locking scheme of the single Fabry-Perot cavity. The Pound-Drever-Hall signal extracted in transmission to the cavity is filtered in order to derive a controller proportional to the relative velocity of the mirrors, and is fed back to the end mirror.

### Transmission locking

In Virgo, the local oscillator at 6.26 MHz is transported up to the end of the 3-km cavity. The use of the Anderson technique for automatically aligning the ITF, in fact, requires that demodulated signals are extracted from the quadrant photodetectors placed in transmission. Therefore, at the same time, demodulation is also applied to the signals detected by photodiodes.

Even if the first-order sidebands are poorly transmitted, when the carrier is at resonance, a transmitted Pound-Drever-Hall signal is generated by their beating with the carrier, and can be applied to lock the cavity [39]. This technique is referred to as *Pound-Drever-Hall transmission locking*. By using the usual formula, specified to the case of transmitted fields, the Pound-Drever-Hall signal is written as:

$$Q_{tr} = -2t_{tr}^2 P_{in,0} \frac{J_1(m)}{J_0(m)} \frac{t_1 t_2}{|1 - r_1 r_2 e^{i\Phi_0}|^2} \text{sen}\left(\frac{\Phi_0}{2}\right) \quad (3.21)$$

$$= -2t_{tr}^2 \frac{t_2}{t_1} P_{in,0} \frac{2\mathcal{F}}{\pi} \frac{J_1(m)}{J_0(m)} \text{sen}\left(\frac{\Phi_0}{2}\right) \quad (3.22)$$

As previously, it can be written in terms of a small length variation of the cavity  $\Delta L$  within the region of linearity in order to have a Pound-Drever-Hall signal useable for control purposes, such as the one used in reflection:

$$Q_{tr} \simeq 2t_{tr}^2 \frac{\omega_0}{c} \frac{t_2}{t_1} P_{in,0} \frac{2\mathcal{F}}{\pi} \frac{J_1(m)}{J_0(m)} \Delta L \quad (3.23)$$

### 3.2.2 Lock acquisition

The locking scheme described in the previous paragraph is complicated by the fact that the region of linearity of the Pound-Drever-Hall signal is generally extremely small. For Virgo:

$$\frac{\lambda}{4\mathcal{F}} \sim 5 \cdot 10^{-9} m \quad (3.24)$$

which is much smaller than the typical motion of the mirrors of the order of 1  $\mu m$  RMS. This means that with mirrors freely swinging the region of linearity of the Pound-Drever-Hall is repetitively crossed. The longitudinal feedback loop has therefore to be able to stop the cavity on resonance acting only during the resonance crossing and by impressing a force which is limited by the small dynamics of the actuation system.

#### Threshold velocity

The threshold velocity is defined as the maximum value of the cavity velocity below which the controller is able to acquire and hold the cavity on resonance. It is determined by the bandwidth of the control loop and the maximum force which can be applied to the mirrors by the actuation system.

The cavity crosses the resonance in a time which can be estimated by assuming a constant velocity  $v_m$  during the resonance crossing<sup>2</sup>:

$$t_{res} = \frac{\lambda}{2\mathcal{F}} \frac{1}{v_m}$$

For a controller with a bandwidth of angular frequency  $B$ , the maximum velocity allowed for stopping the cavity by the feedback loop is determined by the maximum action time of the feedback, of the order of  $1/B$ :

$$v_{max} < \frac{\lambda B}{2\mathcal{F}} \quad (3.25)$$

The other constraint is due to the maximum force  $F_{max}$  which can be applied by the actuation system in order to stop the mirror during the resonance crossing. Using the impulse-momentum theorem, the requirement is:

$$v_{max} < \sqrt{\frac{F_{max}\lambda}{2\mathcal{F}m}} \quad (3.26)$$

---

<sup>2</sup>In fact, the resonance width is usually very small, so that change in the swing velocity can be neglected. In Virgo:  $\frac{\lambda}{2\mathcal{F}} \sim 10^{-8}$  m.

where  $m$  is the mirror mass.

With the Virgo parameters  $F_{max} = 40$  mN and  $m = 20$  kg, and by considering a typical controller with  $B \sim 2\pi \times 100$  rad/s, the constraints on the threshold velocity are:

$$v_{max} < \frac{\lambda B}{2\mathcal{F}} \sim 6 \mu m \quad (3.27)$$

$$v_{max} < \sqrt{\frac{F_{max}\lambda}{2\mathcal{F}m}} \sim 4.5 \mu m \quad (3.28)$$

The threshold velocity of a few microns/second is comparable with the typical velocity of the mirrors due to seismic motion. Moreover, in case of failed locking trials, control forces can excite the mirror itself. In order to increase the probability of acquiring the lock at the first attempt, signal processing techniques such as the linearization of the error signal, are applied.

### Linearization of the error signal

As shown in section 3.2.1, Pound-Drever-Hall signals in reflection and in transmission from the cavity have the same structure, so that in this paragraph a more general Pound-Drever-Hall signal  $S_{PDH}$  will be considered. In order to increase the threshold velocity and shorten the lock acquisition time, the Pound-Drever-Hall signal can be combined with the DC signals extracted from the ITF in order to extend its linear range around the resonance [44]. This enlargement can be obtained by dividing the Pound-Drever-Hall signal by the transmitted power from the cavity  $P_{tr}$ .

In fact, in terms of the carrier power stored inside the cavity  $P_{sto,0}$  (see appendix B):

$$P_{sto,0} = \frac{t_1^2}{|1 - r_1 r_2 e^{i\Phi_0}|^2} P_{in,0}$$

$S_{PDH}$  can be written as:

$$S_{PDH} = -2t^2 r_2 P_{sto,0} \frac{J_1(m)}{J_0(m)} \text{sen}(\Phi_0) \quad (3.29)$$

The linearized signal  $S_{PDH}^{LIN}$  is built as:

$$S_{PDH}^{LIN} \simeq \frac{S_{PDH}}{P_{tr}} \quad (3.30)$$

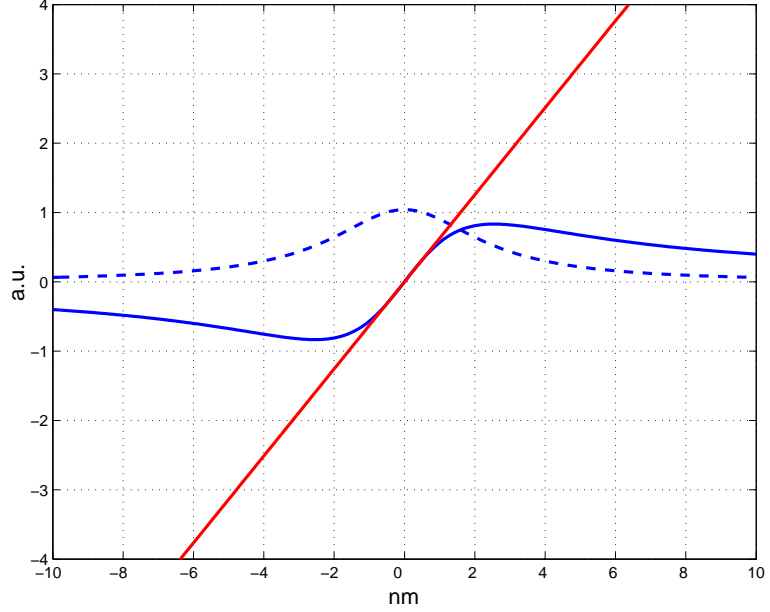


Figure 3.6: Linearized Pound-Drever-Hall signal (in red), compared with the not linearized one (in blue). The dotted line is the transmitted power.

Since the sidebands are poorly transmitted, all of the contributions to the transmitted power can be considered to come from the carrier:

$$P_{tr} \simeq P_{tr,0} = t_2^2 P_{sto,0} \quad (3.31)$$

The linearized Pound-Drever-Hall signal can be therefore written as:

$$S_{PDH}^{LIN} \simeq 2 \frac{t_{ref}^2}{t_2^2} r_2 \frac{J_1(m)}{J_0(m)} \sin\left(\frac{2\Delta L \omega_0}{c}\right) \quad (3.32)$$

and the region of linearity is considerably larger with respect to the not linearized Pound-Drever-Hall signal (see figure 3.6):

$$|\Delta L| < \frac{\lambda}{4\pi} \quad (3.33)$$

However, the range of linearity of the error signal is typically limited by electronic noise and by high order modes of the transmitted power signal, so that the effective enlargement of the linear region has to be directly measured. In general, the feedback loop is engaged when the power transmitted by the cavity is at half of its maximum value, in order to discriminate the fundamental mode by high order modes. By

means of the error signal linearization, as will be better explained in the next chapter, the lock of the Virgo 3-km cavity can be easily acquired at the first trial.

### 3.3 The Recombined ITF

In the recombined ITF the incoming beam is divided by the beam-splitter into two beams, and then injected into the arms. The arms reflect these beams, with the reflectivity coefficients described in the previous section, and the returning light from the arms is recombined at the BS. In order to study the response of the recombined ITF it is useful to consider it as a single mirror, the *compound* mirror, as described in figure C.1. The compound mirror has an amplitude reflectivity  $r_{com}$  and an amplitude transmissivity at the anti-symmetric port  $t_{comASY}$ , both of which depend upon the phase accumulated by the light inside the two Fabry-Perot and the Michelson.

If  $r_{BS} = t_{BS} = \sqrt{2}/2$ ,  $r_{com}$  and  $t_{comASY}$  are:

$$r_{com}(\Phi_X, \Phi_Y, \phi_X, \phi_Y) = \frac{E_{ref}}{E_{inc}} = \frac{1}{2} \left\{ r_X(\Phi_X) e^{i\phi_X} + r_Y(\Phi_Y) e^{i\phi_Y} \right\} \quad (3.34)$$

$$t_{comASY}(\Phi_X, \Phi_Y, \phi_X, \phi_Y) = \frac{E_{asy}}{E_{inc}} = \frac{1}{2} \left\{ r_X(\Phi_X) e^{i\phi_X} - r_Y(\Phi_Y) e^{i\phi_Y} \right\} \quad (3.35)$$

where  $r_X(\Phi_X)$  and  $r_Y(\Phi_Y)$  are the reflectivity of the Fabry-Perot cavities with the relative round-trip phase, and  $\phi_X$  and  $\phi_Y$  are the round-trip phases accumulated in the short Michelson arms. By introducing the new variables:

$$p_+(\Phi_X, \Phi_Y) = \frac{1}{2} \{ r_X(\Phi_X) + r_Y(\Phi_Y) \} \quad (3.36)$$

$$p_-(\Phi_X, \Phi_Y) = \frac{1}{2} \{ r_X(\Phi_X) - r_Y(\Phi_Y) \} \quad (3.37)$$

$$\phi_+ = \phi_X + \phi_Y \quad (3.38)$$

$$\phi_- = \phi_X - \phi_Y \quad (3.39)$$

the previous expression can be written as:

$$r_{com}(\Phi_X, \Phi_Y, \phi_+, \phi_-) = e^{i\frac{\phi_+}{2}} \left\{ p_+ \cos\left(\frac{\phi_-}{2}\right) + ip_- \sin\left(\frac{\phi_-}{2}\right) \right\} \quad (3.40)$$

$$t_{comASY}(\Phi_X, \Phi_Y, \phi_+, \phi_-) = e^{i\frac{\phi_+}{2}} \left\{ p_- \cos\left(\frac{\phi_-}{2}\right) + ip_+ \sin\left(\frac{\phi_-}{2}\right) \right\} \quad (3.41)$$

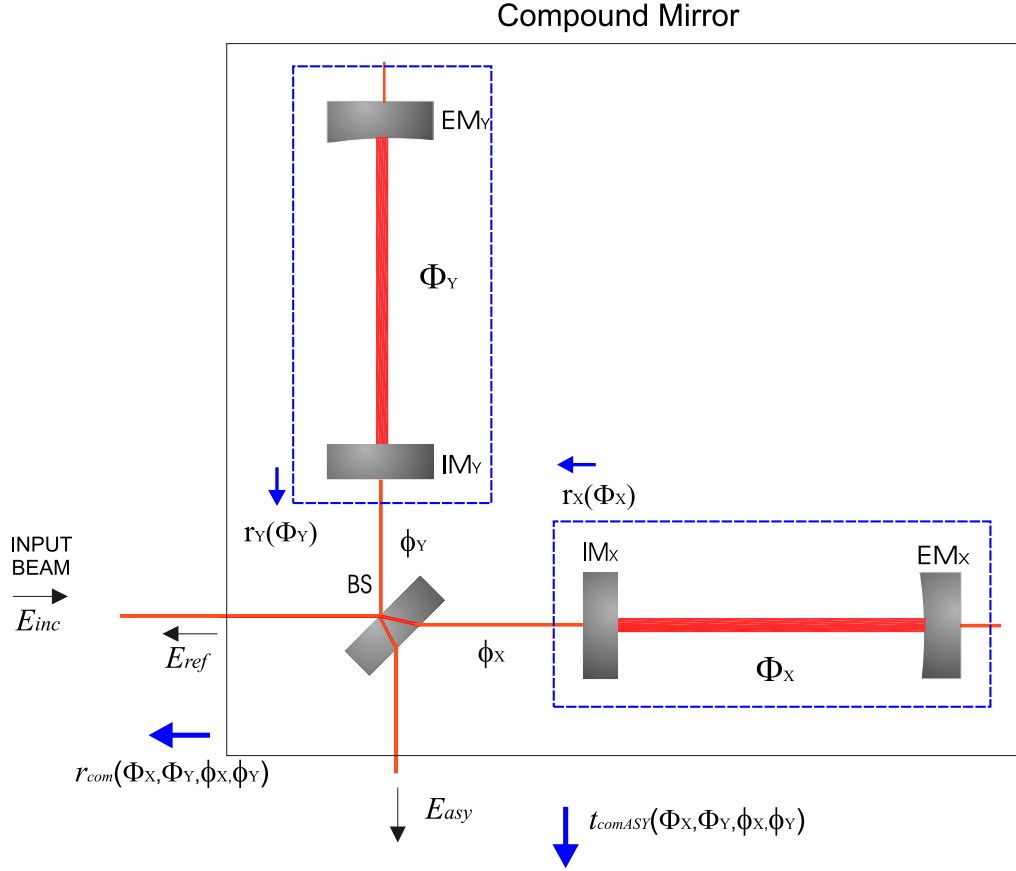


Figure 3.7: The Fabry-Perot Michelson ITF seen as a single mirror with variable reflectivity, the *compound mirror*.

Unless a global phase  $e^{i\frac{\phi_+}{2}}$ , which can be arbitrarily chosen as being equal to 1, the reflection and transmission coefficients of the compound mirror for the carrier can be written as:

$$r_{com,0}(\Phi_{X,0}, \Phi_{Y,0}, \phi_{-,0}) = \left\{ p_{+,0} \cos\left(\frac{\phi_-}{2}\right) + ip_{-,0} \sin\left(\frac{\phi_-}{2}\right) \right\} \quad (3.42)$$

$$t_{comASY,0}(\Phi_{X,0}, \Phi_{Y,0}, \phi_{-,0}) = \left\{ p_{-,0} \cos\left(\frac{\phi_-}{2}\right) + ip_{+,0} \sin\left(\frac{\phi_-}{2}\right) \right\} \quad (3.43)$$

### 3.3.1 Operating Point

At the operating point, the carrier is resonant in both the arm cavities:

$$\bar{\Phi}_{X,0} = \bar{\Phi}_{Y,0} = 0 \pmod{2\pi} \quad (3.44)$$

For Virgo cavities, according to equation B.23:

$$r_X(\bar{\Phi}_{X,0}) \simeq r_Y(\bar{\Phi}_{Y,0}) \simeq r_c \simeq -1 \quad (3.45)$$

so that  $p_- \simeq 0$  and  $p_+ \simeq -1$ .  $t_{comASY,0}$  becomes therefore:

$$t_{comASY,0}(\Phi_{X,0}, \Phi_{Y,0}, \phi_{-,0}) \simeq -i \sin\left(\frac{\phi_{-,0}}{2}\right) \quad (3.46)$$

The dark fringe condition for the carrier at the ASY port ( $t_{comASY,0} = 0$ ) is verified for:

$$\phi_{-,0} = 0 \pmod{2\pi} \quad (3.47)$$

### 3.3.2 Locking Scheme

High sensitivity error signals used to control the recombined configuration can be extracted at the anti-symmetric and reflected ports.

The explicit computation of the Pound-Drever-Hall signals is done in appendix C. Since the demodulation phases of the signals are dependent on the location of photo detectors, the length of the cables for the modulator, photo-detectors, and local oscillators, the definition of in-phase or quadrature-phase components is purely arbitrary. Results can therefore be more generally summarized in the following way:

- the demodulation phase of the reflected signal can be tuned so that one component is sensitive to the common mode variation of the arm lengths and the other one to the differential mode of the Michelson length. In Virgo, the in-phase component is chosen for the arms common mode:

$$I_{ref} \simeq 8|E|^2 J_1 J_0 t_{ref}^2 r_c \cos\left(\frac{\Omega l_-}{c}\right) \frac{2F}{\pi} \frac{\omega_0}{c} \Delta L_+ \quad (3.48)$$

$$Q_{ref} \simeq 2|E|^2 J_1 J_0 r_c t_{ref}^2 \sin\left(\frac{\Omega l_-}{c}\right) \frac{\omega_0}{c} \Delta l_- \quad (3.49)$$

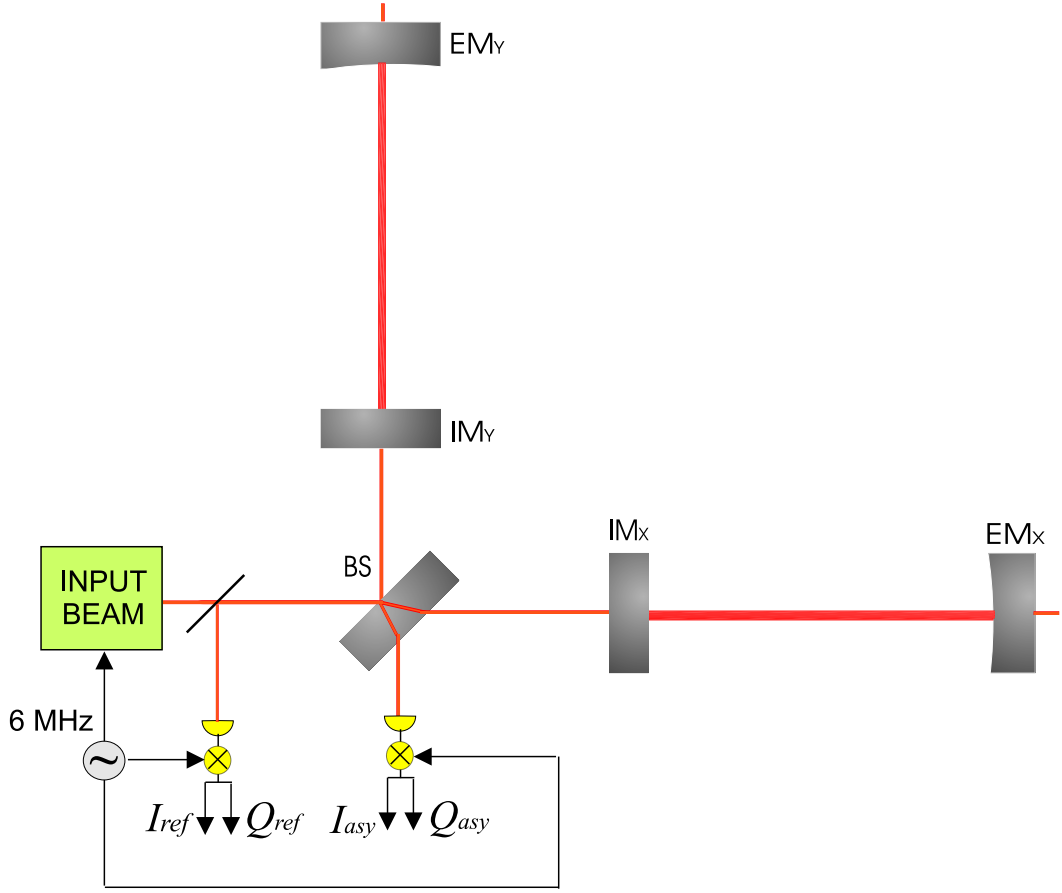


Figure 3.8: Extraction of Pound-Drever-Hall signals in the recombined ITF

- the demodulation phase of the anti-symmetric signal can be tuned so that one component is sensitive to the differential mode variation of the arm lengths and the differential mode of the Michelson length. In Virgo, the quadrature-phase component is chosen:

$$Q_{asy} \simeq 2|E|^2 J_1 J_0 r c t_{dark}^2 \frac{\omega_0}{c} \sin\left(\frac{\Omega l_-}{c}\right) \frac{2F}{\pi} \Delta L_- \quad (3.50)$$

$$Q_{asy} \simeq 2|E|^2 J_1 J_0 r c t_{asy}^2 \sin\left(\frac{\Omega l_-}{c}\right) \frac{\omega_0}{c} \Delta l_- \quad (3.51)$$

On the basis of these considerations, the three degrees of freedom of the recombined ITF can be controlled by involving the reflected and anti-symmetric demod-

ulated signals. However, the lock acquisition with such a scheme is complicated by the fact that the two cavities can not be independently locked. Moreover, the phase of the two carrier fields reflected back from the two cavities changes by  $\pi$  from the unlocked state to the locked state. A sign reversal of the BS loop is therefore needed if this loop is engaged at the beginning of the lock acquisition sequence [40].

The use of pick-off mirrors in the reflection of the two arms can greatly simplify the problem by reducing the lock of the two arms to one of two decoupled cavities [43]. Once the two cavities are locked, the BS loop can be engaged in order to lock the Michelson onto the dark fringe.

In Virgo an independent control of the three degrees of freedom of the ITF can be done as well, using the Pound-Drever-Hall signals in transmission. The lock acquisition problem for the recombined ITF is therefore mainly reduced to the case of the single cavity. A common and differential control of the arms by means of anti-symmetric and reflected signals is engaged once the ITF is locked, in order to have better noise performance (*linear locking*, see section 6.2).

### 3.4 The Recycled ITF

By means of the compound mirror, the full ITF can be modeled as a simple Fabry-Perot cavity, formed by the PR mirror as input mirror, and the compound mirror as output mirror.

The amplitude reflectivity for this cavity is therefore:

$$r_{ref}(\Phi_+, \Phi_-, \phi_+, \phi_-) = \frac{r_{PR} + r_{com}(\Phi_X, \Phi_Y, \phi_+, \phi_-)}{1 + r_{PR}r_{com}(\Phi_X, \Phi_Y, \phi_+, \phi_-)} \quad (3.52)$$

The amplitude recycling gain, defined as the ratio between the incoming field and the field recycled by the ITF, is done by:

$$g(\Phi_X, \Phi_Y, \phi_+, \phi_-) = \frac{t_{PR}}{1 + r_{PR}r_{com}(\Phi_X, \Phi_Y, \phi_+, \phi_-)} \quad (3.53)$$

and the amplitude transmissivity of the recycling cavity is:

$$t_{asy}(\Phi_X, \Phi_Y, \phi_+, \phi_-) = g(\Phi_X, \Phi_Y, \phi_+, \phi_-)t_{com}(\Phi_X, \Phi_Y, \phi_+, \phi_-) \quad (3.54)$$

$r_{com}$  and  $t_{comASY}$  were used in the previous sections unless the definition of the common phase  $\phi_+ = \phi_X + \phi_Y$ , which now has to be specified in order to define the resonance condition for the recycling cavity:

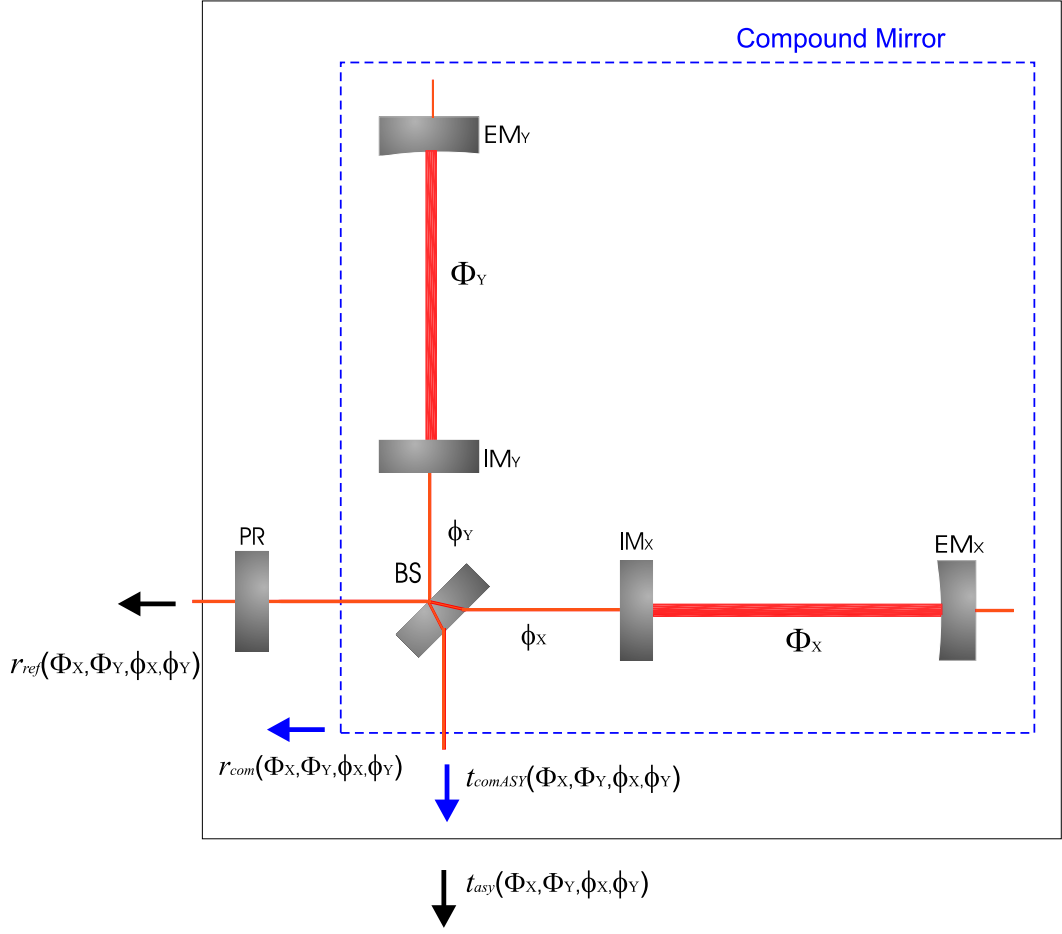


Figure 3.9: The recycling cavity, formed by the power recycling mirror and the compound mirror with variable reflectivity.

$$r_{com}(\Phi_X, \Phi_Y, \phi_+, \phi_-) = e^{i\frac{\phi_+}{2}} \left\{ p_+ \cos\left(\frac{\phi_-}{2}\right) + ip_- \sin\left(\frac{\phi_-}{2}\right) \right\} \quad (3.55)$$

$$t_{comASY}(\Phi_X, \Phi_Y, \phi_+, \phi_-) = e^{i\frac{\phi_+}{2}} \left\{ p_- \cos\left(\frac{\phi_-}{2}\right) + ip_+ \sin\left(\frac{\phi_-}{2}\right) \right\} \quad (3.56)$$

The phase accumulated in the path between the PR and the compound mirror can be encompassed in  $\phi_+$ . In order to maximize the recycling gain of the carrier inside the ITF, the reflectivity of the compound mirror for the carrier has to be maximum. This means:

$$\frac{\phi_{+,0}}{2} = 0 \pmod{2\pi} \quad (3.57)$$

This condition, combined with the previous ones found for the recombined ITF, fixes the operating point of the recycled ITF, which is summarized as:

$$\Phi_X = \Phi_Y = \phi_{+,0} = \phi_{-,0} = 0 \quad (3.58)$$

First-order sidebands have to be resonant in the recycling cavity. Their phase shift  $\phi_{-,1}$  is:

$$\phi_{-,1} = \phi_{-,0} + 2\alpha, \quad \alpha = \frac{l_-\Omega}{c} \quad (3.59)$$

$$\phi_{+,1} = \phi_{+,0} + 4\beta, \quad \beta = \frac{l_+\Omega}{c} \quad (3.60)$$

where  $l_+ = l_0 + \frac{l_x+l_y}{2}$ .

The phase shift of first-order sidebands in the recycling cavity is given by the factor  $\beta$ . Since they are shifted by  $\pi$  with respect to the carrier, being anti-resonant in the arm cavities:

$$\beta = \pi \pmod{2\pi} \quad (3.61)$$

The amplitude reflectivity of the compound mirror for first-order sidebands is therefore:

$$r_{com,1} \simeq r_{com,-1} \simeq -\cos \alpha \quad (3.62)$$

Conventionally, the parameter:

$$r_M = \cos \alpha$$

is used.

On the basis of the previous discussion, the following usual parameters characterizing the ITF on the operating point are defined [46]:

- the amplitude of the recycling gain for the carrier and first-order sidebands,  $g_{cr}$  and  $g_{sb}$ :

$$g_{cr} = \frac{t_{PR}}{1 + r_{PR}r_{com,0}} = \frac{t_{PR}}{1 + r_{PR}r_c} \quad (3.63)$$

$$g_{sb} = \frac{t_{PR}}{1 + r_{PR}r_{com,1}} = \frac{t_{PR}}{1 - r_{PR}r_M} \quad (3.64)$$

- the amplitude reflectivity for reflection from the power recycling mirror, for carrier and sidebands,  $r_{cr}$  and  $r_{sb}$ :

$$r_{cr} = \frac{r_{PR} + r_{com,0}}{1 + r_{PR}r_{com,0}} = \frac{r_{PR} + r_c}{1 + r_{PR}r_c} \quad (3.65)$$

$$r_{sb} = \frac{r_{PR} + r_{com,1}}{1 + r_{PR}r_{com,1}} = \frac{r_{PR} - r_M}{1 - r_{PR}r_M} \quad (3.66)$$

- the amplitude transmissivity to the anti-symmetric port,  $t_{cr}$  and  $t_{sb}$ :

$$t_{cr} \simeq 0 \quad (3.67)$$

$$t_{sb} \simeq \sqrt{1 - r_{sb}^2} = \frac{t_{PR}\sqrt{1 - r_M^2}}{1 - r_{PR}r_M} \quad (3.68)$$

- the derivative of the arm cavity reflectivity with respect to the round trip phase, evaluated on the resonance:

$$r'_c = \frac{(1 - r_1^2)r_2}{(1 - r_1r_2)^2} \quad (3.69)$$

### 3.4.1 Locking signal readout

In order to control the recycled ITF a set of signals has to be chosen in order to reconstruct the four lengths of the ITF. There is not a unique choice, and the preference of one scheme with respect to another is mainly due to the peculiar characteristics of each detector.

It useful to introduce the *sensing matrix*  $\mathbf{M}$ , defined as:

$$\vec{S}_{demod} = \mathbf{M}\vec{\Delta} \quad (3.70)$$

where  $\vec{S}_{demod}$  is the vector formed by the demodulated signals and  $\vec{\Delta}$  represents the deviation from the resonance condition for the four independent lengths:

$$\vec{\Delta} = \begin{pmatrix} \Delta L_+ \\ \Delta L_- \\ \Delta l_+ \\ \Delta l_- \end{pmatrix}$$

These four degrees of freedom are usually referred to in abbreviated form as, respectively, CARM (common arm), DARM (differential arm), PRCL (power recycling cavity length) and MICH (Michelson length).

Each element  $M_{i,j}$  of the sensing matrix  $\mathbf{M}$  is therefore the transfer function from the  $i^{th}$  length variation to the  $j^{th}$  demodulated signal.  $\vec{\Delta}$  can be reconstructed by inverting  $\mathbf{M}$ , so as to get suitable error signals to lock the ITF.

The response of the ITF to a given length variation can be generally described as in [46]. A given length change induces a phase shift in the resonant field, which interacts with the static field where any phase shift is induced (the *local oscillator*). For instance, a DARM length variation produces a phase shift in the carrier field, which is resonant in the arms. Sidebands, which are instead anti-resonant in the arms, are not affected by DARM, which acts as a local oscillator.

Following a convention widely used in the community, demodulation phases of the involved signals are in general tuned so that the in-phase components are sensitive to the common modes of the ITF, and the quadrature ones to the differential modes<sup>3</sup>.

The response of the ITF is frequency-dependent. The carrier field resonant in the arms is filtered by the arm cavity pole at angular frequency  $\omega_c$ :

$$\omega_c = \frac{c}{2L} \frac{1 - r_1 r_2}{\sqrt{r_1 r_2}} \quad (3.71)$$

In Virgo,  $\omega_c \sim 2\pi \times 500$  rad/s. The carrier field resonant in both the arm cavities and in the recycling cavity instead experiences the pole of the double cavity  $\omega_{cc}$ :

$$\omega_{cc} = \frac{1 + r_{PR} r_c}{1 + r_{PR}} \sim 2\pi \times 10 \text{ rad/s} \quad (3.72)$$

In Virgo,  $\omega_{cc} \sim 2\pi \times 10$  rad/s. The frequency response of the ITF to a given length variation has to be taken into account in the design of the control loop, since the feedback has to compensate for it in order to maintain the stability of the system. On the basis of these arguments, the dependency of demodulated signals extracted from the ITF to the different length variations can be computed. Demodulated signals are taken from the reflected beam (*ref*), from the anti-symmetric beam (*asy*) and from the beam extracted from the recycling cavity<sup>4</sup>. Signals at the anti-symmetric port are mainly sensitive to MICH and DARM, both generated by the carrier field beating against the static sideband field:

---

<sup>3</sup>The same convention is applied in Virgo, except for the dark fringe signal extracted at the anti-symmetric port: the in-phase component (*B1-ACP*) is chosen.

<sup>4</sup>This beam is extracted from the recycling cavity in different ways depending on the detector. The different configurations will be detailed in the next sections, and the beam will be referred to as *pick-off* beam

$$Q_{asy} \simeq g_{cr} t_{sb} r'_c \frac{1}{1 + s_c} \Delta L_- \quad (3.73)$$

$$Q_{asy} \simeq g_{cr} t_{sb} r_c \frac{1}{1 + s_c} \Delta l_- \quad (3.74)$$

The phase shift induced by DARM is amplified by a factor  $r'_c/r_c$  with respect to the one induced by MICH, because of the phase shift enhancement due to the Fabry-Perot cavities. With the Virgo parameters:

$$\frac{r'_c}{r_c} \sim 30$$

Signals detected at the reflected port are induced by variations in the carrier and in the sideband fields. CARM affects only the carrier field, since the sidebands are not resonant in the arms and act as a local oscillator. The in-phase signal sensitive to CARM experiences therefore only the double cavity pole. Both carrier and sidebands are instead resonant in the recycling cavity, and are affected by PRCL. The carrier component is filtered above 10 Hz by the coupled cavity resonance, while the contribution produced by sideband beating with the static carrier field is not. The quadrature-phase component is mainly sensitive to MICH. It produces a differential change in the sideband fields reflected towards PR, which beat against the static carrier field.

$$I_{ref} \simeq g_{cr}^2 r_{sb} r'_c \frac{1}{1 + s_{cc}} \Delta L_+ \quad (3.75)$$

$$I_{ref} \simeq g_{sb}^2 r_{cr} r_M + g_{cr}^2 r_{sb} r_c \frac{1}{1 + s_{cc}} \Delta l_+ \quad (3.76)$$

$$Q_{ref} \simeq g_{sb} t_{sb} r_{cr} \Delta l_- \quad (3.77)$$

The signals extracted from the recycling cavity are generated in a similar way to those ones reflected by the ITF:

$$I_{pob} \simeq \frac{g_{cr} g_{sb}}{t_{PR}} r_M r'_c \frac{1}{1 + s_{cc}} \Delta L_+ \quad (3.78)$$

$$I_{pob} \simeq \frac{g_{cr} g_{sb}}{t_{PR}} r_M r_c \left( g_{cr} \frac{1}{1 + s_{cc}} - g_{sb} \right) \Delta l_+ \quad (3.79)$$

$$Q_{pob} \simeq \frac{g_{cr} g_{sb}^2}{t_{PR}} t_M \Delta l_- \quad (3.80)$$

As already mentioned, in Virgo Pound-Drever-Hall signals are taken also in transmission of the two cavities. They are mainly sensitive to CARM and DARM:

$$I_{tr7} \simeq g_{cr} t_{sb7} r'_c \left[ \frac{1}{1+s_c} \Delta L_- + (1+g_{cr}) \frac{1}{1+s_{cc}} \Delta L_+ \right] \quad (3.81)$$

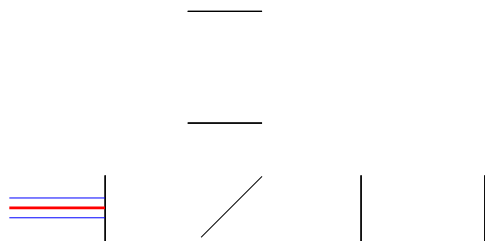
$$I_{tr8} \simeq g_{cr} t_{sb8} r'_c \left[ \frac{1}{1+s_c} \Delta L_- + (1+g_{cr}) \frac{1}{1+s_{cc}} \Delta L_+ \right] \quad (3.82)$$

$$(3.83)$$

### 3.4.2 Lock acquisition

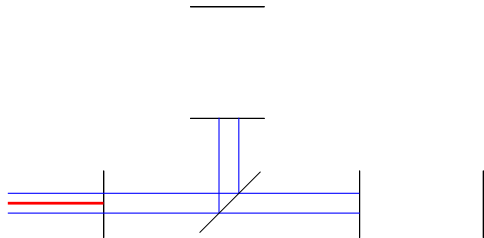
The lock acquisition of the recycled ITF passes through the inversion of the sensing matrix, constructed by choosing a set of suitable demodulated signals extracted from the ITF. Since they are only sensitive to length variation when the ITF is around its operating point, a direct inversion of the matrix would not be efficient. The operating point is only rarely spontaneously crossed by the ITF and the crossing time is generally very short, so that feedback forces would not be able to stop the mirrors and keep the ITF on resonance. A more suitable way to engage the control loops is therefore needed. This problem has been deeply investigated in the commissioning of this kind of detector.

In particular, interferometers with an optical configuration similar to Virgo, such as LIGO and TAMA, designed and successfully applied a *multi-step* technique, in which loops are sequentially engaged [45] [47]. The sequence is the following:



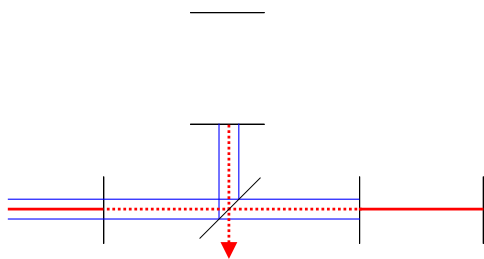
#### State 1

The cavities are freely swinging around resonance and any degree of freedom is controlled.



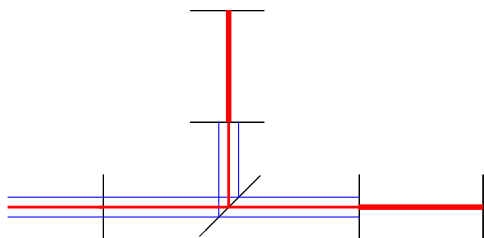
### State 2

PRCL and MICH are controlled so that sidebands are resonant in the recycling cavity. The carrier is anti-resonant in the recycling cavity and zero at the asymmetric port (due to the  $\pi$  shift given by the Fabry-Perot cavities).



### State 3

With the ITF in state 2, the carrier enters in resonance in one arm, and corrections are sent to the corresponding end mirror. The carrier is on the bright fringe at the asymmetric port.



### State 4

With the ITF in state 3, the carrier enters in resonance also in the other arm, so that corrections are sent to both the end mirrors. The power builds-up inside the ITF, and the power stabilizes at its maximum value.

On the other hand, important differences in the two control schemes are present. Since both the two strategies will play an important role in designing the strategy applied in Virgo (see chapter 7), the main aspects of LIGO and TAMA locking schemes will be briefly described in the next paragraphs. In particular, the LIGO technique was experimentally tested in Virgo before moving to the *variable finesse* technique.

### The LIGO multi-step technique

In LIGO the adopted sensing matrix involves signals extracted at the reflected port, at the pick-off port and at the anti-symmetric port 3.10.

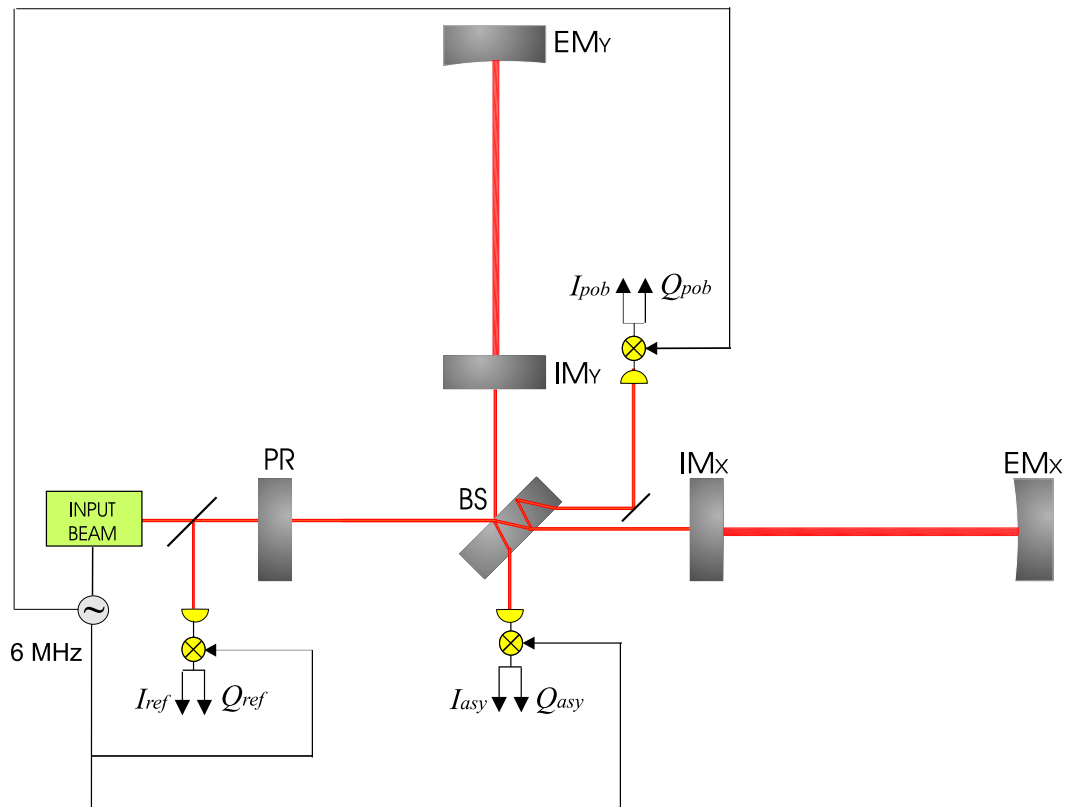


Figure 3.10: Signal extraction in the LIGO interferometer.

The length reconstruction passes through the inversion of the sensing matrix  $M$ , defined as:

$$\begin{pmatrix} I_{ref} \\ I_{pob} \\ Q_{asy} \\ Q_{ref} \\ Q_{pob} \end{pmatrix} = \begin{pmatrix} G_{I_{ref}}^{CARM} & G_{I_{ref}}^{DARM} & G_{I_{ref}}^{PRCL} & 0 \\ G_{I_{pob}}^{CARM} & G_{I_{pob}}^{DARM} & G_{I_{pob}}^{PRCL} & 0 \\ G_{Q_{asy}}^{CARM} & G_{Q_{asy}}^{DARM} & 0 & 0 \\ 0 & 0 & 0 & G_{Q_{ref}}^{MICH} \\ 0 & 0 & 0 & G_{Q_{pob}}^{MICH} \end{pmatrix} \begin{pmatrix} \Delta L_+ \\ \Delta L_- \\ \Delta l_+ \\ \Delta l_- \end{pmatrix} \quad (3.84)$$

Away from the final state, most of the matrix elements vanish. An invertible matrix  $\widetilde{M}$  therefore needs to be extracted from  $M$  at each state of the locking sequence. The corresponding inverse matrix  $M^{-1}$  is computed on the basis of it, changing its dimension according to the number of lengths to be controlled.  $M^{-1}$  is determined continuously from the uncontrolled to the fully controlled state:

- **state 2** - when the sideband power in the recycling cavity goes above a given threshold (usually half of the maximum power reachable when the entire ITF is aligned) a trigger is switched on, so that an invertible 2 by 2 matrix is extracted to keep the sidebands on resonance by acting on the BS and PR mirrors:

$$\begin{pmatrix} I_{ref} \\ Q_{ref} \end{pmatrix} = \begin{pmatrix} G_{I_{ref}}^{PRCL} & 0 \\ 0 & G_{Q_{ref}}^{MICH} \end{pmatrix} \begin{pmatrix} \Delta l_+ \\ \Delta l_- \end{pmatrix} \quad (3.85)$$

This state is unstable: if sidebands go in resonance in one of the two arms, the reflected field from that cavity is de-phased by  $\pi$ , and sidebands go off resonance. In this case the ITF comes back to the uncontrolled state. If the carrier field goes in resonance in one of the two arms, the ITF goes to the successive state of the locking sequence, state 3;

- **state 3** - when the ITF is in the state 2 and the carrier field enters into resonance in one of the two arms, state 3 is reached. A trigger on the corresponding transmitted power goes above its threshold (usually half of the maximum power reachable with the single cavity aligned) and a  $3 \times 3$  sensing matrix is extracted from the general one:

$$\begin{pmatrix} I_{ref} \\ Q_{asy} \\ Q_{ref} \end{pmatrix} = \begin{pmatrix} G_{I_{ref}}^{CARM} & G_{I_{ref}}^{PRCL} & 0 \\ G_{Q_{asy}}^{CARM} & 0 & 0 \\ 0 & 0 & G_{Q_{ref}}^{MICH} \end{pmatrix} \begin{pmatrix} \Delta L_+ \\ \Delta l_+ \\ \Delta l_- \end{pmatrix} \quad (3.86)$$

The correction signal is also enabled on the end mirror of the resonant cavity. This state is also unstable: if the carrier power in the other arm goes above

threshold, the ITF goes to state 4, otherwise it returns to one of the previous states;

- **state 4** - when the transmitted power by both the two cavities goes above its threshold, correction signals are sent at both the end mirrors. These are derived by inverting the  $4 \times 4$  sensing matrix defined as:

$$\begin{pmatrix} I_{ref} \\ I_{pob} \\ Q_{asy} \\ Q_{pob} \end{pmatrix} = \begin{pmatrix} G_{I_{ref}}^{CARM} & G_{I_{ref}}^{DARM} & G_{I_{ref}}^{PRCL} & 0 \\ G_{I_{pob}}^{CARM} & G_{I_{pob}}^{DARM} & G_{I_{pob}}^{PRCL} & 0 \\ G_{Q_{asy}}^{CARM} & G_{Q_{asy}}^{DARM} & 0 & 0 \\ 0 & 0 & 0 & G_{Q_{pob}}^{MICH} \end{pmatrix} \begin{pmatrix} \Delta L_+ \\ \Delta L_- \\ \Delta l_+ \\ \Delta l_- \end{pmatrix} \quad (3.87)$$

If both carrier and sideband powers remain stably at their maximum value for a time longer than the time needed for the full power build-up (typically 100 ms in LIGO), the lock is acquired. Otherwise, the lock is lost and the ITF goes back to one of the previous states.

A crucial point in applying this locking strategy is the estimation of the elements of the sensing matrix. From the uncontrolled state to the fully controlled state, in fact, the resonant power inside the LIGO ITF changes by more than three orders of magnitude, and the response of the involved error signals varies accordingly. In particular, as has been shown in the previous section, their response is proportional to the gains of the carrier and sidebands inside the ITF, which drastically change during the lock acquisition path.

The carrier gain  $g_{cr}$ , for instance, which is less than 1 in step 2, reaches the value of 7 in the final state. In order to maintain a stable control system the locking scheme has to be able to compensate for the increasing of the strength of the demodulated signals. For this reason, the sensing matrix elements  $M_{i,j}$  are estimated in terms of the carrier and sideband fields resonant inside the ITF and the fields acting as local oscillators at the different detection ports. The result is a continuously evolving matrix which changes following the status of the system, by generalizing the error signal linearization described for the single cavity to the case of multiple degrees of freedom.

A detailed explanation of how to estimate all the sensing matrix coefficients in terms of the fields evolving inside the ITF is done in [45]. To clarify the method, the estimation of  $G_{I_{ref}}^{CARM}$  is shown here as an example. As already said in section 3.4.1, the response of  $I_{ref}$  to CARM is produced by the resonant carrier field beating

with the local oscillator field of the sidebands, which are not resonant in the arms.  $G_{I_{ref}}^{CARM}$  can therefore be estimated as:

$$G_{I_{ref}}^{CARM} = g_{ref}^{CARM} A_{ref1} A_+ \quad (3.88)$$

where  $g_{ref}^{CARM}$  is a constant gain coefficient,  $A_{ref1}$  is the amplitude of the field of the sidebands detected at the reflected port, and  $A_+$  is an estimate of the resonant carrier power inside the ITF. In the state that neither arm is close to the resonance, so that  $A_+ \simeq 0$ ,  $G_{I_{ref}}^{CARM}$  vanishes. Instead, in states 3 and 4, it can be written in terms of the transmitted powers by the two cavities, which are directly measurable.  $A_{ref1}$  is dependent up on the mode-matching of the sidebands in the recycling cavity, and is estimated on the basis of the optical parameters of the ITF.

The value of the gain coefficient  $g_{ref}^{CARM}$  is needed as well. The better way to directly measure this coefficient is to excite the CARM degree of freedom and to measure the response in the signal  $I_{ref}$ . On the other hand, performing such a measurement requires the ITF to already be locked on its operating point, while the same gain coefficient is actually needed to acquire the lock. Since the same problem arises for each matrix element, an alternative general procedure to measure the gain coefficients has been designed and applied. This consists of performing the measurement in simpler optical configurations whose sensing matrix elements have the same gain coefficients as the full ITF. In particular,  $g_{ref}^{PRCL}$ ,  $g_{pob}^{PRCL}$ ,  $g_{ref}^{MICH}$  and  $g_{pob}^{MICH}$  are measured by locking the recycling cavity, keeping both the end mirrors misaligned so as to have a stable state. CARM and DARM coefficients can be instead inferred locking the stable state of the ITF formed by the recycling cavity plus one arm, keeping the end mirror of the other arm misaligned.

The multi-step technique was successfully applied in all the three LIGO interferometers. A typical lock acquisition event is shown in figure 3.12: the ITF passes from state 2 to state 5 in about 1 sec.

Typically, some minutes are needed to reach the final state from the fully uncontrolled state. By the time, the ITF crosses several times the previous states, and corrections are accordingly sent to the involved mirrors, until the lock is acquired.

A few concerns complicate this strategy. As has been described in 3.4.1, either involving  $I_{ref}$  or  $I_{pob}$  the sensitivity of these signals to PRCL vanishes in the course of the power build-up, when the response of the recycling cavity becomes the same for carrier and sidebands. To solve this problem, in LIGO the PRCL control is interrupted as the singularity approaches, and is not restored until the singularity is passed. Moreover, because of the phase shift enhancement experienced by the

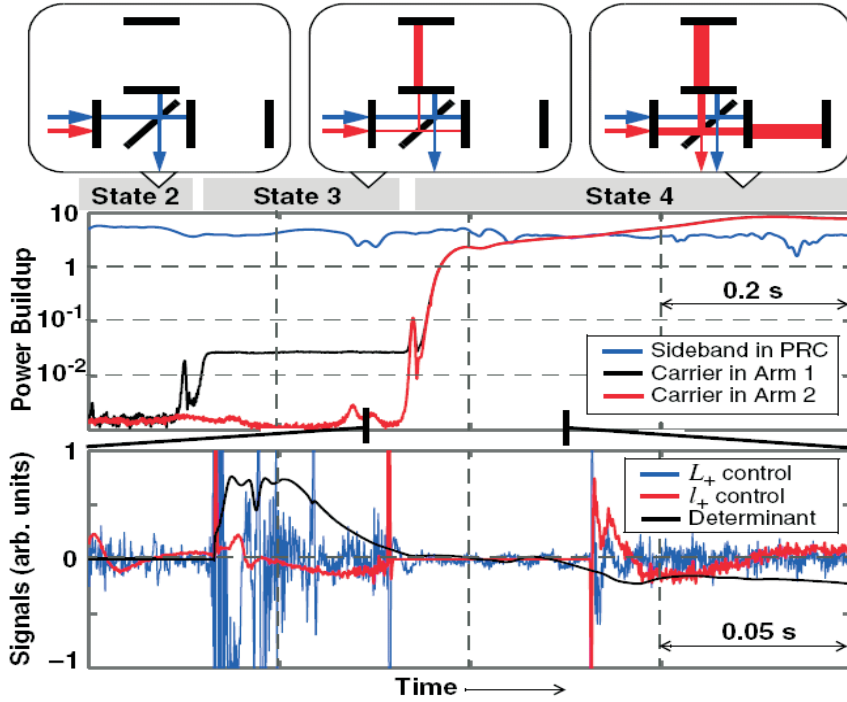


Figure 3.11: Typical lock acquisition of LIGO1, reached by the multi-step locking technique. Courtesy of M. Evans.

carrier in the Fabry-Perot cavities, the extraction of a good error signal for PRCL is difficult, since the demodulated signals which are sensitive to PRCL are also largely sensitive to CARM.

The problem can be solved by feeding-back  $I_{ref}$  to the laser frequency with a very high bandwidth (several kHz). At low frequency the loop gain is so high that in the other signal  $I_{pob}$  the CARM contamination is greatly reduced, making it sensitive mainly to PRCL. On the other hand, such a kind of frequency servo is engaged in LIGO only when the ITF is already locked in a stable state, so that the CARM contamination is still present during the lock acquisition phase.

### TAMA sensing and control

The TAMA locking scheme is also based on the multi-step technique, but is quite different with respect to the LIGO one. In particular, it is simplified by the fact that the recycling gain for the carrier is almost 10 times lower than LIGO, so that the coupling between the two cavities is greatly reduced.

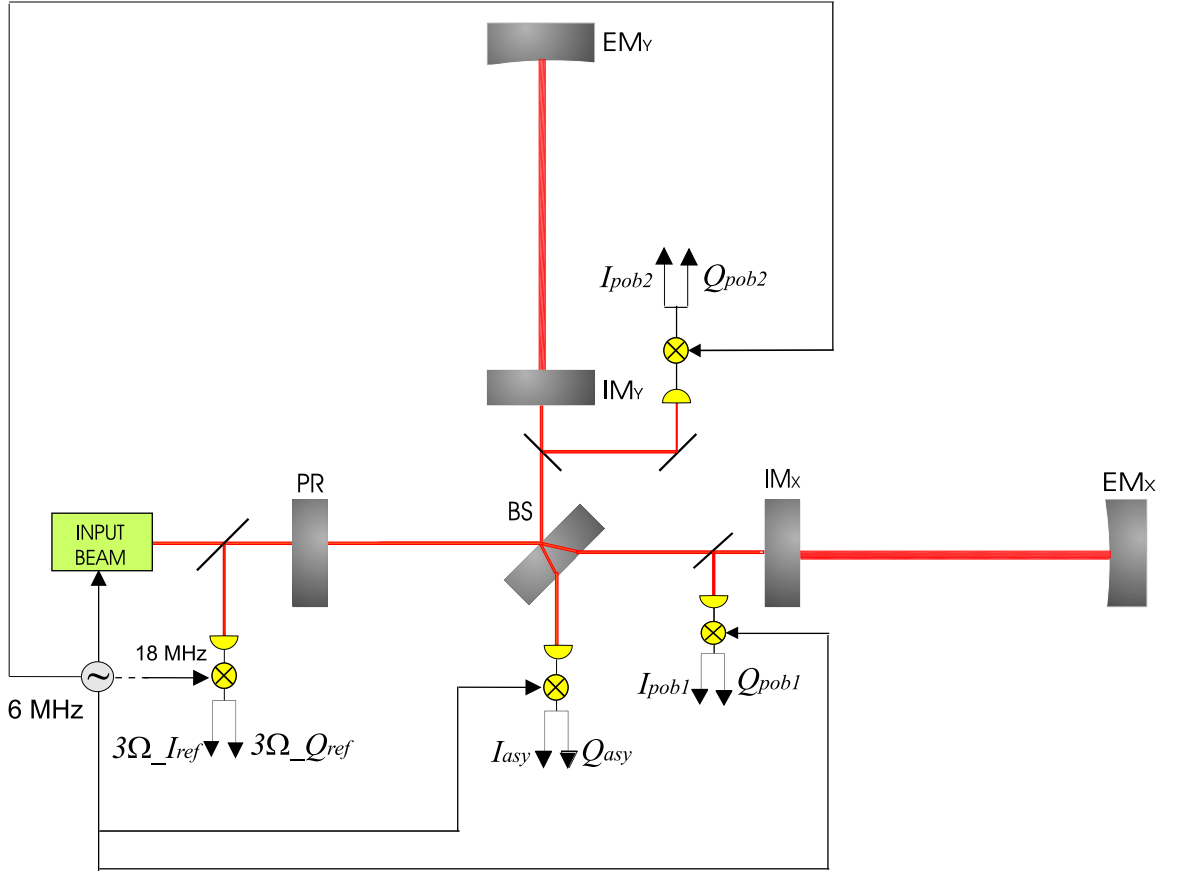


Figure 3.12: Signal extraction in the TAMA interferometer.

Moreover, the TAMA scheme is characterized by a robust extraction of the PRCL and MICH lengths by using the reflected signal demodulated at  $3\Omega$  frequency. Peculiarities of this kind of extraction are detailed in [48], where a deep analysis of the advantages of using this signal with respect to the conventional  $\Omega$ -demodulated one is done.

These are mainly connected with the mechanism by which the  $3\Omega$  signal is generated at the reflected port. It is in fact produced by the beating between first and second-order sidebands: second-order sidebands are not resonant in the recycling cavity, so that a constant amount of them is reflected back to the symmetric port, independently of the resonant conditions of the ITF. A PRCL length variation therefore induces a phase shift in the sidebands, which are resonant only in the

recycling cavity, and no information concerning the long cavities state is therefore present. Actually, even if it is smaller, also the beating between carrier and third order of sidebands contributes to generate the  $3\Omega$  signal. This still leads to a slight contamination by CARM of the  $3\Omega$  PRCL signal, but results in being 20 times lower with respect to the one measured in the  $\Omega$  signal.

Another important advantage in using the  $3\Omega$ -demodulation is that the sign of the lengths  $\Delta l_+$  and  $\Delta l_-$  reconstructed by the reflected  $3\Omega$ -demodulated signal is stable against changes in the optical parameters, where the conventional  $\Omega$ -demodulated signal is not. In this way in TAMA the recycling cavity remains stably locked even when the carrier becomes resonant inside the arms, and the lock of the ITF can be therefore acquired by independently controlling the four degrees of freedom of the ITF.

## Chapter 4

# The Commissioning of Virgo

The first step in the commissioning of a detector such as Virgo is the implementation of all the control systems required to run the ITF. In parallel, noise performances have to be constantly studied and improved, in order to reach the designed sensitivity. The commissioning of Virgo started in September 2003, and was organized in steps of increasing complexity:

### A - Commissioning of the long Fabry-Perot cavities

*(September 2003 - January 2004)*

The North and West cavity (see figures 4 and 4) were separately commissioned.

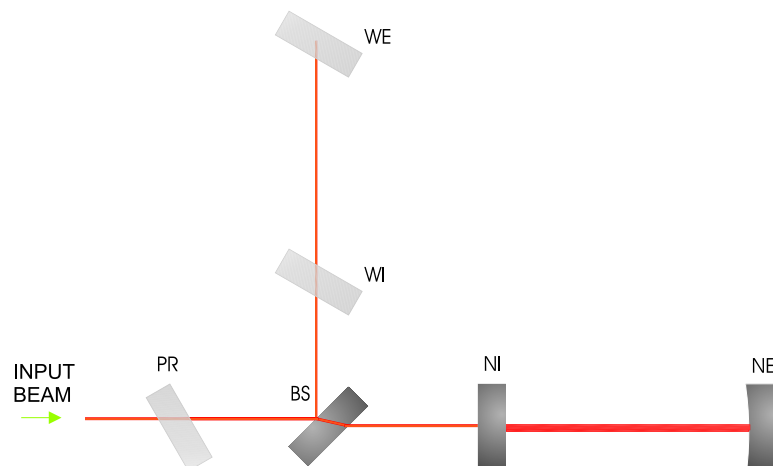


Figure 4.1: North cavity configuration.

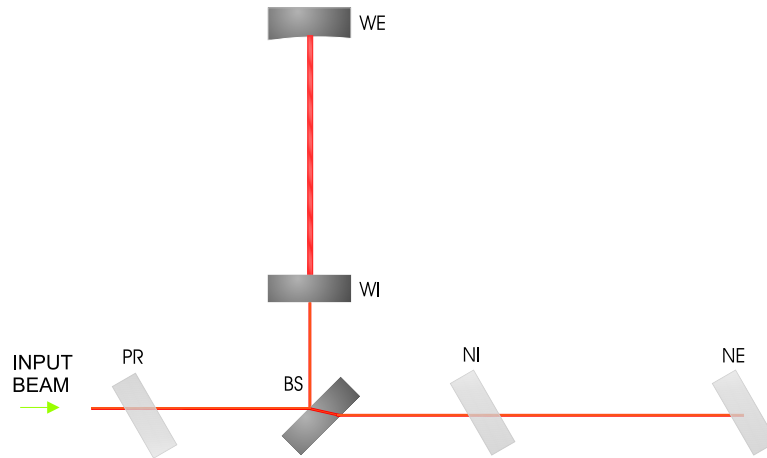


Figure 4.2: West cavity configuration.

Sub-systems like the injection system, the global control, the detection system and the involved suspensions (NI, NE, BS, WI, WE) were tested, debugged and improved. The locking and automatic alignment of a single arm were designed and implemented in this configuration.

### **B - Commissioning of the Fabry-Perot Michelson ITF**

*(recombined ITF) (February 2004 - December 2004)*

All the mirrors were kept aligned, except the PR (see figure 4.3). The light reflected by the two arms was recombined at the level of the BS mirror. For historical reasons this configuration is usually referred to as the *recombined* ITF. With respect to the operation of a single arm, the main difference consisted of a more complex locking scheme, while the other kinds of control systems were mainly the same as for a single arm. Three longitudinal degrees of freedom, instead of one, have to be controlled: the length of each Fabry-Perot cavity and the phase difference between the two beams reflected by the arm cavities. Also, since the detector sensitivity of the recombined ITF is considerably better than the one of the single cavity (which is essentially limited by frequency noise), noise hunting can start during this phase.

### **C - Commissioning of the power-recycled Fabry-Perot Michelson ITF**

*(recycled ITF) (July 2004 - September 2005)*

In the final Virgo configuration all of the six main optics were kept aligned (see figure 4.4).

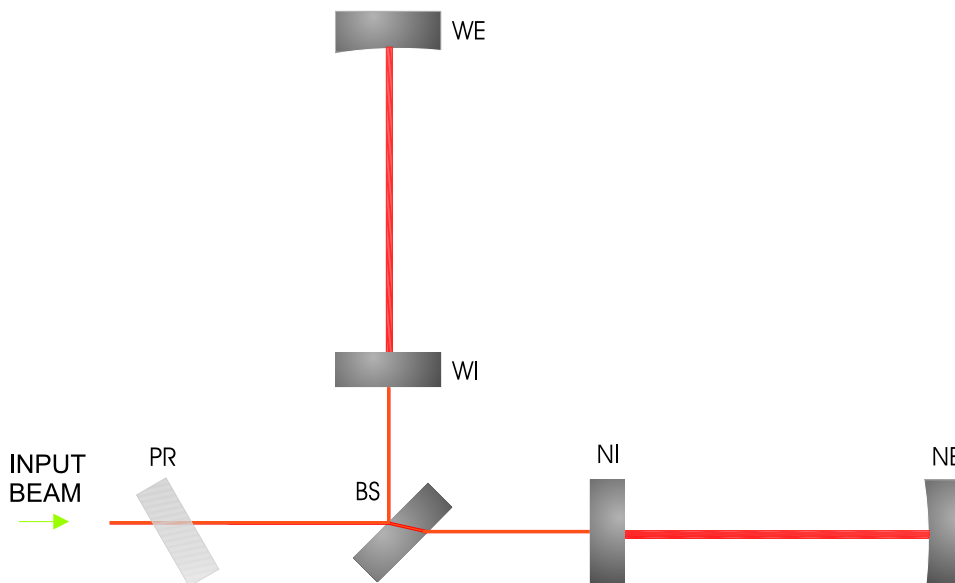


Figure 4.3: Recombined ITF configuration.

If most of the involved sub-systems did not need big changes, locking and automatic alignment controls had to be completely redesigned, because of the large couplings between the arms introduced by the presence of the recycling cavity.

**D - Noise Hunting** With a stably running ITF, the so-called *noise hunting* phase can start, where several noise sources contaminating the sensitivity are systematically investigated and possibly reduced.

The work presented in this thesis was started in spring 2003 in the framework of the commissioning. Its main topic is the longitudinal control of the detector, from its simple scheme in a single arm configuration to the recycled mode. In parallel with the basic implementation of the locking strategies, the analysis of the noise re-introduced in the dark fringe signal by the longitudinal control has been systematically performed, and several improvements to the locking scheme have been progressively studied and implemented. The analysis shown are mainly based on the data collected during the Virgo *commissioning runs*.

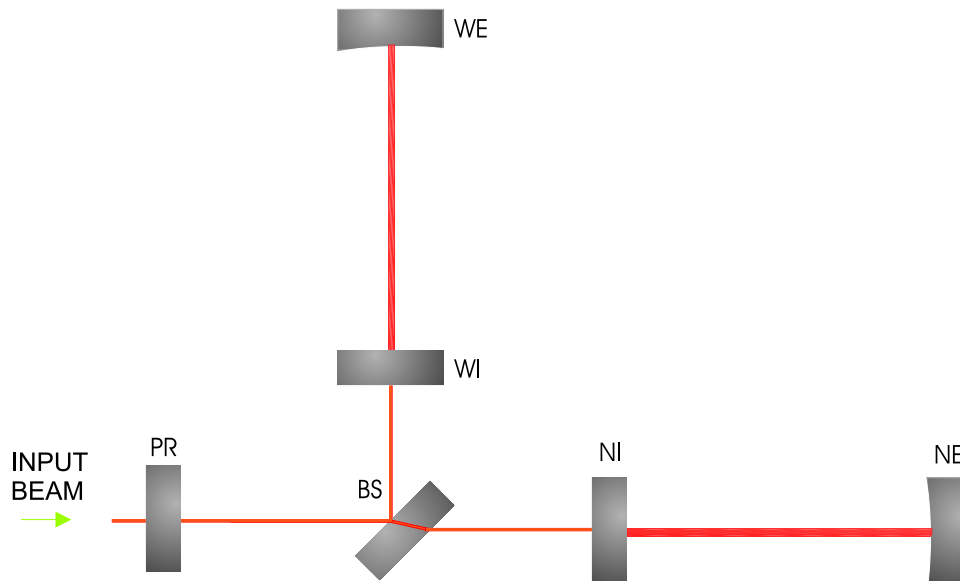


Figure 4.4: Recycled ITF configuration.

### 4.0.3 Commissioning evolution and commissioning runs

The commissioning runs are short periods of continuous data-taking which have taken place every two to three months since November 2003, in order to check the performance of the detector and the progress in the level of sensitivity:

- C1 - North cavity locked (*14-17 November 2003*);
- C2 - North cavity locked and automatically aligned (*20-23 February 2004*);
- C3 - Two configurations:
  - C3 – a/ North cavity as in C2 and frequency stabilization servo (23-26 April 2004)*;
  - C3 – b/ ITF locked in recombined mode (26-27 April 2004)*;
- C4 - ITF longitudinally controlled in recombined mode, with automatic alignment on both the arms and frequency stabilization servo (*24-29 June 2004*).

When the commissioning of the recycled ITF started, in summer 2004, a the problem emerged with the absence of an optical isolation between the IMC and the ITF. The light reflected from the ITF back into the injection system was scattered by the suspended IMC mirror and re-injected in the light path going into the ITF, causing interference fringes and preventing the standard working operations.

A temporary solution was adopted in September 2004, when one of the two mirrors forming the input telescope, (M6), was replaced by a 10% reflecting mirror, reducing by a factor 100 the power reflected back to the IMC. An obvious consequent drawback was that the power injected into the interferometer was reduced by a factor of 10. The induced noise in the IMC caused by the back reflected light was reduced by the expected amount, and the locking of the recycled ITF was acquired at the end of October 2004.

The commissioning activity has been carried out with 10% of the incoming power for almost one year, and three other commissioning runs have since been performed:

- C5 - Two configurations:
  - C5 – a/ ITF in recombined mode as in C4, with full hierarchical control implemented on the end suspensions (2-6 December 2004);*
  - C5 – b/ ITF locked in recycled mode (6-7 December 2004);*
- C6 - ITF locked in recycled mode with a partial automatic alignment (*29 July 2005 - 12 August 2005*);
- C7 - ITF locked in recycled mode and a complete automatic alignment (*14 September 2005 - 19 September 2005*).

At the same time the back-scattered light problem was studied: the installation of a Faraday Isolator after the IMC was singled out as the best solution.

#### **4.0.4 The new suspended input bench**

The suspended input bench previously described can not accommodate a Faraday Isolator, because of space constraints. Moreover, the replacement of the curved PR mirror with a plane one has been considered, in order to prevent misalignment noise possibly induced along the z-axis by its transversal movements. These two changes have required a complete redesign of the bench, with the sufficient space to allocate the Faraday Isolator, and a different collimation optics on the main beam,

since the PR, being plane, cannot be used anymore as a lens to collimate into the interferometer.

A three months long shut-down of the detector has been planned after C7 in order to carry out its assembling. At the same time the new PR mirror is going to be installed. Since this work has been carried out with the old injection bench, details of the new bench will not be described.

## 4.1 Simulation of the Interferometer

Due to the complexity of the optical configuration and the large number of control systems involved, simulation tools are comprehensively adopted in the commissioning of interferometric detectors, with the main goal of supporting, and possibly accelerating, the experimental work. Essentially, *time-domain* simulations and *frequency-domain* simulations are used, depending on the topic to be studied.

Time-domain simulations are largely adopted to study non-stationary processes. They sequentially compute the evolution of the fields inside the ITF, due to dynamic perturbations in the longitudinal or angular degrees of freedom. Because each step of the changes of the system is traced, the program typically is computationally very expensive. Frequency-domain simulations, which calculate steady state fields in a given optical configuration, are therefore usually preferred in studying details of stationary processes.

In order to study the longitudinal control of the ITF, a time domain simulation should be used. During the lock acquisition process, in fact, the optical parameters change dynamically together with the power build-up inside the ITF. A realistic simulation has therefore to reproduce these non-stationary effects.

The Virgo time domain simulation is SIESTA [49] (Simulation of Interferometric Experiments Sensitive To grAvitational waves). SIESTA is a C language tool which permits to describe all the main components of the detector by several kinds of structure, such as laser, suspensions, mirrors, photo-detectors. They are connected each other by a signal structure, produced as output of an element and taken as input by another one.

As will be shown in the next chapters, SIESTA played a crucial role in several aspects of the detector commissioning. It has been a very important tool for designing and testing suitable locking strategies and in the development of procedures for measuring locking parameters. Couplings between the different longitudinal degrees

of freedom and techniques to reduce the impact of the longitudinal control noises in the Virgo sensitivity were investigated as well.



## Chapter 5

# Control of the 3 km cavity

The commissioning of the Virgo ITF was organized in steps of increasing complexity. This choice was made mainly to check the various sub-systems and to test the controls needed to run the ITF in simpler optical configurations.

This chapter concerns the problem of the longitudinal control of the 3 km long Fabry-Perot cavity, in the twin optical configurations of the *north* and *west* cavities.

Before starting experimental tests, some preparatory work was done. A real time SIESTA simulation was developed, and the specifications of the most critical sub-systems for locking the ITF were checked and improved. In particular, the laser frequency noise entering the ITF was measured and compared with the specifications to lock the cavity. The longitudinal local control feedbacks were upgraded in order to improve their response during lock acquisition and minimize their noise.

Once the cavity was stably locked, the longitudinal control was refined to have better noise performance and increased robustness. Last steps of the commissioning of the single cavity were the implementation of the frequency stabilization servo (SSFS) and the automatic alignment. The performance obtained during the commissioning runs C1, C2 and C3 in single arm configuration are described at the end of the chapter.

### 5.1 Experimental set-up

Since all the mirrors of the recycled configuration were already installed when the single Fabry-Perot cavity is commissioned, the only way to have such a optical configuration was to keep the PR and the mirrors composing one of the two arms

misaligned<sup>1</sup> by a few mrad<sup>2</sup>. The two configurations, *north* and *west* cavity, are shown in figures 5.1 and 5.2.

Since the PR is kept misaligned, the laser light is not recycled inside the ITF. Moreover, PR has a reflectivity of 92%, so that only 8% of the light coming out of the injection system is transmitted to the BS. The power injected into each of the two arms is therefore about 500 times less than operating the full ITF.

In the north arm configuration, the light transmitted from the cavity is detected by the photodiode B7. The photodiodes B1p and B5 receive the light reflected from the cavity and by the first and second face of the BS.

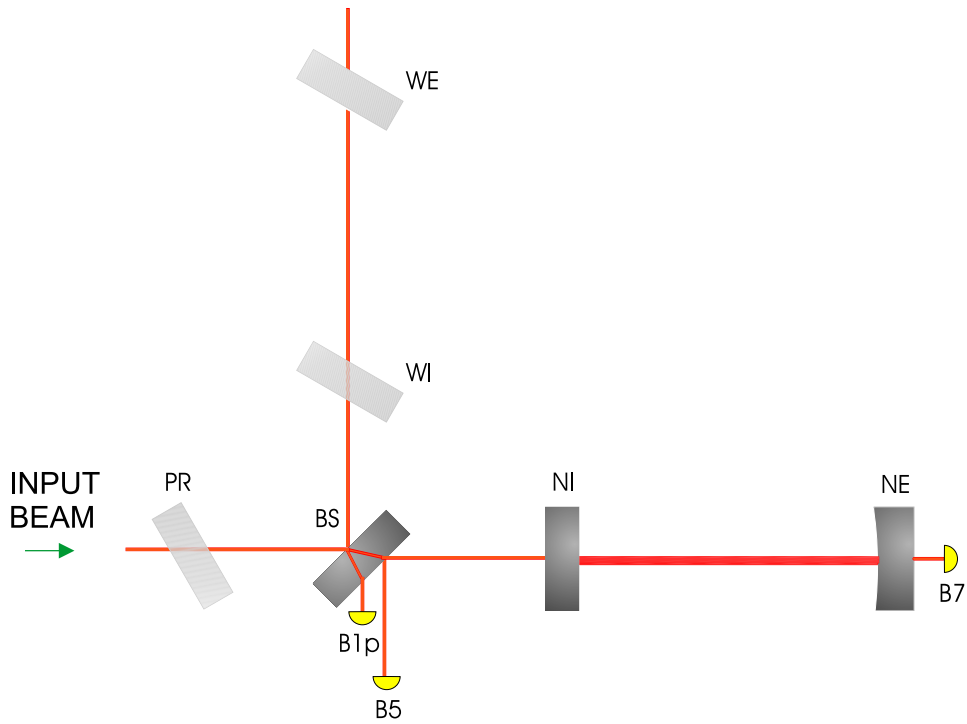


Figure 5.1: North cavity configuration. The light transmitted from the cavity is detected by the photodiode B7, the reflected light is detected by the photodiodes B1p and B5.

With 10 Watts of power coming from the injection system and considering the

<sup>1</sup>An alternative solution is to obtain the two configurations is to exclude the west (north) arm by closing the valve between the BS and the WI (NI).

<sup>2</sup>The requirement is that the misalignment is much larger than the beam divergence  $\theta_\infty$ :

$$\theta_\infty = \frac{\lambda}{\pi\omega} = 16 \mu rad$$

Virgo parameters defined in the previous chapters, the theoretical power impinging the photodiode B7 is:

$$B7\_DC \simeq (10W) \times T_{PR} \times T_{BS} \times \frac{2\mathcal{F}}{\pi} \times T_{NE} \times t_{B7} \sim 250 \mu W \quad (5.1)$$

where  $t_{B7} \sim 0.45$  is the transmission optical path from the ITF to the B7 photodiode.

The theoretical power on B1p is:

$$B1p\_DC \simeq 10W \times T_{PR} \times T_{BS} \times R_{BS} \times t_{B1p} \sim 780 \mu W \quad (5.2)$$

where  $t_{B1p} \sim 0.0039$  is the transmission optical path from the ITF to the B1p photodiode. On B5:

$$B5\_DC \simeq 10W \times T_{PR} \times T_{BS} \times R_{BS}^{2^{nd}face} \times t_{B5} \sim 80 \mu W \quad (5.3)$$

where  $t_{B5} \sim 0.40$  is the transmission optical path from the ITF to the B5 photodiode.

In the west arm configuration, the light transmitted from the cavity is detected by the photodiode B8. The photodiode B1p receives the light reflected from the cavity on transmission through the BS. On both the photodiodes, the impinging power is the same as in the north arm configuration.

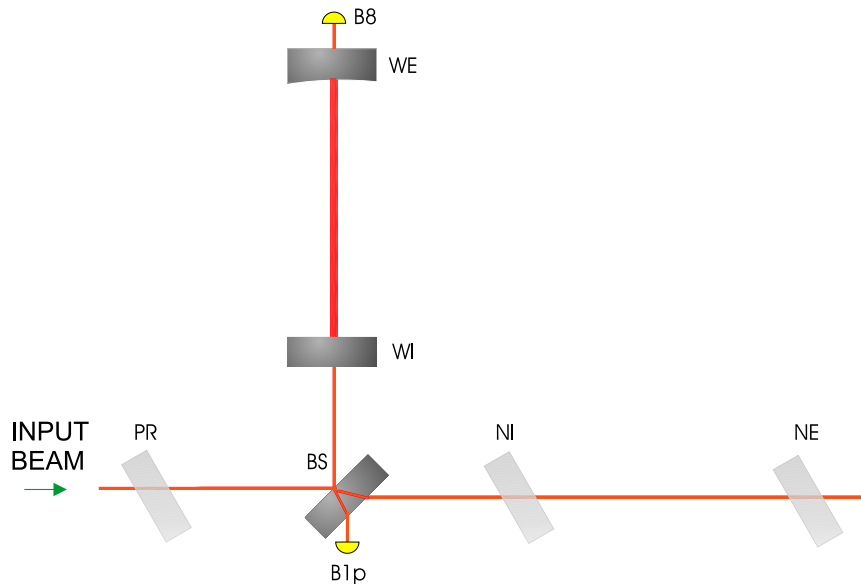


Figure 5.2: West cavity configuration. The light transmitted from the cavity is detected by the photodiode B8, the reflected one is detected by the photodiode B1p.

## 5.2 Single Arm Locking Scheme

As described in the previous chapter, Pound-Drever-Hall signals reflected and transmitted from the cavity around resonance are sensitive to cavity length variations. They are therefore good error signals to derive a controller proportional to the relative velocity of the mirrors, using linear control theory. The correction signal is fed-back to one of the two mirrors (usually the end one), in order to keep the cavity on resonance. Locking schemes for the north cavity are shown in the following plots (figures 5.3 and 5.4). Corresponding schemes<sup>3</sup> were applied for the west cavity, by sending corrections to the WE mirror.

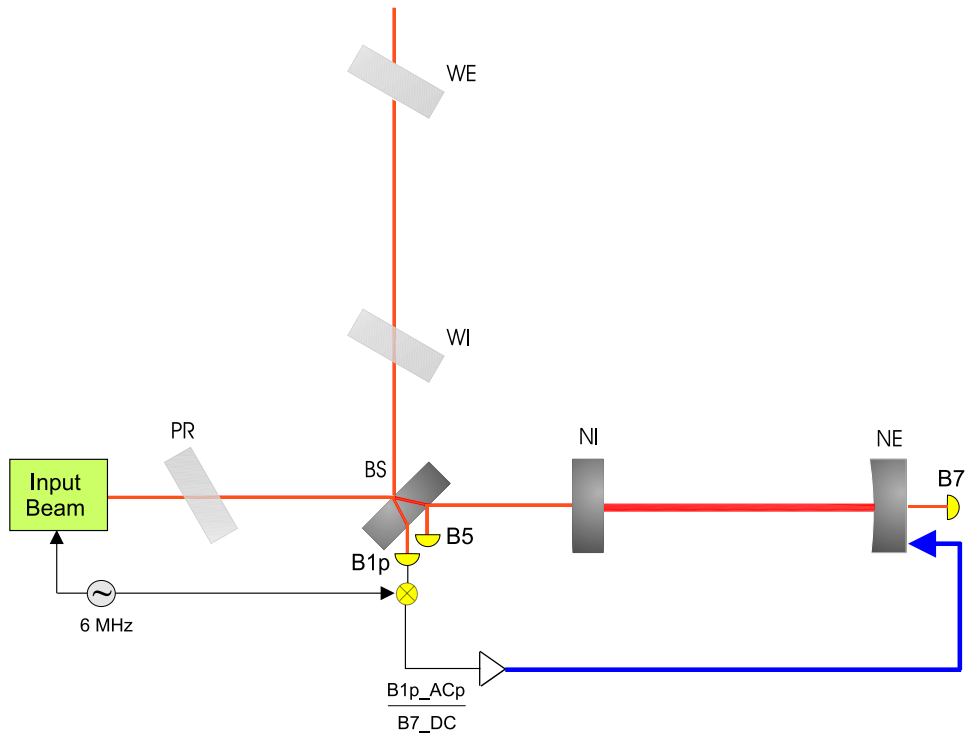


Figure 5.3: Locking scheme of the north cavity according to the Pound-Drever-Hall reflection locking technique.

During the installation of the 3km arms, some aspects of the locking scheme were preliminarily analyzed in simulation:

- the tuning of the demodulation phase<sup>4</sup> of the involved signal, in order to

<sup>3</sup>The linearization is done by using the DC power detected by the photodiode B8 ( $B8_{DC}$ ), instead of B7; in the transmission locking scheme  $B8_{ACp}$  is used instead of  $B7_{ACp}$ .

<sup>4</sup>The demodulation phase is dependent on location of the photo detector and length of cables

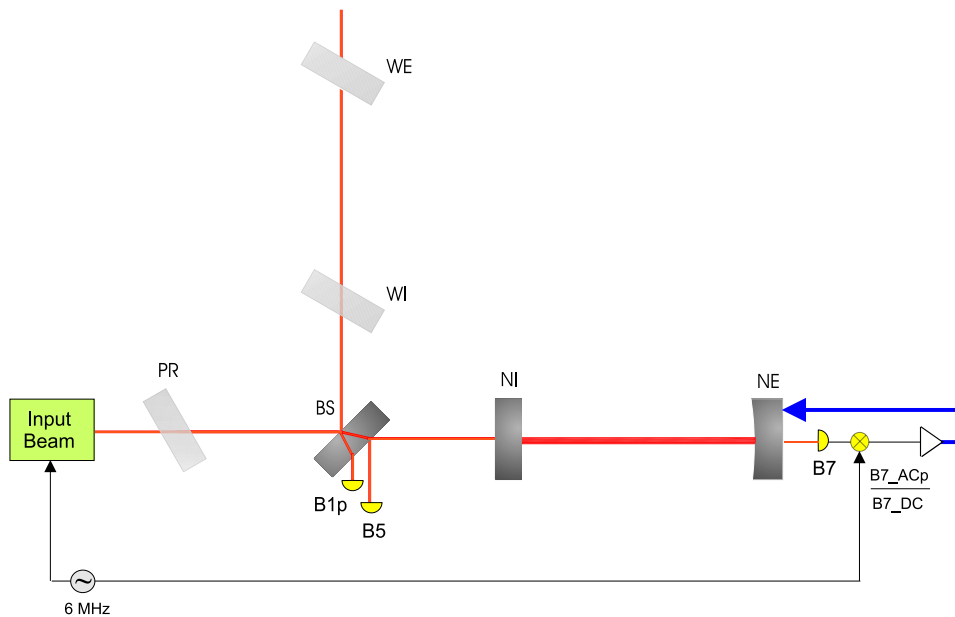


Figure 5.4: Locking scheme of the north cavity according to the Pound-Drever-Hall transmission locking technique.

maximize the strength of one component with respect to the other;

- the procedure to measure the optical gain of the involved error signals, in order to reconstruct the cavity length;
- a suitable way to engage the feedback loop;
- the design of the controller.

### 5.3 Simulation

In order to prepare the experimental activity, the single arm configuration was reproduced in a real time SIESTA simulation, including the main features of the cavity:

---

connecting it with modulator and local oscillator. For this reason, the in-phase and the quadrature-phase components of the demodulated signal are defined up to a global phase which can be arbitrarily tuned.

- the *dynamics*, to include transients<sup>5</sup> and frequency response<sup>6</sup> of the cavity;
- parameters of the *photodiodes*, such as saturations, electronic and shot noise;
- *optical parameters* of mirrors and laser system;
- *seismic noise* and *suspensions* of the mirrors, tuned so that the noise transferred to the mirror induces a mirror motion of the order of 1  $\mu\text{m}$  rms, according to the measured value. In particular, the action of the feed-back forces on the mirror are applied by a Siesta module which reproduces the dynamics of the reference mass-mirror actuators.

The north cavity simulation will be adopted in the next sections to describe the designed locking strategy. Similar considerations are valid as well for the west cavity. Because of its better SNR, usually the reflected signal is involved in the locking scheme, instead of the transmitted one. The scheme referred to in the next sections is therefore the one in figure 5.3.

### 5.3.1 Cavity length reconstruction

The demodulation phase of the reflected signal is adjusted with the cavity freely swinging until the strength of one of the two components, for instance the in-phase component  $B1p\_ACp$ , is maximized with respect to the other<sup>7</sup>. Around resonance the relation of the demodulated signal with the cavity length variation  $\Delta L$  (described in 3.2.1) can be written as:

$$B1p\_ACp = \gamma \Delta L \implies \gamma = B1p\_ACp \frac{1}{\Delta L} \quad (5.4)$$

where  $\gamma$  is the optical gain of the signal, expressed in  $[W/m]$ . By inverting this relation, the cavity length around resonance is reconstructed as:

---

<sup>5</sup>Transients arise once the cavity sweeps the resonance in a time shorter than the cavity storage time [44], being produced by the beating between the incoming laser field and the evolving stored field. The threshold velocity over that transient effects arises can be evaluated imposing that the resonance time crossing is shorter than the light storage time in the cavity. The low finesse of the cavity induce a threshold velocity on dynamics effect at 16  $\mu\text{m/s}$ , which is much larger compared with the typical velocity of the mirrors, of the order of 1  $\mu\text{m/s}$  rms. In case of single cavity, transients are therefore negligible in standard conditions.

<sup>6</sup>The frequency response of the cavity, with a pole at 500 Hz, is not crucial during the design of the control system, because the unity gain frequency of the controllers used is not higher than 100 Hz.

<sup>7</sup>The other component, in this case  $B1p\_ACq$ , can be completely zeroed in simulation.

$$\Delta L = \frac{1}{\gamma} B1p\_ACp \quad (5.5)$$

$\gamma$  can be calculated on the base of the analytical expression of the Pound-Drever-Hall signal. In the experimental activity a direct measurement of this parameter is needed. As confirmed by the simulation, it is a good approximation to assume that the peak to peak value of the  $B1p\_ACp$  linear zone corresponds at a cavity length variation around resonance of  $\frac{\lambda}{2\mathcal{F}}$  (see figure 5.5).

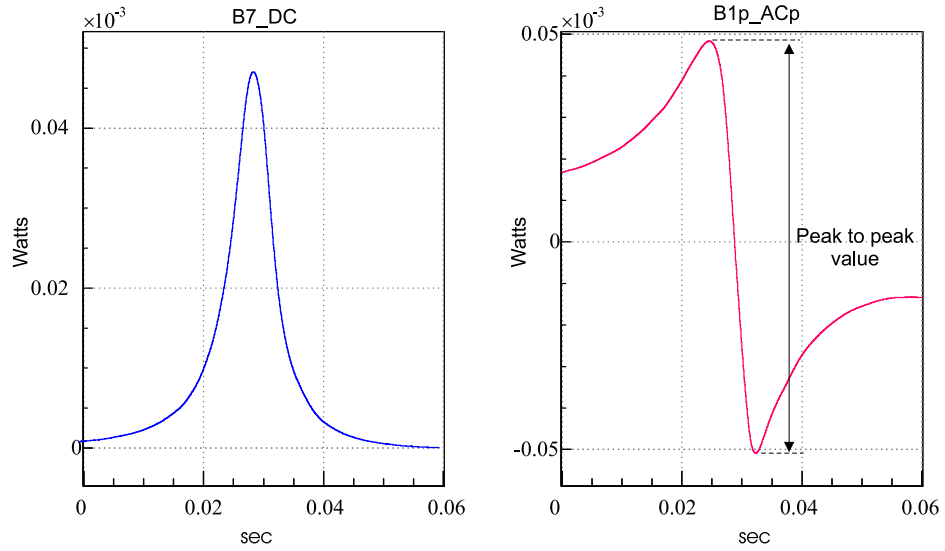


Figure 5.5: Measurement of the optical gain of the  $B1p\_ACp$  signal: the peak to peak value of the linear zone corresponds approximately to  $\lambda/2\mathcal{F}$  cavity length variation around resonance.

### Linearization of the error signal

By means of the linearization technique described in section 3.2.2, the linear region of the error signal is extended by about a factor  $\beta = 10$  (see figure 5.17). The electronic noise of the transmitted power signal, included in the simulation, prevents a further increase. The constraint on the cavity swing velocity can be modified according to the enlargement of the error signal linear range:

$$v_{max} < \sqrt{\frac{\beta F_{max} \lambda}{2 \mathcal{F} m}} \sim 10 \text{ } \mu\text{m/s} \quad (5.6)$$

so that the efficiency of the locking is extended up cavity swing velocity  $\sqrt{\beta} = 3$  times higher than before, making easier lock acquisition. The relation between the demodulated signal and the cavity length variation  $\delta L$  can be therefore re-written as:

$$B1p\_ACp = \gamma' B7\_DC \Delta L \implies \gamma' = \frac{B1p\_ACp}{B7\_DC} \frac{1}{\Delta L} \quad (5.7)$$

where  $\gamma'$ , now expressed in  $[1/m]$ , is the optical gain of  $B1p\_ACp$  as measured before, divided by the maximum value of the transmitted power  $B7\_DC$ .

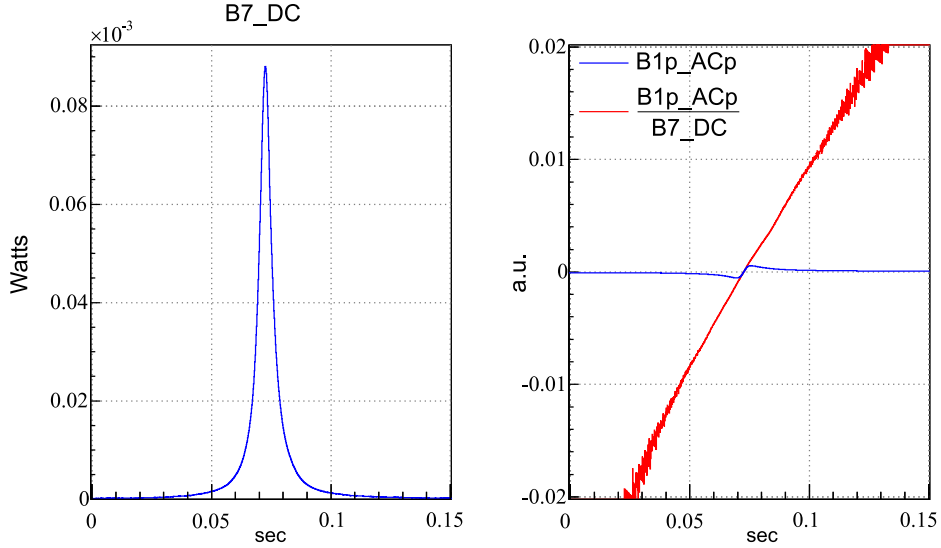


Figure 5.6: Resonance of the transmitted power (left) and Pound-Drever-Hall error signal (right). The red curve shows the enlargement of the signal due to the linearization, compared with the non-linearized one.

The reconstructed cavity length is therefore:

$$\Delta L = \frac{1}{\gamma'} \frac{B1p\_ACp}{B7\_DC} \quad (5.8)$$

Around resonance, this signal can be filtered and sent to the end mirror of the cavity in order to hold it on resonance.

### 5.3.2 Feedback to the mirror

The trigger enabling the feed-back control is asymmetric. It is switched on close to the cavity resonance condition, in order to isolate the fundamental mode of the cavity from high order modes. Corrections start to be computed by the locking algorithm at a few percent of the maximum power, without being sent to the mirrors until the cavity approaches the resonance, typically 50% of the maximum power. This mechanism handles *the loading* of the digital filters, by preventing spikes in the correction signals which can excite the mirror. The trigger is typically switched off at a few percent of the maximum power, with the objective of enlarging the action time interval of the feedback (see figure 5.7).

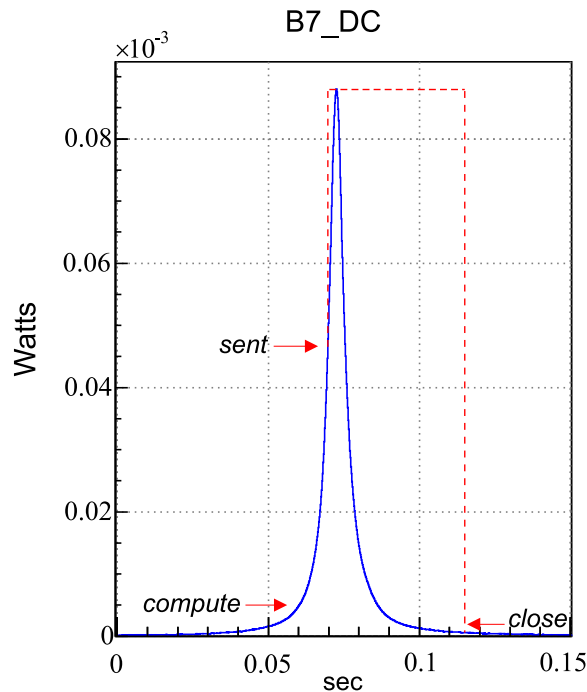


Figure 5.7: *Asymmetric trigger* on the transmitted power to enable the feedback loop. Corrections start to be computed by the locking algorithm at a few percent of the maximum power (*compute*), without being sent to the mirrors until the cavity is typically at 50% of the maximum power (*sent*). The trigger is typically closed at a few percent of the maximum power (*close*).

### The controller

The digital filter used for calculating the correction signal has to be designed taking into account the delay introduced by the Virgo control chain. As described in

section 2.5.4, this implies that controllers can not have bandwidths higher than 100 Hz.

A high gain at very low frequency is needed to compensate the seismic noise motion, so that an integrator is put from 10 mHz to 10 Hz. A derivative response of the filter from 10 Hz to 800 Hz assures a wide range of frequency with a viscous damping of the mirror. The unity gain frequency is usually set around 50 Hz (see figure 5.8).

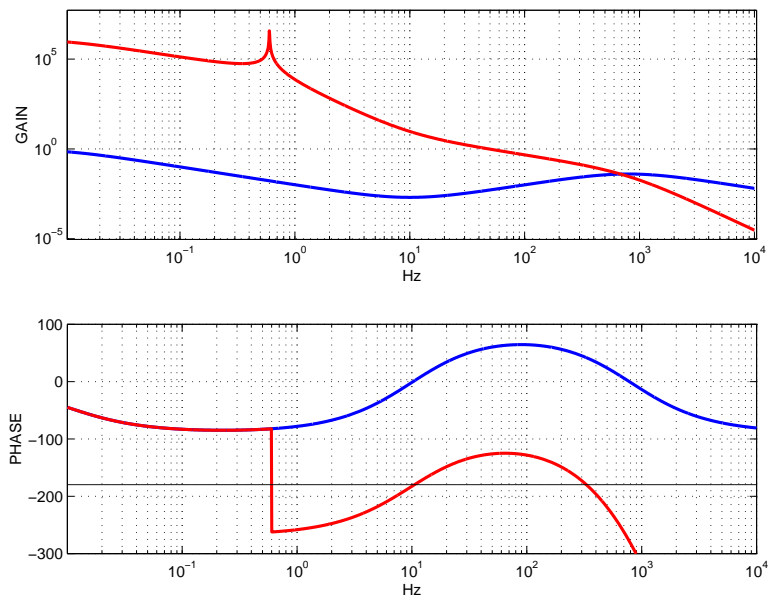


Figure 5.8: Standard controller designed to filter the reconstructed cavity length signal in order to produce correction signals (blue): gain (top) and phase response (bottom). The open loop transfer function is also plotted (red, including the 350  $\mu$ s of delay of the control chain: gain (top) and phase (bottom)). The phase margin is about 60 degrees at 50 Hz, where the unity gain is usually set.

### 5.3.3 Locking efficiency

With the locking strategy previously described, the lock of the single cavity is acquired in simulation at the first trial.

Performance is studied by increasing the cavity motion. As long as the relative velocity of the mirrors remains below 10  $\mu$ m/s, the lock is always acquired at the first attempt, in agreement with the velocity constraints described in the previous chapter. This is mainly due to the effectiveness of the linearization technique. Without linearizing the error signal, in fact, the time needed to acquire the lock increases and a few failed locking trials occur before succeeding.

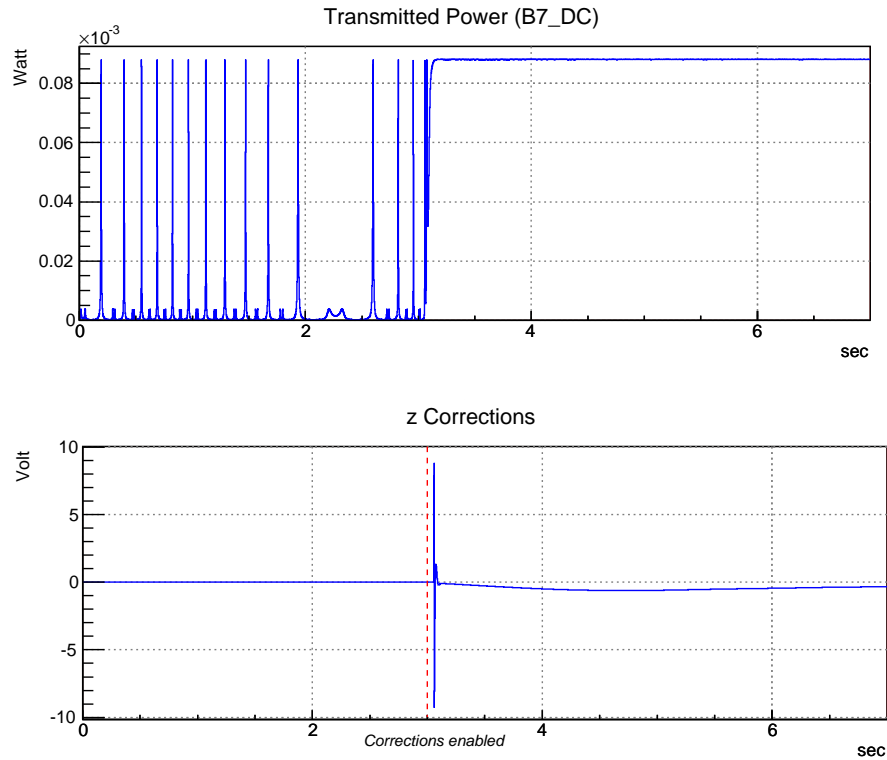


Figure 5.9: Simulation of lock acquisition: when the feedback loop is engaged, corrections (right) are sent to the mirror, and the cavity is brought and kept on resonance (left). In this case the linearization of the error signal is involved in the simulation, and the lock happens at the first attempt.

## 5.4 Check of sub-system specifications

Preliminary checks of the various sub-systems are needed before trying to experimentally test the designed locking strategy. In particular, the laser frequency noise entering the ITF was compared with the maximum level required to lock the cavity. Moreover, the longitudinal local control system was studied and improved in order to optimize its performance during the lock acquisition phase.

### Laser frequency noise

The frequency noise of the laser beam coming into the ITF after the pre-stabilization loop was measured. Its spectrum is shown in figure 5.11. The RMS value obtained

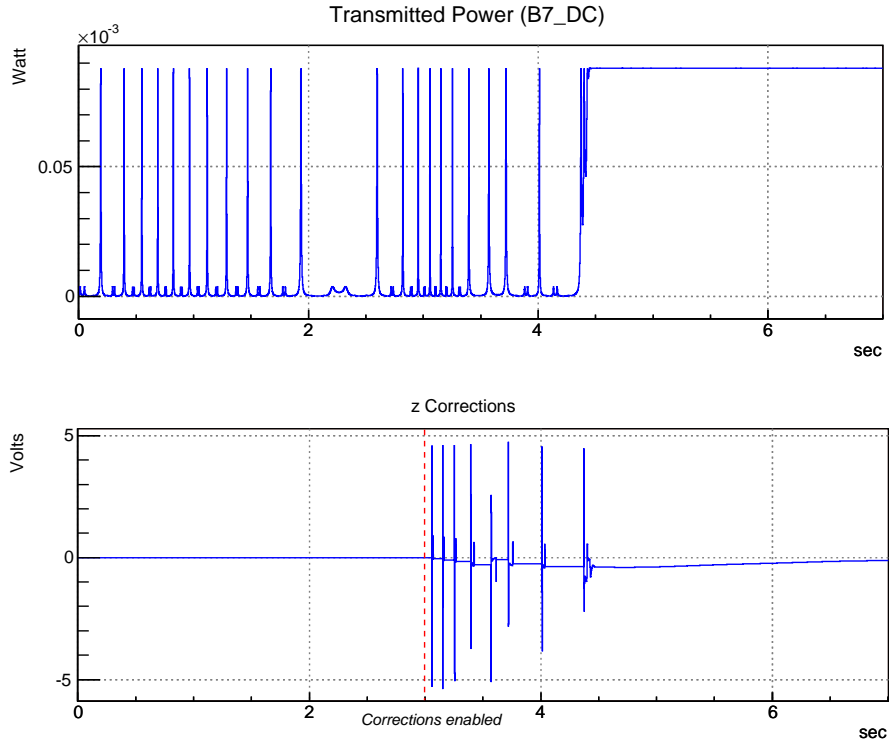


Figure 5.10: Lock acquisition simulation of the north cavity, but without applying the linearization of the error signal. Few failed events occur before the cavity is locked.

by integrating the frequency noise spectral density  $\tilde{\nu}(f)$  on all the bandwidth was:

$$\Delta\nu_{RMS} = \sqrt{\int (\delta\tilde{\nu}(f))^2 df} \simeq 60 \text{ Hz} \quad (5.9)$$

This frequency noise can be translated in a variation of the cavity length:

$$\Delta L_{RMS} = \frac{\Delta\nu_{RMS}}{\nu} L$$

An upper limit to  $\Delta L_{rms}$  in order to make possible lock acquisition is given by the fact that  $\Delta L_{rms}$  has to be lower than half width at half maximum of the resonance peak:

$$\Delta L_{RMS} < \frac{\lambda}{4\mathcal{F}} \implies \Delta\nu_{RMS} < \frac{\lambda}{4L\mathcal{F}}\nu \simeq 500 \text{ Hz} \quad (5.10)$$

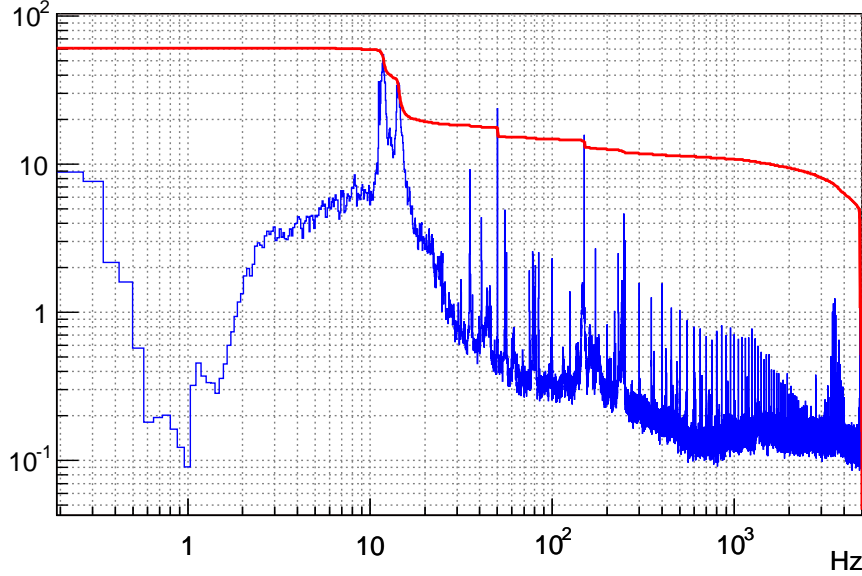


Figure 5.11: Spectrum of the frequency noise entering the ITF (blue) and rms integrated on over the bandwidth (red): its value is about 60 Hz. The rms frequency noise is dominated by two peaks, at 11.5 Hz and 14.5 Hz. They turned out to be due to the air conditioning system of the cleaning rooms, located in the central building, close to the laser laboratory.

which is about 10 times greater than the measured level shown in figure 5.11 and it therefore does not prevent lock acquisition<sup>8</sup>.

### Improving lock performance by damping the motion of the cavity mirrors

By means of a combination of passive attenuation and active damping, the Virgo suspension is able to keep the longitudinal mirror motion below 1  $\mu\text{m}$  RMS. However, during lock acquisition, the pendulum mode at 0.6 Hz of the reference mass-mirror

<sup>8</sup>Actually  $\Delta L_{RMS}$  is suppressed by the locking loop  $G(f)$ , so that its effective rms value should be computed as:

$$\Delta L_{RMS}^{eff} = \sqrt{\frac{L}{\nu} \int \frac{\delta \tilde{\nu}(f)}{1 + G(f)}^2 df} \quad (5.11)$$

The maximum level of frequency noise entering the ITF acceptable in order to maintain locked the cavity has therefore an even less stringent condition than 500 Hz rms.

system can be excited. Because of its high quality factor  $Q \sim 10^6$ , once this resonance is excited it is very difficult to recover a slow cavity motion without damping it directly from the reference mass. To deal with this problem a local longitudinal damper for the mirror was designed and implemented. The idea is to keep the damping active on those mirrors receiving corrections during the lock acquisition phase, and which could otherwise become excited. Once the lock is acquired, the damping is switched off.

The response of the z-damper control system was studied in order to optimize its efficiency and to be able to damp the 0.6 Hz oscillation in the shortest time as possible. This condition is usually referred to as *critical damping*, corresponding at the fastest exponential decay behavior of the impulse response. The transfer function of the reference mass-mirror system, modeled as a simple pendulum with resonant frequency  $\omega_{res}$ , is:

$$H(\omega) = \frac{\omega_{res}^2}{\omega_{res}^2 - \omega^2} \quad (5.12)$$

The controller is a simple derivative filter, in order to impress a viscous damping to the mirror. The transfer function of the controller is therefore:

$$G(\omega) = i\omega A \quad (5.13)$$

where A is a gain which has to be set in order to optimize the impulse response of the control system.

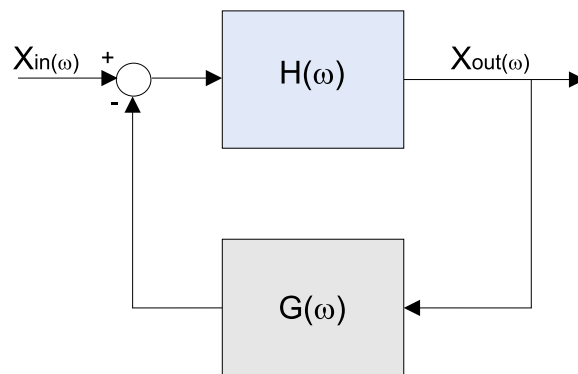


Figure 5.12: Block diagram of the longitudinal local control system.

The control system can be described as in figure 5.12, so that the closed loop transfer function is:

$$G_{CL}(\omega) = \frac{x_{out}(\omega)}{x_{in}(\omega)} = \frac{H(\omega)}{1 + H(\omega)G(\omega)} = \frac{\omega_{res}^2}{-\omega^2 + i\omega_{res}^2 A\omega + \omega_{res}^2} \quad (5.14)$$

According to control system theory, the *critical damping* condition means a double real pole in the system closed loop transfer function:

$$(i\omega_{res}^2 A)^2 + 4\omega_{res}^2 = 0 \implies A = \pm \frac{2}{\omega_{res}} \quad (5.15)$$

Moreover, only poles with a negative real part make the system stable, so that:

$$A = \frac{2}{\omega_0}$$

The corresponding open loop transfer function  $G_{OL}$  is:

$$G_{OL}(\omega) = H(\omega)G(\omega) = \frac{2i\omega_{res}\omega}{\omega_{res}^2 - \omega^2} \quad (5.16)$$

and the unity gain frequency  $f_{UG}$ , corresponding at  $|G_{OL}(\omega_{UG})| = 1$ , is:

$$f_{UG} = \frac{\omega_{UG}}{2\pi} \simeq 1.5 \text{ Hz} \quad (5.17)$$

The open loop transfer function of the z-damping system was experimentally measured in closed loop, and the gain of the controller was adjusted in order to have the unity gain frequency around 1.5 Hz, corresponding to the critical damping. However, sensor noise was also amplified when the gain was increased to reach critical damping, causing saturations in the DAC. Because of that, the simple pole at 100 Hz in the original damping filter was replaced by a double pole at 10 Hz with  $Q = 0.5$ , reducing by a factor  $1/f^2$  the noise between 10 and 100 Hz.

The performance of the z-damping tuned at the critical damping is shown in the following plot. The mirror is intentionally excited along the z-axis, in order to produce the 0.6 Hz oscillation. Then the z-damping is engaged, and figure 5.13 shows that the oscillation is completely damped in about 2 seconds.

The behavior of the viscous damping performance during lock acquisition trials was tested. Typical correction signals sent to the mirror in order to acquire the lock were artificially reproduced by filtering steps with a derivative filter, in such a way to saturate the actuators. These artificial *kicks* were sent to the mirror keeping the z-damper switched on tuned at the critical damping. No significant increasing of the mirror motion was observed with respect to the case without kicks: the mirror motion was kept within specifications even in presence of external excitations.

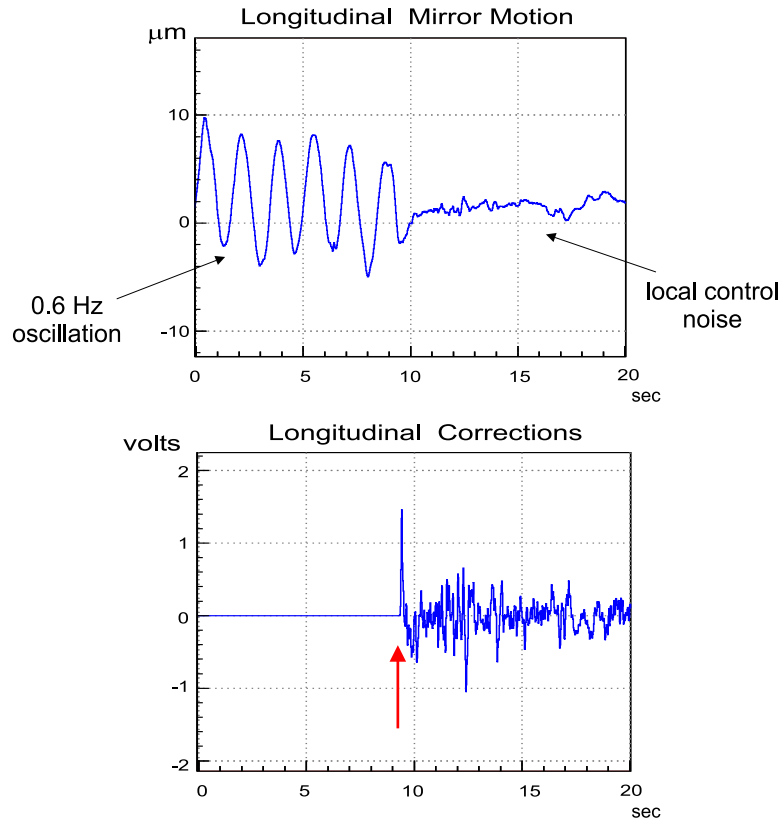


Figure 5.13: Damping of the 0.6 Hz longitudinal oscillation of the mirror by engaging the z-damping loop tuned at the critical damping. The oscillation is completely damped in about 2 seconds.

In order to further reduce the sensing noise reintroduced in the bandwidth of the locking controller, a new filter was finally adopted. It was designed to work near the critical damping, but with a steeper roll-off starting from a few Hz. The corresponding open loop transfer function is shown in figure 5.14, where it is compared with the one given by the previous simpler filter. The gain attenuation at 10 Hz is 30 db.

## 5.5 Experimental performance

The locking strategy designed in simulation was experimentally applied. Some analysis were done in order to characterize, and eventually improve, the efficiency of the locking scheme.

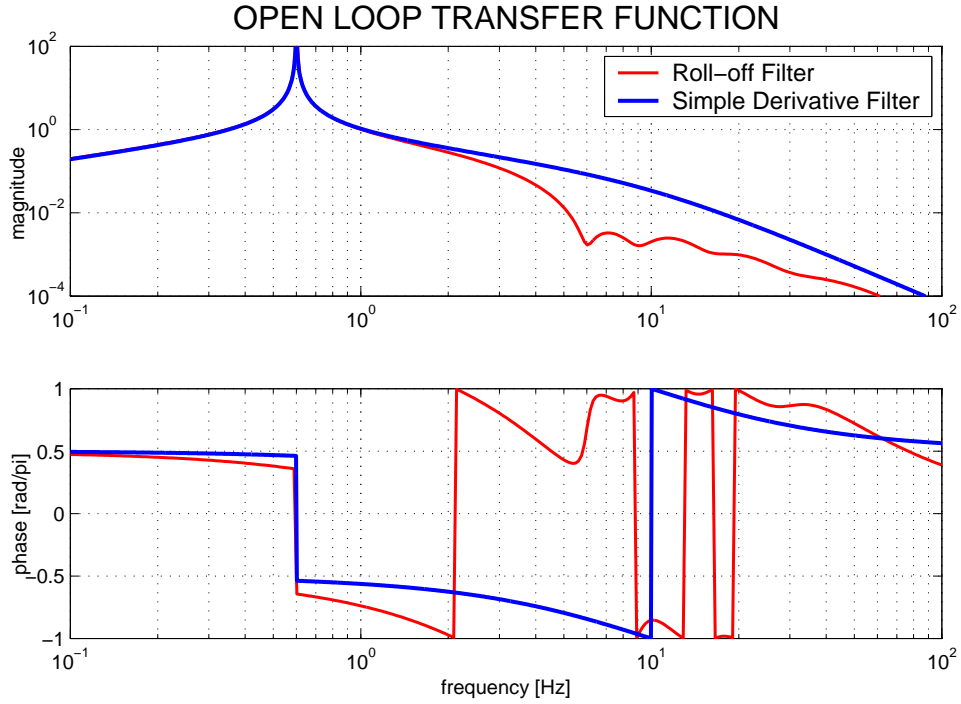


Figure 5.14: Open loop transfer function of the z-damper, by adopting a simple derivative filter with a double pole at 10 Hz (blue) and by adopting a steeper roll-off filter starting from a few Hz.

By tuning the demodulation phase with the cavity freely swinging, the ratio between the amplitude of the in-phase component with respect to the quadrature-phase is about a factor 10 5.15, which turned out to be good enough for locking purposes.

By means of the linearization technique, the linear region of the error signal is extended by about a factor  $\beta \sim 10$ . A further increase is prevented mainly by the electronic noise of the transmitted power signal. Moreover, the slope of the signal changes because of the presence of higher order modes 5.17 in the transmitted power.

In order to estimate the threshold velocity, mirrors were artificially excited before engaging the feedback loop. Characterizing each trial by the relative velocity of the mirrors it turns out that the value of the threshold velocity corresponds to the theoretical one of  $10 \mu\text{m/s}$ . Without applying the linearization technique, the time between the engagement of the feedback loop and the lock acquisition is of some seconds, with typically tens of locking failures. Results are therefore in agreement with what foreseen by the simulation.

The extremely good efficiency of lock acquisition made it unnecessary to keep

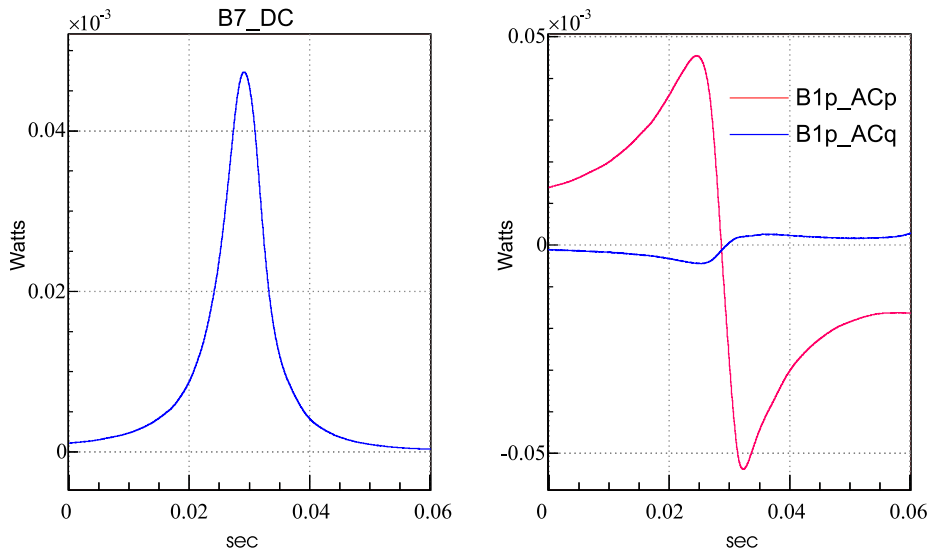


Figure 5.15: Tuning of the error signal demodulation phase: in-phase and quadrature-phase signals around resonance.

the z-dampers active during lock acquisition of the single cavity. They were instead used in the first steps of the lock acquisition of the full recycled ITF (see section 7.12).

## 5.6 Commissioning of the single arm

Once the lock of the cavity was acquired, there were two other main goals of the commissioning activity: to complete the implementation of the other global control systems, the automatic alignment and the frequency servo, and to start the investigation of the noise sources spoiling the sensitivity, possibly reducing them to prepare the commissioning of the ITF in more complex optical configurations.

### 5.6.1 Lock of the OMC

The beam used to lock the cavity ( $B1p$ ) receives only a small fraction of the beam coming out of the ITF at the asymmetric port, less than 1%. The rest of the beam goes to the OMC, but before using the high power beam transmitted by the OMC ( $B1$ ) for sensitivity measurements or for controlling the cavity, the OMC has to be

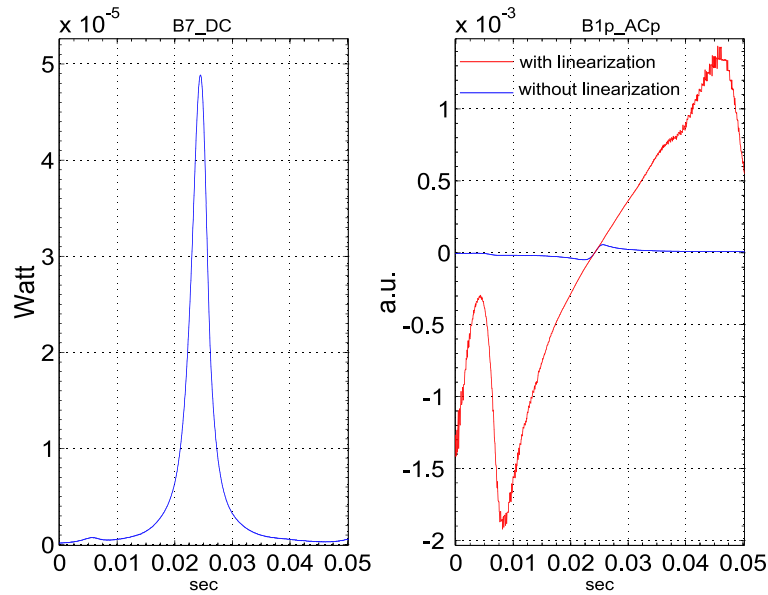


Figure 5.16: Example of enlargement of the linear region obtained by dividing the demodulated signal  $B1\_ACp$  by the transmitted power (the signal has been scaled to have the same slope of the not linearized one): the estimated increasing is about a factor 10.

locked on the fundamental mode.

OMC resonance is found through a temperature scan and identified using a CCD camera: the beam shape is compared to a gaussian profile by mean of a  $\chi^2$  reconstruction. An error signal giving the deviation from the resonance is obtained by applying a 28 kHz modulation of the OMC length, detecting the OMC transmitted beam by a photodiode, and by extracting the Pound-Drever-Hall signal by demodulation. When the right mode is identified, the error signal is used to control the OMC optical length using two Peltier cells [32]. The lock takes only a few minutes if the OMC is already resonant on the right mode. If it is not, a temperature scan is needed to search for the fundamental mode.

When the lock of the single cavity is acquired and the OMC is locked on its fundamental mode, the error signal can be moved from the photodiode  $B1p$  to the photodiode  $B1$ , placed after the OMC. The amount of light impinging  $B1$  is in fact almost 100 times higher than that one on  $B1p$ , so that the electronic noise of the extracted signals is 100 times lower. The demodulation phase of  $B1$  was tuned as it was for  $B1p$ , and the control switched from  $B1p\_ACp$  to  $B1\_ACp$ .

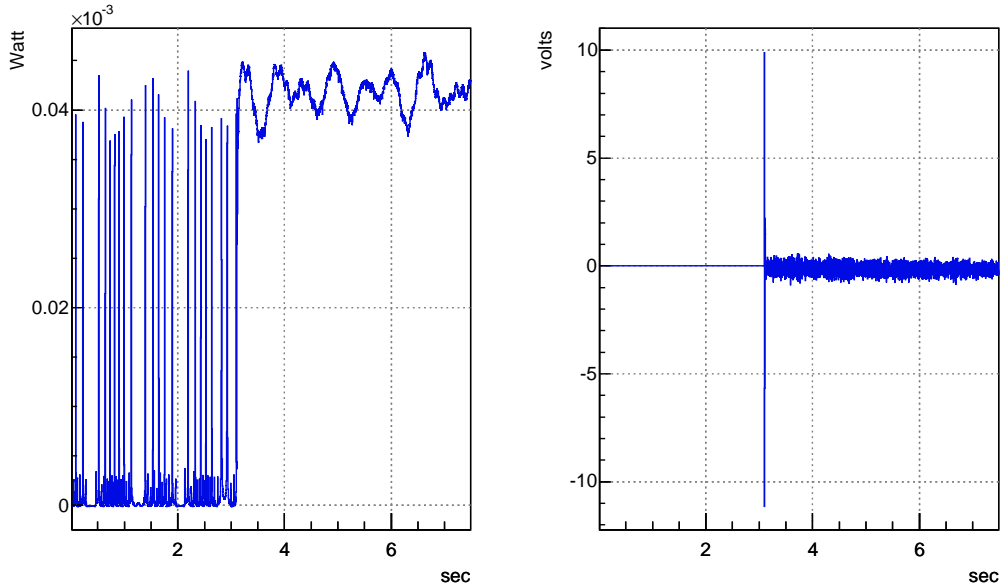


Figure 5.17: Typical lock acquisition event: transmitted power (left) and correction signal (right). The lock is acquired at the first trial.

### 5.6.2 Automatic alignment (AA)

In single arm configuration, the automatic alignment is simpler than in the full ITF, consisting only in aligning the two mirrors with respect to each other and with respect to the incoming beam. Suitable error signals are provided by the two quadrant photo-detectors detecting the transmitted beam from the cavity. Horizontal and vertical degrees of freedom can be treated separately. Moreover, the coupling between the two mirrors is reduced by setting telescopes in front of the quadrants in order to adjust the Guoy phases and by tuning the demodulation phases of the demodulated quadrant signals. When the cavity is on its operating point, the dependence of the quadrant signals on the mirror positions can be described by static matrices, one for horizontal and one for vertical degrees of freedom. For instance, by considering the vertical alignment of north arm cavity mirrors NI and NE, the signals on the quadrant diode Q71 and Q72 are given by:

$$\begin{pmatrix} B7\_q1\_ACpv \\ B7\_q1\_ACqv \\ B7\_q2\_ACpv \\ B7\_q2\_ACqv \end{pmatrix} = \vec{M} \begin{pmatrix} \theta_{xNI} \\ \theta_{xNE} \end{pmatrix} \quad (5.18)$$

An analogous matrix involving horizontal quadrant signals can be built for  $\theta_{yNI}$  and  $\theta_{yNE}$ . In the same way, demodulated quadrant signals extracted in transmission of the west cavity are used to compute the angles of the west arm mirrors. By a linear reconstruction method, misalignments angles are reconstructed by the Global Control, which sends the alignment error signals to DSP controlling the suspensions. The DSPs do the necessary control filters and send correction signals to mirrors' actuators.

The AA system has been implemented on both the cavities with similar performance. Figure 5.18 shows the reduction of the NE angular motion ( $\theta x$ ) when the AA is active on the north arm. After engaging the AA, power fluctuations due to residual motion of degrees of freedom other than longitudinal are suppressed, and the remaining fluctuations come from the input beam (that will be controlled by a dedicated automatic alignment system).

### 5.6.3 Frequency stabilization

The *Second Stage of Frequency Stabilization* servo (SSFS) in single arm configuration was designed to stabilize the laser frequency onto the cavity itself, once it is locked on resonance. The starting point is the pre-stabilization scheme described in chapter 2. Once the cavity is stably locked, the longitudinal correction signal sent to the end cavity mirror is held at zero, while the analog electronic loop of the SSFS is closed<sup>9</sup>. The cavity is therefore left free, and the laser frequency is adjusted in order to follow the cavity motion.

The scheme of the SSFS servo is described in figure 5.19. The signal reflected from the cavity is processed by analog electronics, then it is sent to the IMC suspended mirror (with a loop bandwidth of about 150 Hz) and summed with the error signal of the pre-stabilization stage.

As already said, the ITF is the best reference to stabilize the laser frequency noise above the resonance frequencies of the mirror suspension. Below a few Hz,

---

<sup>9</sup>This is done by means of a remotely controllable logical trigger.

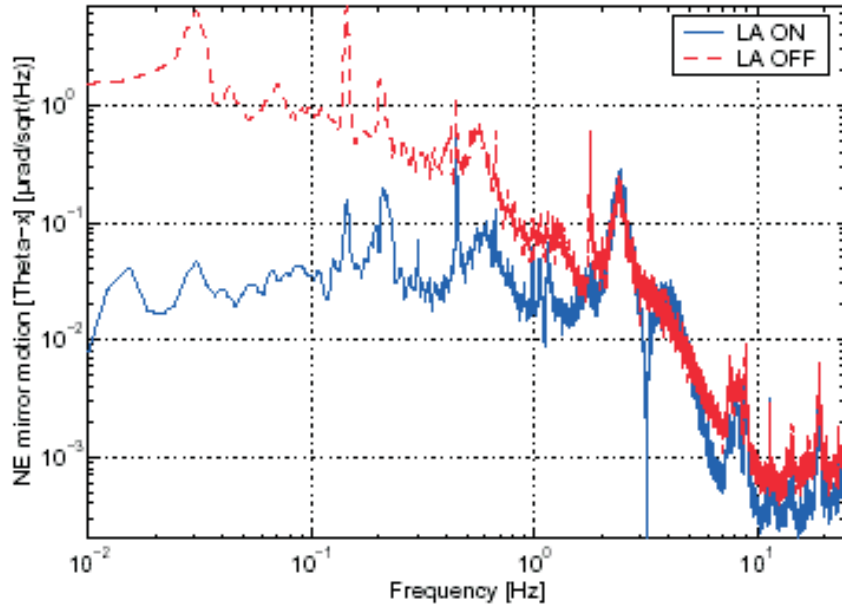


Figure 5.18: Noise spectral density of the NE mirror angular motion ( $\theta_x$ ). Angular fluctuation are strongly reduced once the AA is switched on, from DC to about 3 Hz, corresponding at the AA loop bandwidth.

the RFC is a better reference, so that the ITF was locked on it with a very low bandwidth (typically 5 Hz).

#### 5.6.4 Noise reduction

Three commissioning runs (C1, C2 and C3) were dedicated to monitoring the progresses in robustness and stability of the control systems implemented in the single arm configuration, and to follow the improvement in the noise performance 5.20.

In the **C1 run** the north cavity was longitudinally locked with the OMC locked, so that the error signal to control the cavity was taken after the OMC. The laser frequency was stabilized according to the pre-stabilization scheme. The cavity was continuously locked for two long periods: the first one 19 hours long and the second 15 hours long. The sensitivity curve was essentially limited by laser frequency noise, which was the main noise source from a few Hz up to a few kHz.

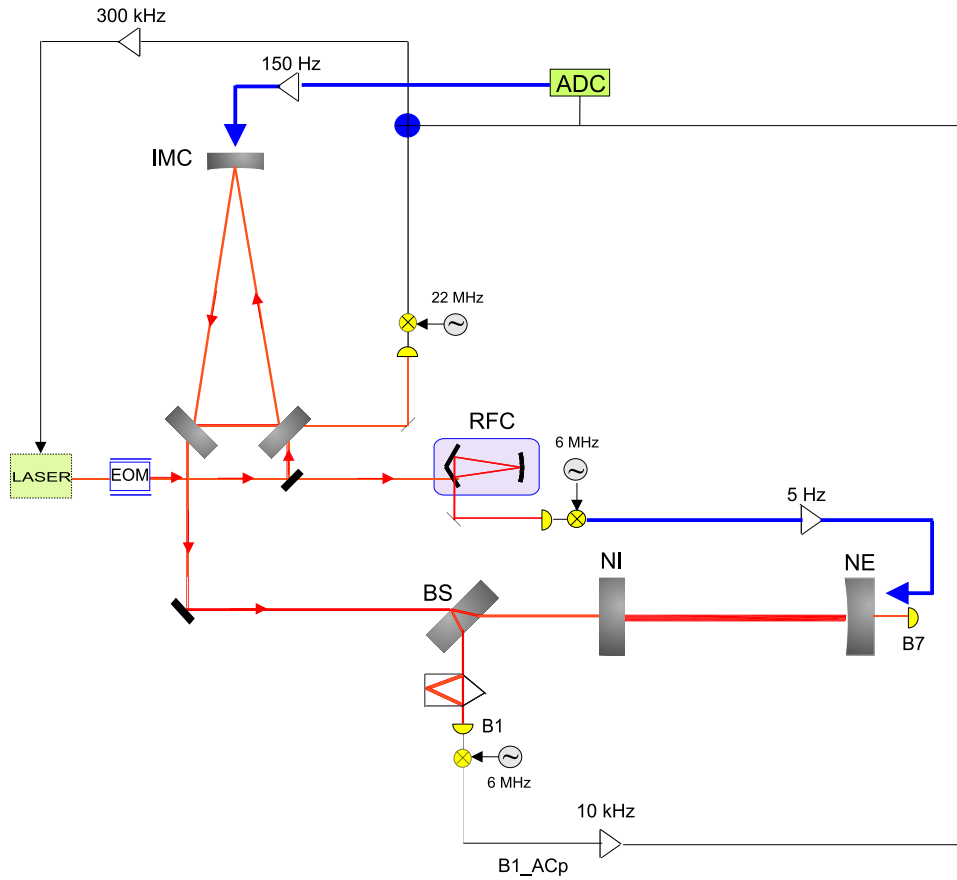


Figure 5.19: SSFS control scheme.

In the **C2 run** both the two cavities were kept locked, and no relevant differences were observed in their performance. On the north cavity the automatic alignment was tested, with four control loops acting on the angular positions of NI and NE mirrors. This considerably improved the stability of the power stored inside the cavity. Between C1 and C2 the performance of the frequency pre-stabilization scheme was studied and improved. The reduction of the laser frequency noise was obtained with the new design of IMC longitudinal and angular feedbacks, and the improvement of the input bench local control system:

- the IMC auto-alignment loops were modified by re-allocating from the reference mass to the marionette the force applied to the mirror, so that the noise transferred to the mirror up to a few Hz is filtered by a further stage of the suspension chain and accordingly reduced;

- the input bench local control loops for the angular degrees of freedom were re-designed, by applying more aggressive filter in order to reduce the noise reintroduced into the dark fringe signal from a few Hz to 100 Hz;
- the longitudinal controller of the IMC was re-designed in order to reduce the noise at high frequency (above 100 Hz).

In the **C3 run** the north cavity was commissioned as in C2, locked and automatically aligned, with the SSFS running as well. More than 32 hours without any interruption were collected with all these control systems working properly. Since in single arm configuration there is no common mode noise rejection as in the case of a Michelson ITF, the laser frequency noise was still the main source of noise. The improvement in the low frequency region, up to 100 Hz, is due to a further change of the control scheme of the injection system, the reference cavity being controlled with a smaller bandwidth (a few Hz) with respect to the previous pre-stabilization scheme.

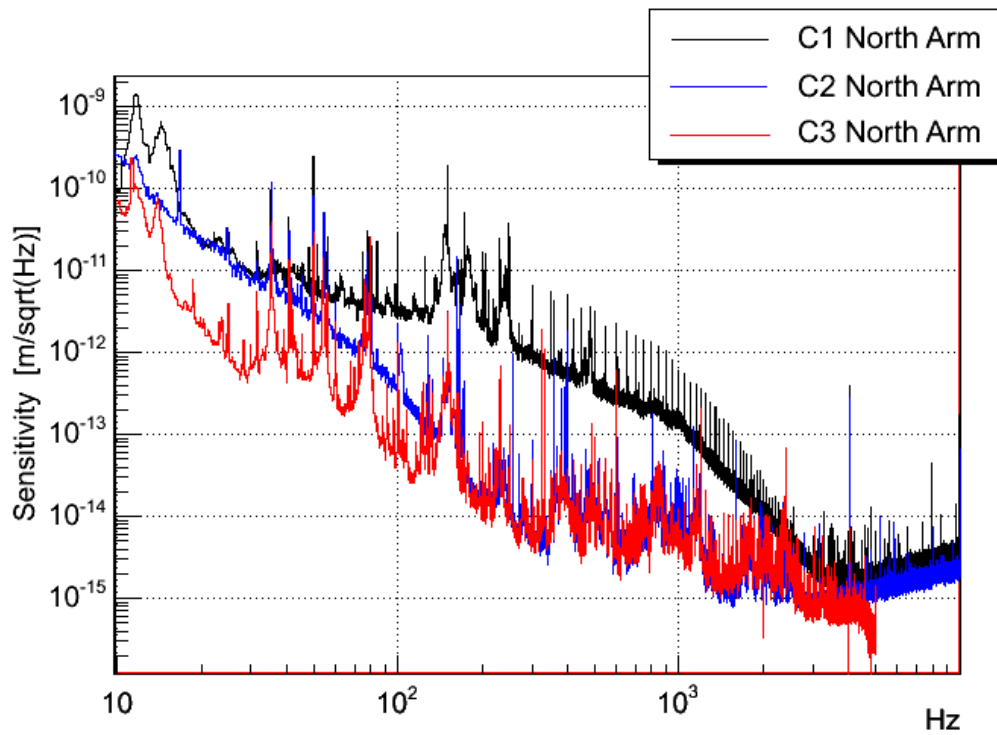


Figure 5.20: Sensitivity measured in single arm configuration as measured during C1, C2 and C3: the frequency noise is the limiting source of noise. These curves refers to the north arm. Similar performance was measured in west arm configuration.



## Chapter 6

# Control of the Fabry-Perot Michelson (*recombined*) interferometer

The recombined ITF is an intermediate optical scheme from the point of view of the longitudinal control. It is more complicated than the simple cavity, since three are the degrees of freedom to be controlled (the length of the two cavities and the Michelson length). However, fields inside the two Fabry-Perot cavities are not mixed by the PR, so that independent signals can be found to acquire the lock.

As for the single cavity, the control of the recombined ITF was simulated by SIESTA in order to prepare the experimental activity. A *two step* lock acquisition strategy was designed: first the two cavities are independently locked using the end transmitted photodiodes, then the simple Michelson is locked onto the dark fringe by using the asymmetric port signal (B1p) and acting on the BS.

By using this scheme the lock acquisition was easily acquired in simulation. On the contrary, first experimental locking attempts failed. The reason of that turned out to be related with the sensitivity of the dark fringe error signal to interferometer misalignments, due to the particular choice of the Anderson modulation frequency for the automatic alignment. The effect, referred to as *Anderson offset*, was not foreseen by simulation, since it was performed in plane wave approximation. In order to investigate this problem and understand its generation mechanism, a more complete simulation including high order modes was developed, and experimental tests were done. The appearance of the *Anderson offset* made it clear that a stable lock of the recombined ITF was possible only by drastically decreasing misalignments

of the cavities by implementing the automatic alignment control system. Once the automatic alignment of north and west cavity was running, the lock of the ITF was routinely acquired and maintained. Less noisy signals were then involved in the locking scheme.

The complete lock acquisition procedure of the recombined ITF was tested during the commissioning runs C4 and C5. Some analysis of the sensitivity response of the ITF was also done.

## 6.1 Lock acquisition strategy for the Recombined ITF

The recombined optical configuration, together with the photodiodes used for locking, is shown in figure 6.1.

The single cavity can be locked using the signal reflected or transmitted from the cavity. Because of its higher SNR, the beam reflected from the single cavity (detected at the asymmetric port B1p) is usually used. However, in recombined configuration this signal is sensitive to the length variation of both the cavities. In order to be able to control the two cavities independently, making easier lock acquisition, the two signals transmitted from the cavities were used instead.

By adjusting the demodulation phases of the transmitted signals, for instance so that mainly the in-phase component is sensitive to the length variation of the cavity, the two cavities can be controlled as described in figure 6.2: the north cavity is locked using  $B7\_ACp$ , linearized by the north transmitted power  $B7\_DC$ ; the west cavity is controlled using  $B8\_ACp$  linearized by the west transmitted power  $B8\_DC$ . An asymmetric trigger on  $B7\_DC$  and  $B8\_DC$  activates the feed-back loops, so that correction signals are respectively sent to the end mirrors. Once the lock of the two cavities is acquired, the Michelson is locked onto the dark fringe (see figure 6.3). As shown in the previous chapter, by tuning the demodulation phases, both the signals extracted at the asymmetric and the symmetric ports ( $B1p$  and  $B2$ ) can be made sensitive to the Michelson length variation, and one of the two can be chosen in order to be filtered and fed-back to the BS.

### 6.1.1 Simulation

This *two step* lock acquisition technique was preliminarily tested in simulation. Once the two cavities are locked, the demodulated signal sensitive to the Michelson length variation has a sinusoidal behavior. The demodulation phase was therefore tuned so that one of the two components (the quadrature-phase, according to the previ-

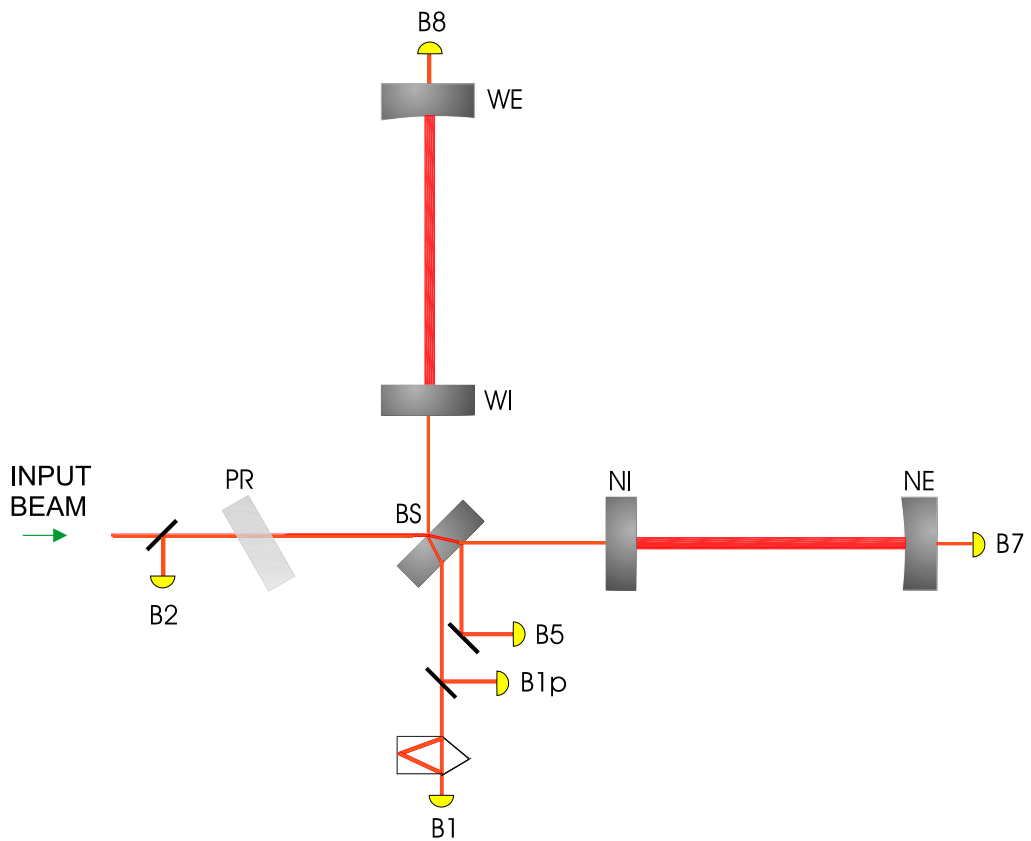


Figure 6.1: Optical scheme of the recombined ITF with the photo-detectors used for the longitudinal control. Beams transmitted from the north and west cavities are detected by photodiodes B7 and B8, respectively. The beams reflected back from the arms are recombined on BS, and detected at the symmetric port by the photodiode B2, and at the asymmetric port. Here two photodiodes are used: B1p, placed before the OMC and receiving less than 1% of the light, and B1, placed after the OMC and receives almost all the light. The photodiode B5 receives instead the light reflected back only from the north cavity.

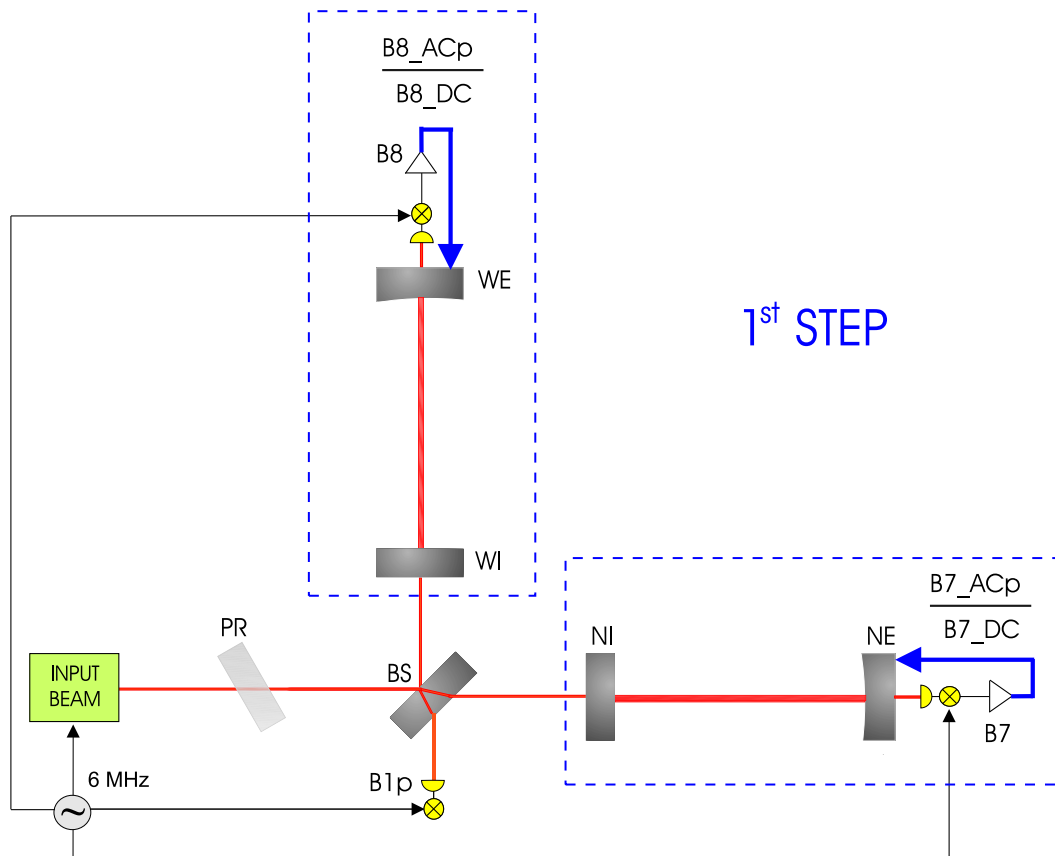


Figure 6.2: Lock acquisition scheme of the recombined ITF by applying the *two step* technique: first, the two cavities are locked by using the end transmitted signals,  $B7\_ACp$  and  $B8\_ACp$  (top); then, the Michelson is locked by the asymmetric port signal  $B1p\_ACq$ (bottom).

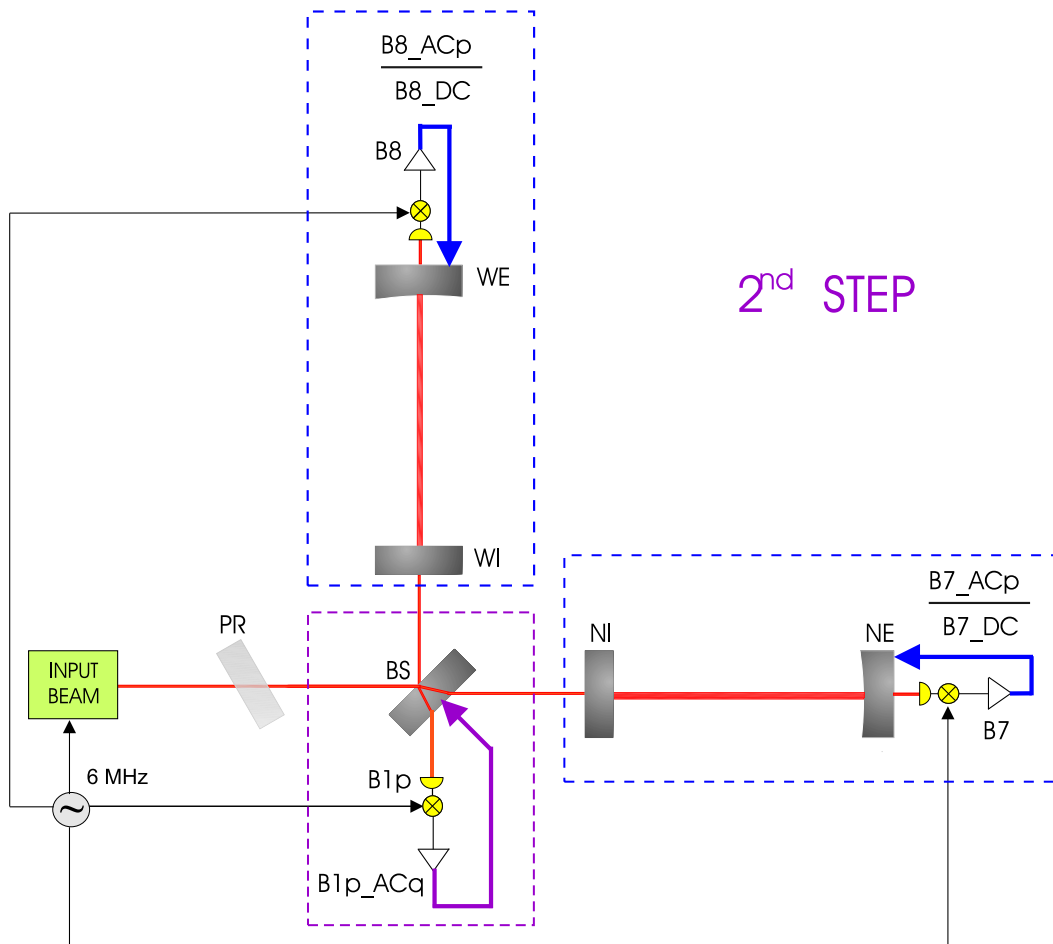


Figure 6.3: Lock acquisition scheme of the recombined ITF by applying the *two step* technique: first, the two cavities are locked by using the end transmitted signals,  $B7\_ACp$  and  $B8\_ACp$  (top); then, the Michelson is locked by the asymmetric port signal  $B1p\_ACq$  (bottom).

ous convention) maximizes the amplitude of the oscillation, by crossing zero when the power transmitted at the asymmetric port ( $B1p\_DC$ ) is minimum (*dark fringe* condition).

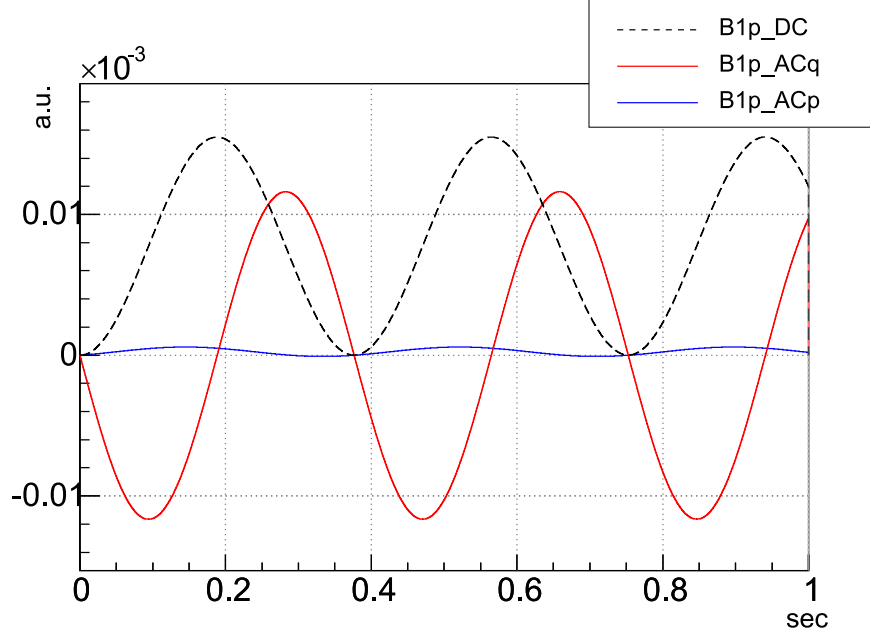


Figure 6.4: SIESTA simulation. Tuning of the B1p signal demodulation phase. The amplitude of B1p\_ACq (red) is maximized with respect to that one of B1p\_ACp (blu). B1p\_ACq crosses zero when the B1p\_DC power (dot line) is maximum and minimum, so that this signal can be used to lock the Michelson either on the dark and on the bright fringe. The operating point is selected by choosing the sign of the loop.

Around the dark fringe, when the cavities are locked, the Michelson length variation is proportional to  $B1p\_ACq$ , as described in section 3.3.2:

$$B1p\_ACq = \frac{4\pi}{\lambda} A \delta l_- \quad (6.1)$$

$A$  is the amplitude of the oscillating signal. The optical gain of  $B1p\_ACq$  can be therefore directly obtained by measuring  $A$ .

An asymmetric trigger on  $B1p\_DC$  enables the feedback only when this signal is lower than 50% of its maximum. With these procedure, and applying standard controller filters, the lock of the recombined ITF was easily acquired in simulation (see figure 6.5), in the two configurations with  $B1p\_ACq$  and  $B2\_ACq$ .

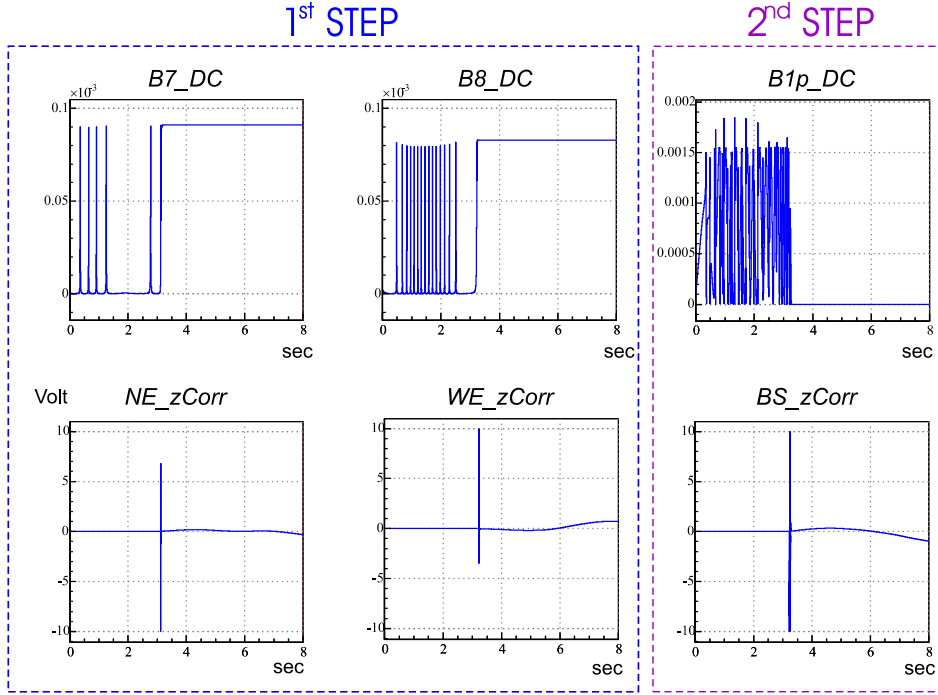


Figure 6.5: Lock of the recombined ITF acquired in simulation by applying the three steps technique. Correction signals ( $NE\_zCorr$  and  $WE\_zCorr$ ) are sent the end mirrors to lock the two cavities, and the  $BS\_zCorr$  signal is sent BS to lock the Michelson onto the dark fringe.

### 6.1.2 The *Anderson offset*

The two step lock acquisition technique as designed in simulation was experimentally tested. The asymmetric signal  $B1p\_ACq$  was initially tested to control the Michelson, since the reflected one was not available when experimental tests in recombined configuration started<sup>1</sup>.

First attempts to lock the recombined ITF revealed a behavior completely different from the simulated one. The Michelson, in fact, could be kept onto the dark fringe only for a few seconds, and not in a reliable way. A deep analysis of the  $B1p\_ACq$  signal was therefore done. The evidence was that, with the two cavities locked, this Michelson signal had an offset dependent on the cavity alignment. In order to put in evidence this effect, a simple experimental test was done in single arm configuration (west cavity). The cavity was locked with the in-phase component

<sup>1</sup>Spurious fringes were in fact observed in the B2 signals. Several tests were performed in order to understand their origin. Finally, it was discovered that the beam reflected from the ITF was clipped before impinging upon the photodiode, so that only a small fraction of it was actually detected.

of the ASY signal ( $B1p\_ACp$ ), according to the usual scheme. The end mirror was misaligned by a few  $\mu\text{rad}$  with respect to the aligned position. At the same time, the behavior of the other phase of the signal ( $B1p\_ACq$ ), out of loop, was monitored. As it is shown in figure 6.6,  $B1p\_ACq$  is around zero when the transmitted power is maximum, while an offset arises as soon as the power starts to decrease because of the induced misalignment.

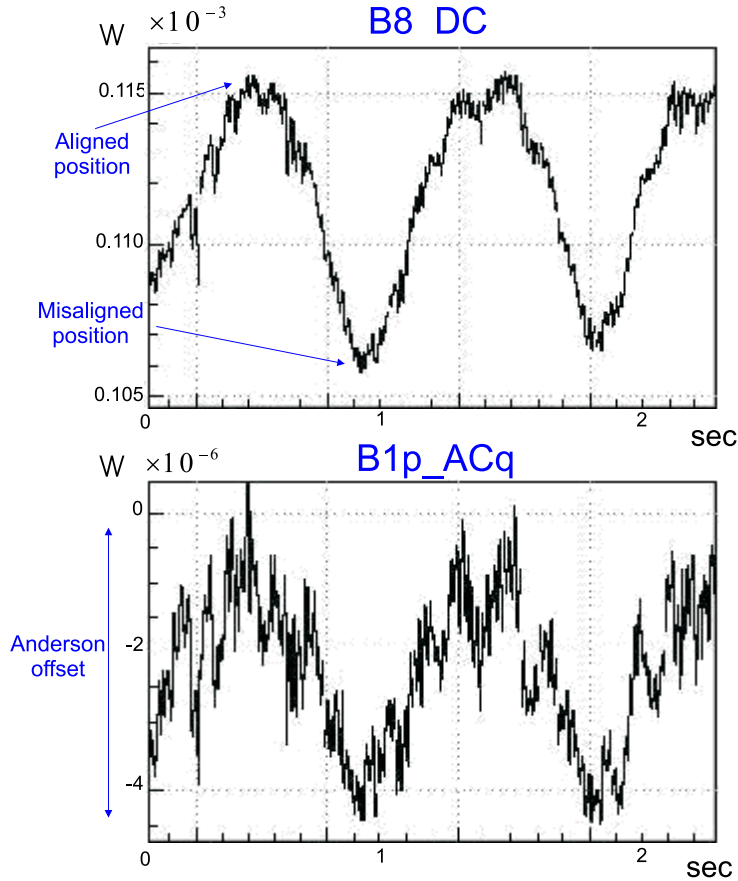


Figure 6.6: With the west cavity locked by means of  $B1p\_ACp$ , the WE mirror is misaligned by  $2 \mu\text{rad}$ , causing a decreasing of the transmitted power by about 10%. The corresponding behavior of the out of loop quadrature component is shown:  $B1p\_ACq$  is around zero when the cavity is well aligned. An offset is instead present as soon as WE starts to be misaligned. In particular, a few  $\mu\text{W}$  is the value of the offset with  $2 \mu\text{rad}$  of misalignment.

Modal simulations both of the single cavity and the recombined ITF were performed including mirror misalignments for further investigating the observed effect. Results, shown in the next paragraph, are in agreement with the experimental ones. Since the offset in the quadrature-phase turned out to be related with the particular

Virgo choice of the Anderson modulation frequency, this effect is usually referred to as the *Anderson offset*.

### 6.1.3 Simulation

A simple optical simulation of a single 3km cavity was used to investigate the effect induced by mirror misalignments in the reflected signal. High order modes ( $n + m \leq 5$ ) of the laser beam were included, and the Anderson modulation frequency was set.

The demodulation phase of the reflected signal was tuned according to the convention that the in-phase component  $B1p\_ACp$  is sensitive to the cavity length variation. The behavior around the cavity resonance of the quadrature-phase component (which is the one used to lock the Michelson in recombined configuration) was investigated (see figure 6.8). With the end mirror misaligned by a few  $\mu rad$  an offset appears in the quadrature-phase  $B1p\_ACq$ , so that the signal does not cross zero exactly in correspondence of the resonance. When the Anderson modulation frequency is shifted so that the first mode of the upper sidebands is not resonant inside the cavities, or when only the  $TEM_{00}$  mode is included in the simulation, the offset disappears.

The same simulation was done in recombined configuration, keeping the cavities on resonance, and sweeping the BS longitudinal position. The behavior of the Michelson signal around the dark fringe condition was studied as done before, including cavity mirror misalignments and high order modes of the laser beam. Results show that an offset in the Michelson error signal is present (red curve in figure 6.9) when the modulation frequency is the Anderson frequency. By shifting the modulation frequency by 3 kHz, no offset is visible (blue curve).

### 6.1.4 Generation Mechanism

In order to try to understand the generation mechanism of the Anderson offset, the Pound-Drever-Hall signal reflected from the single cavity was computed in presence of mirror misalignments.

Misalignments of the cavity mirrors generate a translation and rotation of the optical axis of the cavity with respect to the beam axis. In particular, a misalignment  $\theta_{mis}$  of the end curved mirror generates a translation  $a$  of the optical axis of the cavity with respect to the beam axis:

$$a = R_1 \sin \theta_{mis} \tag{6.2}$$

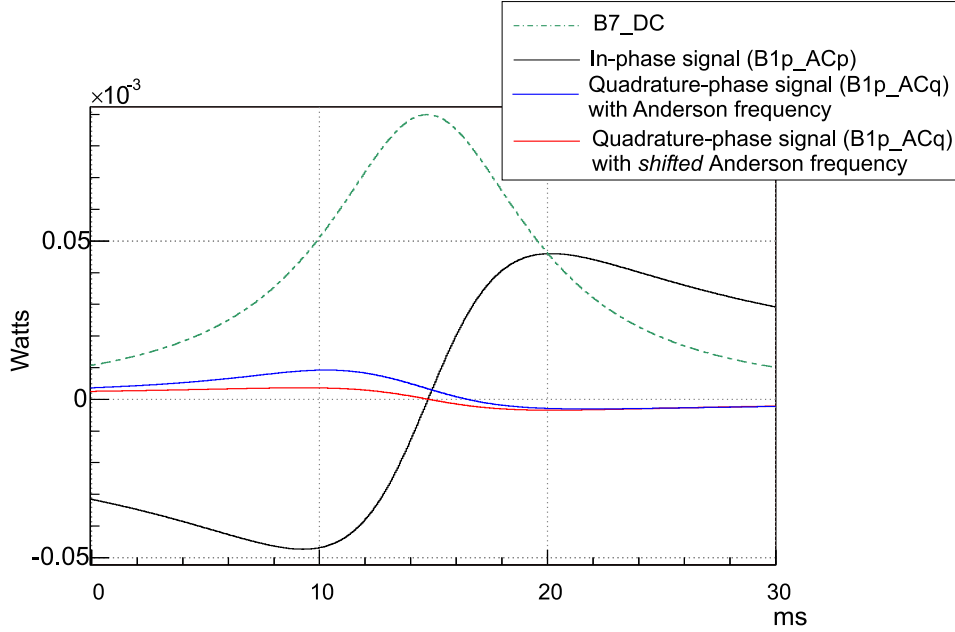


Figure 6.7: Modal simulation of a single 3km cavity, with the end mirror kept misaligned by 2  $\mu\text{rad}$ . The plot shows the behavior of the quadrature-phase of the reflected signal,  $B1p\_ACq$ , with the Anderson modulation frequency (blue curve) and the Anderson frequency shifted by 3 kHz (red curve). The transmitted power (green curve) and the in-phase signal  $B1p\_ACp$  (black curve) are plotted as well.

where  $R_1$  is the radius of curvature of the mirror.

Misalignment effects can be studied by expressing the laser beam propagating in the  $z$ -direction in terms of Hermite-Gaussian  $TEM_{mn}$  modes, as done in [42]. In the cavity reference system, in fact, the effect of an angular misalignment is equivalent to considering the incoming beam as a linear combination of  $TEM_{mn}$  modes. By considering an angular misalignment such that:

$$\frac{a}{w_0} \ll 1$$

the incoming beam can be expanded in terms of its fundamental and first transverse mode:

$$E \simeq TEM_{00} + \frac{a}{w_0} TEM_{10} \simeq TEM_{00} + \left( \frac{R_1 \theta_{mis}}{w_0} \right) TEM_{10} \quad (6.3)$$

where  $a/w_0$  is the coupling coefficient with the first transverse mode. The computa-

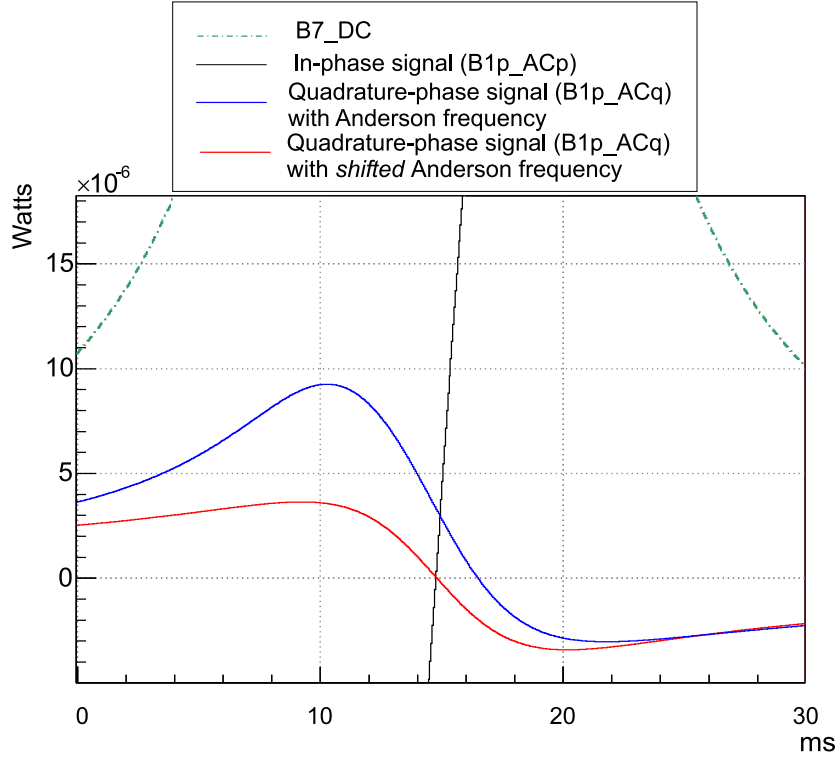


Figure 6.8: The zoom relative to the previous plot shows more clearly that, with the Anderson modulation frequency,  $B1p\_ACq$  has an offset, which disappears shifting the demodulation frequency enough to make the first mode of the upper sideband not resonant inside the cavity.

tion of the in-phase and quadrature-phase components of the reflected signal from the cavity has to be done by including the first transverse mode in the expression of carrier and sidebands field. Since the Hermite-Gaussian  $TEM_{mn}$  modes form a complete and orthogonal set of functions, contributions of  $TEM_{00}$  and  $TEM_{10}$  modes to the demodulated signals can be computed independently.

The computation of the reflected demodulated signals by considering the fundamental mode was already done in section 3.2.1. Only the carrier field is resonant inside the cavity, while sidebands are anti-resonant. The result is that one of the two components of the demodulated signal vanishes and the other one is sensitivity to the cavity motion around resonance.

Concerning the first transverse mode, because of the Anderson modulation frequency, only the first transverse mode of the upper sideband is resonant inside the cavity together with the carrier, while the first mode of the lower sidebands is anti-

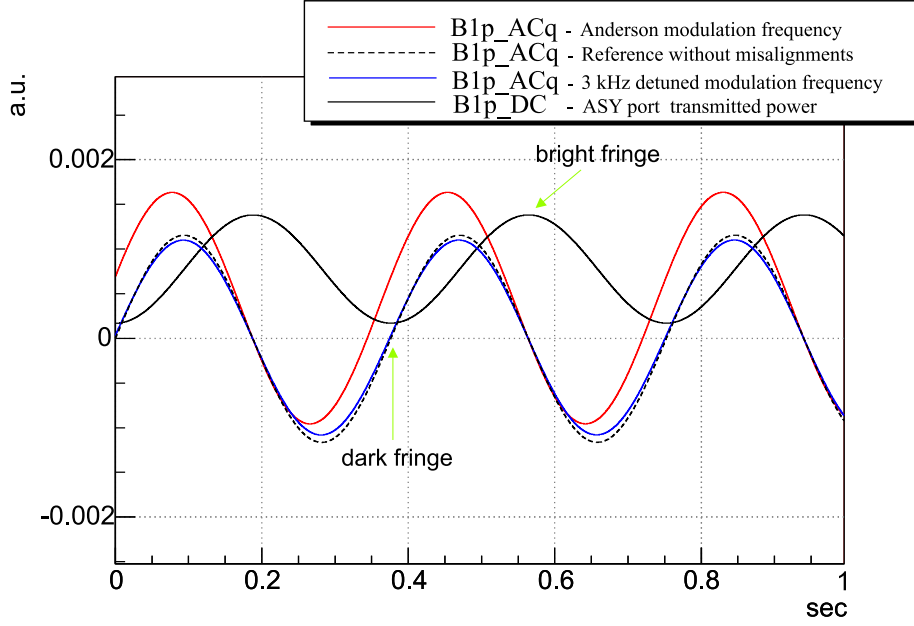


Figure 6.9: Simulation of the Michelson error signal  $B1p\_ACq$  in presence of misalignments. An offset is visible in the signal, in correspondence of the dark fringe condition, if the modulation frequency is tuned according to the Anderson frequency.

resonant (see figure 6.10).

By applying the formula 2.13, both the components of the Pound-Drever-Hall signal turn out to be different from zero. In particular, by adjusting the demodulation phase of the reflected signal so that the in-phase component  $B1p\_ACp$  is sensitive to the cavity length variation around resonance, an offset proportional to the square of the misalignment angle,  $\theta_{mis}$ , is present in the quadrature-phase  $B1p\_ACq$ :

$$B1p\_ACq \simeq 2P_{in,0}J_0J_1 \left( \frac{\theta_{mis}R}{w_0} \right)^2 \quad (6.4)$$

In single cavity configuration only the demodulated signal sensitive to the cavity length variation is involved in the locking scheme ( $B1p\_ACp$ ). The Anderson offset is present in the other component ( $B1p\_ACq$ ), which is out of loop, so that it does not prevent stable operations.

In recombined configuration, instead, the quadrature component is used to control the Michelson length. The Anderson offset induces an equivalent displacement

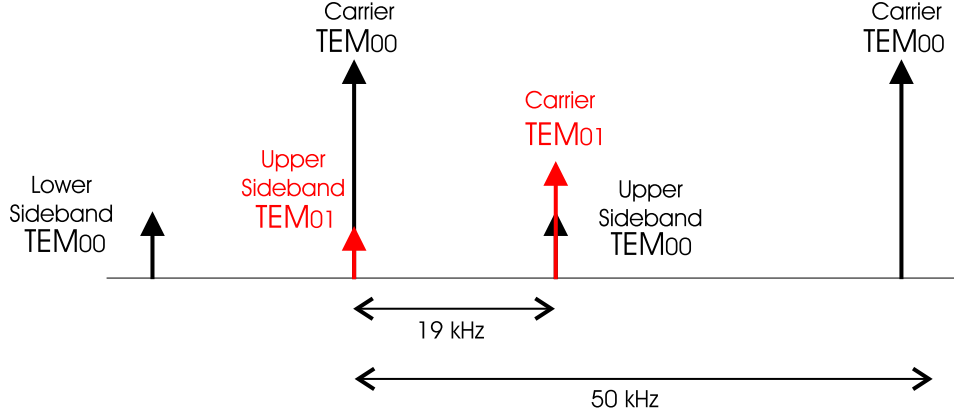


Figure 6.10: Carrier and sidebands fields in the ITF by modulating at the Anderson frequency.

of the Michelson length  $\delta l$ , which can be estimated comparing this signal with the Pound-Drever-Hall signal sensitive to the Michelson length variation (see appendix C), so that:

$$\delta l \simeq 5 \times 10^{-8} \left( \frac{\theta_{mis}}{1 \mu\text{rad}} \right)^2 m \quad (6.5)$$

First locking trials of the recombined ITF were carried out without having the automatic alignment implemented. By considering typical angular misalignments of the mirrors under local control of the order of  $1 \mu\text{rad}$ , the Michelson length variation induced by the Anderson offset is therefore:

$$\delta l \simeq 5 \times 10^{-8} m$$

This value is more than one order of magnitude above the level required to move the ITF off the dark fringe, so it can explain the locking failures.

### 6.1.5 How to deal with the Anderson offset

According to the model and simulations presented in the previous section, the Anderson offset is generated by the coupling between high order modes of the incoming beam and angular misalignments of the cavity. In order to deal with this problem, different solutions were tested:

- the control of the Michelson length was moved to the signal transmitted from the OMC. The OMC, in fact, filters high order modes, so that the demodulated signal is generated only by the fundamental mode of carrier and sidebands. As

soon as the control was moved to  $B1\_ACq$ , the recombined remained stably locked onto the dark fringe for several hours;

- after implementing the automatic alignment on both the cavities, the Anderson offset in the  $B1p\_ACq$  signal essentially disappeared. The locking strategy of the recombined ITF required therefore to engage the automatic alignment on both the cavities, once they were locked, before locking the Michelson.

Figure 6.11 shows the behavior of the  $B1p\_ACq$  signal with respect to the asymmetric port power  $B1p\_DC$ , with the two cavities locked and the BS freely swinging: if the automatic alignment is not running, when the ITF crosses the dark fringe the Anderson offset is present. On the contrary, when the automatic alignment is running, the offset is not present anymore.

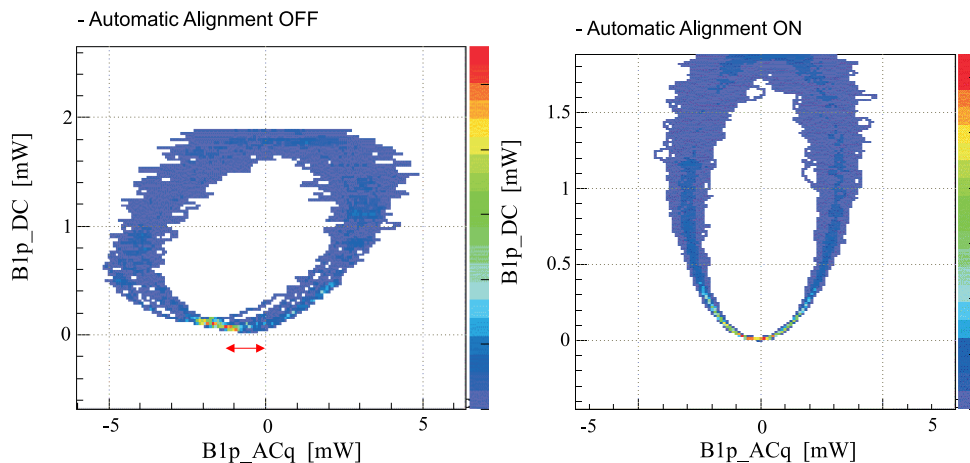


Figure 6.11: Behavior of the  $B1p\_ACq$  signal with respect to the asymmetric port power  $B1p\_DC$ , when the cavities are locked and the BS is freely swinging. When the ITF is on the dark fringe, the offset is visible in the  $B1p\_ACq$  signal only if the mirrors are under local controls (left). When the automatic alignment is running (right), the offset is not present anymore.

- Once the B2 signals were available,  $B2\_ACq$  was involved in the control scheme to replace  $B1p\_ACq$ . Since this signal is not affected by the Anderson offset (see figure 6.1.5), stable operations of the ITF were possible even by keeping mirrors under local controls.

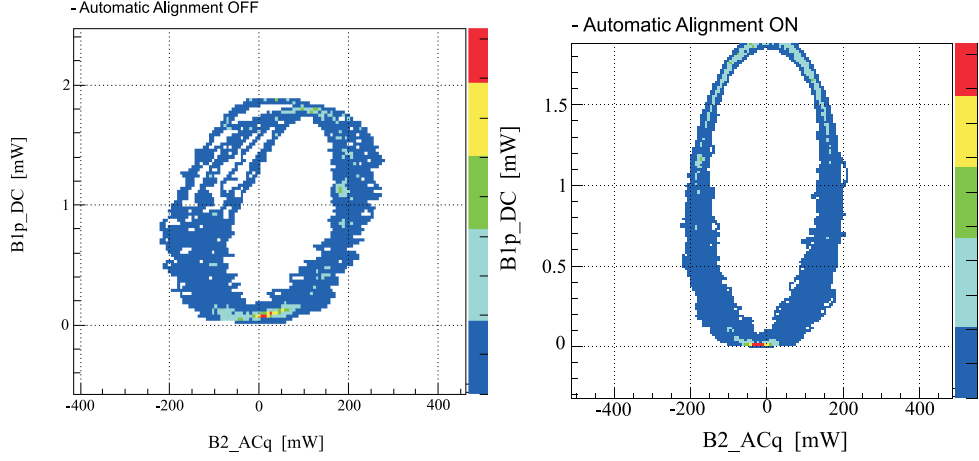


Figure 6.12: Behavior of the  $B2\_ACq$  signal with respect to the asymmetric port power  $B1p\_DC$ , when the cavities are locked and the BS is freely swinging. No offset is present in the reflected demodulated signal when the ITF crosses the dark fringe, even if the automatic alignment is not working.

## 6.2 Linear Locking

The use of the end photodiodes to acquire the lock makes possible to independently control the three degrees of freedom of the recombined ITF. However, in order to improve the sensitivity of the detector, they need to be replaced by less noisy signals detected at the asymmetric and symmetric ports. The applied locking strategy was therefore to independently control the two cavities and to use the reflected signal  $B2\_ACq$  to control the Michelson length. Once the lock was acquired, the control was passed to signals detected at the antisymmetric and symmetric ports, sensitive respectively to differential and common motion of the cavities (*linear mode*). By including the dependence on the transmitted powers, the sensing matrix connecting the demodulated signals and the cavity length variation  $\delta L_N$  and  $\delta L_W$  is:

$$\begin{pmatrix} B1p\_ACq \\ B2\_ACp \end{pmatrix} = \begin{pmatrix} \alpha_{11}B7\_DC & -\alpha_{12}B8\_DC \\ \alpha_{21}B7\_DC & \alpha_{22}B8\_DC \end{pmatrix} \begin{pmatrix} \delta L_N \\ \delta L_W \end{pmatrix} \quad (6.6)$$

The measurement of the gain coefficients  $\alpha_{ij}$  was done by injecting a sinusoidal line at a few hundreds of Hz (well above the unity gain frequency of the loops, set at 50 Hz) on the end mirrors. The gain of the reference mass actuators is:

$$g_{act}(f) = 1.3 \times 10^{-5} \frac{\text{m}}{\text{V}} \left( \frac{0.6}{f} \right)^2$$

so that the value of  $\alpha_{ij}$  can be found by measuring the amplitude of the line in the demodulated signal. For instance,  $\alpha_{11}$  is given by:

$$\alpha_{11} = \frac{B1p\_ACq(\bar{f}) [\text{W}]}{A(\bar{f}) [\text{V}]} \frac{1}{g_{act}(\bar{f})[\text{V/m}]} \frac{1}{B7\_DC [\text{W}]} \quad (6.7)$$

where  $\bar{f}$  is the frequency of the injected line.

Before engaging the automatic alignment system on both the cavities, variations of about 30% in the measured value of these gain coefficients were systematically observed. Frequent readjustments were therefore needed in order to keep the ITF stably locked in linear locking scheme. Once the automatic alignment system was implemented, no significant variations of these parameters were observed.

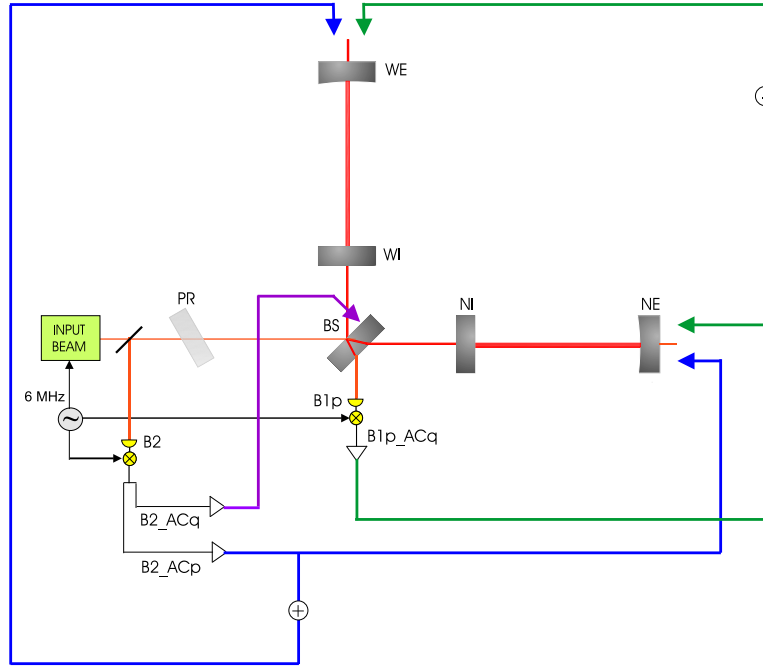


Figure 6.13: Locking scheme of the recombined ITF in *linear mode*.

## 6.2.1 Controller

In the lock acquisition phase, the controller used for all the three degrees of freedom is based on the standard filter adopted during the commissioning of a single arm (see

section 5.3.2). The gain of the controller is chosen in order to have a unity gain frequency of the open loop transfer function around 50 Hz. Once the lock is acquired, more complex filters were tested mainly in order to reduce the noise reintroduced by feed-back loops into the dark fringe signal. In the commissioning run C3, for example, the sensitivity curve was dominated by the electronic noise of the west transmitted demodulated signal, above 200 Hz. Before changing the locking scheme involving less noisy signals, a filter with a roll-off at 300 Hz was tested in the control loop of the two cavities, preventing the reintroduction of this noise above 300 Hz.

In *linear mode*, the controller used for all the three d.o.f. 's is based on the standard filter used in the lock acquisition. Once the automatic alignment of the arms was running and the stability of the system improved, a more complex filter with a roll-off at 50 Hz was tested (in C4 and C5) on the BS in order to reduce the noise reintroduced into the sensitivity curve starting from a few tens of Hz. The bandwidth of the control was also reduced to 10 Hz.

### 6.3 Commissioning of the Recombined ITF

Once the two cavities of the recombined ITF were locked, the automatic alignment control system and the frequency stabilization servo were implemented. Since the fields inside the in recombined configuration ITF are not mixed by the PR, the alignment control for the recombined configuration consists of automatically aligning the two cavities at the same time.

The frequency stabilization scheme in recombined configuration is similar to the one described for the single cavity. The laser frequency is stabilized onto the common mode of the ITF, so that the interferometer signal added to the pre-stabilization loop (section 2.5.2) is the signal reflected from the ITF ( $B2\_ACp$ ). Finally, according to the procedure already described in the single cavity lock, the OMC is put on resonance and the  $B1\_ACq$  signal replaces the  $B1p\_ACq$ .

During the commissioning of the recombined ITF, the *hierarchical control* of the superattenuator was implemented as well. It consists of splitting locking forces over three actuation stages in a hierarchical way, instead of applying them on the mirror only at the level of the reference mass. The need for this kind of control is explained in the next paragraph.

### 6.3.1 Suspension hierarchical control

In the locking schemes described so far, longitudinal forces are applied to the mirror by means of reference mass actuators, which have a large dynamic range in order to make easier lock acquisition. However, the actuation noise injected into the ITF is a severe limit to the sensitivity: at 20 Hz it is in fact more than 1000 times larger than the designed sensitivity 6.14.

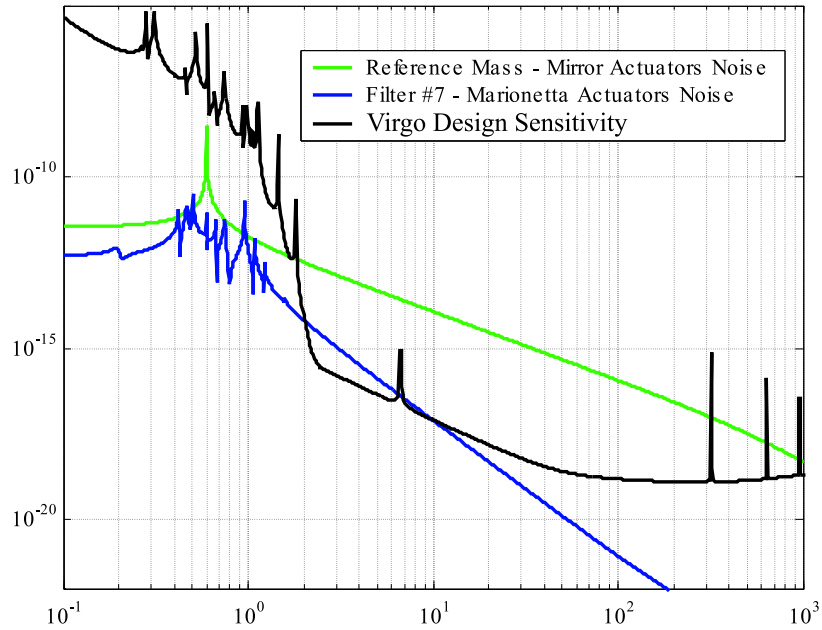


Figure 6.14: Actuator noise of marionette and reference mass compared with the Virgo design sensitivity.

The noise is mainly due to DAC noise ( $300 \text{ nV}/\sqrt{\text{Hz}}$ ) and coil driver noise ( $70 \text{ nV}/\sqrt{\text{Hz}}$ ), and is converted into equivalent mirror displacement by a large coupling factor,  $13 \mu\text{m}/\text{V}$ . Such a large coupling factor is very useful in the lock acquisition phase, when mirrors have to be brought onto the working point and large dynamics are needed. Once the lock is acquired, the residual force to be applied is largely in the low frequency region (DC-5 Hz), where tidal drifts and mirror internal resonances have to be compensated, and very small elsewhere. Therefore, the gain of the coil driver (and the corresponding noise) cannot be reduced, unless a large fraction of the low frequency force is re-allocated to upper stages.

The *suspension hierarchical control* was designed in order to reduce the force ap-

plied to the reference mass once the lock is stably acquired<sup>2</sup>. It involves splitting the locking force over three different actuation stages: inverted pendulum, marionette and reference mass. The compensation for earth tides, in the range DC-0.01 Hz, is reallocated upon the soft inverted pendulum; the force in the range 0.01-8 Hz, where all the suspension resonances fall, is reallocated to the marionette.

As tested during C5, after reallocating the force to upper stages of the end mirrors, the reference mass residual correction always remained below 10 mV, a factor 1000 lower than the full dynamic range of the actuators. This allows the coil driver amplification to be reduced by a factor of 1000, switching to *low noise* coil-drivers, thereby fulfilling the final requirements.

## 6.4 Sensitivity and Noise Budget

Three commissioning runs, (C3, C4 and C5) were performed with the ITF in recombined mode, in order to test the involved control systems in long term operations and to monitor the sensitivity progress. At high frequency the sensitivity curve of the recombined ITF is designed to be  $\sqrt{500} \sim 22$  times worse than the recycled ITF one<sup>3</sup>. However, keeping the interference between the two beams locked onto the dark fringe, all common mode noises linked with the laser source are considerably reduced with respect to the single arm configuration. As a consequence, in the recombined ITF more noise sources become relevant and can be investigated.

In the last part of C3 the recombined ITF was kept locked for one day with the standard lock acquisition scheme. Because of the use of the noisy transmitted signal *B8\_Acp* to control the west arm, the sensitivity is limited in all the bandwidth by the electronic noise of this signal. By applying the new controller described in section 6.2.1, about one order of magnitude was gained in the sensitivity curve above 300 Hz.

---

<sup>2</sup>Once the lock is acquired using the reference mass only, the recombined ITF should be fully locked before reallocating the force to the upper stage: it is necessary that the second stage of frequency stabilization is engaged, otherwise the frequency noise would cause saturation of the marionette actuators.

<sup>3</sup>By assuming an incoming power of 10 W, and a recycling gain of 50, in recycled configuration the total amount of power impinging upon the BS is 500 W. In recombined configuration, the 10 W entering the ITF are attenuated by a factor the transmissivity of the PR mirror, kept misaligned, which is roughly 0.1. The total amount of power impinging upon the BS is therefore 1 W. At high frequency the sensitivity is shot noise limited, and depends on the square root of the circulating power.

In C4 more complex control schemes were tested, with the recombined ITF locked in linear mode and both the automatic alignment and the frequency stabilization servo engaged. A procedure was established to bring the ITF from the uncontrolled state to the final *science mode* configuration, where all the planned control systems were running.

#### 6.4.1 Commissioning run C4

A large number of control systems were running in C4. In order to bring the ITF to science mode in a reliable way, the following locking procedure was established.

- lock acquisition of the two cavities;
- after closing the automatic alignment, lock of the Michelson on the dark fringe;
- linear locking scheme configuration;
- engagement of the SSFS: correction signals sent to the end mirrors to control the ITF common mode are zeroed, and the laser frequency is forced to follow the common mode cavity motion;
- the reference cavity is put on resonance, and the common mode of ITF is locked on it at a very low frequency;
- the last step consists of putting on resonance the OMC, and move the differential control of the arms to B1.

All the actions were managed by the Locking Process of the Global Control: the different locking schemes were applied by changing the running locking algorithm.

The sensitivity curve and the noise budget of C4 are shown in the picture 6.15.

The main noise sources limiting the ITF sensitivity in C4 were:

- **BS control noise** in the low frequency region, from 10 Hz to 50 Hz. It is due to both angular and longitudinal control noises. Because a BS automatic alignment system was not implemented yet, BS was still kept under local control, explaining the angular control noise contribution to the dark fringe. The BS longitudinal control noise was instead more deeply analyzed. Around a few tens of Hz, in fact, a set of resonances are visible in the *B2\_ACq* Michelson error signal, then propagated to the dark fringe signal. They were found to be

## C4 Noise Budget

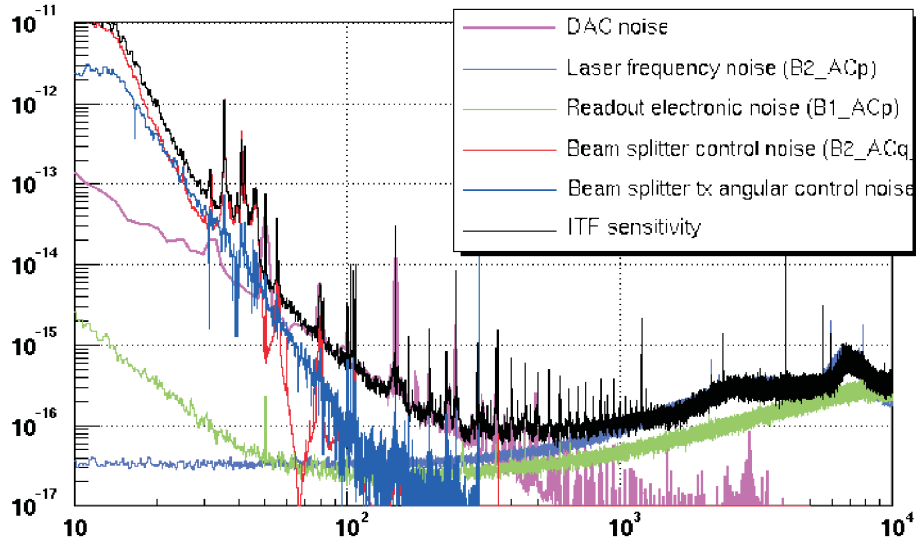


Figure 6.15: Sensitivity curve and noise budget of the recombined ITF [34].

input bench mechanical resonances. The mechanism of this kind of coupling turned out to be due to a mistuning between the IMC length and the modulation frequency. Because of an offset in the IMC lock induced by the frequency servo<sup>4</sup>, the upper and lower sidebands become unbalanced, producing a signal in the quadrature component of the reflected signal  $B2\_ACq$ . By tuning the modulation frequency with respect to the IMC cavity length (the mistuning was found to be 70 Hz), the contribution of these resonances to the dark fringe signal disappeared. Moreover, since the controller adopted in linear locking mode has an aggressive roll-off at 50 Hz, longitudinal control noise was not re-injected above that frequency.

- **DAC noise** in the intermediate frequency region, going to be reduced after the implementation of the suspension hierarchical control;
- **laser frequency noise** above 500 Hz, because of the shot noise and the electronic noise of the frequency servo error signal  $B2\_ACp$ .

<sup>4</sup>Once the SSFS is engaged, the signal reflected from the ITF is summed with the error signal of the pre-stabilization stage and sent to the laser (see section 5.6.3), thereby offsetting the laser frequency from the IMC resonance.

## 6.4.2 Commissioning run C5

During C5 the recombined ITF was running in the C4 configuration, having also the hierarchical control running on both the end suspension. From the point of view of the noise budget, even if the suspension hierarchical control made possible to reduce the DAC noise (see figure 8.3), worse performances with respect to C4 were measured. In fact, as already explained, in between C4 and C5 the power injected into the ITF was reduced by a factor 10, to deal with the too high frequency noise level coming from the injection system. For this reason, at high frequency the C4 sensitivity was about a factor 10 better than the C5 one 6.17.

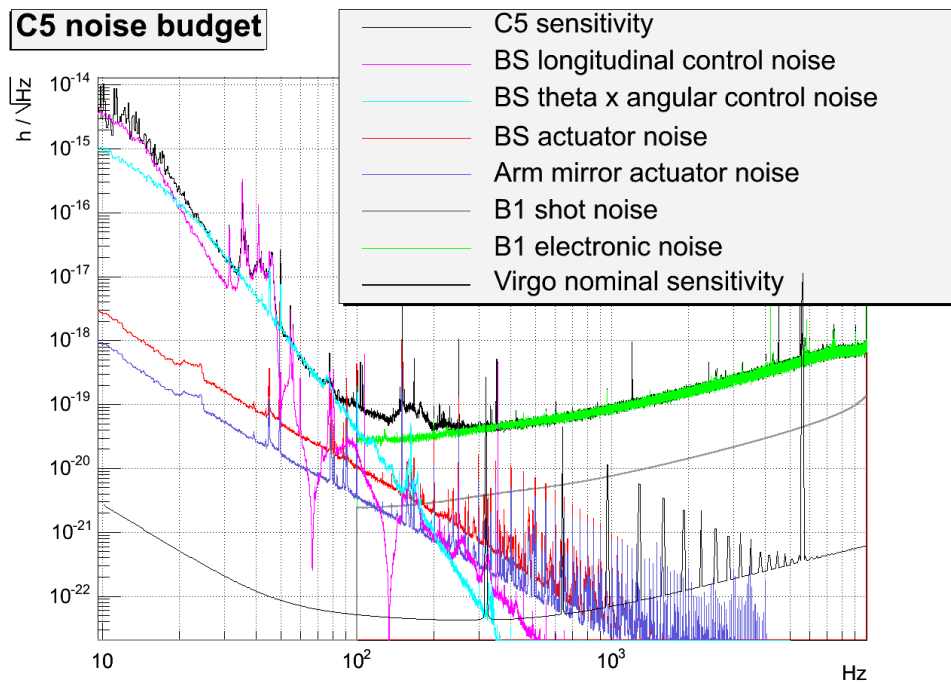


Figure 6.16: Sensitivity curve and noise budget of the recombined ITF in C5 [34].

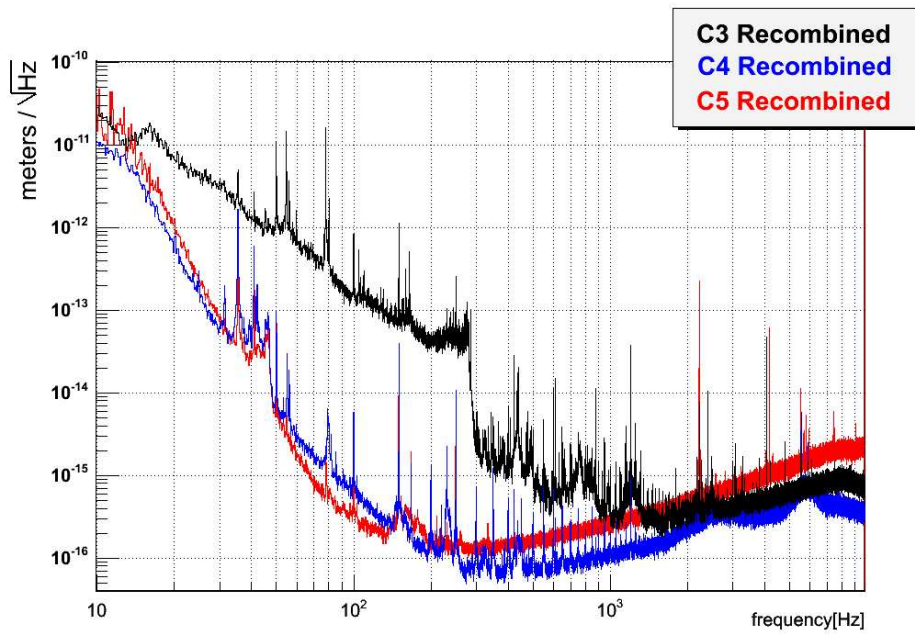


Figure 6.17: Comparison of the sensitivity curves measured in recombined configuration during C3, C4 and C5.



## Chapter 7

# Lock Acquisition of the Recycled Interferometer

With respect to the single Fabry-Perot cavity and the recombined ITF, the longitudinal control of the recycled configuration is complicated mainly by the fact that fields in the long cavities are mixed by the presence of the recycling mirror, so that the error signal extraction is much more difficult. When the problem of the Virgo lock acquisition started to be studied, a lock acquisition strategy had already been designed and implemented in LIGO. Since Virgo and LIGO have similar optical configurations, it was decided first to test in simulation the LIGO strategy.

The first part of this chapter describes simulations and experimental tests performed by applying the LIGO multi-step technique (see section 3.4.2). Even if the final strategy adopted to lock Virgo was different, potential problems for acquiring the lock became evident during this activity. Moreover, the use of an alternative error signals extraction was explored, in particular concerning the  $3\Omega$  demodulation, already adopted in the TAMA project (see section 3.4.2).

While tests on the multi-step technique were being carried out several experiments were done by exploring an alternative approach, as it is described in the second part of this chapter. The main idea was to get a stable state of the ITF at the beginning of the lock acquisition phase, by locking it away from its working point, and then to bring the ITF on the dark fringe in a sequence of adiabatic stable steps. Since encouraging experimental results were reached in a short time, the commissioning activity was focused mainly on this alternative approach. The lock of the interferometer was obtained two weeks after the first attempt. This new technique is referred to as *variable finesse* lock acquisition since the finesse of the

recycling cavity changes during the lock acquisition.

## 7.1 Simulation of the multi-step technique

The optical configuration of the Virgo recycled ITF is shown in figure 7.1.

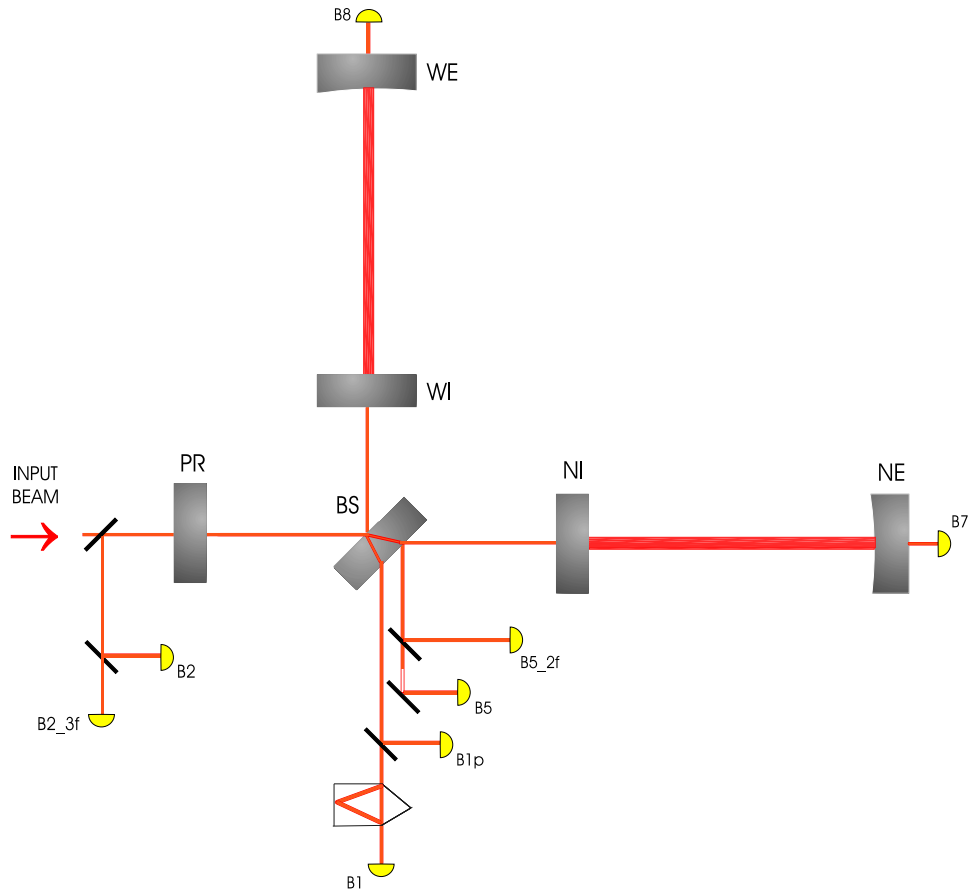


Figure 7.1: Virgo recycled optical configuration.

In parallel with the experimental activity carried out with the single cavity and the recombined ITF, a SIESTA simulation was started in order to study and prepare the lock of the full recycled ITF by following the multi-step technique [51]. The sensing matrix initially tested was derived by analyzing the response of the demodulated signals to the different degrees of freedom (CARM, DARM, MICH and PRCL), and, in first approximation, by considering only the dominant elements:

$$\begin{pmatrix} B2\_ACp \\ B1p\_ACp^1 \\ B5\_ACq \\ B5\_ACp \end{pmatrix} = \begin{pmatrix} G_{B2\_ACp}^{CARM} & 0 & G_{B2\_ACp}^{PRCL} & 0 \\ 0 & G_{B1\_ACp}^{DARM} & 0 & 0 \\ 0 & G_{B5\_ACq}^{DARM} & 0 & G_{B5\_ACq}^{MICH} \\ G_{B5\_ACp}^{CARM} & 0 & 0 & 0 \end{pmatrix} \begin{pmatrix} \Delta L_+ \\ \Delta L_- \\ \Delta l_+ \\ \Delta l_- \end{pmatrix} \quad (7.1)$$

As explained in chapter 3, each sensing matrix element can be written in terms of the amplitude of the resonant fields and local oscillators, by generalizing the linearization technique adopted to lock the single cavity. The amplitude of the involved fields is then estimated by direct measurement.

By applying the multi-step technique, the ITF passes through all the unstable steps of the sequence several times and correction signals are sent to the involved mirrors until the final state is reached. Power levels during a typical lock acquisition event are shown in figure 7.2. According to the simulation results, once corrections start to be sent, typically a few minutes are needed in order to acquire the lock. Since this technique relies on the random motion of the mirrors, and has several failure modes, the time required to lock the ITF is best treated statistically (e.g., "mean time to lock").

After succeeding in reaching the locked state, the simulation was used as starting point for studying other possible choices of the involved signals, in order to make the lock acquisition sequence more robust. In particular, the use of the  $3\Omega$ -demodulate reflected signal ( $B2\_3f\_ACp$ ) to control PRCL, instead of the  $\Omega$ -demodulate one ( $B2\_ACp$ ), was considered.

## 7.2 Use of the $3\Omega$ signal

In the sensing matrix 7.1  $B2\_ACp$  is the only signal sensitive to PRCL. However, as already said in section 3.4.2, because of the phase shift enhancement experienced by the carrier in the Fabry-Perot cavities, this signal is also greatly sensitive to CARM. Once the ITF is locked, the frequency servo can be engaged, as done in LIGO, thereby reducing the CARM contamination in the PRCL signal. On the other hand, a robust extraction of PRCL during lock acquisition would be difficult.

A different extraction of the PRCL length was investigated by using the reflected signal demodulated at  $3\Omega$  frequency, as adopted in the TAMA locking scheme. The sensitivity of this signal to CARM is much smaller than in case of a simple  $\Omega$  demodulation. The sensitivity of the two signals to PRCL and CARM can be

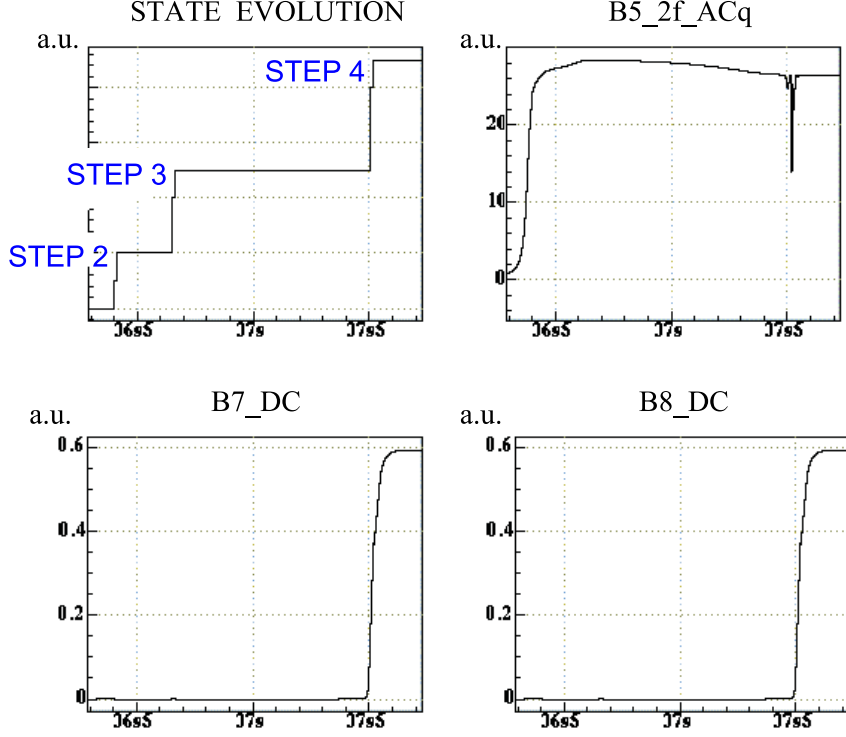


Figure 7.2: Lock of Virgo acquired in simulation by using the multi-step technique.

described in terms of their separation ratio:

$$S_3 = \frac{\partial(B2\_3f\_ACp)}{\partial l_+} / \frac{\partial(B2\_3f\_ACp)}{\partial L_+} \quad (7.2)$$

$$S_1 = \frac{\partial(B2\_ACp)}{\partial l_+} / \frac{\partial(B2\_ACp)}{\partial L_+} \quad (7.3)$$

where a bigger separation ratio means a lower contamination from the CARM component for extracting the PRCL signal.

As shown in [48], the ratio between  $S_3$  and  $S_1$  can be written in term of the optical parameters of the ITF (see section 3.4):

$$\frac{S_3}{S_1} \sim \frac{J_1(m)J_2(m)}{J_0(m)J_3(m)} \frac{r_{sb}}{r_{sb,3}} \frac{g_{sb}^2}{g_{sb}^2 r_c - g_{cr}^2 r_{sb}} \quad (7.4)$$

With the nominal Virgo parameters:

$$r_M = 0.9945 \quad (7.5)$$

$$r_c \simeq -1 \quad (7.6)$$

$$r_{sb} \simeq -0.767 \quad (7.7)$$

$$g_{cr}^2 = 50, \quad g_{sb}^2 = 35 \quad (7.8)$$

and by assuming that the reflectivity of first and third order sidebands ( $r_{sb}$  and  $r_{sb,3}$  respectively) is almost the same:

$$\frac{S_3}{S_1} \sim 30 \quad (7.9)$$

which means that the CARM contamination in  $B2\_3f\_ACp$  at low frequency is reduced by a factor 30 with respect to  $B2\_ACp$ .

The frequency response of  $B2\_ACp$  to PRCL is also strongly dependent on the optical parameters of the ITF. When losses of 600 ppm in the Fabry-Perot cavities (which are comparable with the measured value, see section 7.12.1) are added in simulation, the frequency response shows a *non-minimum phase* behavior, which might make the feedback loop unstable. In order to use  $B2\_ACp$  to control PRCL the control system would need therefore to compensate for that [46], by appropriately defining a feedback topology.

On the contrary, the frequency response of the  $B2\_3f\_ACp$  signal to a PRCL length variation is at *minimum phase*, corresponding to a stable response of the control system, even including losses in the Fabry-Perot twice the measured ones.

A new locking scheme involving the  $B2\_3f$  signals was tested in simulation. The applied sensing matrix was:

$$\begin{pmatrix} B5\_ACp \\ B1p\_ACp \\ B2\_3f\_ACp \\ B2\_3f\_ACq \end{pmatrix} = \begin{pmatrix} G_{B5\_ACp}^{CARM} & 0 & 0 & 0 \\ 0 & G_{B1\_ACp}^{DARM} & 0 & 0 \\ 0 & 0 & G_{B2\_3f\_ACp}^{PRCL} & 0 \\ 0 & 0 & 0 & G_{B2\_3f\_ACq}^{MICH} \end{pmatrix} \begin{pmatrix} \Delta L_+ \\ \Delta L_- \\ \Delta l_+ \\ \Delta l_- \end{pmatrix} \quad (7.10)$$

Being simpler and more robust than the previous one, this matrix was designed to be experimentally tested on the ITF.



the sidebands resonant. Since the sidebands are anti-resonant in the Fabry-Perot cavities, their behavior in the central ITF is similar to their behavior in the full recycled ITF, and this configuration is the stable analogue of step 2 of the lock acquisition sequence. PRCL and MICH gain coefficients of the sensing matrix elements in 7.14 were measured in this configuration;

- two similar configurations obtained keeping all but one of the mirrors aligned: the *Step3North*, where WE is misaligned (see figure 7.6), and the *Step3West* where NE is misaligned (see figure 7.7). These two stable configurations were locked in order to have sidebands resonant inside the recycling cavity, and carrier resonant inside the arm, as in step 3 of the full lock acquisition sequence. CARM and DARM gain coefficients of the sensing matrix elements 7.14 were measured in these configurations.

The locking schemes of these two configurations are described in the next paragraphs.

### 7.3.1 Lock of the central ITF (CITF)

The CITF was locked so as to have the sidebands resonant inside the recycling cavity, as in step 2 of the full lock acquisition sequence. PRCL and MICH are the two degrees of freedom to be controlled in this optical configuration. Both of the components of the  $B2.3f$  signal are involved in the control scheme. The demodulation phase was adjusted so that the in-phase component is mainly sensitive to PRCL and the quadrature-phase component mainly sensitive to MICH<sup>2</sup>. In order to identify a sideband resonance crossing the  $B5.2f\_ACq$  signal was used. It is extracted by the beam reflected from the second face of BS and demodulated at twice the modulation frequency. Second order sidebands are completely reflected from the ITF, so that this signal is essentially generated by the beating between the first order resonant sidebands. By tuning its demodulation phase,  $B5.2f\_ACq$  can be made proportional to the first order sidebands power (see figure 7.5).

The adopted sensing matrix is diagonal:

$$\begin{pmatrix} B2.3f\_ACp \\ B2.3f\_ACq \end{pmatrix} = \begin{pmatrix} G_{B2.3f\_ACp}^{PRCL} & 0 \\ 0 & G_{B2.3f\_ACq}^{MICH} \end{pmatrix} \begin{pmatrix} \Delta l_+ \\ \Delta l_- \end{pmatrix} \quad (7.11)$$

---

<sup>2</sup>The adopted tuning procedure was the following. The 0.6 Hz resonance of the PR suspension was slightly excited and the demodulation phase was adjusted so to maximize the strength of  $B2.3f\_ACp$  with respect to  $B2.3f\_ACq$  during a sideband resonance crossing.

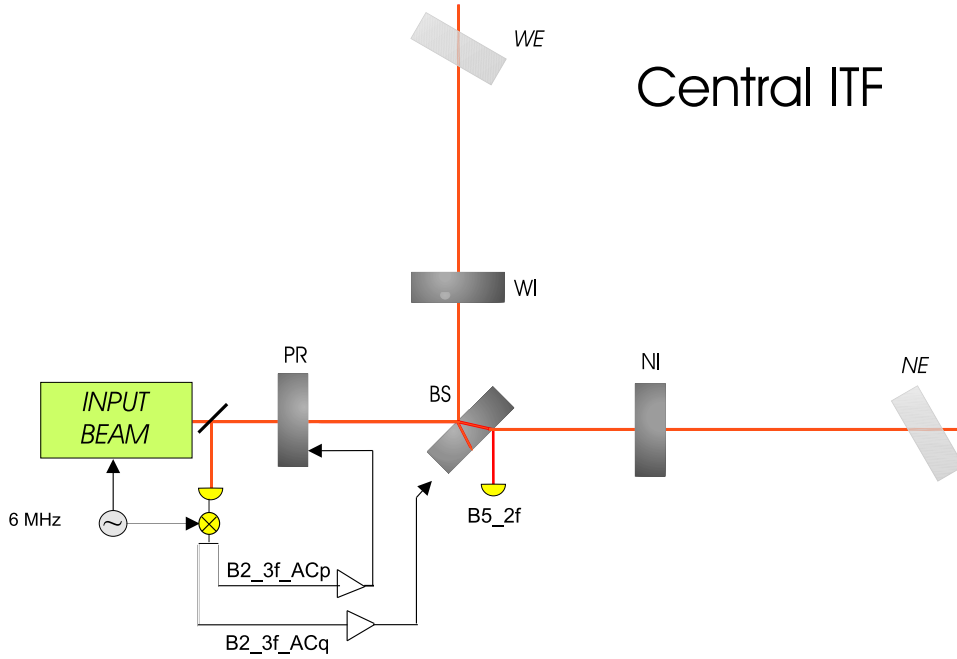


Figure 7.4: CITF configuration. The adopted locking scheme involves both components of the  $B2.3f$  signal.

The sensing matrix elements were estimated by considering that the  $B2.3f$  signals are generated by the beating between the constant second-order sideband field reflected by the central ITF and the resonant sidebands field, so that:

$$G_{B2.3f\_ACp}^{PRCL} = g_{B2.3f\_ACp}^{PRCL} B5.2f\_ACq \quad (7.12)$$

$$G_{B2.3f\_ACq}^{MICH} = g_{B2.3f\_ACq}^{MICH} B5.2f\_ACq \quad (7.13)$$

where  $g_{B2.3f\_ACp}^{PRCL}$  and  $g_{B2.3f\_ACq}^{MICH}$  are the gain coefficients which can be directly measured. However, the direct measurement can be done only once the CITF is locked, while they need to be previously estimated in order to acquire the lock:

- $g_{B2.3f\_ACp}^{PRCL}$  is estimated as done in the case of the single Fabry-Perot cavity, by assuming that the linear portion of the Pound-Drever-Hall signal corresponds to a cavity resonance width  $\lambda/2\mathcal{F}_{CITF}$  crossed by a PRCL motion, where  $\mathcal{F}_{CITF} \sim 30$ ;
- in order to have a direct estimate of  $g_{B2.3f\_ACq}^{MICH}$  once having  $g_{B2.3f\_ACp}^{PRCL}$ , the simulation was used to infer the relative ratio of these two gains, which was

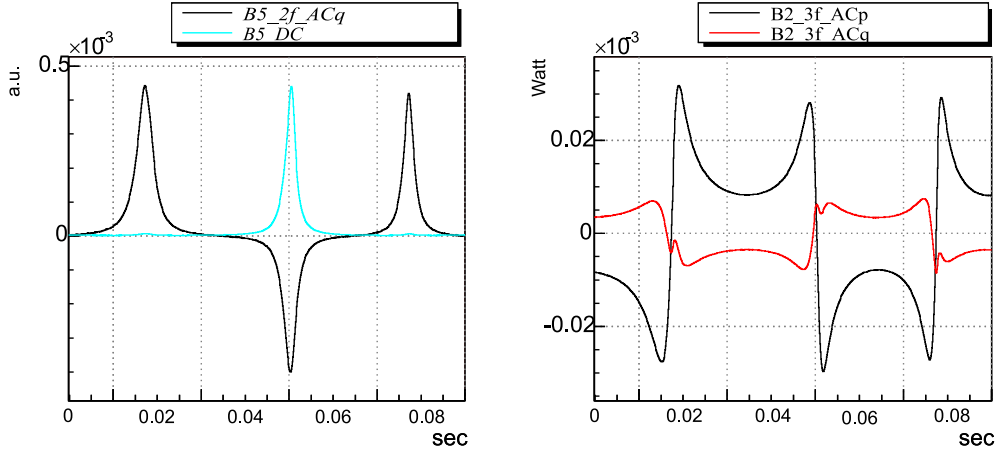


Figure 7.5: Signals in the CITF: the  $B5.2f$  demodulation phase is maximized so to have  $B5.2f\_ACq$  maximum in correspondence of a sideband resonance crossing.

found to be  $1/20$ .

After reconstructing, the two lengths were filtered by applying the standard filter described in section 5.3.2 Correction signals were sent to the PR and BS mirrors (see section 7.8.2), as described in figure 7.4, with a control bandwidth of 50 Hz and 30 Hz respectively. Corrections were engaged once  $B5.2f\_ACq$  was at least half of its maximum value.

Using this method, the lock was usually acquired in a few seconds. Once the CITF was locked, the demodulation phase of  $B2.3f$  was better tuned in order to improve the decoupling between the two degrees of freedom, by injecting a sinusoidal line on PR at a few hundred of Hz (well out of the loop bandwidth) and maximizing the ratio between the amplitudes of the line visible on  $B2.3f\_ACp$  and  $B2.3f\_ACq$ . The measured decoupling was about a factor 10.

### 7.3.2 *Step3North* and *Step3West*

The locking scheme of the *Step3North* configuration is here described, but similar schemes are applicable to the *Step3West* configuration as well.

*Step3North* was locked so to have the sidebands resonant inside the recycling cavity and the carrier resonant in the North arm, as in step 3 of the full lock acquisition sequence.

Together with the  $B2.3f$  signals used to control MICH and PRCL as in the CITF, the  $B1p\_ACq$  signal was used to control the length of the North arm (see figure 7.6). The adopted sensing matrix was the 3 by 3 matrix:

$$\begin{pmatrix} B1p\_ACq \\ B2.3f\_ACp \\ B2.3f\_ACq \end{pmatrix} = \begin{pmatrix} G_{B1\_ACp}^{DARM} & 0 & 0 \\ 0 & G_{B2.3f\_ACp}^{PRCL} & 0 \\ 0 & 0 & G_{B2.3f\_ACq}^{MICH} \end{pmatrix} \begin{pmatrix} \Delta L_- \\ \Delta l_+ \\ \Delta l_- \end{pmatrix} \quad (7.14)$$

$G_{B1\_ACp}^{DARM}$  was estimated by considering that it is generated by the beat between the carrier resonant inside the arm (measured by the transmitted power  $B7\_DC$ ) with the static sidebands field transmitted to the asymmetric port (measured by  $\sqrt{B5.2f\_ACq}$ ):

$$G_{B1\_ACp}^{DARM} = g_{B1\_ACp}^{DARM} \sqrt{B5.2f\_ACq} B7\_DC$$

$G_{B2.3f\_ACp}^{PRCL}$  and  $G_{B2.3f\_ACq}^{MICH}$  were estimated as described in the CITF configuration.

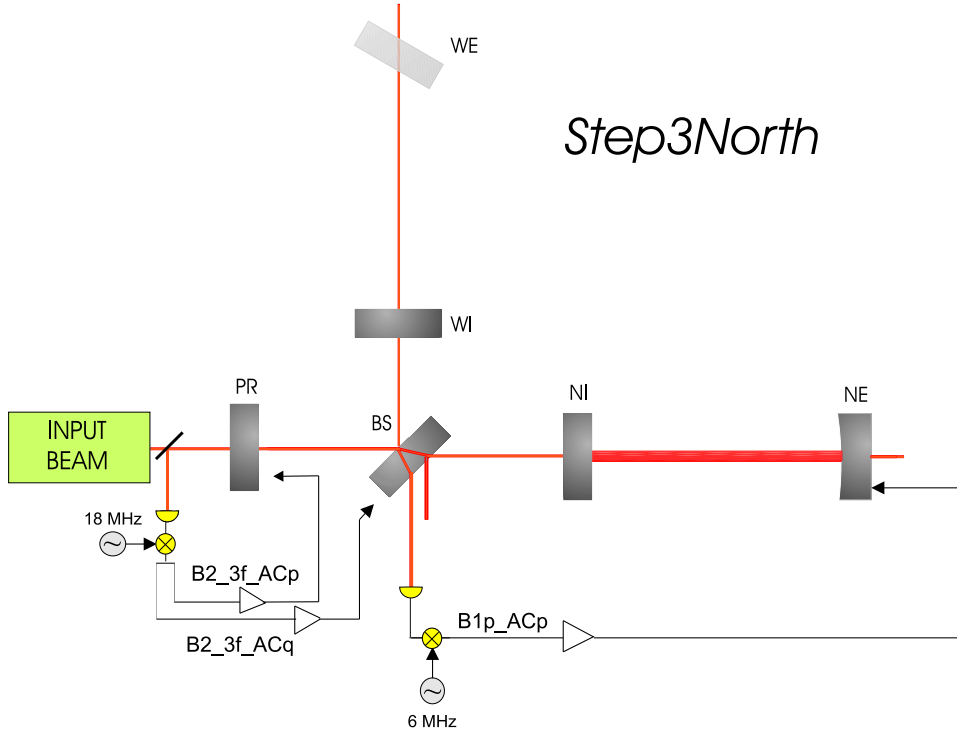


Figure 7.6: *Step3North* configuration.

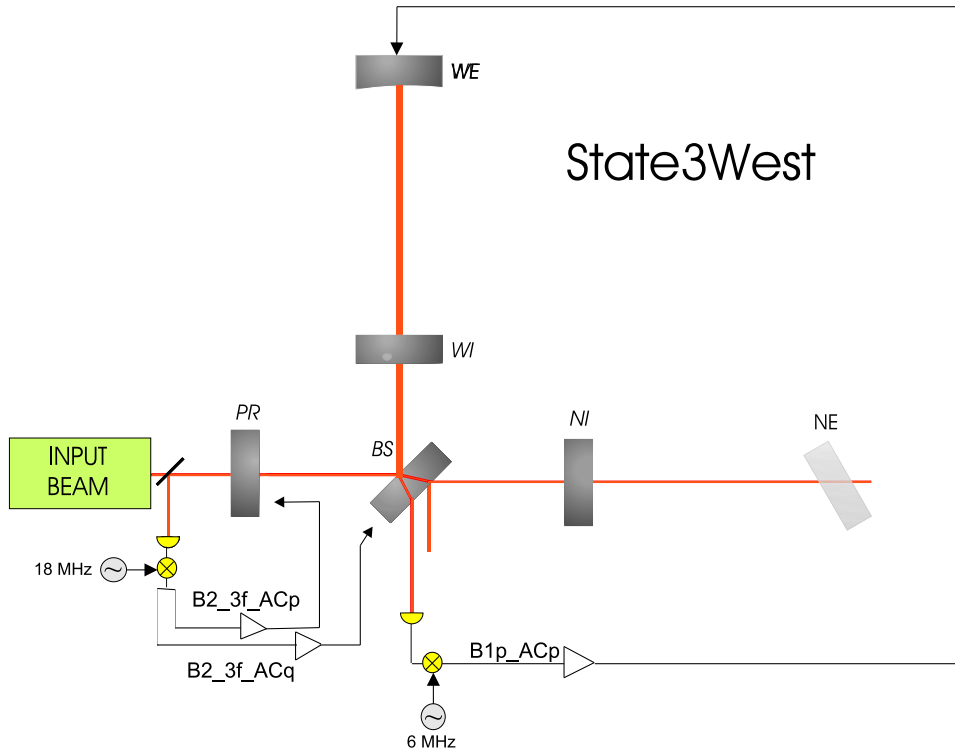


Figure 7.7: *Step3West* configuration.

When the sideband power had become higher than half its maximum value, a first trigger engaged the control loops on PR and BS, in order to keep the sidebands resonant inside the central cavity. From this condition, the control loop acting on NE was engaged as soon as the north transmitted power, proportional to  $B7_{DC}$ , would cross a given threshold.

By using this scheme the lock of both *Step3North* and *Step3West* configurations was typically acquired in a few seconds.

## 7.4 Absence of optical isolation between input mode-cleaner and interferometer

During the first tests performed with the *central ITF* and the *Step3North* configuration, the absence of an optical isolation between the input mode-cleaner and the ITF turned out to be a problem for lock acquisition because of the backscattered light inside the IMC. In fact, as already observed during the commissioning of the

central ITF [52], the IMC curved mirror has a residual roughness so that the light coming back from the ITF was backscattered in the opposite direction and resonated inside the IMC. Therefore, as described in figure 7.8, inside the spurious interferometer formed by the IMC and the PR mirror the input beam interfered with the beam reflected back from PR, causing two main effects: low frequency amplitude modulation of the beam entering the ITF, and spurious signals on the photodiode used to lock the IMC. Consequently, the frequency noise injected into the ITF was greatly increased.

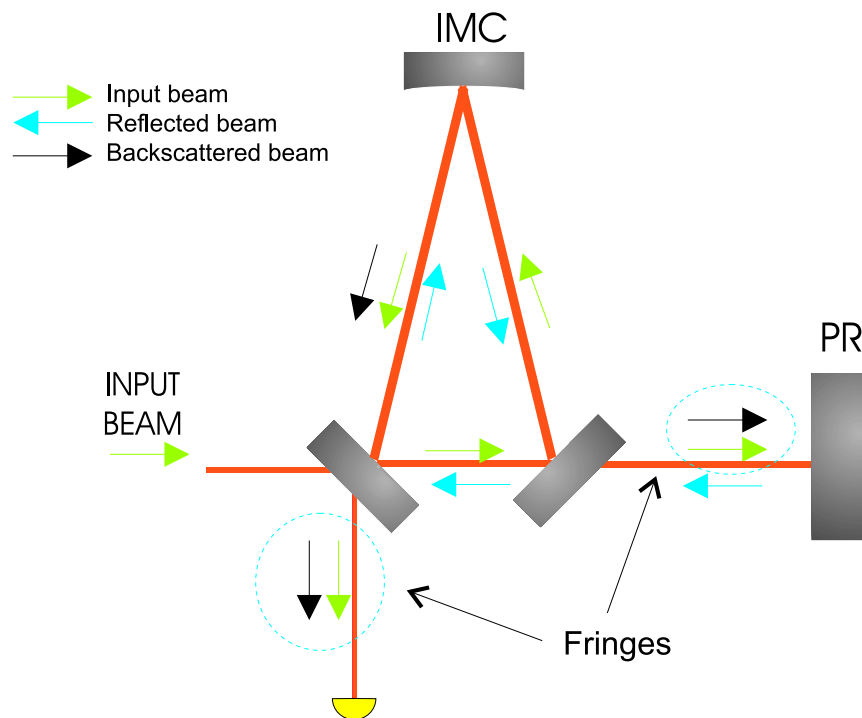


Figure 7.8: Interference fringes produced by the reflected beam from PR to the IMC, which is backscattered by the IMC curved mirror. Fringes are produced both in the beam entering the ITF and in the beam reflected by the IMC and used to lock the IMC itself.

The frequency noise measured in recombined configuration was compared with that one measured with the full aligned ITF. The comparison is plotted in figure 7.9: when the full ITF crossed the resonance, big spikes were visible in the frequency noise signal as function of time (red curve), while it was 10 times smaller and independent of the ITF alignment conditions in recombined configuration (black curve).

Moreover, fringes were produced between the PR and the IMC, so that fringes were also present in the light finally injected inside the ITF. In this condition a

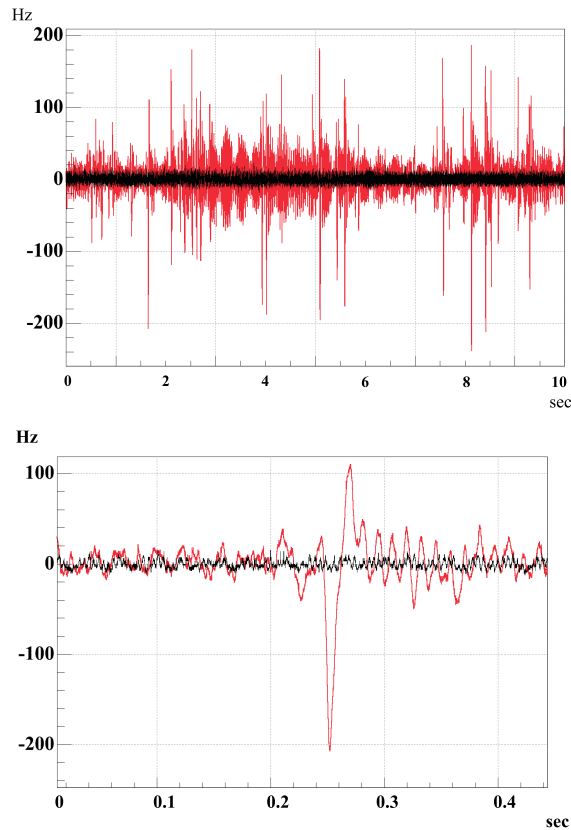


Figure 7.9: (Top) Laser frequency noise injected into the ITF when the PR mirror is misaligned (black curve, ITF aligned in recombined configuration) and when the PR mirror is aligned (red curve, ITF aligned in recycled configuration). (Bottom) Zoom - Spikes in the frequency noise are produced when the aligned recycled ITF crosses the resonance.

stable lock of the *Step3North* configuration was quite difficult, so that a solution to the backscattered light problem was needed in order to continue the commissioning activity<sup>3</sup>.

The adopted temporary solution was the replacement of one of the M6 mirror of the telescope which focalizes the beam entering the ITF (see section ??) with a 10% reflecting mirror. In this way, the interfering beams were both reduced by a

---

<sup>3</sup>In order to estimate the impact of such a level of frequency noise in acquiring the lock of the full ITF, a dedicated simulation was also done. The frequency noise measured with the PR mirror aligned was injected in entrance to the ITF in the full Virgo lock acquisition simulation. Results showed that with such high frequency noise it was not possible to acquire the lock, while it was possible with the level of noise measured with PR misaligned.

factor 10, reducing by the same quantity the interfering fringes. After this patch, the level of frequency noise measured with the PR aligned decreased as expected. The obvious drawback was the consequent reduction by a factor 10 of the amount of power injected into the ITF.

## 7.5 The control of the power recycling mirror

The PR mirror, shown in the picture 7.10, has a composite structure which makes it different from all the other main optics. The real mirror is located in an aluminium support inserted in a holder of herasil. The aluminium support is connected to the PR mirror and to the holder of suprasil by means of three joints having minimum length so to keep the resonances of the system at the highest possible frequency.

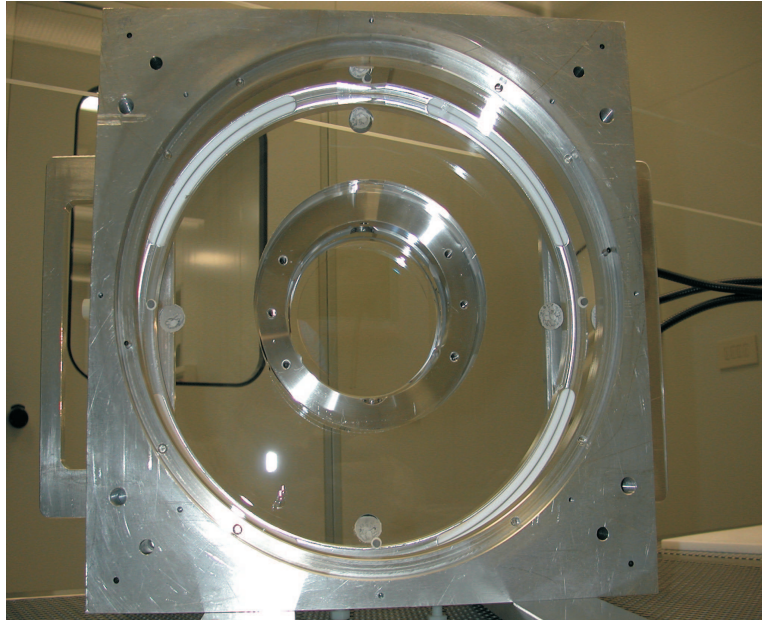


Figure 7.10: Picture of the composite structure of the PR mirror.

Several reasons led to this complex solution. The PR mirror was designed to be a lens with 120 mm diameter, to transform the divergent beam emitted by the IB into a parallel beam<sup>4</sup>. A few substrates were bought in order to be able to optimize the

---

<sup>4</sup>The choice to make PR as a lens was made because it was not possible to put a low aberration telescope on the IB, using spherical mirrors (parabolic mirrors were not commercially available 10 years ago, and would have been too expensive). The size of the lens/mirror was also determined by

reflectivity of this mirror with respect to the losses of the ITF. A first requirement on the PR mirror structure was therefore to be easily dismantlable [54]. Moreover, the possibility to change the length of the recycling cavity to accommodate different modulation frequencies seemed desirable. On the other hand, the dimension of the optic had to be compatible with the standard size of the marionette, so a composite structure was finally adopted [53].

The mechanical response of such a system exhibited several resonances in the frequency range between 100 Hz and 1 kHz (see figure 7.11). They were found by measuring the open loop transfer function of the PR-NI locking feedback (see figure 7.12).

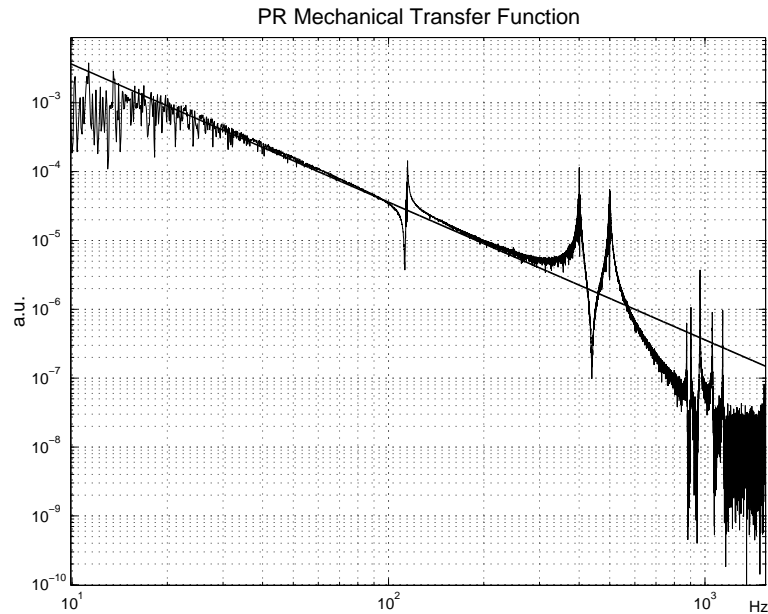


Figure 7.11: Mechanical transfer function of the composite PR mirror compared with that one of a Virgo standard mirror.

In particular, those one around 400 Hz, having a high  $Q$ , were easily excited during lock acquisition. A notch was included in the PR control filter (see figure 7.13), in order to compensate for these resonances, but it was observed that their frequencies changed every few days.

Also, after a shock due to an excess of noise at the level of the inverted pendulum of the SA, the 400 Hz resonance moved to 280 Hz. This made it necessary to tune  


---

the cost.

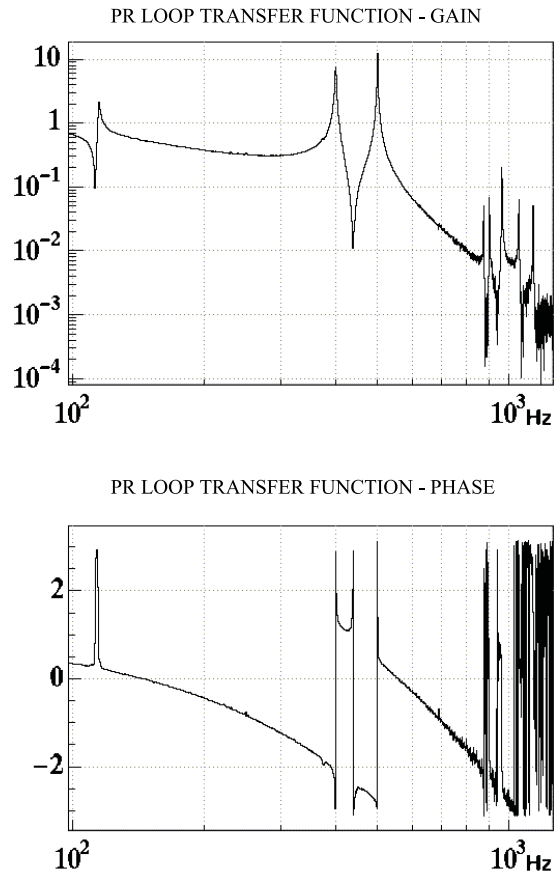


Figure 7.12: Gain and phase of the transfer function of the PR loop, as measured by injecting white noise in the longitudinal degree of freedom.

the PR control filter frequently in order to have an effective compensation.

## 7.6 Experimental tests of the multi-step technique - II

After replacing the M6 mirror in the input telescope, a two week long test of the multiple-step technique for locking the Virgo recycled ITF was performed. Locking attempts were collected and analyzed. At the same time, the simulation was continuously tuned on the real data, in order to reproduce experimental results and to try to investigate the causes of locking failures. An example locking trial is shown in figure 7.14.

The ITF remained in state 4 for a few hundreds of milliseconds, as shown in the first plot. The sideband power went to its maximum value at the beginning of

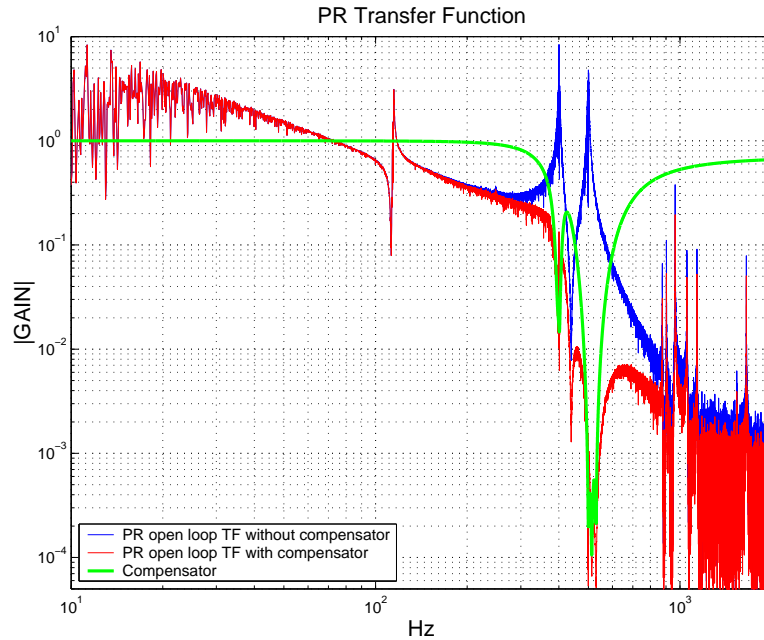


Figure 7.13: Filter (in green) added to the longitudinal controller of the PR in order to compensate for the moving resonances above 400 Hz. The other curves are the gain of the open loop transfer function measured without (blue) and with (red) compensation.

the locking sequence, in state 2. Corrections signals sent to the BS and PR mirrors were able to keep the recycling cavity on resonance: big fluctuations are visible in the sideband power ( $B5\_2f\_ACq$ ), without losing the lock. Correction signals sent to the end mirrors seem to be less efficient: they were able to keep the cavities on resonance for a shorter time, and the resonance was lost while the recycling cavity was still resonant. Eventually, due to the success of the variable finesse technique, (discussed in the following sections) the multi-step method was abandoned without further analysis.

## 7.7 *Variable finesse locking technique*

The tuning of the parameters needed to compute the sensing matrix is generally quite difficult in a LIGO like technique. In fact, they can not be directly measured until the ITF is stably locked on its final working point. Diagnosing of the lock failures is also difficult, as shown in the previous section.

The multi-step technique applied to Virgo had other weak points. In particular:

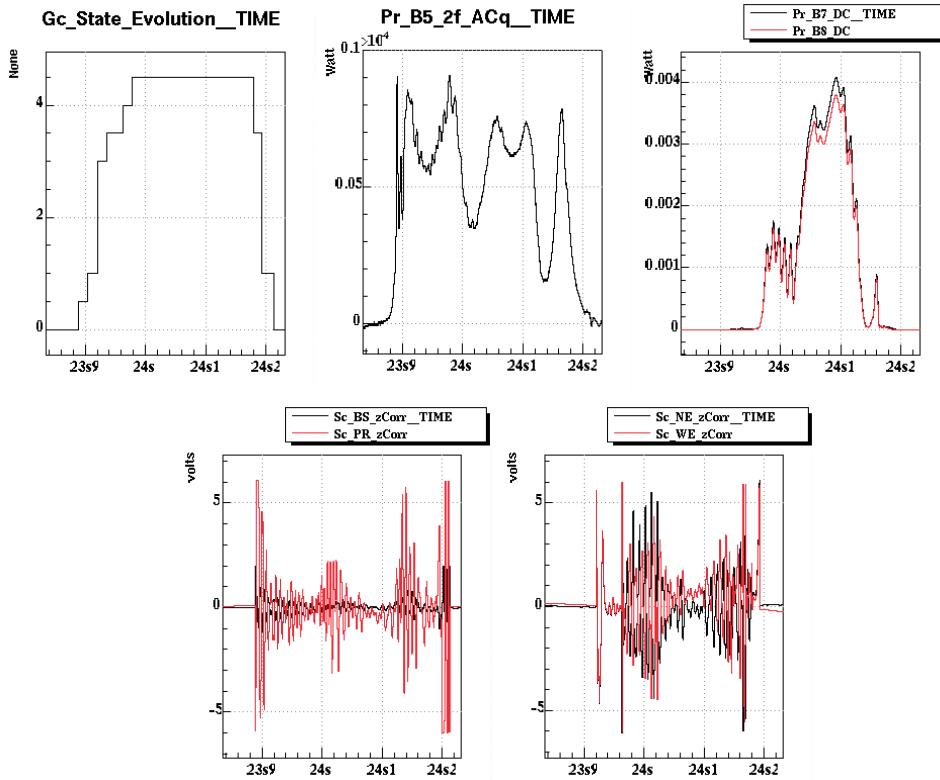


Figure 7.14: Example of locking trial by applying the multi-step technique.

- even after tuning correctly all the gains, during the lock acquisition phase the mirror are typically shaken for a few minutes before achieving the lock. The 0.6 Hz pendulum resonance of the Virgo mirrors and the PR mirror resonances, easily excited by this process, can greatly complicate the lock acquisition phase;
- in order to reduce the CARM contamination in the PRCL degree of freedom, the CARM loop is usually controlled in LIGO with a high bandwidth, around 200 Hz. Because of additional delays in the digital control system (see section 2.5.4), in Virgo it can not be set higher than 100 Hz, making it difficult to deal with the CARM contamination during the lock acquisition phase.

To overcome these problems a new *variable finesse* technique was designed and applied to Virgo. Its name arises by the fact that the finesse of the recycling cavity changes during the lock acquisition sequence (see figure 7.15).

The main feature of this new strategy is that all four longitudinal degrees of

freedom of the ITF are stably locked from the beginning of the acquisition sequence, in a configuration that is easy to lock: a recycled ITF with a very low recycling gain. The complexity of the control of the full ITF arises from the couplings between the fields which are recycled inside the ITF by the presence of PR. By reducing the recycling gain, the longitudinal control of the recycled ITF becomes similar to that one of the recombined ITF: all the degrees of freedom are weakly coupled and independently controllable, making the control scheme much easier.

A controlled state of the ITF is therefore attained at the beginning of the locking sequence by initially locking it on the half fringe, so that a large fraction of light escapes through the antisymmetric port and the power build-up inside the recycling cavity is extremely low. From this stable state, the ITF can be adiabatically brought to the operating point, with the Michelson on the dark fringe.

The first experimental tests about this technique were started on mid-October 2004, and the first lock was obtained after ten days.

By controlling the ITF from the beginning of the locking sequence the excitations of the 0.6 Hz resonance, and those of the PR mirror, are avoided. Moreover, by moving to the operating point through stable states, optical parameters needed to correctly reconstruct the lengths can be directly measured as needed.

### 7.7.1 Reconstruction of the lengths

The curve in figure 7.16 shows the gain of the recycling cavity versus the reflectivity  $r_c^2$  of the compound mirror formed by the Michelson and the Fabry-Perot arms (as defined in chapter 3). By keeping the Michelson close to the bright fringe, corresponding to a very low value of  $r_c$ , a recycling gain for the carrier about 200 times lower than the nominal value of 48 can be obtained.

In this condition the fields inside the recycled ITF are so weakly coupled that the end photodiodes can be used to control independently the two cavities. In fact, as it was shown in section 3.4.1, their dependence on a differential and common mode of the long cavities can be written as:

$$B7\_ACp \simeq \Delta L_- + (1 + \sqrt{G_{cr}})\Delta L_+ \quad (7.15)$$

$$B8\_ACp \simeq -\Delta L_- + (1 + \sqrt{G_{cr}})\Delta L_+ \quad (7.16)$$

where  $G_{cr}$  is the recycling gain of the carrier. When the amplitude of the recycling gain of the carrier  $\sqrt{G_{cr}}$  is lower than 1:

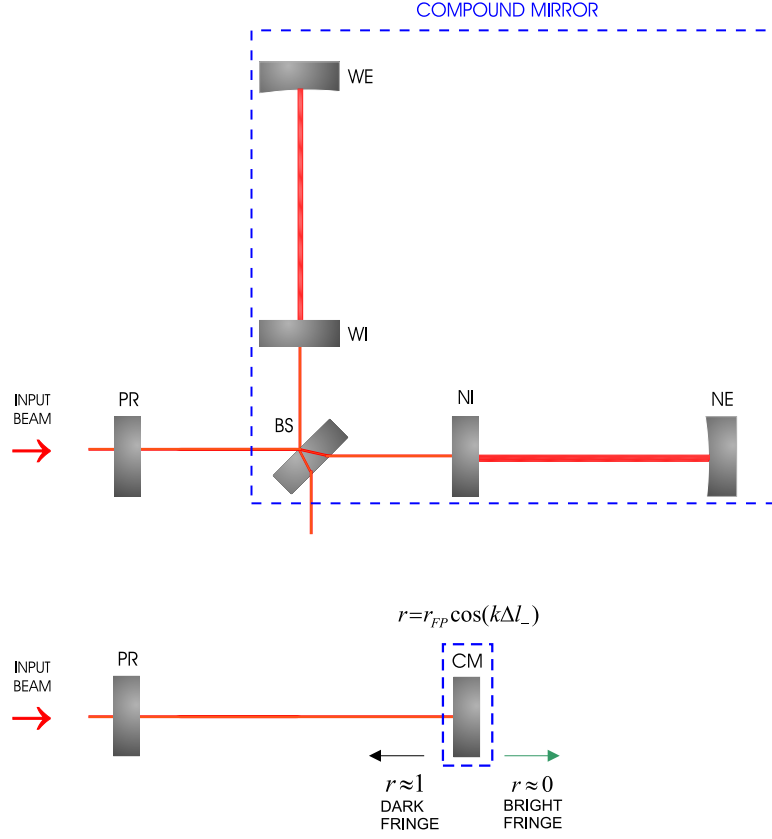


Figure 7.15: The ITF seen as a *variable finesse* cavity formed by the PR mirror and the *compound* mirror. The reflectivity on the compound mirror depends on the detuning of the ITF from the dark fringe condition: it is maximum when the ITF is on the dark fringe, while it vanishes on the bright fringe, when all the power is transmitted.

$$B7\_ACp \simeq \Delta L_- + \Delta L_+ \implies \simeq L_N \quad (7.17)$$

$$B8\_ACp \simeq -\Delta L_- + \Delta L_+ \implies \simeq L_W \quad (7.18)$$

so that  $B7\_ACp$  can be used to control the north cavity length, and  $B8\_ACp$  to control the west cavity length. In particular, the condition of weak mixing of the fields remains acceptable up to mid-fringe ( $r_c^2 = 0.5$ ), where the recycling gain is still greatly reduced, about 60 times below its maximum value ( $\sqrt{G_{cr}} \simeq 0.9$ ).

On the basis of these considerations, the four degrees of freedom of the ITF are initially controlled at mid-fringe as described in the next paragraphs.

Concerning the demodulation phase of the signals involved in the locking scheme,

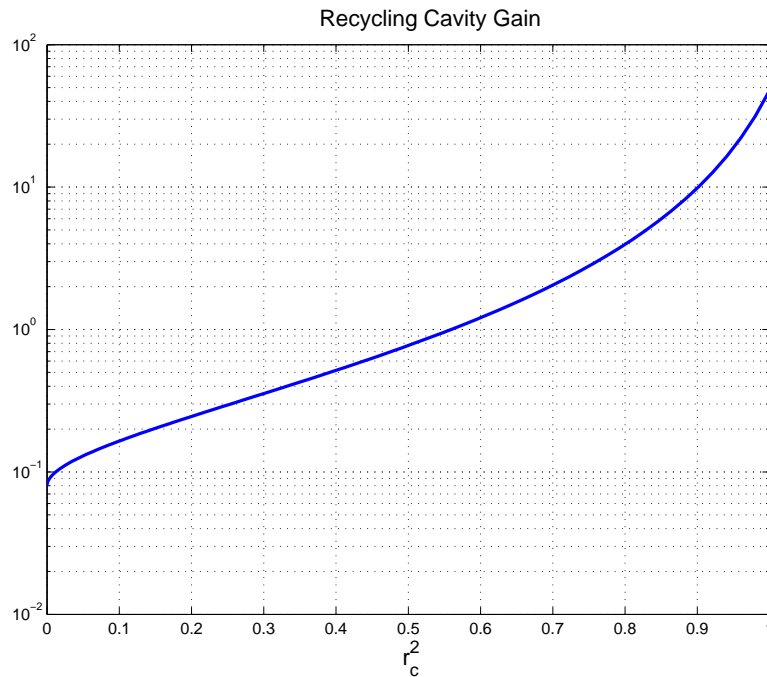


Figure 7.16: The plot shows the gain of the recycling cavity for the carrier versus  $r_c^2$ . With the ITF on the half fringe,  $r_c^2 = 0.5$ .

a general comment is needed. These phases are usually tuned to make one of the two demodulated signal as sensitive as possible to the degree of freedom which it is designed to control, by zeroing the other component. As already said, the more direct way to perform this kind of tuning is to inject a sinusoidal excitation into the given degree of freedom and measuring the amplitude of this line in the corresponding demodulated signals. The demodulation phase is then set so that the amplitude of the line is maximized on one of the two components, arbitrarily chosen. Of course, this method can be applied only once the ITF is already locked, and it is actually used to refine the tuning. On the other hand, before they can be measured in this way, the demodulation phases need to be set well enough for lock acquisition, so that some procedure that does not require lock is obviously needed.

In simpler configurations, such as the the single cavity and the recombined ITF, the sensitivity of a signal to a given length variation can be easily evaluated with the mirrors freely swinging, as described in the previous chapters. With the full aligned ITF, on the other hand, signals are in general sensitive to all the degrees of freedom of the ITF at the same time, and no single length variation can be identified. For

this reason, alternative procedures were investigated. In general, the first rough tuning was done in simpler optical configuration having response to a given degree of freedom similar to that of a degree of freedom foreseen in the full ITF.

### Fabry-Perot arm length

The lengths of the two long cavities are reconstructed as previously described for the recombined ITF, by using the linearized transmitted signals:

$$\Delta L_W = \frac{1}{g_W} \frac{B8\_ACp}{B8\_DC} \quad (7.19)$$

$$\Delta L_N = \frac{1}{g_N} \frac{B7\_ACp}{B7\_DC} \quad (7.20)$$

where  $g_N$  and  $g_W$  are the optical gains for the two signals.

When the ITF is locked at mid-fringe the response of the transmitted signals is similar to that one they have in recombined configuration. The demodulation phases of B7 and B8 signals are therefore tuned as done in that case, with a single cavity freely swinging.

### Michelson length

Unlike the other degrees of freedom, a Pound-Drever-Hall signal can not be used in order to reconstruct the Michelson length, as it would be out from its linear range with the Michelson at mid-fringe. Since the ITF is well outside the dark fringe condition, the most suitable signal to reconstruct the Michelson length is given by the dark port DC signal,  $B1\_DC$ , normalized by the  $B5\_DC$  power signal (see figure 7.17).

An offset is added into this signal in order to select the desired working point, so that the reconstructed Michelson length  $\Delta l_-$  is written as:

$$\Delta l_- = g_{MICH} \left( \frac{1}{\beta} \frac{B1\_DC}{B5\_DC} - \alpha_{offset} \right) \quad (7.21)$$

where  $\beta$  is the measured ratio between  $B1\_DC$  and  $B5\_DC$ <sup>5</sup>.  $\alpha_{offset}$  is the fringe offset, which corresponds to 0.5 for the mid-fringe lock<sup>6</sup>.

<sup>5</sup>The parameter  $\beta$  is measured with the two cavities locked and the Michelson freely swinging. For the measurement the PR mirror is kept misaligned not less than  $150 \mu m$ .

<sup>6</sup>0.4 when 60% of the light is reflected and 40% is transmitted, and so on. A fringe offset of zero corresponds to the dark fringe condition, with 100% of reflected light, in an ideal case.

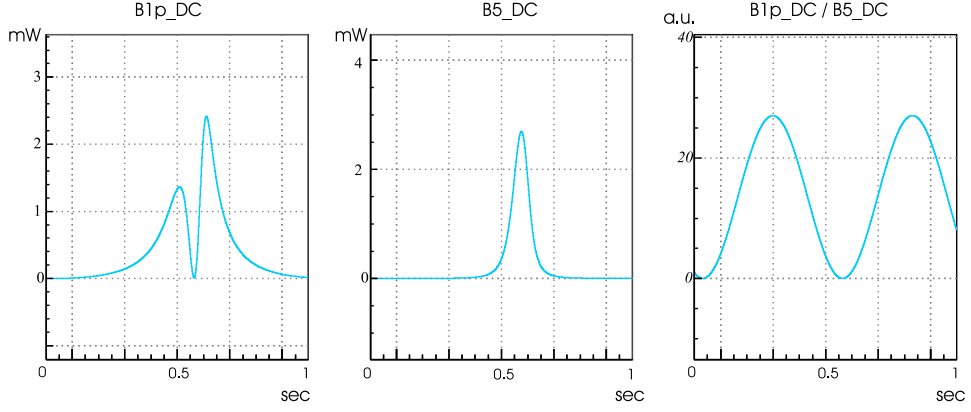


Figure 7.17: Signals involved in the DC Michelson control.

### Power recycling cavity length

As previously studied in simulation and comprehensively tested in the TAMA control scheme, a  $3\Omega$ -demodulation is applied to the reflected beam, and the  $B2.3f\_ACp$  signal is used to reconstruct the power recycling cavity length  $\Delta l_+$ . Its property of sign stability against changing of the optical parameters proves to be essential in the variable finesse technique. As discussed in section 3.4.2, the conventional  $\Omega$ -demodulated signal vanishes when the gain of carrier and sidebands inside the recycling cavity are the same. The use of this signal during the lock acquisition sequence would greatly complicate the scheme in order to compensate for its sign variation.

The  $B2.3f\_ACp$  signal is mainly proportional to the sidebands power stored inside the recycling cavity, so that:

$$B2.3f\_ACp = g_{PRCL} B5.2f\_ACq \Delta l_+$$

The tuning of the  $B2.3f$  demodulation phase is initially done by misaligning the end mirrors, so that only the central ITF remains aligned, with mirrors freely swinging around resonance. The applied procedure is that one described in (see section 7.3.1). On the other hand, the demodulation phase of  $B2.3f$  turned out to be somewhat more complicated than expected. Deeper investigations were therefore done during the commissioning activity to study its behavior as the dark fringe is approached, as will be described in the next chapter.

## 7.8 Feedback to the mirrors

After reconstruction, the four lengths are filtered and sent to the mirrors in order to keep the ITF stably locked on the half fringe.

### 7.8.1 The control filters

The lock at mid-fringe is acquired by engaging simple derivative filters with a very low unity frequency gain. Once the ITF is locked in a stable way, the DC gain is increased, in order to reduce the residual motion of the degrees of freedom (see figures 7.18 and 7.19).

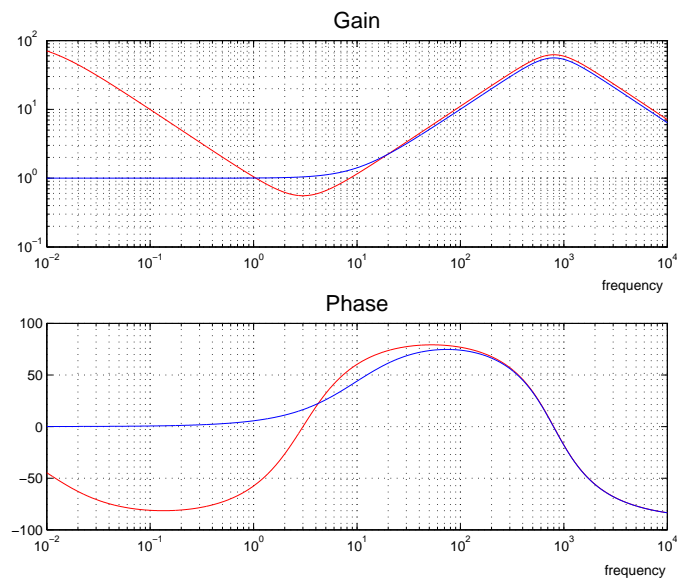


Figure 7.18: Control filters for MICH and PRCL: the simpler blue one is used to acquire the lock at mid-fringe. Once lock is acquired, a new filter with 100 times higher gain in DC is engaged.

### 7.8.2 The driving matrix

Since the North and West cavities were independently controlled, the corresponding correction signals were sent separately to NE and WE mirror. The Michelson length was controlled by acting on BS, and the power recycling cavity length on PR. The adopted driving matrix was therefore diagonal:

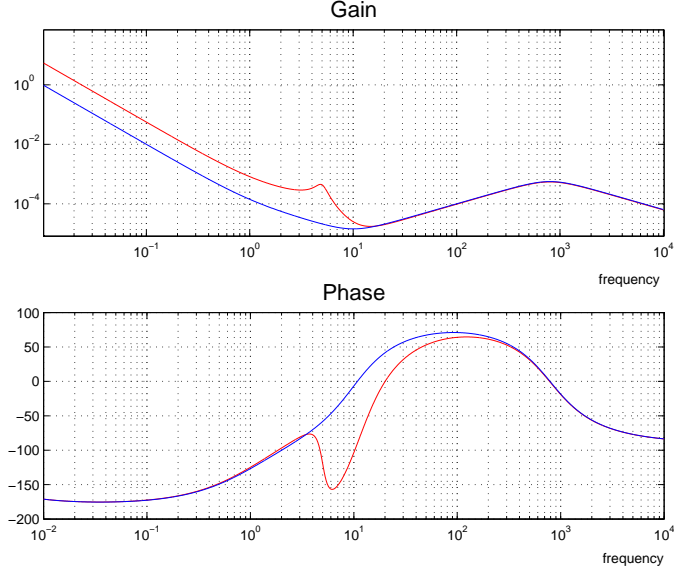


Figure 7.19: Control filters for DARM: the blue one is applied in the first steps of the sequence; when the fringe offset is decreased up to 0.2, the red one is switched on, in order to further increase the DC gain.

$$\begin{pmatrix} z_{NE} \\ z_{WE} \\ z_{PR} \\ z_{BS} \end{pmatrix} = \begin{pmatrix} 1 & 0 & 0 & 0 \\ 0 & 1 & 0 & 0 \\ 0 & 0 & 1 & 0 \\ 0 & 0 & 0 & 1/\sqrt{2} \end{pmatrix} \begin{pmatrix} \Delta L_N \\ \Delta L_W \\ \Delta l_+ \\ \Delta l_- \end{pmatrix} \quad (7.22)$$

However, a geometrical coupling between PRCL and MICH is intrinsically present, so that by moving BS also the power recycling cavity length is changed:

$$l'_+ = l_0 - \sqrt{2}\Delta l + \frac{l_N + \sqrt{2}\Delta l + l_W}{2} = l_+ - \frac{\sqrt{2}}{2}\Delta l \quad (7.23)$$

$$l'_- = l_N + \sqrt{2}\Delta l - l_W = l_- + \sqrt{2}\Delta l \quad (7.24)$$

where  $l'_+$  and  $l'_-$  are the new lengths obtained after the BS movement, both changed with respect to the previous ones  $l_+$  and  $l_-$  (see figure 7.20).

A non-diagonal driving matrix should therefore be used.

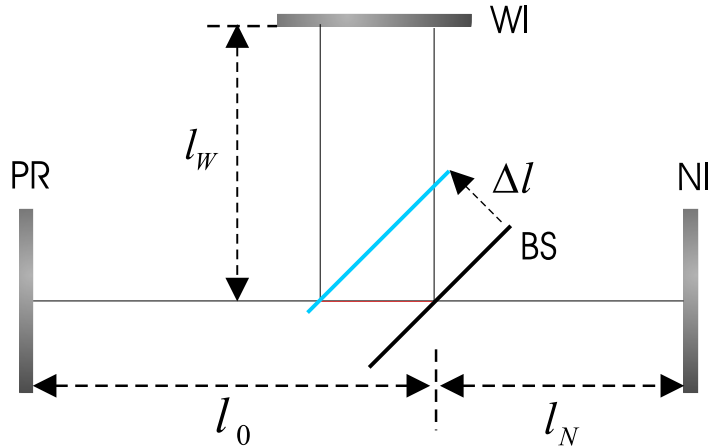


Figure 7.20: Geometrical coupling between PRCL and MICH degrees of freedom.

## 7.9 Misalignment of the PR mirror

With the described locking scheme, the ITF is brought from the uncontrolled state to the lock at mid-fringe in a few minutes. Several experiments were performed in order to accelerate this process. The best solution found was to keep PR slightly misaligned (by about  $10 \mu rad$ ) at the beginning of the locking sequence, and to realign it in course of lock acquisition, once a stable state of the ITF is reached. As it is shown in figure 7.21, this reduces the lock acquisition time from a few minutes to a few seconds. In fact, the misalignment of the PR makes the two cavities less coupled and easier to be controlled by means of the end photodiodes, in a similar way as for the recombined ITF.

The locking scheme in the first step of the lock acquisition sequence is shown in figure 7.22.

## 7.10 Moving to the dark fringe

Once the ITF is locked in a stable state, the offset in the Michelson error signal needs to be slowly decreased in order to increase the recycling gain and to bring the ITF on its working point. At the same time, the control scheme has to take into account the increasing coupling between the different degrees of freedom. In particular, as already said, the end photodiodes can be used to independently control the two cavities only when the recycling gain is low. Moving to the dark fringe increases the recycling gain, so the control scheme needs to evolve accordingly, as shown in

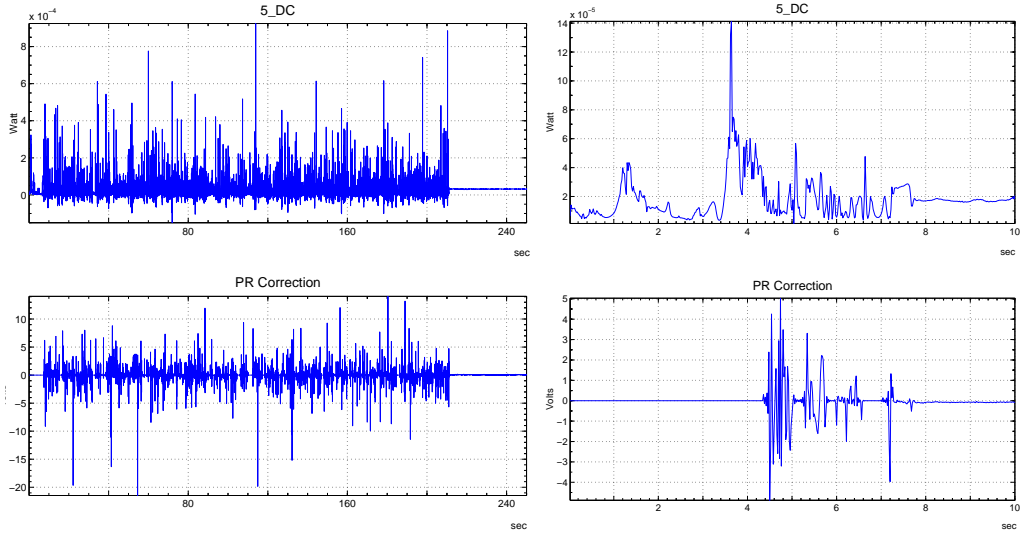


Figure 7.21: Lock acquisition of the ITF at mid-fringe done with PR aligned (left) and PR misaligned by  $10 \mu\text{rad}$  (right). The lock acquisition time is reduced from a few minutes to a few seconds.

figure 7.23: DARM is controlled by one of the end photodiode demodulated signals ( $B8\_ACp$ ) and the frequency stabilization servo is switched on in order to control CARM (see section 7.11).

When PR is realigned the gain of sidebands and carrier inside the recycling cavity increases by factors of 2.5 and 3. By keeping the same control scheme, the offset in the Michelson error signal is then adiabatically reduced in several steps, until the ITF is brought to  $r_c^2 = 0.95$ .

In order to finally bring the ITF on its working point, the control scheme needs to be further changed. The control of the Michelson length by means of the DC signal is not possible close to the dark fringe: the derivative of that signal vanishes, so that it is not sensitive anymore to the Michelson length variation. A demodulated signal has therefore to be involved in the control scheme. This is actually the last step of the variable finesse technique (see figure 7.24): it consists in switching from the DC signal to a demodulated one to control the Michelson length. It is done with a ramp of a few seconds, by removing at the same time the offset in the DC signal. The involved demodulated signal is  $B5\_ACq$ .

The ITF goes on the dark fringe and the recycling cavity gain increases up to its maximum value.

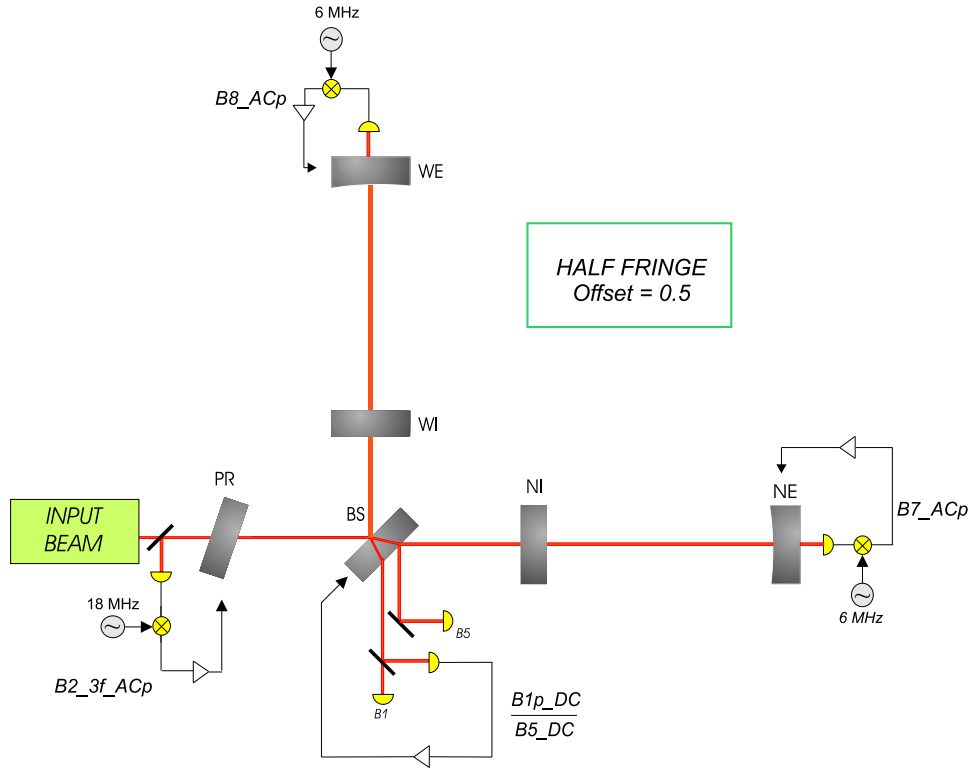


Figure 7.22: Locking scheme in the first step of the lock acquisition sequence: the two long cavities are independently locked by the end demodulated signals, the Michelson is controlled by a DC error signal. The PR mirror is kept slightly misaligned, and the small quantity of light reflected back by the ITF is used to control the recycling cavity length by the  $3\Omega$ -demodulated signal.

### 7.10.1 The dynamic sensing matrix

From the mid-fringe PR misaligned initial state to the dark fringe well aligned final state, the power of carrier and sidebands inside the ITF increases more than a factor 100. In order to take into account the large change in the optical gains and to keep the control system stable, the demodulated signals adopted to control the system have to be written by including the dependence on the fields in the ITF, as described in the previous paragraphs. On the other hand, it was observed that the adopted linearizations are not completely effective. Servo gains of the involved loops need in fact to be adjusted at each step of the locking sequence. Because the ITF approaches the dark fringe trough stable states and gains can be measured at each step, no conclusive deeper analysis was done in order to improve the linearization of the error signals.

Concerning CARM, changes in the optical gain of the error signal of frequency

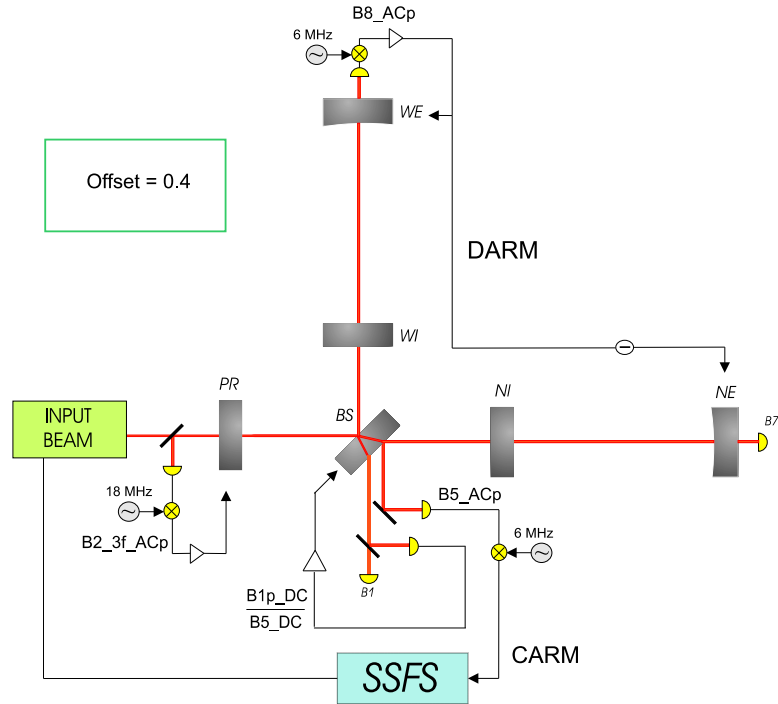


Figure 7.23: Evolution of the locking scheme: when the fringe offset is reduced, a differential and common control of the arms is needed to take into account the increasing coupling between the two cavities.  $B8\_ACp$  is applied for the differential control, the frequency stabilization servo is engaged for the common control.

servo  $B5\_ACp$  is compensated directly in the analog loop of the frequency stabilization servo itself, as it is described in 7.11.

## 7.11 The frequency stabilization servo

Since the variable finesse technique allows us to reach the dark fringe by going through stable states, the frequency servo can be engaged even during the locking sequence, before reaching the operating point. This has the main advantage of reducing the CARM contamination in all the error signals, making the lock acquisition easier. The frequency servo is therefore engaged as soon as the two Fabry-Perot cavities signals start to be mixed, when the offset in the Michelson error signal is reduced from the initial value of 0.5. On the other hand, the main drawback in engaging the analog frequency servo before being in the final state is that during all the lock acquisition sequence the optical gain of the involved error signal changes

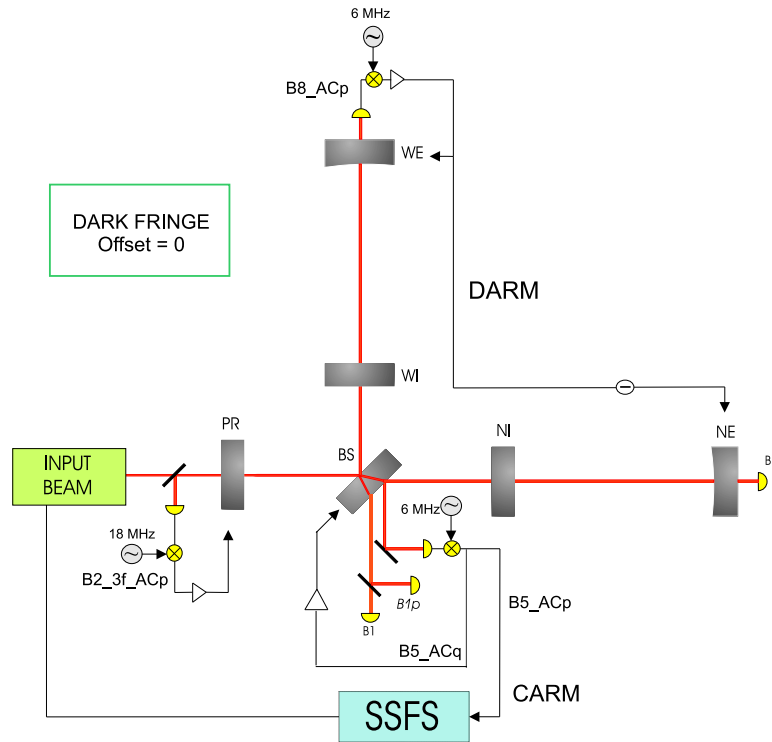


Figure 7.24: Evolution of the locking scheme: close to the dark fringe the offset in the DC signal is removed and it is replaced by the demodulated signal  $B5\_ACq$ .

greatly, so that the loop architecture has to be able to compensate for that.

The unity gain frequency of the second stage of frequency stabilization servo (SSFS) was designed to be around 10 kHz with the ITF locked on the dark fringe. The loop is stable down to a unity gain frequency of a few hundred Hz. When the SSFS is engaged, just before aligning the PR mirror, the DC power measured by the photodiode B5 is 100 times less than the power on the dark fringe. The unity gain frequency of the servo loop would be therefore around 100 Hz, out of its range of stability. In order to keep the servo loop in the stable region during the lock acquisition sequence, the SSFS electronics was modified to include the possibility to have two different gains of the analog loop and to move from one to the other by means of digital switch.

For this reason, the SSFS is engaged with the gain of the analog loop higher than the gain in the final state, in order to have a unity gain frequency around 1 kHz to prevent loop instabilities (see figure 7.25). When the amplification is not needed anymore, because of the increasing of the  $B5\_ACp$  optical gain, the gain of the loop

is switched to the lower value. With this strategy, the unity gain frequency of the servo increases as the dark fringe is approached, is switched to a lower value, and increases again to its nominal value of 10 kHz in the final state (see figure 7.26).

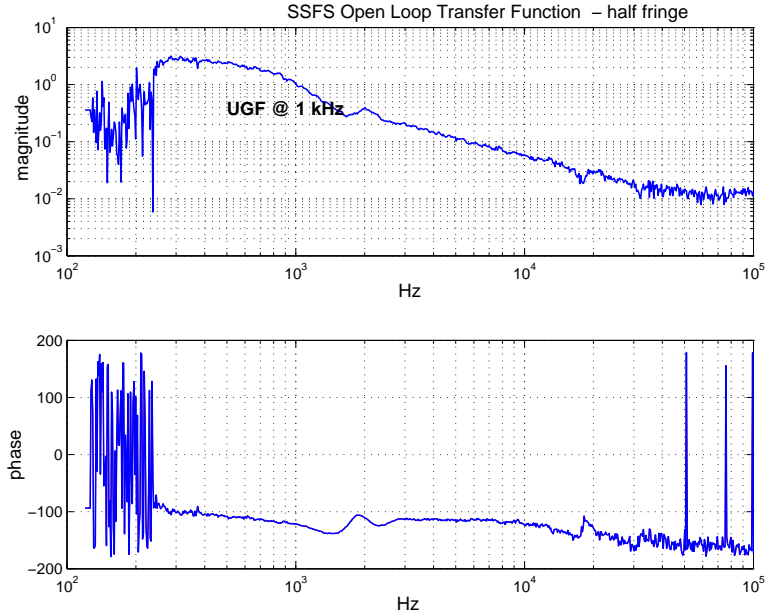


Figure 7.25: Open loop transfer function of the SSFS loop at the beginning of the locking sequence. The unity gain frequency is about 1 kHz.

## 7.12 Lock acquisition sequence

The figure 7.27 shows the evolution of the power of the carrier beam during a lock acquisition sequence, as measured by the signals B5\_DC (power stored inside the recycling cavity), B1\_DC (power at the dark port) and B2\_DC (power reflected by the ITF). The first plot shows the fringe offset, which is reduced from 0.5, with the lock at mid-fringe, to 0, when the dark fringe is achieved. The first increase in the stored power is due to the alignment of the PR mirrors; all others are connected with the reduction of the fringe offset.

Until the fringe offset is higher than 0.08 the recycling cavity is under-coupled, with  $r_{PR} > r_c$ . The optimal coupling is reached when the value of the fringe offset is 0.08, which means  $r_c = \sqrt{0.92} \sim 0.96$ , equal at  $r_{PR}$ . At that point there is the lowest reflected power and highest power transmitted through the dark port. When the fringe offset is further reduced, the recycling cavity becomes over-coupled

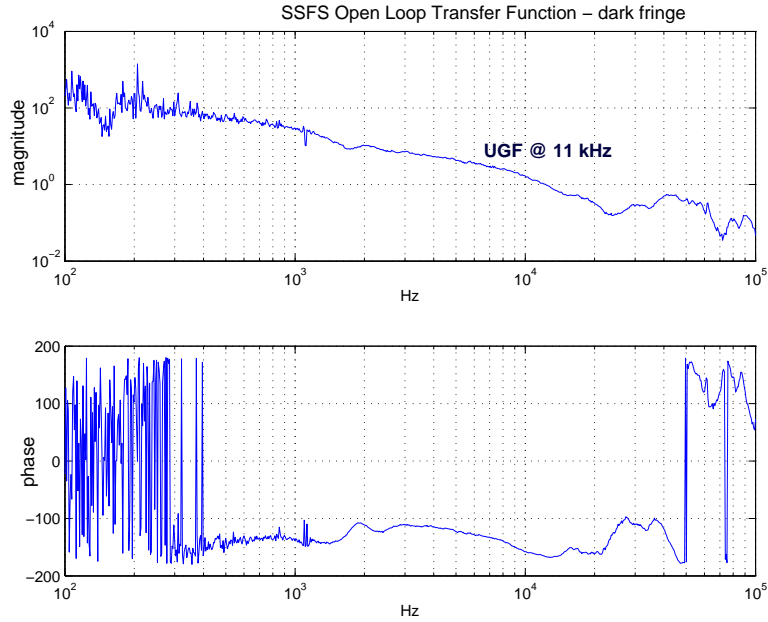


Figure 7.26: Open loop transfer function of the SSFS loop at the beginning of the locking sequence. The unity gain frequency is about 1 kHz.

$(r_{PR} < r_c)$ .

As previously described, the control scheme evolves along the lock acquisition path. The adopted full lock acquisition procedure is summarized in a sequence of 8 steps:

**STEP 1** (*Fringe Offset = 0.5*)  $\frac{B1\_DC}{B5\_DC}$  controls MICH,  $B2.3f\_ACp$  controls PRCL, the end photodiodes control independently the two cavities. Standard control filters are used. Longitudinal mirror damper are active.

**STEP 2** Boosts are added in MICH and PRCL filters.

**STEP 3** (*Fringe Offset = 0.4*) SSFS engaged: CARM and DARM control of the two cavities. Longitudinal mirror dampers are switched off.

**STEP 4** Alignment of the PR mirror.

**STEP 5** (*Fringe Offset = 0.2*) Low frequency gain is added to the DARM loop and the SSFS gain is reduced.

**STEP 6** (*Fringe Offset = 0.08*)

**STEP 7** *Fringe Offset = 0.05* Start switch from DC signal to demodulated signal for MICH.

**STEP 8** (*Fringe Offset = 0*) Only demodulated signal is used (*B5\_ACq*) to control MICH.

### 7.12.1 Evolution of the recycling gain

The recycling gain for a given beam can be expressed as:

$$G = \frac{P_{PR}}{P_{WPR}} = T_{PR} \frac{P_{PR}}{P_{misPR}} \quad (7.25)$$

where  $P_{PR}$  is the power of the beam stored inside the recycling cavity when PR is aligned, and  $P_{WPR}$  is the power as measured by the same signal, but without the PR mirror.  $P_{WPR}$  can also be written in terms of the power measured when PR is misaligned,  $P_{misPR}$  taking into account the transmissivity  $T_{PR}$  of the mirror.

In order to estimate how the recycling gain for carrier and sidebands change during the lock acquisition, it is possible to compare the signals *B5\_DC* and *B5.2f\_ACq*, which are respectively proportional to those powers, in recycling and in recombined configuration.

#### Recycling gain of the carrier

The recycling gain of the carrier can be estimated as:

$$G_{cr} = T_{PR} \frac{B5\_DC_{recyc}}{B5\_DC_{recomb}} \quad (7.26)$$

where  $B5\_DC_{recyc}$  and  $B5\_DC_{recomb}$  are the carrier power measured by *B5\_DC* in recycling and in recombined configuration.

By applying equation 7.26 the recycling gain of the carrier can be computed. Its behavior is plotted in figure 7.28. With the ITF locked on the dark fringe, its measured value is 33 (while the theoretical value, without considering cavity losses,

is around 50). By assuming that all losses are located inside the Fabry-Perot cavities, this leads to a reflectivity of the Fabry-Perot cavities  $r_{FP}^2 \sim 98\%$ , corresponding to round trip losses of  $570 \pm 50$ ppm <sup>7</sup>. Losses of the same order of magnitude (300 ppm for the north arm and 380 ppm for the west arm) were found in simulation by including real mirror surface maps, which have long range surface defects [50].

### Recycling gain of the sidebands

The recycling gain of the sidebands can be estimated as:

$$G_{sb} = 2T_{PR} \frac{B5\_2f\_quad_{recyc}}{B5\_2f\_quad_{recomb}} \quad (7.27)$$

where  $B5\_2f\_quad_{recyc}$  and  $B5\_2f\_quad_{recomb}$  are the sideband power measured by  $B5\_2f\_quad$  in recycling and in recombined configuration. The factor of two in the formula comes from the fact that both sidebands are resonant inside the recycling cavity. The maximum value, reached at the dark fringe, is around 20, while the designed value is 35. By including surface defects of the mirrors in simulation, a gain of 30, which is significantly higher than the measured one, would be instead expected. The mismatch between the measured and the expected value might be due to a not well simulation of the BS mirror surface [50].

---

<sup>7</sup>A direct measurement of the cavity losses was tried to be done by comparing the power reflected from the cavity out of resonance with the power reflected on resonance. Because of dynamical effects and fluctuations with the alignment, a precise measurement was not possible with this method [50].

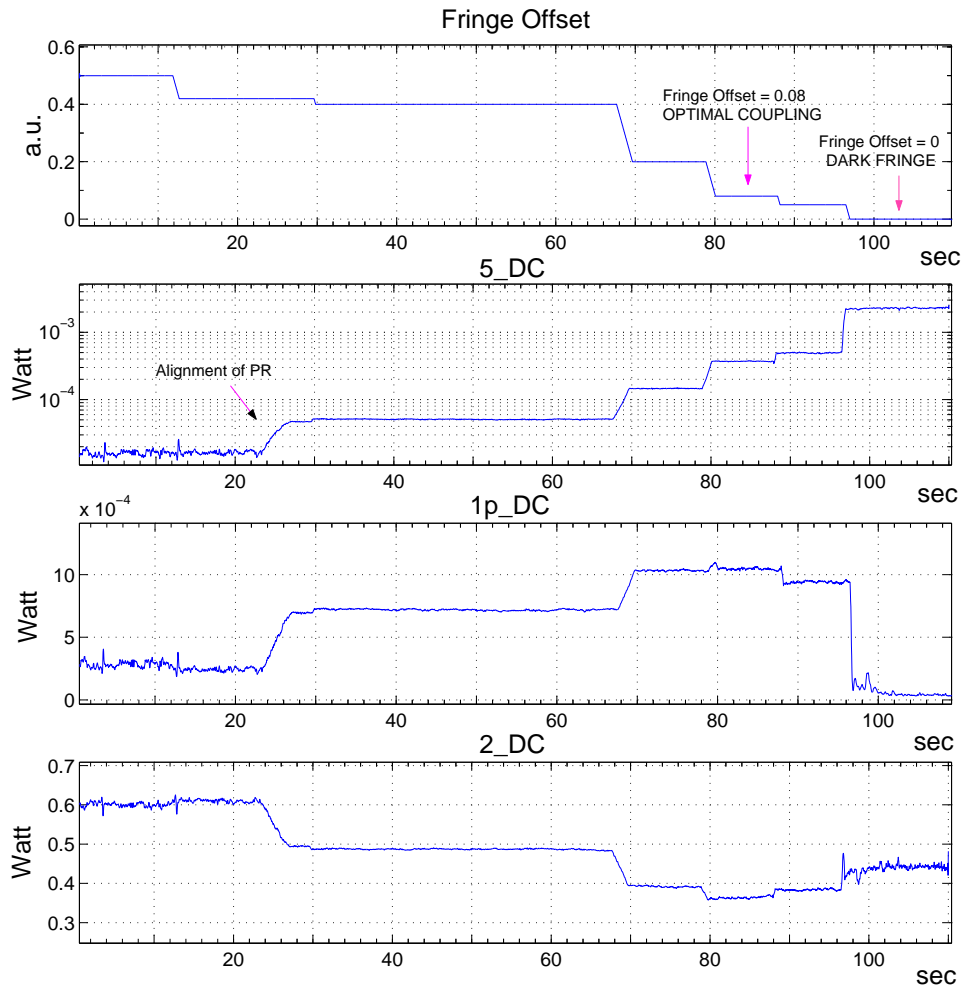


Figure 7.27: Trend of the power stored inside the recycling cavity (B5\_DC ), the power at the dark port (B1\_DC ) and power reflected by the ITF (B2\_DC ) during a lock acquisition sequence. The first plot shows the value of the fringe offset: its value of 0.08 corresponds at the optimal coupling for the recycling cavity, 0 is the dark fringe condition.

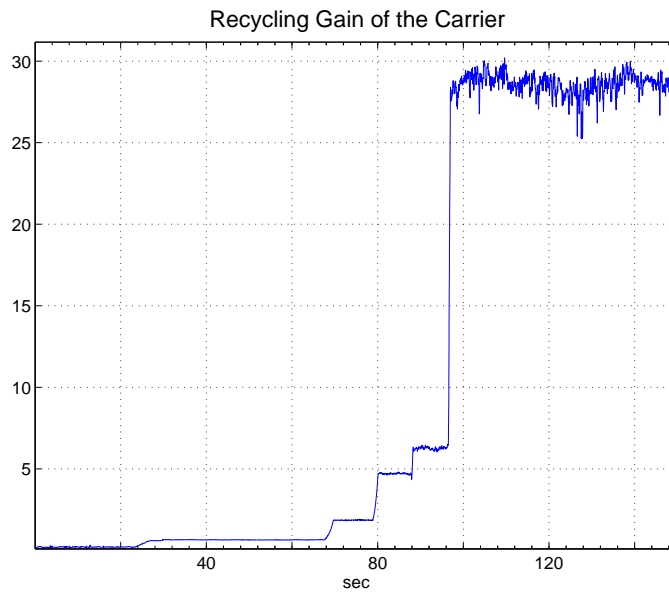


Figure 7.28: Trend of the recycling gain of the carrier during a lock acquisition sequence: with the ITF at the dark fringe, the maximum gain is around 30.

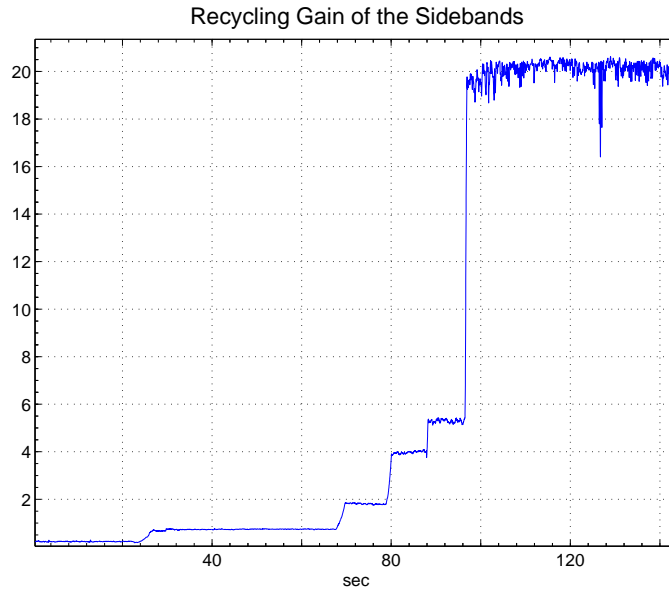


Figure 7.29: Trend of the recycling gain of the sidebands during a lock acquisition sequence: with the ITF at the dark fringe, the maximum gain is around 20.

## Chapter 8

# Commissioning of the recycled ITF

The recycled ITF was locked for the first time at the end of October 2004 using the variable finesse technique. The first long term analysis of the locking performance was done after a few weeks, during the commissioning run C5. No automatic alignment system was implemented at that time. Drifts and fluctuations of the mirror angular position were the main cause of unlock and locking periods were not longer than a few tens of minutes. After C5 an unexpected behavior of the ITF slowed down the overall commissioning activity. Instabilities in the ITF internal power, which caused the unlock of the ITF or in any case prevented the commissioning work, were systematically present. This problem was solved after 5-6 months and more stable working conditions were recovered. The commissioning activity continued as planned, and it was mainly dedicated to the implementation of the automatic alignment in recycled configuration. To facilitate the measurement of the parameters needed for this global alignment system, the efficiency of the variable finesse technique was also increased. The linearizations of the error signals were refined, as well as the control filters.

A dedicated software package (ALP, *Automation of Locking Procedure*) was also designed in order to automate the locking procedure.

Locking performance was analyzed in the commissioning runs C6 and C7, respectively two weeks and five days long, carried on in August and September 2005.

In C6 the duty cycle was greatly increased with respect to the previous commissioning run, mainly due to the stability gained by implementing the full bandwidth

automatic alignment of the differential mode of the end mirrors, and a low bandwidth automatic alignment of the other degrees of freedom. Moreover, a full automatic procedure to bring the ITF to science mode was adopted.

In C7 the complexity of the system increased, since the full bandwidth automatic alignment system was working for all the degrees of freedom, and the full hierarchical control of the Superattenuator was successfully tested for the first time in recycled configuration.

Noise performance of the detector were analyzed and improved as well. In particular, the sensitivity curve measured in C5 showed that the low frequency region was dominated by longitudinal control noise of MICH and PRCL. Several techniques were studied and tested in C6 and C7 to reduce this noise.

## 8.1 Commissioning run C5

During C5 (6-7 December 2004, 32 hours) the ITF was operated in recycled configuration:

- the ITF was locked on the dark fringe using the variable finesse technique;
- mirrors were kept under local controls, since the automatic alignment system was not implemented yet.

As explained in the previous chapter, in the final state of the variable finesse technique, the differential degree of freedom of the ITF is controlled with the end transmitted signal. Once the lock of the ITF was acquired, this signal was replaced by the signal extracted from the asymmetric port,  $B1p\_ACp$ . In order to improve the noise performance of the detector, in the last part of the run the control was moved to the  $B1$  photodiode (see figure 8.1) after putting the OMC on resonance.

The lock acquisition sequence was not automatized yet, so that about 15 minutes were needed in order to realign and to bring the ITF back on its working point after each unlock.

The trend of the recycling cavity power measured in C5 is shown in figure 8.2. The duty-cycle was around 30%. Locking periods longer than few tens of minutes were prevented mainly by drifts in the angular position of the mirrors. The maximum continuous locking stretch was 1 hour and a half.

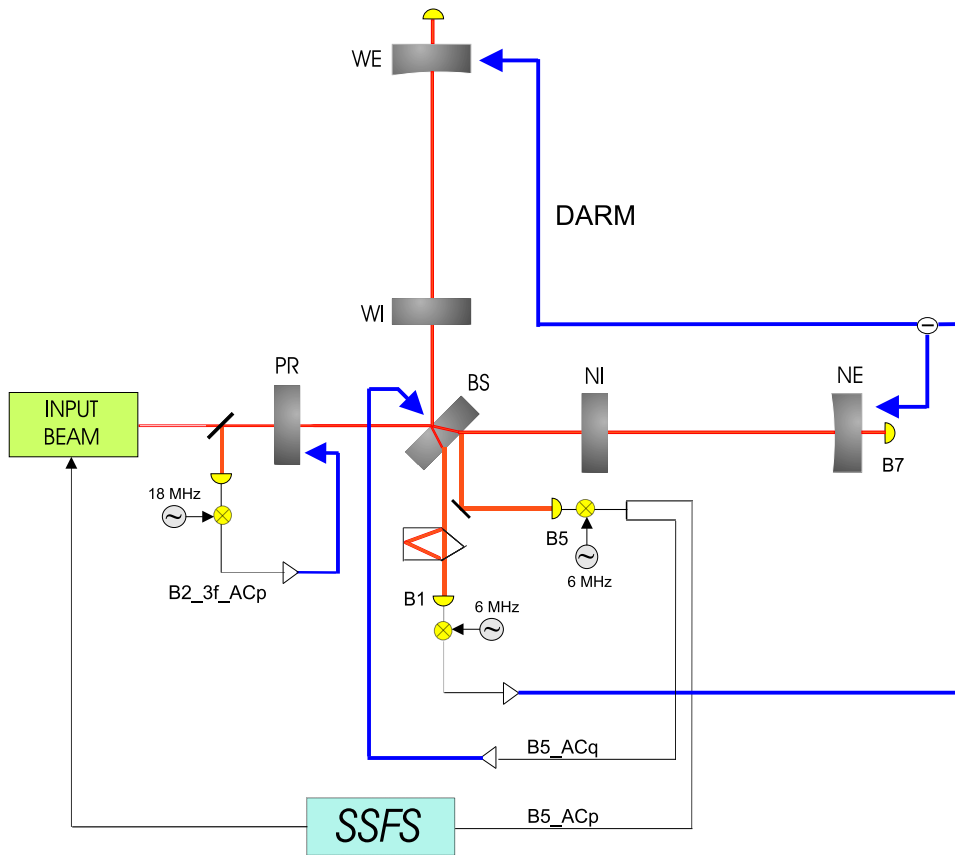


Figure 8.1: Locking scheme in C5. Linearizations of the longitudinal error signals are not reported in the picture (see previous chapter).

### 8.1.1 C5 noise budget

Figure 8.3 shows the noise budget measured with the OMC on resonance and the differential mode of the arms controlled by  $B1\_ACp$ .

The main noise sources can be summarized as follows:

- *control noises* - The low frequency region, below 100 Hz, is limited mainly by the noise reintroduced by the BS longitudinal control and by local controls of the pitch degree of freedom, both of the BS and the WI.
- *oscillator phase noise*, induced by the phase noise of the local oscillator boards - In the high frequency region, above 400 Hz, the sensitivity is spoiled by phase noise, which couples to the dark fringe signal through misalignments of the mirrors, still locally controlled.

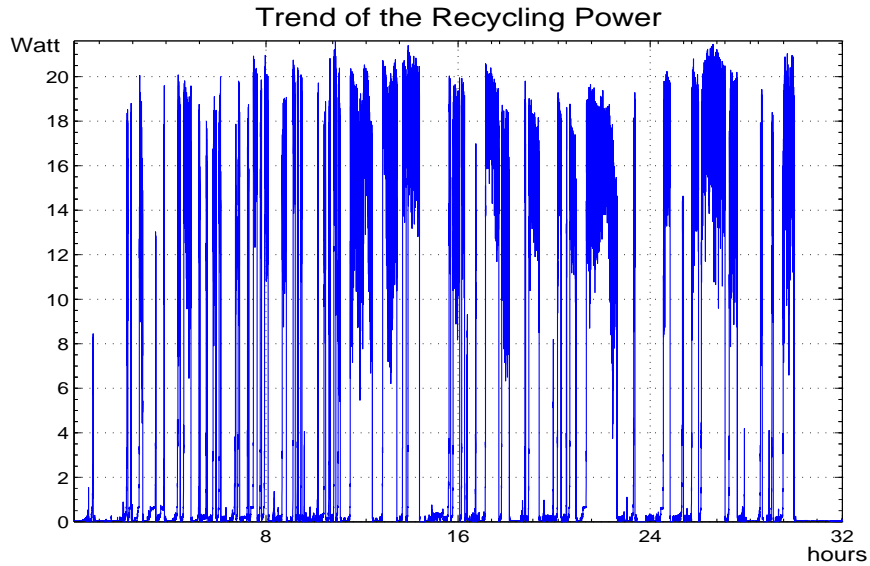


Figure 8.2: Trend of the recycling cavity power during C5.

- in the mid-frequency region the noise is not understood.

## 8.2 Instabilities in the ITF power

After C5 a technical shut-down was made mainly to perform some reshuffling of the electronics. At that time, a full re-alignment of the injection system and the photodiodes was done.

Once the commissioning activity re-started, in January 2005, the ITF was re-locked, but sudden instabilities were observed in the ITF stored power (see figure 8.2). These fast (a few tens of ms) transitions to a lower power level occurred with different rates, depending on some unknown combination of slowly changing variables. Sometimes transitions would occur every few seconds, making it very difficult to keep the ITF locked, sometimes every few minutes, preventing any long term operation, or sometimes there would be just a few over hours, without really disturbing the working conditions. Since the presence of these *jumps* did not guarantee any stability and reliability of the system, much effort was spent in order to understand their origin. The evidence was that the power in the recycling cavity, after the jump, stayed in a low level state (around half of the standard power value) for a variable period of a few tenths of seconds, then returned to the original value.

Even if reasons causing jumps were not fully understood, several tests excluded

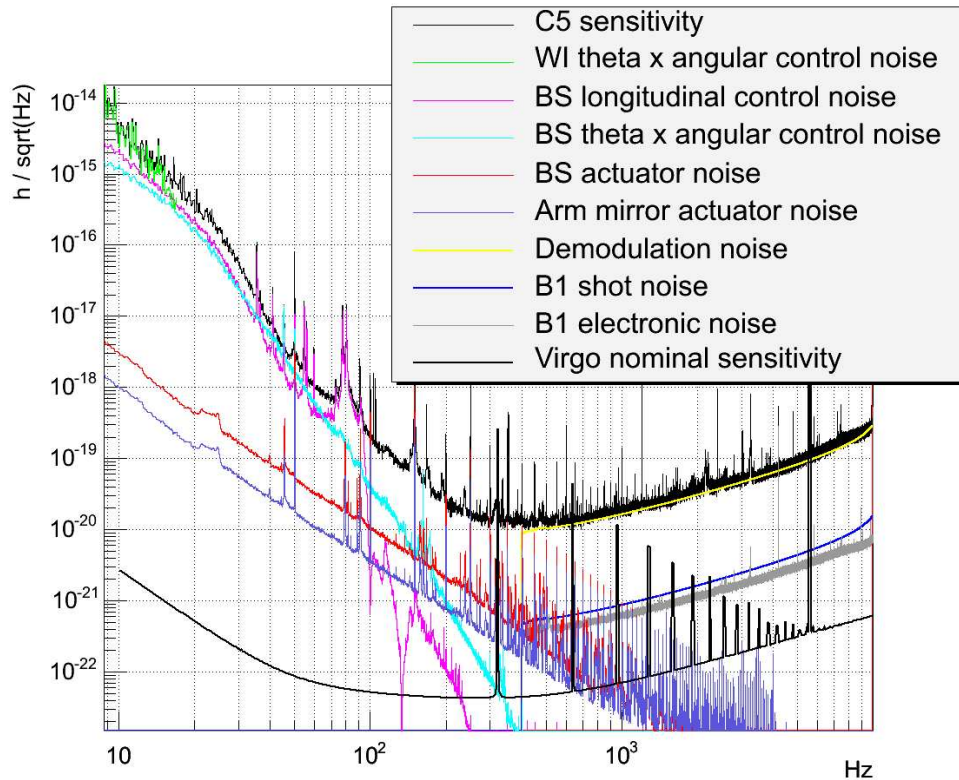


Figure 8.3: C5 noise budget [34]. The sensitivity curve is limited at low frequencies mainly by the BS longitudinal control noise and by phase noise at high frequency. In the middle region, between 100 and 500 Hz, a dominant source of noise was not identified.

electronics and environmental noise as their source, leading to the conclusion that the mechanism had was to be found in the interferometer optics. It was experimentally shown in dedicated experiments that jumps could be clearly triggered by slightly misaligning the mirrors with respect to the aligned position. Just half a  $\mu\text{rad}$  of misalignment was in fact enough to make jump appear. Several operations were performed in order to try to fix the problem. In particular, after a few months of investigations, the photodiode B5 was found not correctly centered. After centering it, these bi-stabilities seemed to have disappeared.

Unperturbed operations were carried out for one week. Then the injection bench needed to be re-aligned, because of a malfunctioning of a laser used in its local control system. After this operation the bi-stabilities appeared again, despite the fact that the B5 photodiode was correctly centered. The injection bench was then moved to its previous orientation: after this operation the bi-stabilities completely disappeared.

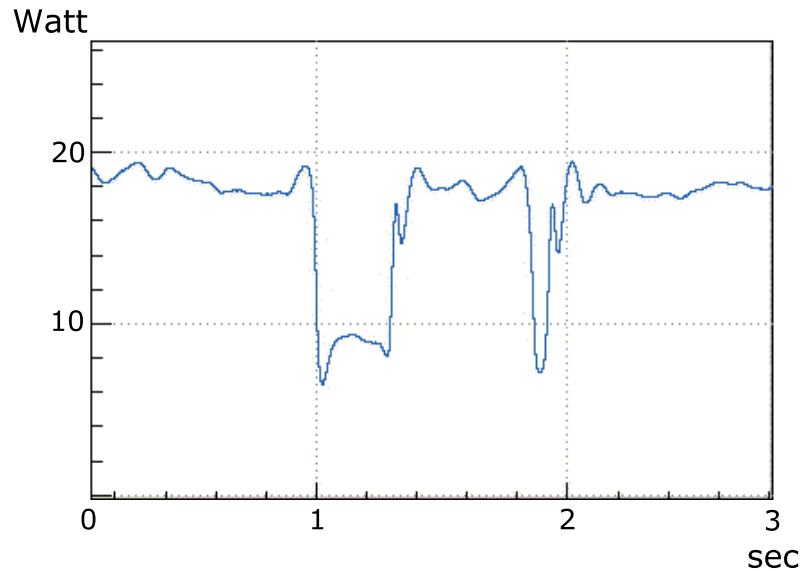


Figure 8.4: Example of the jump observed in the recycling power.

Why special alignment positions of the injection bench could generate this kind of bi-stabilities was not understood. Some hypothesis were connected with some problems observed at the level of the injection system:

- beam clipping on injection bench mounting;
- spurious light;
- secondary beams reflected from the ITF and not correctly managed at the injection bench level.

These problems at the injection bench level could contaminate the beams impinging upon the photodiodes involved in the control of the ITF, perturbing the working position of the interferometer itself. The same mechanism could explain the fact that bi-stabilities were observed when the B5 photodiode was not correctly centered.

Despite the fact that the problem of jumps was cured, the lock of the ITF was not robust and stable enough for taking data over periods of hours, because of another kind of instability. These seemed not to be connected with a second stable state of the ITF, but with another mechanism producing oscillations in the stored power at

a few Hz, not related with longitudinal loop oscillations or angular fluctuations.<sup>1</sup>. The problem was removed by detuning the optimal demodulation phase of the *B2\_3f* signal (used to control the power recycling cavity) by some tens of degrees.

The mechanism for this effect, which is not understood yet, might also be due to spurious light at the at the interferometer reflected port. Since the upgrade of the injection bench was already plan, all the observed problems connected with spurious beams and beam clipping were taken into account for the new design.

### 8.3 Interferometer automation

Because of the increasing complexity of the control systems implemented in the ITF, the standard working condition could be reached only by means of about four hundred of commands sent to the several real-time processors of the main sub-systems.

An automatic procedure based on a specially designed script language (ALP) was therefore needed in order to manage all these operations and guarantee a high reliability of the system. Data acquired by the standard *Data Acquisition* system are collected by ALP in order to compute the state of all the sub-systems involved in the interferometer operations. According to the state of each sub-system, specified actions can be performed using the system calls or directly sensing messages by means of the VIRGO inter-processes communication protocol Cm. Each task, such as locking and alignment, is managed by a dedicated server. It is configured by means of several ALP scripts, known as *macros*, coded to perform a specific step of the automation sequence.

The first steps of the automatic procedure concerned the lock of the ITF, taking it from the uncontrolled state to the dark fringe (see previous chapter). After locking, the automation enables the automatic alignment system and takes the ITF to its lowest noise state (*science mode*).

### 8.4 Automatic alignment

In recycled configuration, the large number of involved degrees of freedom and the couplings between the extracted signals make the implementation of the automatic alignment system a very complex problem.

---

<sup>1</sup>Even if these other kind of instabilities had a different shape with respect to the jumps, they were confused often with the first ones, and this probably slowed down the diagnostics.

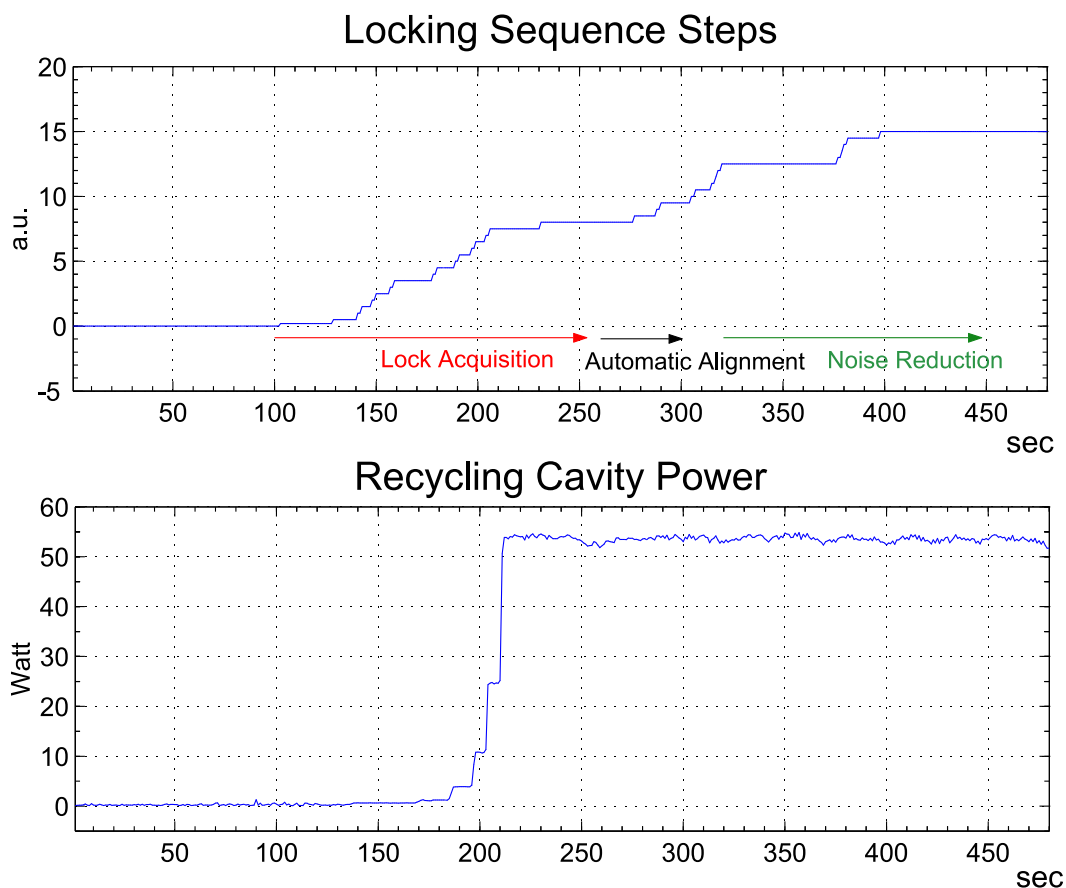


Figure 8.5: Locking sequence, for the uncontrolled state of the ITF to *science mode*.

A simplified scheme was implemented and tested during commissioning run C6, with the main goal to guarantee a better stability of the ITF by reducing power fluctuations in the dark fringe signal. In this scheme, only the differential modes of the end mirrors (pitch and yaw) were controlled with the full bandwidth of a few Hz, by using quadrant demodulated signals extracted from the asymmetric port ( $B1p$ ) and acting on the NE mirror. This kind of control improved very significantly the power stability of the ITF, as shown in figure 8.4.

All the other angular degrees of freedom of the ITF were kept controlled with very narrow bandwidths ( $\sim 10$  mHz). This *drift control* reduced the slow drifts of the mirror angular positions by readjusting the set-point of the local control system, which remained switched on at all times. In this way the local control reduced the high frequency angular fluctuations, while slow motions were controlled with the drift control, which is less sensitive to signal couplings thanks to its narrow

bandwidth and is therefore easier to implement.

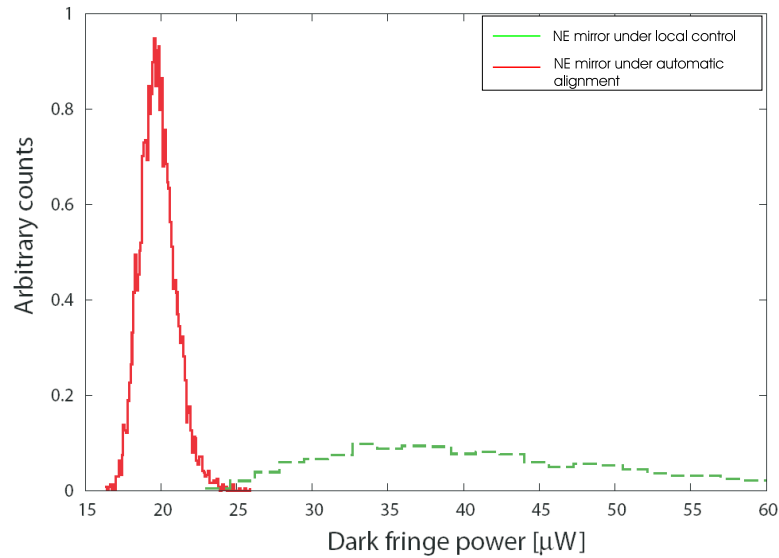


Figure 8.6: Histogram of the dark fringe power measured with the NE mirror kept under local control (green) and with the automatic alignment at full bandwidth (red) [37].

The automatic alignment system was improved for C7 (see figure 8.4). Five mirrors, corresponding to 10 out of 12 control loops, were controlled with about 3 Hz of bandwidth, leaving only one mirror under local control. The remaining degrees of freedom referred only to the long-term stabilization of the beam position drift in the two arms.

## 8.5 Reduction of the longitudinal control noise

As seen in the C5 noise budget, the reduction of the longitudinal control noise introduced by the auxiliary degrees of freedom (MICH, PRCL and CARM) played a crucial role in improving the Virgo sensitivity.

The CARM length was controlled by the laser frequency servo with a bandwidth of 10 kHz. The impact of the frequency noise in the Virgo sensitivity was mainly at high frequency, mostly due to the sensing of the demodulated error signal used for the frequency stabilization<sup>2</sup>. The sensing noise can be reduced in at least three ways:

<sup>2</sup>The coupling of the frequency noise with the dark fringe signal depends also on the Common Mode Rejection Factor (CMRF), which is affected by the loss asymmetry between the two arms and by the alignment of one arm with respect to the other.

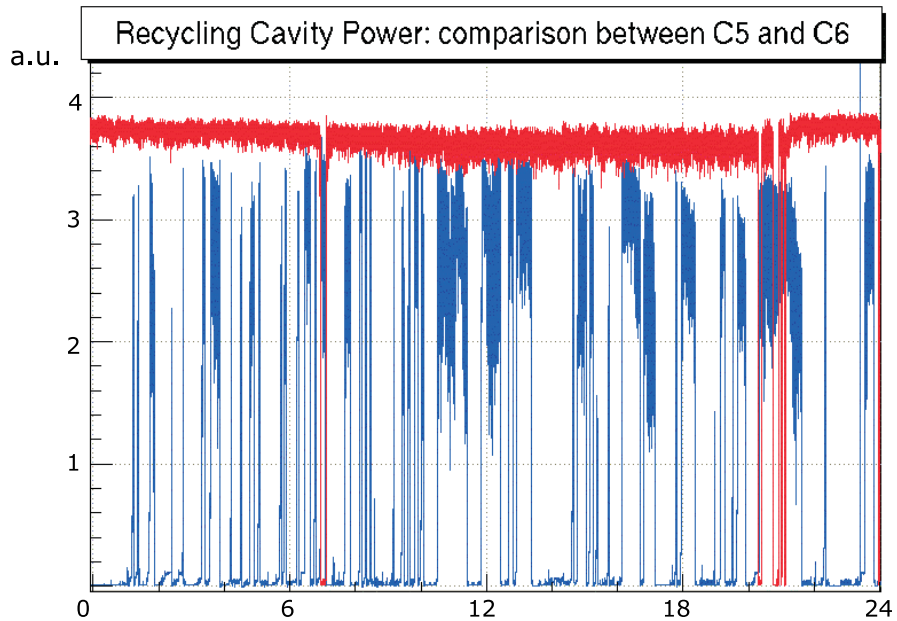


Figure 8.7: Comparison of the recycling cavity power, over 1 day of data taking in C5 (blu) and C6 (red).

- by increasing the power of the input beam;
- by increasing the fraction of the light impinging the photodiode;
- by increasing the modulation index.

The last two solutions were applied in C7.

The impact of the CARM control noise at the anti-symmetric port will not be analyzed here in more details (see [34]). This section will be instead dedicated to the control noises of the other two auxiliary lengths, MICH and PRCL. The techniques studied and applied so far in order to reduce their contamination at the anti-symmetric port are described.

### 8.5.1 Use of more sensitive signals

The large number of signals extracted at the output ports of the ITF makes the choice of a suitable set of error signals to be involved in the locking scheme non-trivial. The general strategy, already applied in the recombined configuration, is

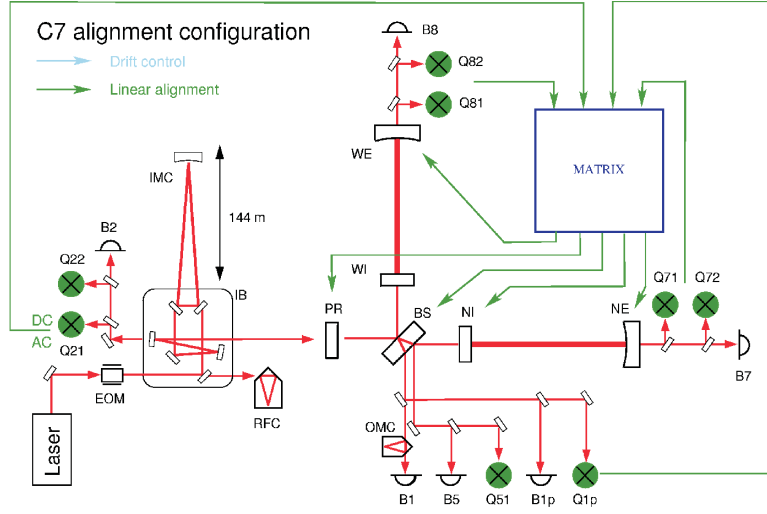


Figure 8.8: Automatic alignment locking scheme in C7.

to use more robust signals during the lock acquisition phase, and once the ITF is locked onto the dark fringe, to replace them with less noisy signals.

### Switch from $B2_{3f}$ to $B2$

Once the ITF was stably locked on the dark fringe, the switch from the reflected  $3\Omega$ -demodulated signal to the  $\Omega$ -demodulated signal to control PRCL was tested. The  $3\Omega$ -demodulated signal is more robust than the  $\Omega$ -demodulated signal, but it is also noisier. In fact, at the operating point, the sensitivity of the  $3\Omega$ -demodulated signal to a PRCL length variation can be written as:

$$B2_{3f\_ACp} \propto J_1(m)J_2(m)g_1^2 r_{sb,2} r_M \Delta l_+ \quad (8.1)$$

Since second order of sidebands are not resonant in the interferometer, they are all reflected at the symmetric port, so that  $r_{sb,2} \sim 1$ .

By assuming the same quantity of light impinging the two photodiodes and the same noise performance of the photo-detectors, for the  $\Omega$ -demodulated signal we have:

$$B2_{ACp} \propto J_0(m)J_1(m)(g_0^2 r_{cr} r_{sb} + g_1^2 r_{cr} r_M) \Delta l_+ \quad (8.2)$$

The ratio between the amplitude of the  $\Omega$ -demodulated signal and of the  $3\Omega$ -demodulated signal is therefore:

$$\frac{B2\_ACp}{B2\_3f\_ACp} \propto \frac{J_0(m)J_1(m)(-g_0^2 r_{cr} r_{sb} + g_1^2 r_{cr} r_M)}{J_1(m)J_2(m)g_1^2 r_M} \quad (8.3)$$

$$= \frac{-g_0^2 r_{sb} + g_1^2 r_{cr} r_M}{\left(\frac{m}{2}\right)^2 g_1^2 r_M} \quad (8.4)$$

In particular, by substituting the nominal Virgo parameters:

$$r_M = 0.9945 \quad (8.5)$$

$$r_c \simeq -1 \quad (8.6)$$

$$r_{sb} \simeq -0.767 \quad (8.7)$$

$$r_{cr} \simeq 1 \quad (8.8)$$

the ratio becomes:

$$\frac{B2\_ACp}{B2\_3f\_ACp} \sim 250 \quad (8.9)$$

As confirmed by the simulation [55], this means that *B2.3f\_ACp* has a SNR about two orders of magnitude worse than *B2\_ACp*. For this reason, in order to optimize the locking scheme noise performance, the transition from the reflected  $3\Omega$ -demodulated signal to the  $\Omega$ -demodulated signal was tested<sup>3</sup>.

However, with the ITF stably locked on the dark fringe, an offset was present in the *B2\_ACp* signal<sup>4</sup>. The offset in this signal corresponded to an offset of about 10 nm in the PR mirror position<sup>5</sup>. The switch to *B2\_ACp* was tested anyway. Even electronically removing the offset, a stable lock of the ITF with the *B2\_ACp* signal was never held for more than a few minutes.

<sup>3</sup>An alternative solution is to move the PR control from the reflected  $3\Omega$ -demodulated signal to the demodulated signal extracted from the second face of BS: this requires previously to stabilize the laser frequency by involving the reflected  $\Omega$ -demodulated signal.

<sup>4</sup>The demodulation phase of B2 was tuned by injecting a sinus line on PR to displace the mirror along the z-axis, at a frequency of a few hundreds of Hz, and by setting the demodulation phase so to maximize the in-phase component with respect to the quadrature phase component

<sup>5</sup>The calibration of the offset visible in the *B2\_ACp* signal was done by knowing the gain of the PR actuators,  $1.3 \times 10^{-5} m/V$ , and by measuring the amplitude of a sinusoidal line injected on the PR to displace the mirror along the z-axis. Moreover, by involving this signal in the locking scheme without removing the offset, a fast decrease by a factor 3 of the power stored inside the interferometer was observed before the ITF unlocked. Since the recycling cavity has a finesse  $\mathcal{F} \sim 75$ , it is compatible with a change of about 10 nm of the PR mirror from the resonant position.

The origin of this offset was not understood. Possible generation mechanisms were thought to be connected with spurious beams and stray-light detected in the injection system, as for the problem of jumps (see section 8.2). A partial dumping of the unwanted beams impinging upon the B2 photodiode was performed, but no change was observed in the  $B2\_ACp$  offset value. The centering of the B2 photodiode was checked as well, without significant improvements.

### Increase of the modulation index

One way to improve the SNR of locking signals limited by shot-noise and electronic noise is to increase the modulation index  $m$  of the incoming laser beam.

The  $\Omega$ -demodulated signals are proportional to  $m$ , so that, by increasing the modulation index by a factor 2, for instance, the amplitude of these signals would increase by a factor 2 as well. In particular, the impact of the electronic noise on  $B1\_ACp$  and  $B5\_ACp$  would be decreased by the same factor. Concerning the shot noise, its impact would be decreased only on  $B5\_ACp$ . The shot-noise on B1, on the other hand, is dominated by the sideband power, so that it increases by the same factor as the amplitude of the demodulated signal.

The  $3\Omega$ -demodulated signal  $B2.3f\_ACp$  used to control PRCL is instead proportional to  $m^3$ , so that its amplitude would be increased by a factor 8, greatly reducing both the electronic and the shot noise impact. During the commissioning runs C5 and C6  $m = 0.16$ , where the commissioning run C7 was performed with  $m = 0.30$ .

### 8.5.2 Optimization of the control filters

The control filters have to be optimized in order to reduce the noise reintroduced in the detection band. The solution adopted was to reduce as much as possible the bandwidth of the control loops, around 10 Hz for the MICH and 30 Hz for the PRCL loop, and to design aggressive roll-off at a few tens of Hz.

Figure 8.5.2 shows the 7<sup>th</sup>-order elliptic filter with a roll-off at 50 Hz designed for reducing the noise reintroduced into the dark fringe signal by the MICH loop (red). At 100 Hz, the reduction of the gain with respect to the simpler derivative filter used in the lock acquisition phase (blue), is about 20 dB.

The spectrum of the corresponding correction signals applied to the BS is shown in figure 8.5.2. A further reduction of the gain, and a consequent reduction of the unity gain frequency, can not be applied without compromising the stability of the loop. It was experimentally found, for instance, that a unity gain frequency lower than 6 Hz could not be adopted for the MICH loop.

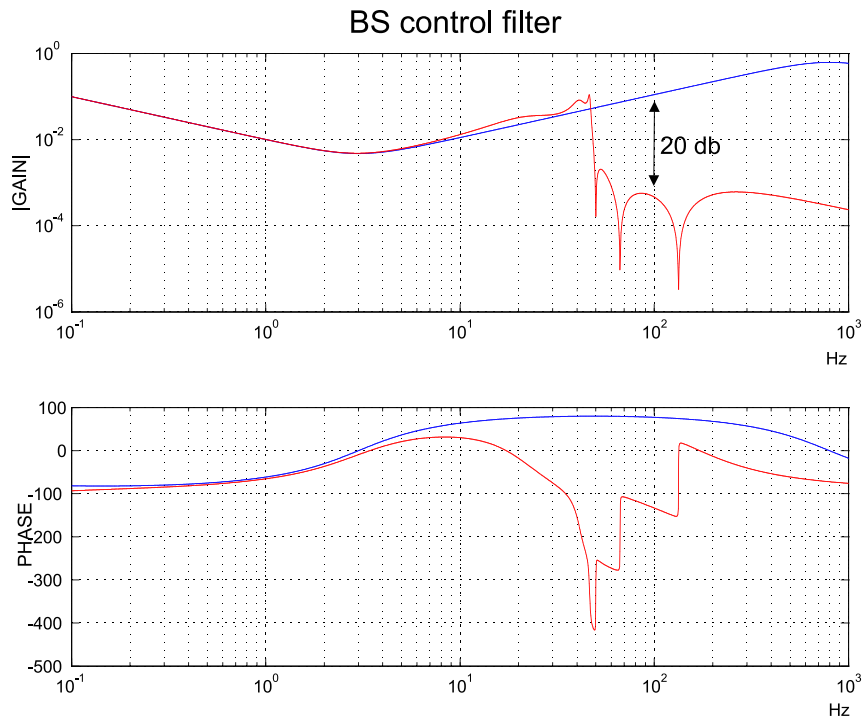


Figure 8.9: Comparison between the simple derivative filter used for lock acquisition (blue) and the 7<sup>th</sup> order elliptic filter applied to reduce the MICH control noise reintroduced in the dark fringe signal.

A similar filter was tested after C6 on the PRCL loop, with a roll-off at 100 Hz, in order to reduce the longitudinal control noise limiting the C6 sensitivity at a few hundreds of Hz (see C6 noise budget 8.6.2). It was not applied during C7 since the increasing of the modulation index (see section 8.5.1) made the longitudinal control noise of the PRCL loop not the noise source anymore in that frequency range.

### 8.5.3 Subtraction of the beam-splitter control noise

Aggressive filters to reduce the longitudinal control noise have to provide the required attenuation without compromising the loop stability. As shown in the previous section, a roll-off in the MICH control filter at frequency lower than 50 Hz could not be implemented, even if the MICH control noise limited the sensitivity up to lower frequencies.

One possible solution to overcome the problem of these strong requirements on the controller filters consists in applying the *noise subtraction technique*, as done in

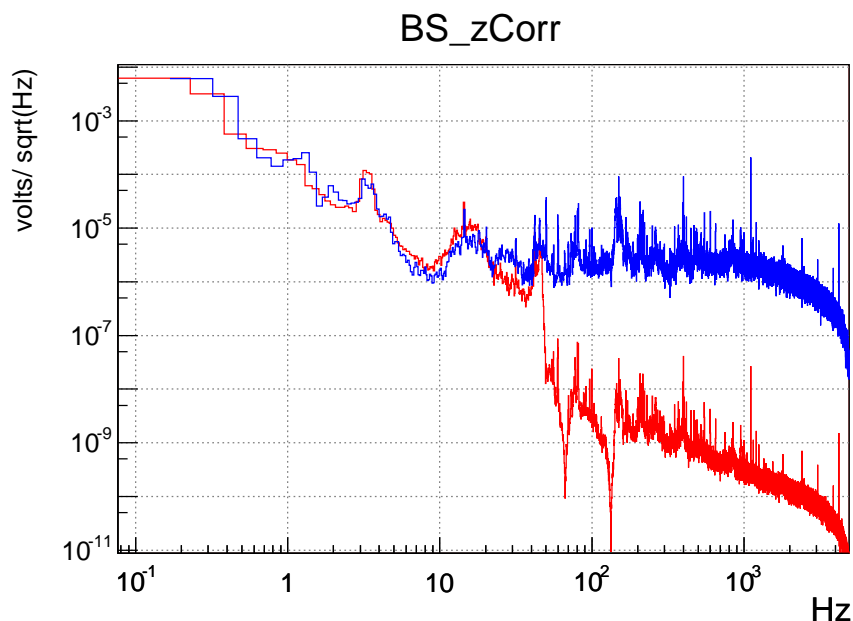


Figure 8.10: Spectrum of the correction signal applied on BS when the simple derivative filter is applied (blue), compared with the one given by the 7<sup>th</sup> order elliptic filter with a 50 Hz roll-off.

LIGO. This technique was adopted in C6 and C7 to subtract the BS control noise reintroduced in the dark fringe signal  $B1\_ACp$ , limiting the sensitivity below 50 Hz. The BS correction signal was added in differential mode to the end mirrors (see figure 8.5.3), in order to cancel the noise reintroduced by this signal at the dark port. In general, the coupling between the BS corrections and the end mirror correction is frequency dependent, where the applied strategy used a simple constant coupling coefficient  $\alpha$ .

Figure 8.5.3 shows the dark fringe signal  $B1\_ACp$  when the noise subtraction technique is applied: the contribution of the BS control noise to the dark fringe signal is suppressed by a factor 10 (see figure 8.5.3) in the frequency range between 10 Hz and 50 Hz.

In order to efficiently apply the subtraction technique, a fine measurement (with 90% of accuracy) of the coupling coefficient  $\alpha$  was needed<sup>6</sup>.

<sup>6</sup>This is in agreement with that observed in LIGO. In fact, in order to have an attenuation of the BS control noise of about 20 dB, the transfer functions ( $l_- \rightarrow B1\_ACp$ ) and ( $L_- \rightarrow B1\_ACp$ )

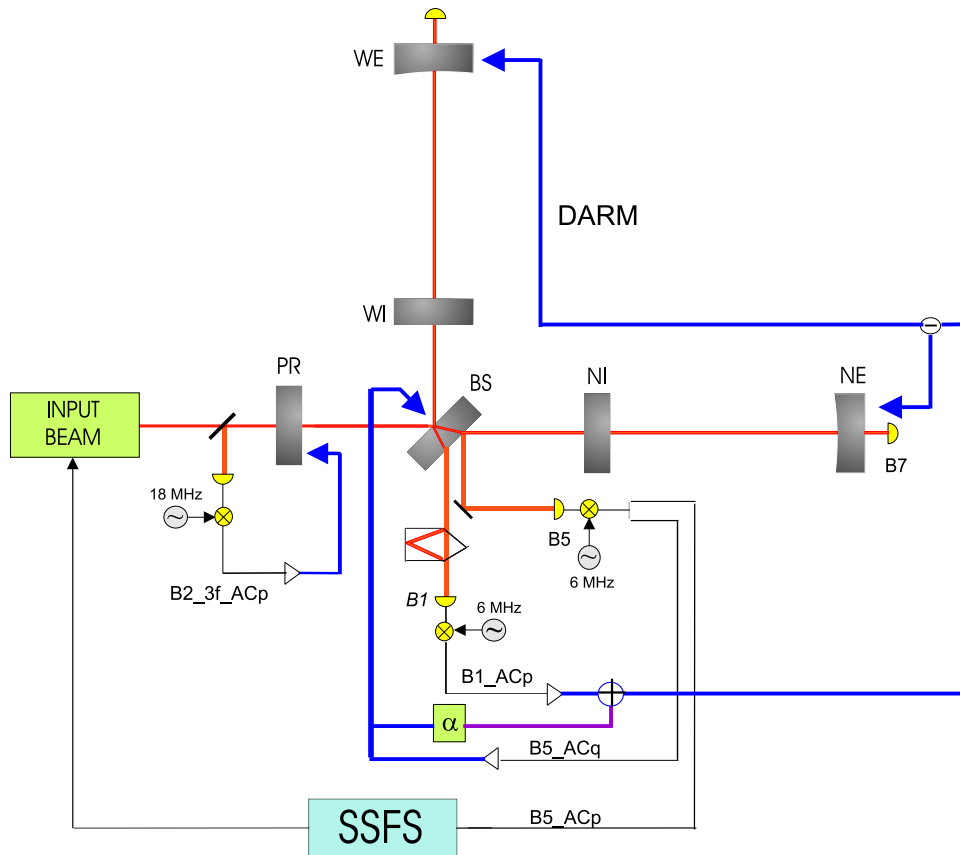


Figure 8.11: Locking scheme with the subtraction of the BS longitudinal control noise.

### 8.5.4 Next steps

Next possible steps in the longitudinal control noise reduction can be identified on the base of the previous discussions:

- the transition from the reflected  $3\Omega$ -demodulated signal to the  $\Omega$ -demodulated one was not successful, and the offset present in this signal was not understood. Further tests with the new injection bench will be needed in order to clarify this point;
- the optimization of the demodulation phases of the involved signals plays a crucial role also in reducing the coupling in the read-out phase between the different degrees of freedom. In particular, a deeper analysis of the  $B2.3f$  demodulation phase is needed. In fact, as discussed in 8.2, some instabilities

have to be known with 90% of accuracy [56].

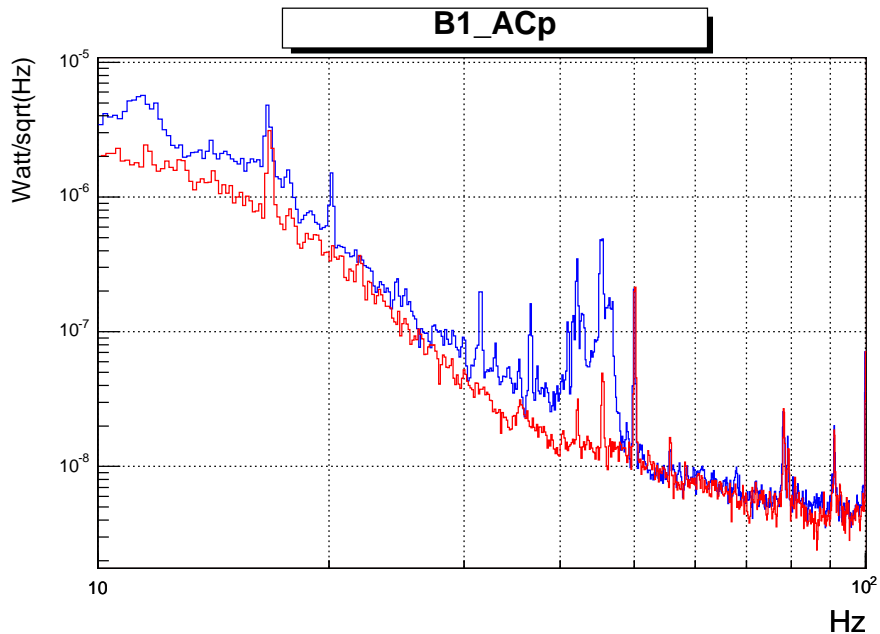


Figure 8.12: Dark fringe signal before (blue) and after (red) the subtraction of the BS longitudinal control noise.

of the ITF were connected with the tuning of this parameter. Moreover, in order to prevent any possible reintroduction of frequency noise in the MICH loop, a fine tuning of the *B5* demodulation phase might be needed as well<sup>7</sup>.

- the optimization of the subtraction of the BS control noise and possibly application of the same technique to subtract the PR control noise.

## 8.6 Commissioning run C6

The run C6 was a 14 days-long run (29th July - 12th August 2005). The C6 science mode configuration consisted of the ITF locked in recycled mode, as tested in C5, with the main difference of the implementation of the automatic alignment control system (as described in section 8.4), which greatly improved the detector stability making long term operations possible.

All the operations were automatically managed by ALP, so that the science mode configuration was automatically recovered, usually after only a few minutes.

<sup>7</sup>Both the components of B5 are involved in the locking scheme: *B5\_ACp* is the frequency servo error signal, *B5\_ACq* is used to control MICH.

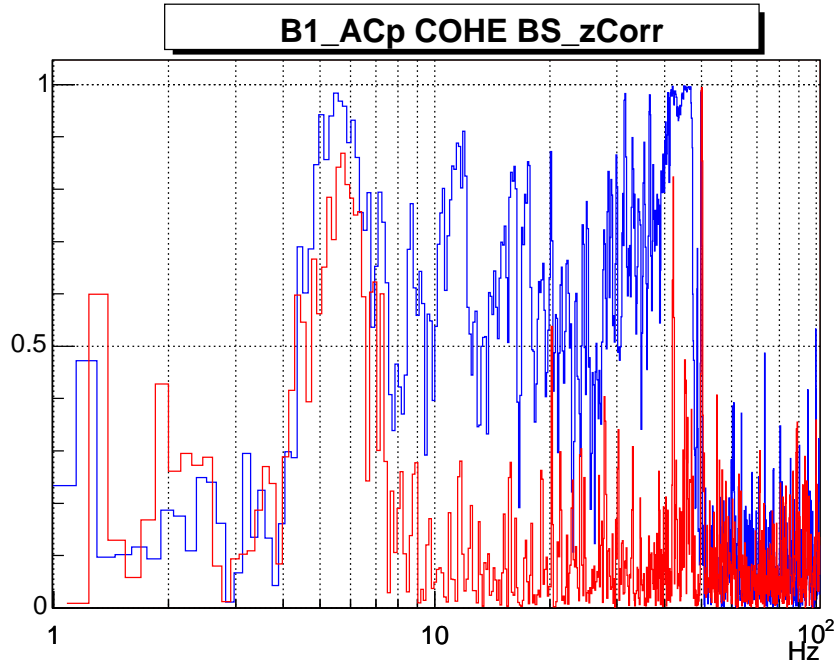


Figure 8.13: Coherence between the dark fringe signal and the BS longitudinal corrections before (blue) and after (red) the subtraction of the BS longitudinal control noise.

### 8.6.1 Duty-cycle and lock losses

The trend of the recycling power over the entire run is shown in figure 8.6.1.

The ITF was locked for about 90% of the time, with the longest continuous locked stretch being about 40 hours. The duty-cycle in *science mode* configuration was about 85%.

About 40 lock losses occurred during C6. They were all investigated. The main causes of unlock were found to be the followings:

- bad centering of one quadrant photo-detector, which caused drifts in the automatic alignment signals, introduced misalignments in the mirrors and eventually unlocked the ITF;
- saturations in the correction signals sent to the end mirrors. The low noise configuration for the coil drivers of the end mirrors reduced the dynamic range of the voltage applicable to the reference mass by a factor 25, so that the maximum range was  $-0.4 \pm 0.4$  Volts and even a small excess of seismic noise easily induced saturations in the correction signals. This problem was expected

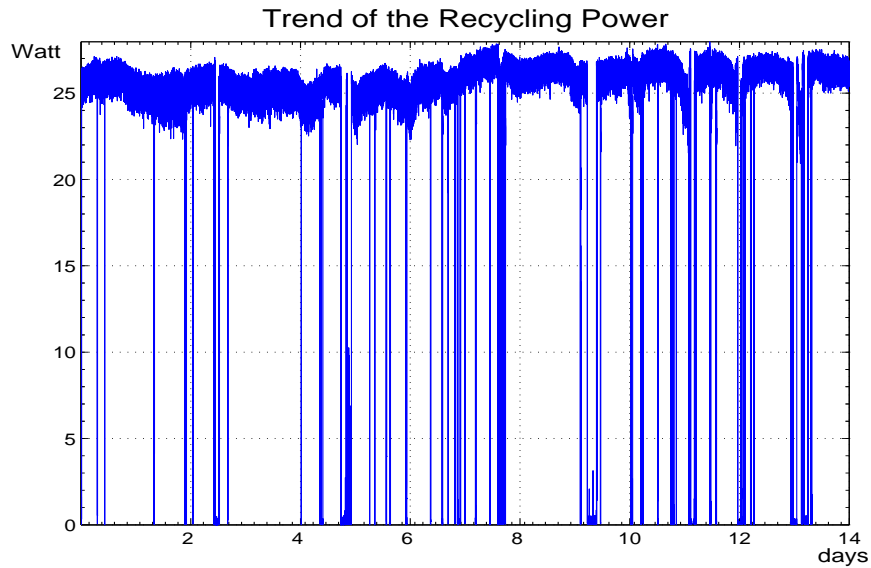


Figure 8.14: C6 recycling power trend.

to be fixed in the C7 run, by the full hierarchical control of the superattenuator, with the split of the longitudinal control to the marionette and the consequent reduction of the correction signals sent to reference mass.

- unlocks of the IMC.

### 8.6.2 C6 noise budget

As already said, several operations were performed in C6 in order to reduce the noise reintroduced into the dark fringe signal:

- the optimization of the local control system performance, in particular concerning the BS mirror, which made the ITF generally more stable, with a reduction of the coupling of the phase noise into the dark fringe signal above 1 kHz;
- the subtraction of the noise reintroduced into the dark fringe signal by the longitudinal BS control, in between 40 and 50 Hz;
- the implementation of a low noise configuration of mirrors' actuators, able to reduce the DAC noise around 100 Hz by a factor 25;

- more aggressive filtering for the BS longitudinal control loop, with a roll-off at 50 Hz (instead 100 Hz) preventing noise reintroduction at higher frequencies.

Moreover, the detector performance during the run suggested other possible improvements, mainly devoted to improving the sensitivity above 100 Hz:

- dumping of stray beams discovered in the NE bench, which caused an excess of noise in the sensitivity curve around 100-300 Hz;
- reduction of the power noise, which coupled into the dark fringe signal at few hundreds of Hz. The power noise reduction was performed improving the alignment of the main beam on the IMC, and changing the control scheme of the power stabilization loop;
- increase of the power impinging upon the photodiode B1, by changing the optical set-up. This reduced the electronic noise limiting the dark fringe signal by a factor  $\sqrt{2}$ , thereby improving the sensitivity at high frequency.

Thanks to all these actions, almost one order of magnitude was gained in sensitivity at the end of C6 relative to C5 8.7.1.

The noise budget is shown in figure 8.6.2.

The low frequency region of the sensitivity curve is limited by control noises. In particular, below 30 Hz the main contribution comes from mirror angular control noise, where between 30 and 50 Hz it is the BS longitudinal control noise that dominates. The actuator noise limits the sensitivity from 50 Hz to 200 Hz. Between 100 and 500 Hz a slight contribution is given also by the PR longitudinal control noise. The electronic noise and the shot noise of the B5 photodiode determine the level of the laser frequency noise, which limits the sensitivity above 600 Hz.

## 8.7 Commissioning run C7

The run C7 was five days long (14th September, 19th September). The alignment drift control used in C6 was replaced by an almost complete automatic alignment of the mirrors and the full hierarchical control was operating on the NE superattenuator. The duty cycle was around 65%. It decreased with respect to C6 mainly because of less favorable weather conditions and failures in the input mode-cleaner lock. Moreover, the increased complexity of the newly implemented control systems required further optimizations in order to guarantee stability and robustness to the detector. The trend of the recycled power during C7 is shown in figure 8.7.

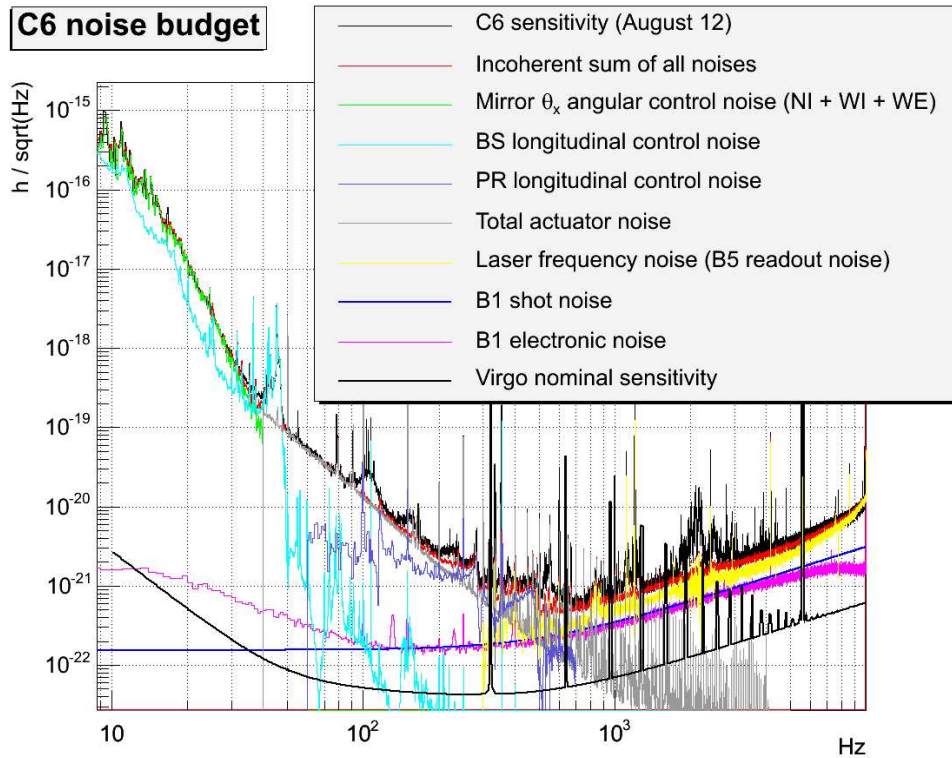


Figure 8.15: Noise budget in C6 [34].

With respect to C6, the sensitivity was improved across the whole spectrum:

- the implementation of the *automatic alignment* reduced by about a one order of magnitude the noise reintroduced below 50 Hz;
- the hierarchical control of the super attenuator allowed the electronics of the actuators to be further optimized, so as to reduce the contribution of the DAC noise up to 100 Hz. Moreover, the increase of the SNR of the  $B2.3f\_ACp$  signal reduced the contribution of the PR longitudinal control noise around 100 Hz;
- the increase of the modulation depth by a factor 2 and the optimization of the B5 optical set-up increased by a factor three the power impinging upon this photodiode, reducing the impact of the shot noise and electronic noise in the frequency servo error signal  $B5\_ACp$ . The result was an improvement by a factor 2 in the sensitivity curve.

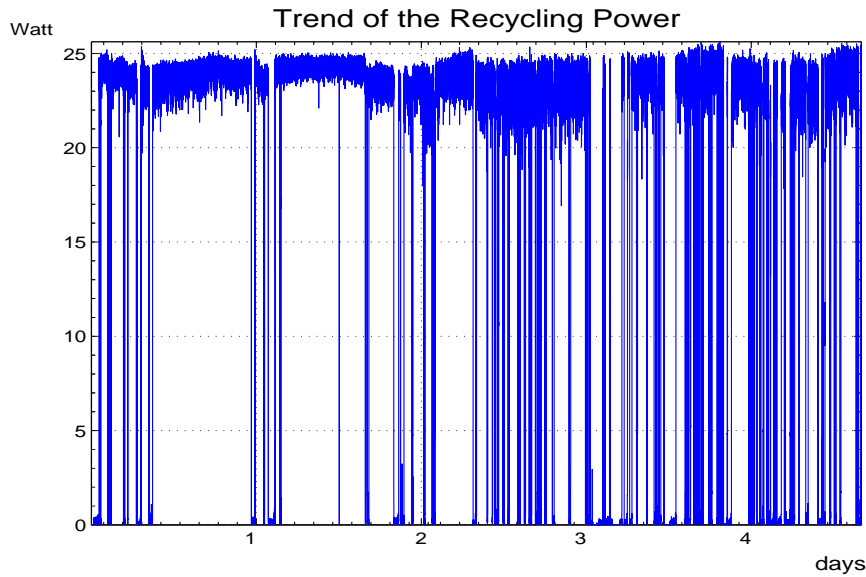


Figure 8.16: Trend of the recycling power during the 5 days-long C7 run.

The C7 noise budget is shown in figure 8.7. Up to 100 Hz longitudinal and angular control noises are still the main sources of noise. In the mid-frequency region (100-300 Hz) both control noises and photodiode readout noises contribute to the sensitivity curve, but a dominant noise source was not identified. Above 300 Hz the sensitivity floor is limited by the shot noise of the B1 and B5 photodiodes. Moreover, several structures visible above 400 Hz were connected with environmental noise in the laser laboratory, reintroduced into the dark fringe signal as laser frequency noise.

### 8.7.1 Noise hunting: next steps

Figure 8.7.1 summarizes progresses made in almost 1 year of commissioning to improve the performance of the Virgo recycled ITF.

Several actions are planned in order to improve the noise performance of the detector in the further stages of the commissioning activity:

- high frequency region (above 300 Hz) - The limiting sources are read-out noise (shot-noise of the dark fringe signal and of the frequency servo error signal). The main action will be to increase by a factor 10 with respect to C7 the incoming power, with the put in operation of the new injection bench;
- mid frequency region (between 100 and 300 Hz) - Different sources of noise were

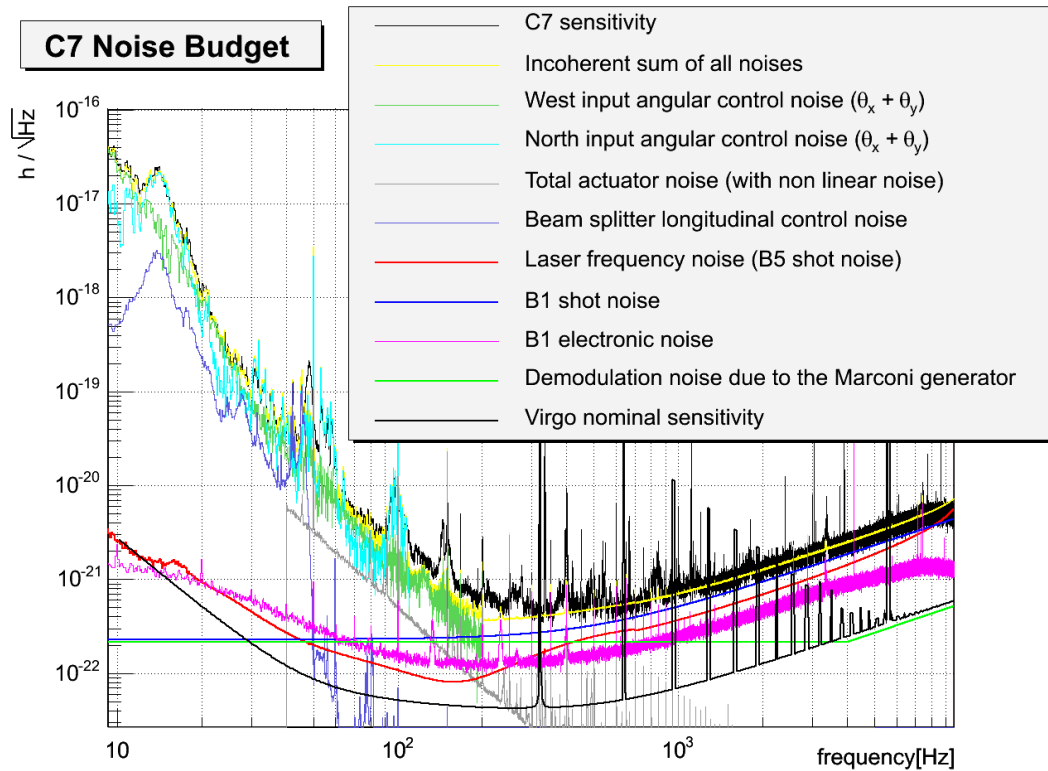


Figure 8.17: C7 noise budget [34].

identified, such as actuator noise, diffused light and acoustic noise. Several actions are already defined: the reduction of the actuator noise by means of improvements of the electronics, further investigations on the stray-beams at the end detection tables, better isolation of the laser laboratory and of the external detection bench in order to decrease the acoustic noise coupling into the dark fringe signal;

- low frequency region (below 100 Hz) - Angular and longitudinal control noises are still limiting the sensitivity. Concerning the angular noise, the final automatic alignment system was not yet implemented, so that during C7 the WI mirror was still under local control. Even with the final scheme running, the angular noise will need to be further reduced, mainly by optimizing the control filters, combining low bandwidth loops (100 mHz) with steeper roll-off so as to reduce the noise introduced in the detection band.

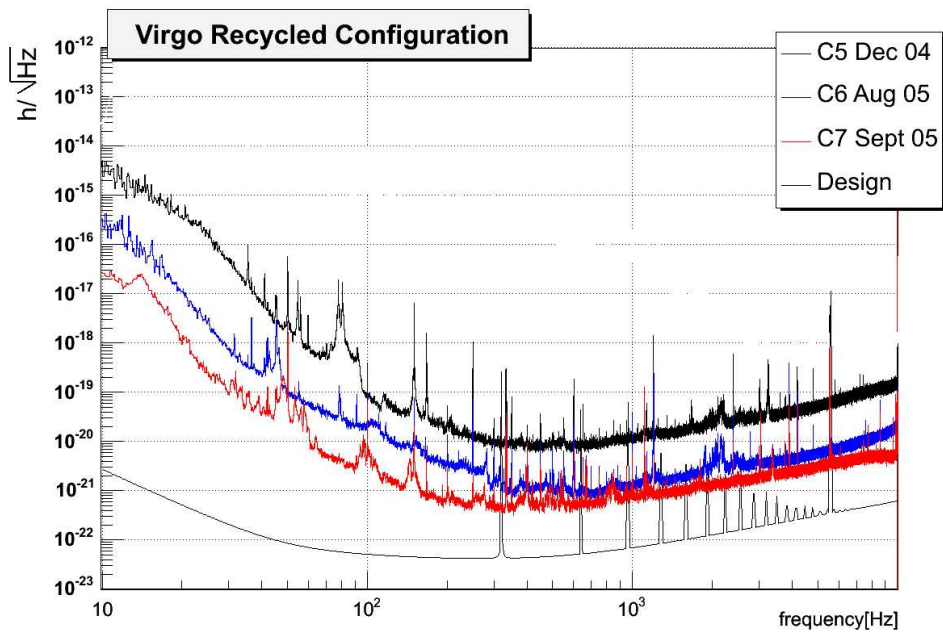


Figure 8.18: Sensitivity curves of the Virgo recycled ITF as measured in the commissioning runs C5, C6 and C7.

# Conclusion

The lock of the Virgo interferometer was achieved through an original technique, called *variable finesse lock acquisition*. Its design and implementation takes advantage of the preliminary commissioning steps (3 km cavity and recombined interferometer) and the solutions for interferometer control developed in other gravitational wave detectors. When possible, a real time simulation has been used as support for the experimental activity, mainly in order to test the locking algorithm but also to test their implementation in the Virgo real time control system.

The various difficulties encountered during the commissioning activity were also described, together with Virgo upgrades that they have driven. Once the interferometer was locked in a robust configuration, the reduction of the longitudinal control noises was addressed. Various changes were made to the detector and associated control systems which resulted in a significant improvement in sensitivity and duty-cycle.

The stability and noise level achieved during the commissioning run C7 allowed to reach for several hours an "horizon" for detecting 1.4-1.4 solar mass neutron stars at a distance of 1.5 Mpc with SNR of 8. Several studies for new noise sources ones could take place paving the way for sensitivity improvements. Full beam intensity has now been restored in the interferometer and it is expected that a soon a significantly better sensitivity will be achieved.



## Appendix A

# Definition of Acronyms

ITF	Interferometer
CITF	Central Interferometer
PR	Power Recycling mirror
BS	Beam-Splitter mirror
NI	North Input mirror
NE	North End mirror
WI	West Input mirror
WE	West End mirror
PRCL	Power Recycling Cavity Length
MICH	Michelson length
CARM	Common Arm length
DARM	Differential Arm length
SA	Superattenuator
AA	Automatic Alignment
IMC	Input Mode-Cleaner
IB	Input Bench
SSFS	Second Stage of Frequency Stabilization
OMC	Output Mode-Cleaner



## Appendix B

# Fabry-Perot cavities

A Fabry-Perot cavity formed by the input mirror  $IM$  and the end mirror  $EM$  is shown in figure B.1. The reflectivity and transmissivity amplitude of the two mirrors are connected by the relation:

$$r_1^2 + t_1^2 + L_1 = 1 \quad (\text{B.1})$$

$$r_2^2 + t_2^2 + L_2 = 1 \quad (\text{B.2})$$

where  $L_1$  and  $L_2$  are the losses of the input and end mirror respectively.

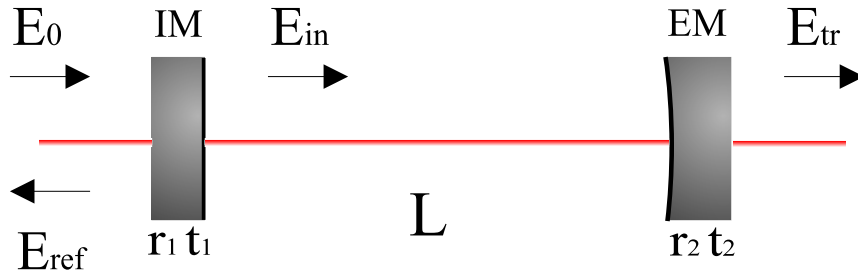


Figure B.1: Fields in the Fabry-Perot cavity.

Given  $E_{in} = Ee^{i\omega t}$  the electric field of the monochromatic input beam of angular frequency  $\omega$ , the stored field inside the cavity  $E_{sto}$  and the transmitted and reflected fields from the cavity,  $E_{tr}$  and  $E_{ref}$ , are described by the following equations:

$$E_{sto} = \frac{t_1}{1 - r_1 r_2 e^{i\Phi}} E_{in} \quad (\text{B.3})$$

$$E_{tr} = \frac{t_1 t_2 e^{i\Phi/2}}{1 - r_1 r_2 e^{i\Phi}} E_{in} \quad (\text{B.4})$$

$$E_{ref} = \frac{r_1 - r_2 (1 - L_1) e^{i\Phi}}{1 - r_1 r_2 e^{i\Phi}} E_0 \quad (\text{B.5})$$

where  $\Phi$  is the phase of the light accumulated in the round-trip between the two mirrors, placed at the distance  $L$ :

$$\Phi = \frac{2\omega L}{c} \quad (\text{B.6})$$

The resonance condition which maximizes the stored and the transmitted powers  $P_{sto} = |E_{sto}|^2$  and  $P_{tr} = |E_{tr}|^2$ , is given by:

$$\Phi = 0 \quad (\text{mod } 2\pi) \quad (\text{B.7})$$

At resonance they are:

$$P_{sto,res} = \frac{t_1^2}{(1 - r_1 r_2)^2} P_{in} \quad (\text{B.8})$$

$$P_{tr,res} = \frac{t_1^2 t_2^2}{(1 - r_1 r_2)^2} P_{in} \quad (\text{B.9})$$

With respect to the incoming power  $P_{in} = |E_{in}|^2 = |E|^2$ , the stored power inside the cavity is enhanced by the so-called *gain* of the cavity:

$$G = \frac{t_1^2}{(1 - r_1 r_2)^2} \quad (\text{B.10})$$

The Fabry-Perot cavity is usually characterized in terms of its finesse  $\mathcal{F}$ . It is defined as the ratio of the distance between two consecutive resonances and the full width at half maximum of a resonance (FWHM). For optical resonators, the reflectivity are generally chosen so that  $1 - r_1 r_2 \ll 1$  so that  $\mathcal{F}$  can be approximated as:

$$\mathcal{F} \simeq \frac{\pi \sqrt{r_1 r_2}}{1 - r_1 r_2} \quad (\text{B.11})$$

The distance in frequency and in length corresponding to the half width at half maximum (HWHM) of a resonance can be expressed in terms of  $\mathcal{F}$ . They are:

$$(\Delta L)_{HWHM} = \frac{\lambda}{4\mathcal{F}} \quad (\text{B.12})$$

$$(\Delta L)_{HWHM} = \frac{\lambda}{4L\mathcal{F}} \quad (\text{B.13})$$

## B.1 The reflected field

The most important characteristic of a Fabry-Perot is the phase behavior of the reflected light from the cavity, described by the complex reflectivity  $r_{arm}(\Phi)$ . According to equation B.3, it is defined as:

$$r_{arm}(\Phi) = \frac{r_1 - r_2(1 - L_1)e^{i\Phi}}{1 - r_1r_2e^{i\Phi}} \quad (\text{B.14})$$

At resonance:

$$r_{arm}(0) = \frac{r_1 - r_2(1 - L_1)}{1 - r_1r_2} \quad (\text{B.15})$$

Depending on the losses, three cases are possible:

- $r_1 - r_2(1 - L_1) = 0$ , **optimal-coupled cavity**

The reflected field at resonance is null. If  $P_1 = 0$ , this condition is verified when  $r_1 = r_2$ ;

- $r_1 - r_2(1 - L_1) < 0$ , **over-coupled cavity**

The incident and the reflected beam are de-phased by  $\pi$ . If  $P_1 = 0$ , this condition is verified when  $r_1 < r_2$ ;

- $r_1 - r_2(1 - L_1) > 0$ , **under-coupled cavity**

The incident and the reflected beam are in phase. If  $P_1 = 0$ , this condition is verified when  $r_2 < r_1$ .

When the light is resonant in the cavity, the phase  $\Psi_{ref}$  of the complex amplitude reflectivity is sensitive to the phase change  $\Phi$  of the light inside the cavity. Its derivative is in fact:

$$\frac{d\Psi_{rif}}{d\Phi} \simeq \frac{r_2[(1 - L_1) - r_1^2]}{(1 - r_1r_2)[r_1 + (1 - L_1)r_2]} \quad (\text{B.16})$$

Depending if the cavity is optimal-coupled, over-coupled or under-coupled, the phase change of the reflected field is amplified in a different way. In particular, it

is interesting to observe the amplification factor in case of over-coupled cavity. By assuming  $P_1 \simeq 0$  and according to the previous definition of  $\mathcal{F}$ :

$$\frac{d\Psi_{rif}}{d\Phi} \simeq \frac{2\mathcal{F}}{\pi} \quad (\text{B.17})$$

Under this assumptions, the amplification factor corresponds to the cavity gain  $G$ :

$$G \simeq \frac{2\mathcal{F}}{\pi} \quad (\text{B.18})$$

In particular, for the Virgo 3-km cavities,  $r_1 = 0.94$  and  $r_2 = 0.999975$ , so that  $\mathcal{F} = 50$  and  $G \simeq 30$ .

## B.2 Operating point

The operating point of the cavity can be defined in terms of its amplitude reflectivity and transmissivity for carrier and sidebands fields. They are derived from the formula reported in the previous section, specifying the relative round-trip-phase accumulated by the different fields inside the cavity. Carrier and sidebands fields can be considered to propagate independently: the carrier field propagates at a frequency  $\omega_0$ , and the  $n^{\text{th}}$ -order sideband fields propagate at frequencies  $\omega_0 \pm n\Omega$ .

For the carrier field (index 0):

$$r_{arm,0}(\Phi_0) = \frac{r_1 - r_2 e^{i\Phi_0}}{1 - r_1 r_2 e^{i\Phi_0}} \quad (\text{B.19})$$

$$t_{arm,0}(\Phi_0) = \frac{t_1 t_2 e^{i\Phi_0/2}}{1 - r_1 r_2 e^{i\Phi_0}} \quad (\text{B.20})$$

where:

$$\Phi_0 = \frac{2L\omega_0}{c} \quad (\text{B.21})$$

and the assumption of  $L_1 \simeq 0$  is done.

The reflected phase from the Fabry-Perot cavity is most sensitive when the carrier resonates inside the cavity. The resonance with respect to the carrier beam is verified if:

$$\Phi_{res,0} = \bar{\Phi}_0 = 0 \pmod{2\pi} \quad (\text{B.22})$$

With the carrier at resonance, the amplitude reflectivity and transmissivity of the cavity become minimized and maximized, respectively:

$$r_{arm,0}(\bar{\Phi}_0) = r_c = \frac{r_1 - r_2}{1 - r_1 r_2} \quad (\text{B.23})$$

$$t_{arm,0}(\bar{\Phi}_0) = \frac{t_1 t_2}{1 - r_1 r_2} \quad (\text{B.24})$$

In particular, with  $r_1 \ll r_2$  as in Virgo  $r_c \simeq -1$ .

The phase accumulated by  $n^{\text{th}}$ -order sidebands (index  $n$ ) is:

$$\Phi_n = \Phi_0 + n\gamma, \quad \gamma = \frac{2L\Omega}{c} \quad (\text{B.25})$$

With the carrier at resonance:

$$r_{arm,n}(\Phi_n) = \frac{r_1 - r_2 e^{in\gamma}}{1 - r_1 r_2 e^{in\gamma}} \quad (\text{B.26})$$

$$t_{arm,n}(\Phi_n) = \frac{t_1 t_2 e^{in\gamma/2}}{1 - r_1 r_2 e^{in\gamma}} \quad (\text{B.27})$$

The modulation frequency  $\Omega$  is chosen so that the arm cavities are near anti-resonant for the first-order sidebands (index 1) when the carrier resonates. Therefore:

$$\Phi_{anti,1} = \bar{\Phi}_1 \simeq \pi \pmod{2\pi} \quad (\text{B.28})$$

so that:

$$r_{arm,1}(\bar{\Phi}_1) = r_{arm,-1}(\bar{\Phi}_{-1}) = \frac{r_1 + r_2}{1 + r_1 r_2} \quad (\text{B.29})$$

$$t_{arm,1}(\bar{\Phi}_1) = -t_{arm,-1}(\bar{\Phi}_{-1}) = i \frac{t_1 t_2}{1 + r_1 r_2} \quad (\text{B.30})$$



## Appendix C

# Pound-Drever-Hall signals in the recombined ITF

The explicit calculation of the Pound-Drever-Hall signals extracted in reflection and in transmission of the recombined ITF is done here.

According to the formula introduced in section B.2, the amplitude reflectivity and transmissivity of the compound mirror for the first order sidebands are computed by considering that, with the carrier around resonance,  $p_{+,1} \simeq p_{+,-1} \simeq 1$  and  $p_{-,1} \simeq p_{-,-1} \simeq 0$ , so that:

$$r_{com,1}(\phi_{-,1}) \simeq \cos\left(\frac{\phi_{-,1}}{2}\right) = \cos\left(\frac{\phi_{-,0}}{2} + \frac{\Omega l_-}{c}\right) \quad (\text{C.1})$$

$$r_{com,-1}(\phi_{-,-1}) \simeq \cos\left(\frac{\phi_{-,-1}}{2}\right) = \cos\left(\frac{\phi_{-,0}}{2} - \frac{\Omega l_-}{c}\right) \quad (\text{C.2})$$

$$t_{comASY,1}(\phi_{-,1}) \simeq i \sin\left(\frac{\phi_{-,1}}{2}\right) = i \sin\left(\frac{\phi_{-,0}}{2} + \frac{\Omega l_-}{c}\right) \quad (\text{C.3})$$

$$t_{comASY,-1}(\phi_{-,-1}) \simeq i \sin\left(\frac{\phi_{-,-1}}{2}\right) = i \sin\left(\frac{\phi_{-,0}}{2} - \frac{\Omega l_-}{c}\right) \quad (\text{C.4})$$

### C.1 Asymmetric-Port signals

The Pound-Drever-Hall signals detected at the asymmetric port of the recombined ITF are now easily derived from the transmission coefficients previously written. Amplitudes of the fields are:

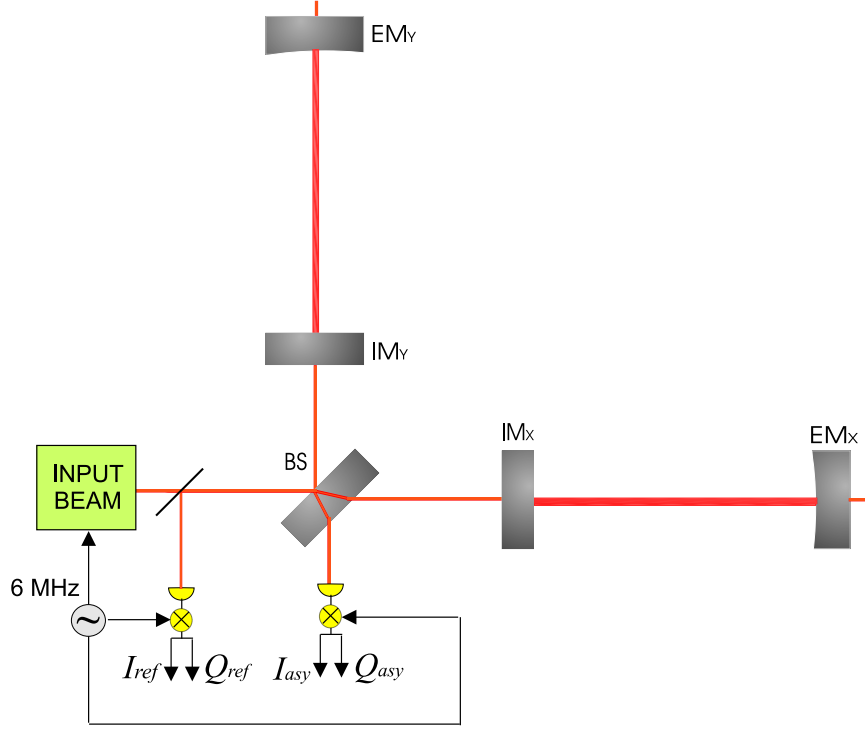


Figure C.1: Extraction of Pound-Drever-Hall signals in the recombined ITF

$$A_{asy1} = iEJ_1 t_{asy} \sin\left(\frac{\phi_{-,0}}{2} + \frac{\Omega l_-}{c}\right) \quad (\text{C.5})$$

$$A_{asy-1} = -iEJ_1 t_{asy} \sin\left(\frac{\phi_{-,0}}{2} - \frac{\Omega l_-}{c}\right) \quad (\text{C.6})$$

$$A_{asy0} = EJ_0 t_{asy} \left\{ p_{-,0} \cos\left(\frac{\phi_{-,0}}{2}\right) + ip_{+,0} \sin\left(\frac{\phi_{-,0}}{2}\right) \right\} \quad (\text{C.7})$$

where  $t_{asy}$  is the transmission path to the photo-detector placed at the asymmetric port.

For a common mode phase variation  $\Delta\Phi_+$ :

$$p_{-,0} \simeq 0 \quad (\text{C.8})$$

$$p_{+,0} \simeq r_c \left(1 + i\frac{2F}{\pi}\Delta\Phi_+\right) \quad (\text{C.9})$$

Moreover, the dark fringe for the carrier requires

$$\phi_{-,0} = 0 \Rightarrow A_{asy0} = 0$$

It means that there is not a Pound-Drever-Hall signal sensitive to  $\Delta\Phi_+$  at the asymmetric port.

For differential mode variation  $\Delta\Phi_+$ ,  $p_{+,0}$  vanishes and  $p_{-,0}$  can be written as:

$$p_{-,0} \simeq i \frac{r_c}{2} \frac{2F}{\pi} \Delta\Phi_- \quad (\text{C.10})$$

Then, by imposing the dark fringe for the carrier:

$$A_{asy1} \simeq iEJ_1t_{asy} \sin\left(\frac{\Omega l_-}{c}\right) \quad (\text{C.11})$$

$$A_{asy-1} \simeq iEJ_1t_{asy} \sin\left(\frac{\Omega l_-}{c}\right) \quad (\text{C.12})$$

$$A_{asy0} \simeq iEJ_0t_{asy} \frac{r_c}{2} \frac{2F}{\pi} \Delta\Phi_- \quad (\text{C.13})$$

So that:

$$[A_{asy-1}^* A_{asy0} + A_{asy0}^* A_{asy1}] \simeq t_{asy}^2 |E|^2 J_1 J_0 r_c \sin\left(\frac{\Omega l_-}{c}\right) \frac{2F}{\pi} \Delta\Phi_- \quad (\text{C.14})$$

The quadrature-phase component of the signal is zero, and the Pound-Drever-Signal is on the in-phase component:

$$I_{asy} \simeq t_{dark}^2 |E|^2 J_1 J_0 r_c \sin\left(\frac{\Omega l_-}{c}\right) \frac{2F}{\pi} \Delta\Phi_- \quad (\text{C.15})$$

$$= 2t_{dark}^2 |E|^2 J_1 J_0 r_c \frac{\omega_0}{c} \sin\left(\frac{\Omega l_-}{c}\right) \frac{2F}{\pi} \Delta L_- \quad (\text{C.16})$$

In order to study the response for a differential variation of the carrier phase inside the Michelson, the amplitudes fields can be simplified by considering that the resonance for the carrier inside the arms leads to  $p_{-,0} \simeq 0$  and  $p_{+,0} \simeq r_c$ :

$$A_{asy1} \simeq iEJ_1t_{asy} \sin\left(\frac{\phi_{-,0}}{2} + \frac{\Omega l_-}{c}\right) \quad (\text{C.17})$$

$$A_{asy-1} \simeq -iEJ_1t_{asy} \sin\left(\frac{\phi_{-,0}}{2} - \frac{\Omega l_-}{c}\right) \quad (\text{C.18})$$

$$A_{asy0} \simeq iEJ_0r_c t_{asy} \sin\left(\frac{\phi_{-,0}}{2}\right) \quad (\text{C.19})$$

Since  $A_{asy0}^* = -A_{asy0}$ ,

$$[A_{asy-1}^* A_{asy0} + A_{asy0}^* A_{asy1}] = A_{asy0} [A_{asy-1}^* - A_{asy1}] \quad (\text{C.20})$$

By considering a differential variation of the Michelson phase  $\Delta\phi_{-,0}$ , around the dark fringe condition:

$$\phi_{-,0} = \bar{\phi}_{-,0} + \Delta\phi_{-,0} \quad (\text{C.21})$$

with some algebra the in-phase Pound-Drever-Hall signal is obtained:

$$I_{asy} \simeq 2t_{asy}^2 |E|^2 J_1 J_0 r_c \sin\left(\frac{\Omega l_-}{c}\right) \frac{\omega_0}{c} \Delta l_- \quad (\text{C.22})$$

## C.2 Reflected port signals

The field amplitudes at the reflection port are obtained in the same way as done before at the asymmetric port, by using the reflection coefficients to find the amplitude of the reflected field detected by the photo-detector:

$$A_{ref1} \simeq E J_1 t_{ref} \cos\left(\frac{\phi_{-,0}}{2} + \frac{\Omega l_-}{c}\right) \quad (\text{C.23})$$

$$A_{ref-1} \simeq -E J_1 t_{ref} \cos\left(\frac{\phi_{-,0}}{2} - \frac{\Omega l_-}{c}\right) \quad (\text{C.24})$$

$$A_{ref0} \simeq E J_0 t_{ref} \left\{ p_{+,0} \cos\left(\frac{\phi_-}{2}\right) + i p_{-,0} \sin\left(\frac{\phi_-}{2}\right) \right\} \quad (\text{C.25})$$

where  $t_{ref}$  is the transmission path to the phot-detector.

The same approximations done before have then to be applied in order to study the response of the ITF to small phase variations around the working point.

For common mode variation  $\Delta\Phi_+$ , the approximations are here summarized:

$$p_{-,0} \simeq 0 \quad (\text{C.26})$$

$$p_{+,0} \simeq r_c \left( 1 + i \frac{2F}{\pi} \Delta\Phi_+ \right) \quad (\text{C.27})$$

$$\phi_{-,0} \simeq 0 \quad (\text{C.28})$$

The fields amplitude are therefore:

$$A_{ref1} \simeq EJ_1 t_{ref} \cos\left(\frac{\Omega l_-}{c}\right) \quad (\text{C.29})$$

$$A_{ref-1} \simeq -EJ_1 t_{ref} \cos\left(\frac{\Omega l_-}{c}\right) \quad (\text{C.30})$$

$$A_{ref0} \simeq EJ_0 t_{ref} r_c \left(1 + i \frac{2F}{\pi} \Delta\Phi_+\right) \quad (\text{C.31})$$

and

$$[A_{ref-1}^* A_{ref0} + A_{ref0}^* A_{ref1}] = A_{ref1} [A_{ref0}^* - A_{ref0}] \quad (\text{C.32})$$

The real part vanishes, so that:

$$Q_{ref} \propto 8|E|^2 J_1 J_0 t_{ref}^2 r_c \cos\left(\frac{\Omega l_-}{c}\right) \frac{2F}{\pi} \frac{\omega_0}{c} \Delta L_+ \quad (\text{C.33})$$

For a differential mode variation  $\Delta\Phi_-$ ,  $A_{ref0} \simeq 0$ , so that there is any Pound-Drever-Hall signal associated to this degree of freedom at the reflected port.

In order to study the response for a differential variation of the carrier phase inside the Michelson:

$$p_{-,0} \simeq 0 \quad (\text{C.34})$$

$$p_{+,0} \simeq r_c \quad (\text{C.35})$$

therefore:

$$A_{ref1} \simeq EJ_1 t_{ref} \cos\left(\frac{\phi_{-,0}}{2} + \frac{\Omega l_-}{c}\right) \quad (\text{C.36})$$

$$A_{ref-1} \simeq -EJ_1 t_{ref} \cos\left(\frac{\phi_{-,0}}{2} - \frac{\Omega l_-}{c}\right) \quad (\text{C.37})$$

$$A_{ref0} \simeq EJ_0 t_{ref} r_c \cos\left(\frac{\phi_{-,0}}{2}\right) \quad (\text{C.38})$$

By making the substitution  $\phi_{-,0} \simeq \bar{\phi}_{-,0} + \Delta\phi_{-,0}$  and developing the usual computation, it is found that only the real part survives, and the Pound-Drever-Hall signal has the same structure of the Michelson signal obtained in transmission:

$$I_{ref} \propto 2t_{ref}^2 |E|^2 J_1 J_0 r_c \sin\left(\frac{\Omega l_-}{c}\right) \frac{\omega_0}{c} \Delta l_- \quad (\text{C.39})$$



# Bibliography

- [1] J.Taylor et al., *Nature* **355** 133 (1992)
- [2] G.F. Moss, L.R. Miller, and R.L. Forward. *Photon-noise-limited laser transducer for gravitational antenna*, *Applied Optics* **10** 2495–2498 (1971)
- [3] D.Sigg (for the LIGO Science Collaboration), *Status of the LIGO detectors* *Class. Quantum Grav.* **23** S51-S56 (2006)
- [4] H. Lück et al., *Status of the GEO600 detector*, *Class. Quantum Grav.* **23** S71-S78 (2006)
- [5] K. Arai for the TAMA collaboration, *Current efforts on the TAMA300 detector* Amaldi 6th (2005)  
[http://tamago.mtk.nao.ac.jp/amaldi6/05.dcd/Tue1330\\_karai\\_amaldi6\\_rev2.pdf](http://tamago.mtk.nao.ac.jp/amaldi6/05.dcd/Tue1330_karai_amaldi6_rev2.pdf)
- [6] F Acernese et al., *The Status of Virgo*, *Class. Quantum Grav.* **23** S63-S69 (2006)
- [7] C.Palomba, *Detectability of Gravitational Radiation from Prompt and Delayed Star Collapse to a Black Hole* (2000)  
[http://arxiv.org/PS\\_cache/astro-ph/pdf/0003/0003321.pdf](http://arxiv.org/PS_cache/astro-ph/pdf/0003/0003321.pdf)
- [8] E.Muller, *Class Quantum Grav.* **14** 1455 (1997)
- [9] J.H.Taylor, R.M. Manchester and A.G. Lyne, *The Astrophysical journal supplement series* **88** 529–568 (1993)
- [10] V.Kalogera et. al., *The Coalescence Rate of Double Neutron Star Systems* *Astrophys. J.* **556** 340-356 (2001) (and references therein)
- [11] E. Nakar, A. Gal-Yam and D. B. Fox, *The Local Rate and the Progenitor Lifetime of Short-Hard Gamma-Ray Bursts: Synthesis and Predictions for LIGO* (2005), [http://www.arxiv.org/PS\\_cache/astro-ph/pdf/0511/0511254.pdf](http://www.arxiv.org/PS_cache/astro-ph/pdf/0511/0511254.pdf)

- [12] B.Schutz, *Gravitational wave astronomy*, Class Quantum Grav. **16** A131 (1999)
- [13] L.P.Grishchuk et al., Phys.Usp. **44** 1-51 (2001); Usp.Fiz.Nauk **171** 3-59 (2001)  
[http://www.arxiv.org/PS\\_cache/astro-ph/pdf/0008/0008481.pdf](http://www.arxiv.org/PS_cache/astro-ph/pdf/0008/0008481.pdf)
- [14] P.S.Saulson, *Fundamentals of Interferometric Gravitational Wave Detectors*, World Scientific Publishing (1994)
- [15] J.Y. Vinet et al, *Optimization of long-baseline optical interferometers for gravitational-wave detection* Phys. Rev. D **38** 433 (1988)
- [16] Peter Fritschel et al, *Demonstration of recycling technique in a Michelson Interferometer with Fabry-Perot cavities*, Applied Optics **31** 1412 (1992)
- [17] Virgo Collaboration, *Final Design Report*, not published (1997)
- [18] H.B. Callen and T.A. Welton, Physical Review **83** (1), 34-40 (1951)
- [19] P.R. Saulson, *Thermal noise in mechanical experiments*, Physical Review D **42** 2437-2445 (1990)
- [20] R. Flaminio et al., *The commissioning of the central interferometer of the Virgo gravitational wave detector* Astroparticle Physics **21** 1 – 22 (2004)
- [21] R.V.Pound, *Electronic Frequency Stabilization of Microwave Oscillators*, Rev. Sci. Instrum. **17** 490–505 (1946)
- [22] R.W.P.Drever et al., *Laser phase and frequency stabilization using an optical resonator*, Appl. Phys. B: Photophys. Laser Chem. **31** 97–105 (1983)
- [23] F. Bondu, *Design of the last stage of frequency stabilisation and laser frequency noise requirements*, Virgo internal note VIR-NOT-OCA-1390-227, (2002)
- [24] F. Bondu et M. Barsuglia, *Laser Frequency Stabilization Topology*, Virgo internal note VIR-NOT-OCA-1390-247, (2003)
- [25] S.Braccini et al., *Measurement of the VIRGO superattenuator performance for seismic noise suppression*, Rev.Sci.Instr **72** 3643-3652 (2001)
- [26] S.Braccini et al., *Measurement of the transfer function of the steering filter of the VIRGO super attenuator suspension*, Rev.Sci.Instr **72** 3635-3642 (2001)

- [27] G.Losurdo et al., *Inertial control of the mirror suspensions of the VIRGO interferometer for gravitational wave detection*, Rev.Sci.Instr Rev.Sci.Instrum. **72** 3653-3661 (2001)
- [28] F.Cavalier, *Le Contrôle Global de Virgo*, Thèse d'Habilitation à diriger des Recherches, Université Paris XI Orsay (2001)
- [29] F.Cavalier et al., *The Global control of the Virgo experiment*, Nuclear Instruments and Methods in Physics Research **550** 467–489 (2005)
- [30] E. Morrison, B. .J. Meers, D. I. Robertson and H. Ward, *Automatic alignment of optical interferometers*, Appl. Opt. **33** 5041-5049 (1994)
- [31] D. Z. Anderson, *Alignment of resonant optical cavities*, Appl. Opt. **23** 2944–2949 (1984)
- [32] L.Derome, *Le système de détection de l'expérience VIRGO dédiée à la recherche d'ondes gravitationnelles*, PhD Thesis, Université de Savoie (1999)
- [33] R.Flamínio, R.Gouaty, E.Tournefier *Analysis of the sensitivity of the recycled interferometer during C5, C6 and C7 runs*, Virgo internal note VIR-NOT-LAP-1390-313 (2006)
- [34] R. Gouaty, *Analyse de la sensibilité du détecteur d'ondes gravitationnelles Virgo*, Thèse de doctorat, Université de Savoie (2006), to be published
- [35] R. Adikhari *Sensitivity and Noise Analysis of 4 km Laser Interferometric Gravitational Wave Antennae*, PhD Thesis, MIT (2004)
- [36] D. Babusci, H. Fang, G. Giordano, G. Matone, L. Matone, V. Sannibale, *Alignment procedure for the VIRGO interferometer: experimental results from the Frascati prototype*, Phys. Lett. A **226**, 31-40 (1997)
- [37] F. Acernese et al., *The Virgo automatic alignment system*, Class. Quantum Grav. **23** S91-S101 (2006)
- [38] M. Barsuglia, L. Di Fiore, G. Giordano, D. Passuello, *Definition of band-width and slope of the servo-loop for SA control*, Virgo internal note, VIR-NOT-NAP-1390-143
- [39] P. La Penna, *Studio di cavità ottiche nell'esperimento Virgo e per misure di rumore termico*, PhD Thesis, Pisa University (1997) and references there in.

- [40] Torrey T. Lyons, *An Optically Recombined Laser Interferometer for Gravitational Wave Detection*, PhD Thesis, Caltech (1997)
- [41] M.W.Regehr, *Signal Extraction and control for an Interferometric Gravitational Wave Detector*, PhD Thesis, Caltech (1995)
- [42] L.Matone, *Etude du Contrôle Global de l'Interferometre Central de VIRGO*, PhD Thesis, UNIVERSITE DE PARIS-SUD Centre d'Orsay (1999)
- [43] M.Ando, *Current Status of the TAMA300 interferometer*, 2<sup>nd</sup> TAMA Workshop (October 1999, Tokyo)
- [44] M.Evans, *Lock Acquisition in Resonant Optical Interferometers*, PhD Thesis, Caltech (2001)
- [45] M.Evans et al., *Lock acquisition of a gravitational-wave interferometer*, Opt. Lett. **27(8)** 598–600 (2002)
- [46] P. Fritschel *et al.*, *Readout and control of a power-recycled interferometric gravitational wave antenna*, LIGO note, LIGO-P000008-A-D (2000)
- [47] K.Arai and TAMA collaboration, *Sensing and controls for power-recycling of TAMA300*, *Class.Quant.Grav.* **19(7)**, 1843–1848 (2002)
- [48] K.Arai, *Robust extraction of control signals for power-recycled interferometric gravitational-wave detectors*, PhD Thesis (2001).
- [49] B.Caron et al., *SIESTA, a Time Domain, General Purpose Simulation Program for the VIRGO Experiment* VIR-TRE-LAP-5700-101 issue 1 (1998)
- [50] Virgo collaboration, *Measurement of the optical parameters of the Virgo interferometer*, to be published
- [51] S.Kreckelbergh, *Contrôle longitudinal caractérisation optique du détecteur VIRGO*, PhD Thesis, Université Paris Sud - Orsay (2005)
- [52] Virgo Collaboration, *Results of the Virgo central interferometer commissioning*, Proceedings Amaldi 5, *Class.Quantum Grav.* **21** (2004) 395-S402
- [53] P.Rapagnani, *private communication*
- [54] A.Brillet, *private communication*
- [55] E.Tournefier, *private communication*

[56] M.Evans, *private communication*